Technical Report

TR-13-21

# Prototype Repository

## Hydro-mechanical, chemical and mineralogical characterization of the buffer and tunnel backfill material from the outer section of the Prototype Repository

Siv Olsson, Viktor Jensen, Lars-Erik Johannesson,
Emelie Hansen, Ola Karnland
Clay Technology AB

Sirpa Kumpulainen, Leena Kiviranta
B+Tech Oy

Daniel Svensson, Svensk Kärnbränslehantering AB

Staffan Hansen, LTH

Johan Lindén, Åbo Akademi

September 2013

**Svensk Kärnbränslehantering AB**
Swedish Nuclear Fuel
and Waste Management Co

Box 250, SE-101 24 Stockholm
Phone +46 8 459 84 00

ISSN 1404-0344
SKB TR-13-21
ID 1405798

# Prototype Repository

## Hydro-mechanical, chemical and mineralogical characterization of the buffer and tunnel backfill material from the outer section of the Prototype Repository

Siv Olsson, Viktor Jensen, Lars-Erik Johannesson,
Emelie Hansen, Ola Karnland
Clay Technology AB

Sirpa Kumpulainen, Leena Kiviranta
B+Tech Oy

Daniel Svensson, Svensk Kärnbränslehantering AB

Staffan Hansen, LTH

Johan Lindén, Åbo Akademi

September 2013

# Abstract

The Prototype Repository field test at Äspö Hard Rock Laboratory is a full-scale experiment simulating conditions relevant for the Swedish KBS-3 concept for final disposal of high-level radioactive waste. According to the concept the spent fuel will be stored in copper canisters enclosed by bentonite buffers and positioned in deposition holes at a depth of ~ 500 m in crystalline rock. The major aims of the project are to test engineered barriers, primarily buffers, backfill and plugs, and develop models for predicting and evaluating their functions and performance.

The Prototype gallery consisted of six deposition holes and was divided into two sections, containing four and two holes, respectively. Each deposition hole had a full-scale buffer of compacted bentonite (MX-80) surrounding a copper canister equipped with heaters to simulate the heat generation from radioactive waste. Required functions of the buffer are to serve as mechanical support for the canister and to act as barrier to water flow across the deposition hole. A buffer of highly compacted bentonite is considered to fulfill these requirements thanks to favourable hydro-mechanical and chemical properties, such as low hydraulic conductivity, good swelling ability, and high cation retention capacity. The stability of the bentonite when subjected to elevated temperatures and hydration by more or less saline groundwater is, however, of vital importance for the long-time performance of the buffer. The present laboratory investigations of the two buffers from the outer section (deposition holes 5 and 6), retrieved in 2010–2011 after about 8 years of hydrothermal exposure, aim at improving the understanding of the hydro-mechanical and chemical behavior of bentonite buffers at temperatures around 100°C during the water saturation transient. In the first part of this report the hydro-mechanical, chemical and mineralogical properties of the bentonite before and after the field experiment are compared in order to assess how the 8-year-long hydrothermal experiment affected the bentonite buffer.

None of the two buffers was homogeneous after almost 8 years of wetting and large variations in water saturation existed, both between the deposition holes, between blocks from the same hole, and also within one and the same block. The maximum temperature had never exceeded ~ 85ºC during the test period and higher temperature had been maintained for longer time in deposition hole 5 than in deposition hole 6.

Hydro-mechanical tests were performed on samples from one radial profile from the warmest part of each of the buffers and included determinations of hydraulic conductivity, swelling pressure, unconfined compression strength, and shear strength. Chemical-mineralogical analyses were carried out in parallel at two different laboratories on four radial profiles from three blocks with variable water content (one block from deposition hole 5 and two from deposition hole 6). The analyses included determinations of water-soluble salts, chemical composition, cation exchange capacity, exchangeable cations, and mineralogy. When relevant, both the bulk samples and the Na-converted < 0.5 µm fractions of the bentonite were analyzed. Supplementary, specialized analyses, including determinations of the oxidation state of iron and copper (Mössbauer, XANES) and element mapping (SEM-EDX), were performed on selected intervals of some blocks. The same tests/analyses were made on reference samples.

The main results were as follows:

- No large variations were observed in the swelling pressure of the reference bentonite and the field-exposed bentonite.
- Trimmed specimens of the field-exposed bentonite had somewhat lower hydraulic conductivity than the reference specimens, especially at higher densities. The changes observed were not correlated to the position of the samples in the buffer, and thus, not to the maximum temperature to which the samples had been exposed.
- The triaxial tests showed that the deviator stress at failure was larger and the strain at failure lower for the field-exposed specimens than for the reference specimens, indicating a more brittle behaviour of the field-exposed bentonite.

- The unconfined compression tests showed no large differences in strength between the reference specimens and the field-exposed material. The strain at failure suggested that the field-exposed bentonite was somewhat more brittle than the reference bentonite and the brittle behavior was more pronounced for specimens taken close to the canister.
- Due to the wetting with groundwater (~ 8,000 mg Cl/L) the chloride concentration in the three saturated profiles had increased. Soluble accessory minerals in the bentonite, mainly gypsum but also calcite in one profile, had been redistributed and re-precipitated close to the canister. The chloride and sulfate concentrations in the "driest" profile had remained at the level of the reference bentonite.
- The major change in the exchangeable cation pool was a small but general loss in magnesium relative to the reference concentration in a large part of all four profiles investigated.
- Non-exchangeable magnesium in bulk samples had increased relative the reference level in the inner parts of all four profiles investigated, suggesting a transfer of magnesium along the thermal gradient, and accumulation in the warmest part of the buffer. The sink for magnesium could not be identified, but the Mg-bearing phase was apparently of low solubility, since the magnesium content was elevated also in the Na-converted < 0.5 μm fractions of most of the profiles.
- The FTIR-and XRD-characteristics, the calculated structural smectite formulae, and the CEC properties of purified, Na-converted < 0.5 μm fractions provided no evidence of any structural changes in the montmorillonite. All formula calculations were, however, based on the assumption that all magnesium in the chemical analyses was in the octahedral sheet of the smectite, and it remains to establish whether this allocation of magnesium has a true structural foundation, or whether a neoformed phase is the sink for magnesium.
- Samples of the canister/bentonite interface (~ 1 mm thick samples) had elevated copper concentrations in all blocks, but the maximum concentration in the profiles was variable, ranging from 35 to 670 ppm Cu. Area analyses (50 μm × 50 μm) performed from the canister/bentonite interface to a depth of ~ 1 mm by use of SEM-EDX showed that copper was irregularly distributed - the copper content ranged from background values up to a few weight % in nearby areas. Copper existed mainly in an insoluble, non-exchangeable form and, according to Cu K XANES spectra, copper was probably present as Cu(0), Cu(I) or as a copper sulfide.
- Mössbauer and Fe K XANES spectra both indicated an increase of Fe(II) in the field-exposed bentonite, indicating reduction of iron under field conditions.

The changes in hydro-mechanical properties of the bentonite and the main geochemical reactions highlighted in the investigation of the Prototype Repository buffer are in most respects qualitatively analogous to those observed in other field tests with buffers of MX-80 bentonite and heaters/canisters of copper.

The tunnel above the deposition holes was backfilled with a mixture of bentonite from Milos, containing mainly calcite and dolomite in addition to smectite, and 70% ballast of crushed granodioritic rock and each tunnel section was sealed with a plug of concrete. Numerous laboratory and field observations have demonstrated that the reactions in concrete will generate a diffusive hyper-alkaline plume, which will modify the porewater chemistry in the bentonite near a concrete/bentonite interface. Apart from cation exchange reactions, reactions between the fluid and smectite and/or other minerals in the bentonite may occur over time, and secondary phases may precipitate.

The second part of the report presents chemical and mineralogical characteristics of the tunnel backfill material in the vicinity of one of the concrete plugs. Basically, the same chemical and mineralogical parameters were determined for the samples of the tunnel backfill as for the buffer bentonite. The investigations of the < 1 mm and the < 0.5 μm fractions of the backfill material, sampled within the interval 0–16 cm from the inner concrete plug, suggested that some modification of the backfill mineralogy had occurred:

- Exchangeable magnesium and calcium had been replaced primarily by sodium in the vicinity of the concrete.
- Neoformed calcite and an apparently amorphous Mg-phase of low solubility had precipitated in the innermost centimeters of the backfill. These precipitation reactions must have exerted control on the pore fluid composition, and hence, on the pool of exchangeable cations in the backfill material

- XRD-data for the < 1 mm fractions indicated that the increase in calcite in the innermost centimeters of the backfill was paralleled by dissolution of dolomite. XRD-data for the < 0.5 μm fractions suggested that also fine-grained chlorite, quartz and feldspars were partially dissolved in the samples proximal to the concrete.
- No secondary phases were detected in the < 0.5 μm fractions, but several of the potential reaction products tend to be poorly crystalline and their detection by XRD-analysis is therefore generally problematic. The secondary Mg-phase in the samples proximal to the concrete was thus identified only through a substantial increase in the MgO-content of the Na-converted, carbonate-free < 0.5 μm fractions.
- CEC of < 0.5 μm fraction had increased by 10 meq/100 g in the sample at the concrete, but tests of the expansion behavior and of the charge distribution in the smectite provided no clear evidence of any structural changes of the smectite. The cation exchange properties of the secondary Mg-phase is not known and other, undetected, secondary phases with exchange capacity might have formed.

The backfill material for the Prototype Repository consisted of a large proportion of crushed rock mixed with bentonite, and was compacted *in situ* in the tunnel. The technique for backfilling the deposition tunnels has been changed since the installation of Prototype and according to the current reference technique, pre-compacted bentonite blocks will be used, together with a filling of bentonite pellets close to the tunnel walls. Thus, the hydro-mechanical and chemical-mineralogical properties of the currently recommended backfill material will be different from those of the backfill used in the Prototype Repository test.

# Contents


**1 Introduction** 9
1.1 Prototype Repository experiment 9
1.2 The bentonite buffers 15
1.2.1 Test philosophy 15
1.2.2 Sampling 16
1.3 The tunnel backfill material 18
1.3.1 Test philosophy 18
1.3.2 Sampling 19

**2 Hydro-mechanical analyses on the buffer material** 21
2.1 General 21
2.1.1 Basic geotechnical properties 21
2.2 Hydraulic conductivity and swelling pressure 22
2.2.1 General 22
2.2.2 Test equipment 22
2.2.3 Preparation of specimen and the test procedure 22
2.2.4 Results 23
2.2.5 Discussion 26
2.3 Triaxial tests 29
2.3.1 General 29
2.3.2 Test equipment 29
2.3.3 Preparation of specimen and test procedure 29
2.3.4 Results 30
2.3.5 Discussion 32
2.4 Unconfined compression test 33
2.4.1 General 33
2.4.2 Test equipment 33
2.4.3 Preparation of specimen and test procedure 33
2.4.4 Results 35
2.4.5 Discussion 39
2.5 Summary of the hydro-mechanical analyses 42

**3 Chemical and mineralogical analyses of the bentonite buffer** 45
3.1 Introduction 45
3.2 Materials and methods 45
3.2.1 Sampling 46
3.2.2 Sample preparation 49
3.2.3 Aqueous leachates 49
3.2.4 Chemical analysis of bentonite and purified, homoionic Na-clay 49
3.2.5 Cation exchange capacity (CEC) and exchangeable cations (EC) 50
3.2.6 X-ray diffraction analysis (XRD) 50
3.2.7 Optical microscopy of coarse fractions 52
3.2.8 Scanning Electron Microsopy (SEM) 52
3.2.9 Fourier transform infrared spectroscopy (FTIR) 52
3.2.10 Mössbauer analysis 53
3.2.11 XANES analysis 53
3.3 Results for profiles P6R05 165, P5R06 050 and P5R10 270 54
3.3.1 Aqueous leachates 54
3.3.2 Exchangeable cations (EC) and cation exchange capacity (CEC) 56
3.3.3 Chemical composition of the bulk bentonite and the fraction < 0.5 μm 60
3.3.4 Structural formula of the smectite 75
3.3.5 Mineralogical composition – XRD-analysis 76
3.3.6 Scanning electron microscopy (SEM) 82
3.3.7 FTIR 88
3.3.8 Mössbauer spectroscopy 93

3.4 Results for profiles P5R06 250 and P6R08 355 96
3.4.1 Visual observations 96
3.4.2 Aqueous leachates 97
3.4.3 Cation exchange capacity (CEC) 98
3.4.4 Exchangeable cations 100
3.4.5 Chemical composition of the bentonite 103
3.4.6 Structural formula of the smectite 111
3.4.7 Mineralogical composition 113
3.5 Results for profile P6R10 210 127
3.5.1 Visual observations 127
3.5.2 Fe K and Cu K X-ray absorption spectroscopy (XANES) 128
3.5.3 Synchroton powder X-ray diffraction 129
3.6 Summary of the chemical-mineralogical investigations 131

**4 Conclusions** 133

**5 Chemical and mineralogical characterization of the tunnel backfill material** 135
5.1 Introduction 135
5.2 Materials and methods 135
5.2.1 Materials 135
5.2.2 Sampling 136
5.2.3 Methods 136
5.3 Results 137
5.3.1 Composition of the < 1 mm fraction of the backfill material 137
5.3.2 Composition of the < 0.5 µm fraction of the backfill material 148
5.4 Summary and conclusions 154

**References** 155

**Appendix 1** Report on the P6_R05 series and R10-270-525 B+Tech bentonite samples 159

**Appendix 2** Rejected XRD-scans of oriented mounts of the clay fractions from profile P6R08 355A. 167

# 1 Introduction

The Prototype Repository project at Äspö Hard Rock Laboratory is a full-scale field experiment simulating conditions relevant for the Swedish KBS-3 concept for final disposal of high-level radioactive waste. The major aims of the project are to gain experience in designing and constructing a repository in crystalline rock, and to test engineered barriers, primarily buffers, backfill and plugs, and develop models for predicting and evaluating their functions and integrated performance.

According to the KBS-3 concept the spent fuel will be stored in copper canisters enclosed by buffers of bentonite and positioned in deposition holes at a depth of ~ 500 m in crystalline host rock. Required functions of the buffer are to serve as mechanical support for the canister and to act as barrier to water flow across the deposition hole (SKB 2006). A buffer of highly compacted bentonite is considered to fulfill these requirements thanks to favourable hydro-mechanical and chemical properties, such as low hydraulic conductivity, good swelling ability, plasticity, and high cation retention capacity. The stability of the bentonite, and of the predominant mineral smectite, when subjected to elevated temperatures and hydration by more or less saline water from the host rock is, however, of vital importance for the long-time performance of the buffer.

The Prototype gallery consisted of six deposition holes with bentonite buffers and canisters and was divided into two sections. The present laboratory investigations of the two buffers from the outer section, retrieved after about 8 years, aim at improving the understanding of the hydro-mechanical and chemical behavior of bentonite buffers at temperatures around 100°C during the water saturation transient. In the first part of this report (Section 2.4) the hydro-mechanical, chemical and mineralogical properties of the bentonite before and after the field experiment are compared in order to assess how the 8-year-long hydrothermal experiment affected the bentonite in the buffer.

The two sections of the deposition tunnel were backfilled with a mixture of bentonite and crushed rock and each tunnel section was sealed with a plug of concrete. Numerous laboratory and field observations have demonstrated that the reactions in concrete generate a diffusive hyper-alkaline plume, which will modify the porewater chemistry in the bentonite near a concrete/bentonite interface. The pore fluid chemistry of concretes is complex and depends on the concrete composition and its alteration stage and evolves over time. Apart from fast cation exchange reactions, slow reactions between the fluid and smectite and/or other minerals in the bentonite may occur, and secondary phases may precipitate. The second part of the report (Chapter 5) presents chemical and mineralogical characteristics of the tunnel backfill material in the vicinity of one of the concrete plugs after the eight year-long field test, during which the backfill was subjected to hydration by a Na-Ca-Cl type groundwater (~ 8,000 mg $Cl^-$/L) and to contact with leachates from the concrete.

## 1.1 Prototype Repository experiment

The Prototype gallery consisted of six full-scale deposition holes in the TBM-tunnel, at a depth of 450 metres. The location of the Prototype tunnel is shown in Figure 1-1 together with other tunnels at the approximate level –450 m. Each deposition hole was installed with a full-scale bentonite buffer (MX-80) and a full-scale copper canister equipped with heaters to simulate the heat generation from spent nuclear fuel. The gallery was divided into two sections, the inner section I consisting of four deposition holes and the outer section II of two deposition holes. The deposition tunnel was backfilled with a mixture of crushed rock and bentonite (30 % bentonite) and each tunnel section was sealed with a plug of concrete. The layout and dimensions of the tunnel and deposition holes are shown in Figure 1-2.

Sensors were installed in the rock, backfill and buffer to monitor the pressure build-up and wetting of the buffer and backfill. The experimental set-up is described in detail in Persson and Broman (2000) and in Svemar and Pusch (2000).

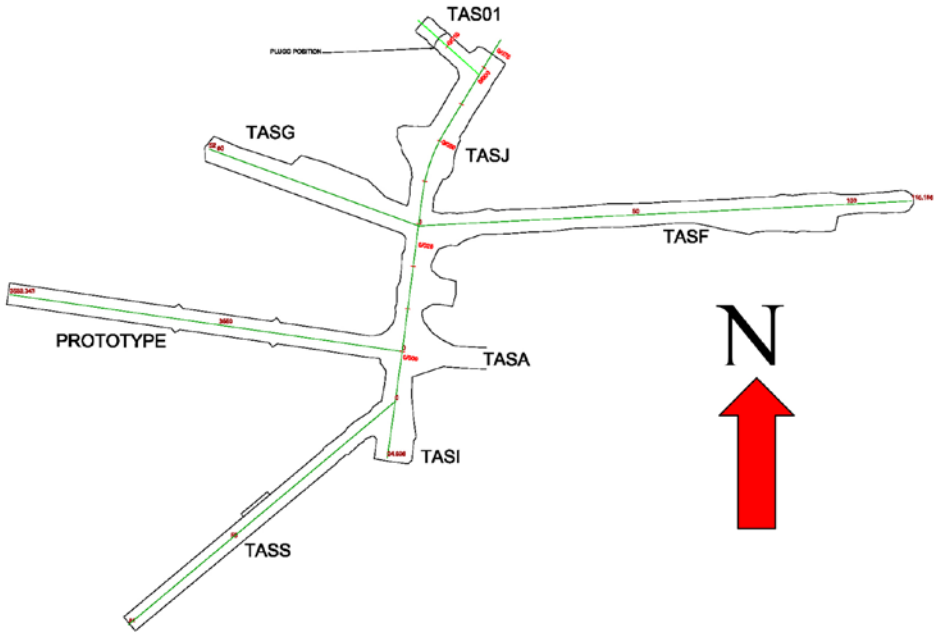


***Figure 1-1.*** *Contours of the Prototype and other tunnels at the –450 m level at Äspö HRL.*

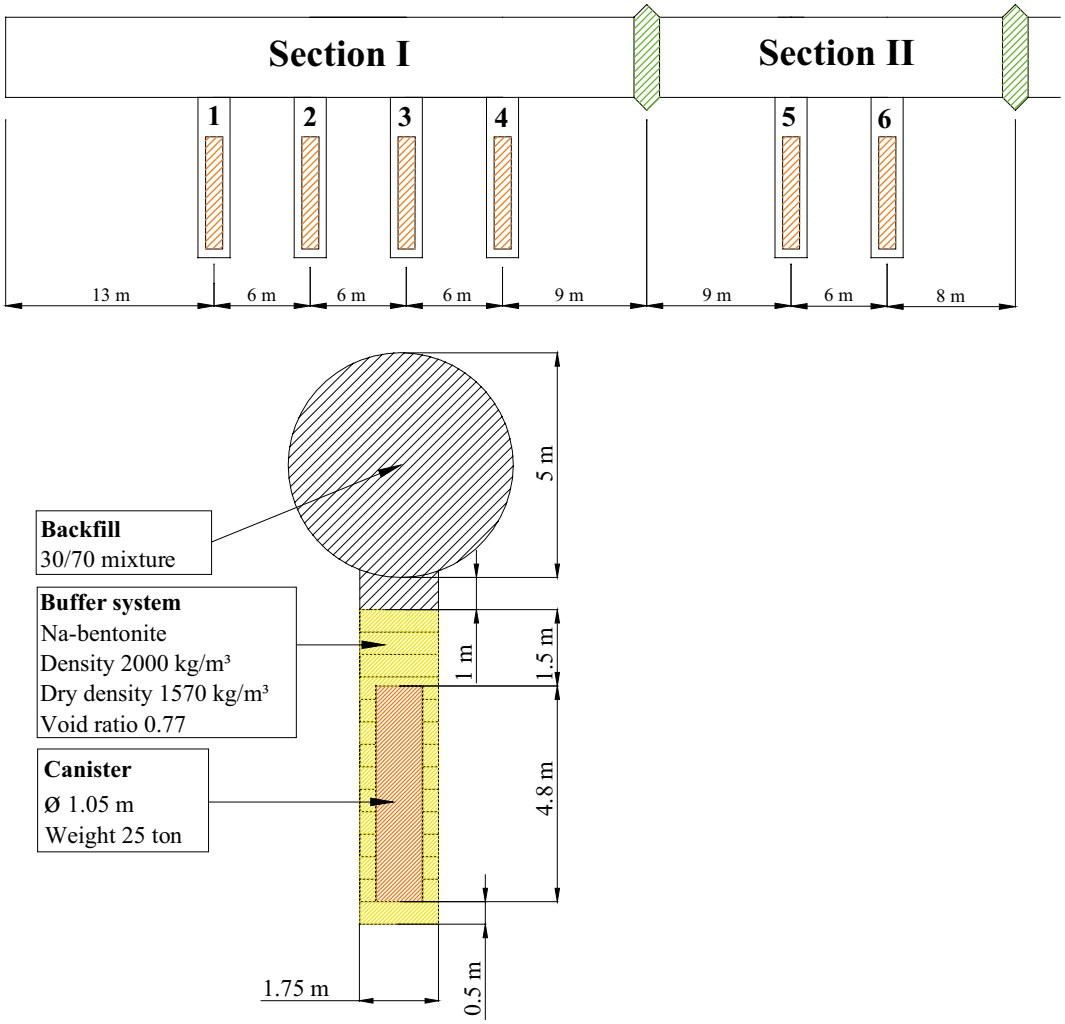


***Figure 1-2.*** *Schematic drawing of the deposition tunnel (concrete plugs in green) and the deposition holes of the Prototype Repository field test.*

The installation of buffers, canisters with heaters, packing of the backfill, and casting of the concrete plug in section I was done during the autumn of 2001. Corresponding installations in section II were made during the spring and autumn of 2003. After the filling of the tunnel had reached beyond the respective deposition hole, heating of the canisters was commenced. The heaters in canister 1 were activated on October 3rd 2001 and the heaters in canister 6 were activated on May 23rd 2003. The sealing of section II with a concrete plug was completed on October 11th 2003. The wetting of the buffer and backfill started on that date and continued until the end of year 2010, when the dismantling of section II started.

The canisters were heated with a power output from the heaters of 1,800 W from May 2003 and the power was decreased by about 30 W per year. The recorded temperature evolution in the buffers (Figure 1-3 to Figure 1-5) shows that steady-state heat flow conditions were reached during the first year of the experiment. Due to problems with the heaters in canister 6, the power had to be reduced by 200–300 W twice during the test, and at the dismantling the power output was about 1,150 W in canister 6 and about 1,600 W in canister 5 (Goudarzi 2012). The temperature evolution in the buffers in deposition hole 5 and 6 suggests that the temperature never reached the maximum temperature, 100°C, stipulated in the design premises for the buffer of the KBS3 concept (SKB 2010), and also that higher temperature had been maintained for longer time in deposition hole 5 than in deposition hole 6.

The removal of the tunnel backfill material in section II was phased over two periods, February – March and July–August, in 2011. The buffer in deposition hole 6 was dismantled during the period April – July 2011 and that in deposition hole 5 in September – December 2011. The dismantling operation is described in a separate report (Johannesson and Hagman 2013).

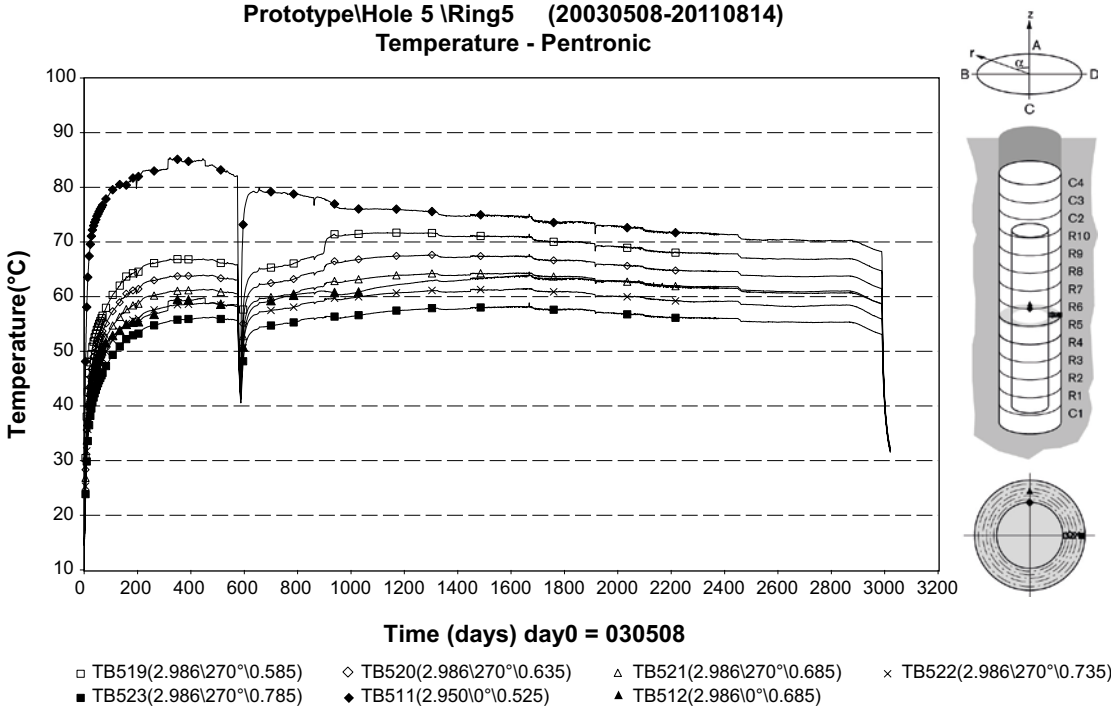


***Figure 1-3.*** *Temperature evolution in block R5 in deposition hole 5 at mid height of the canister (from Goudarzi 2012).*

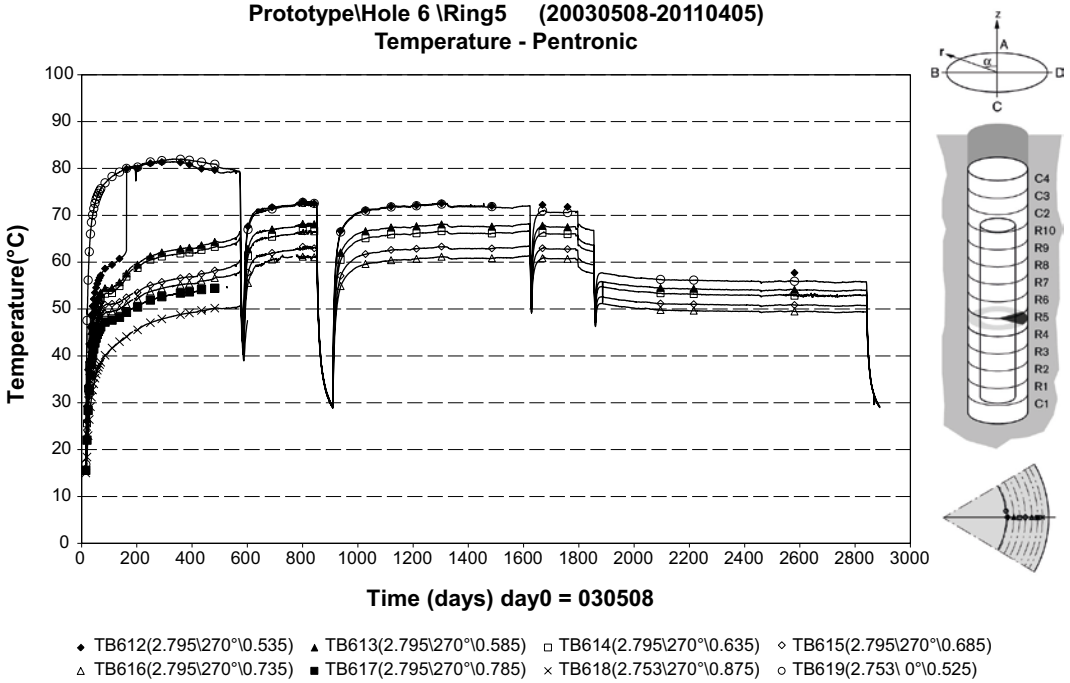


***Figure 1-4.*** *Temperature evolution in block R5 in deposition hole 6 at mid height of the canister (from Goudarzi 2012).*

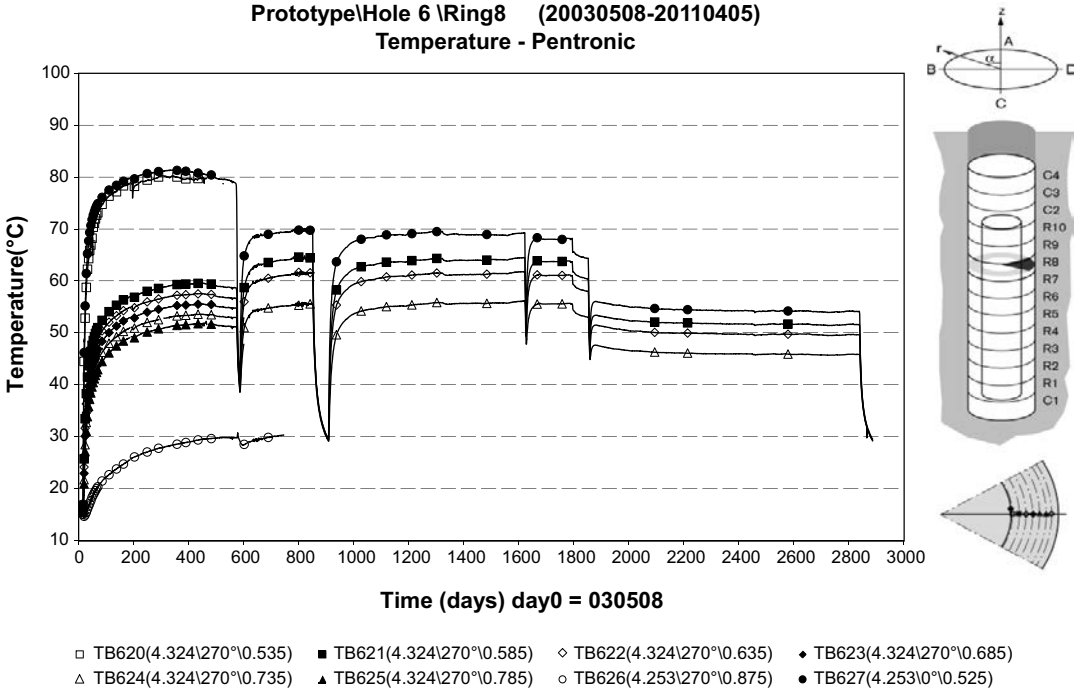


***Figure 1-5.*** *Temperature evolution in block R8 in deposition hole 6 (from Goudarzi 2012).*

The retrieved buffer and backfill materials were sampled for laboratory analyses, which were carried out in two phases:

1. The water content and the density were determined at the Äspö Hard Rock Laboratory immediately after the sampling, which minimized the risk of drying and redistribution of the water in the samples. More than 7,000 determinations were made on the buffer material, and about 1,000 determinations on the backfill material. The results of these analyses are described in a separate report (Johannesson 2013).

2. The second phase included more comprehensive investigations of the buffer and backfill material, such as determination of hydraulic conductivity, swelling pressure and chemical-mineralogical composition, which were made at Clay Technology AB in Lund, B+Tech in Helsinki and SKB at Äspö. The results of these investigations are described in this report. Parallel chemical and mineralogical investigations were also performed at BGR, Germany, and are reported in Dohrmann and Kaufhold (2013). Microbiological and molecular biological analyses of samples from backfill, buffer and canister surfaces were performed at Micans AB in Gothenburg and the results are described in a separate report by Arlinger et al. (2013).

The water content and density of the buffers (Figure 1-6 to Figure 1-8) show that none of the buffers was homogeneous after almost 8 years of wetting (Johannesson 2013) and large variations existed between the two buffers, within one and the same buffer, as well as within one and the same block, both in azimuthal direction and radial distance from the canister. Most of the laboratory tests were performed on bentonite from blocks R05 and R08 in deposition hole 6 and from blocks R06 and R10 in deposition hole 5. The position of the investigated profiles in the blocks is indicated with radial lines in Figure 1-6 to Figure 1-8.

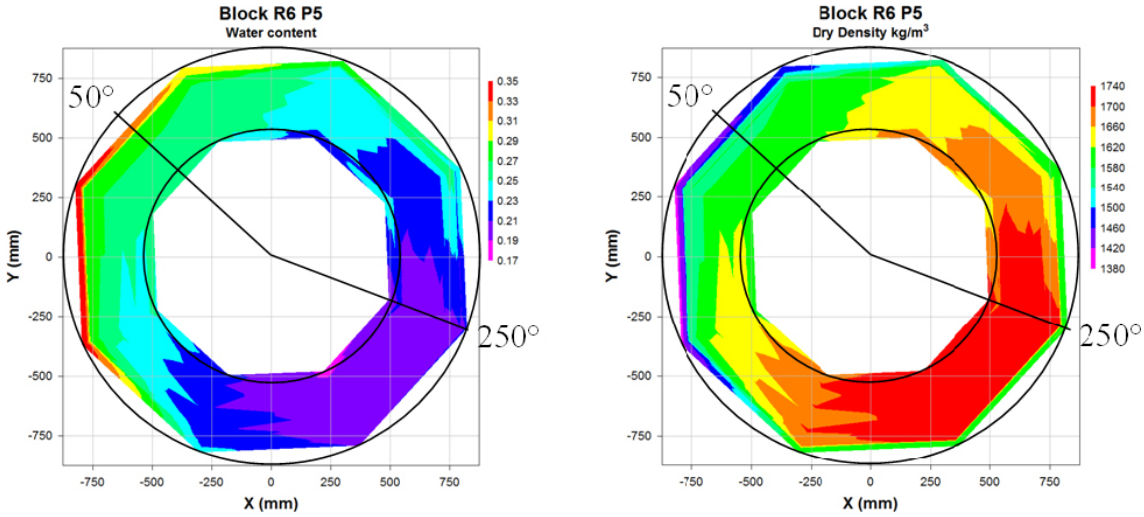


*Figure 1-6. The water content and dry density of block R6 in deposition hole 5 (from Johannesson 2013). The position of the investigated profiles is indicated with radial lines.*

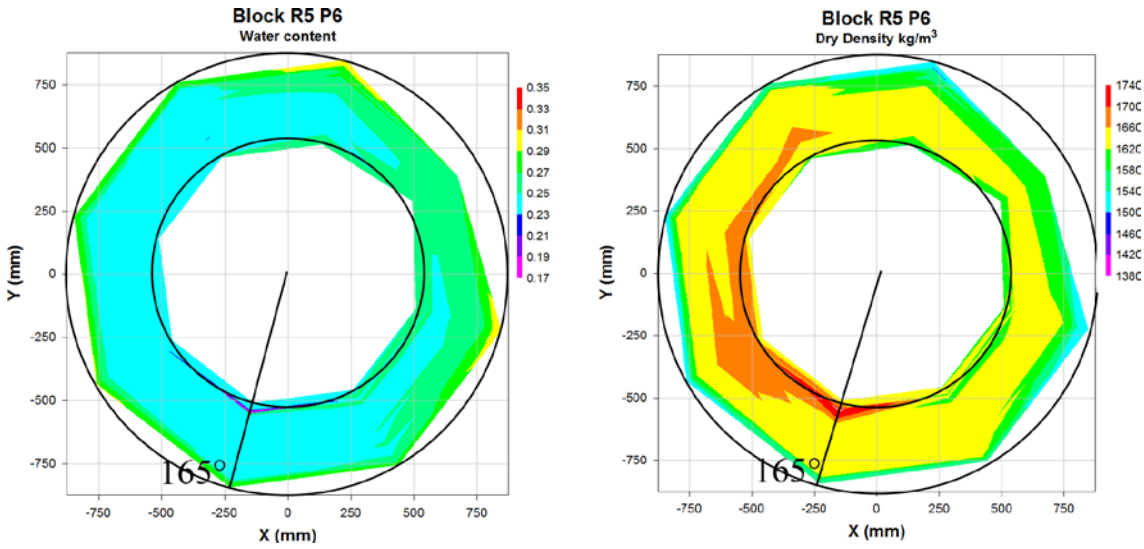


*Figure 1-7. The water content and dry density of block R5 in deposition hole 6 (from Johannesson 2013). The position of the investigated profile is indicated with radial lines.*

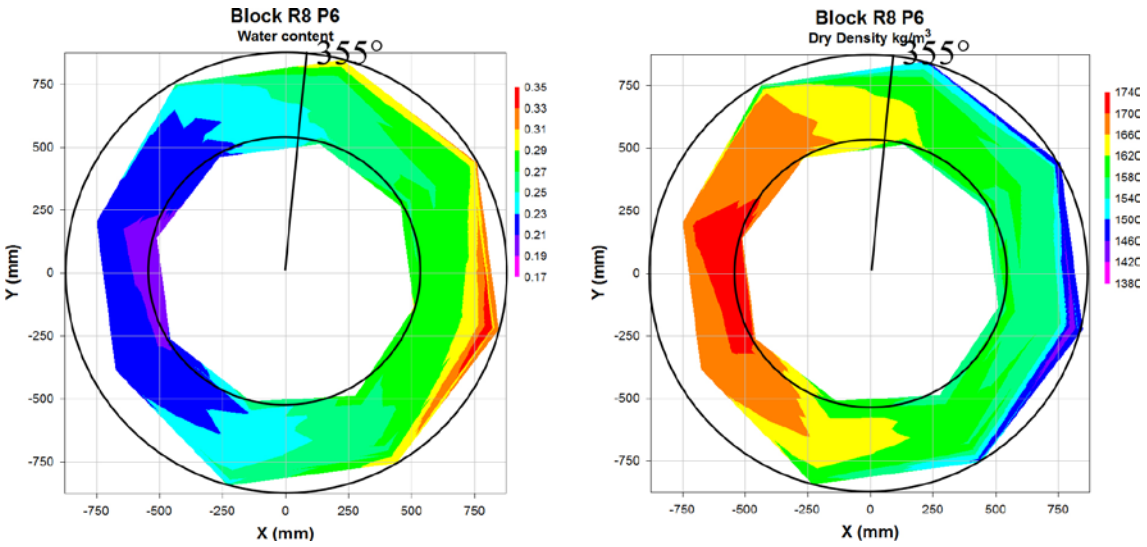


***Figure 1-8.*** *The water content and dry density of block R8 in deposition hole 6 (from Johannesson 2013). The position of the investigated profile is indicated with radial lines.*

Samples for water content and density determinations of the backfill material in section II were taken in cross sections every two meters along the length of the tunnel. The results show that the backfill material was fully saturated and also that the backfill material at the ceiling and at the plug was wetter and had lower density than the material in the central part of the tunnel (Johannesson 2013). The water content and density in two sections approximately 2 m from (Section 10) and at the inner plug (Section 11) are shown in Figure 1-9 and Figure 1-10. The samples for geochemical investigations of the backfill material were taken along a 1 meter-long profile perpendicular to the inner concrete plug at mid height in the tunnel.

Groundwater from the host rock was used for wetting both the buffers and the backfill material. The composition of the groundwater in one deposition hole situated nearby the Prototype tunnel is given in Table 1-1. The water from this deposition hole was also used in the hydro-mechanical tests of the buffer material from the two deposition holes (Section 2).

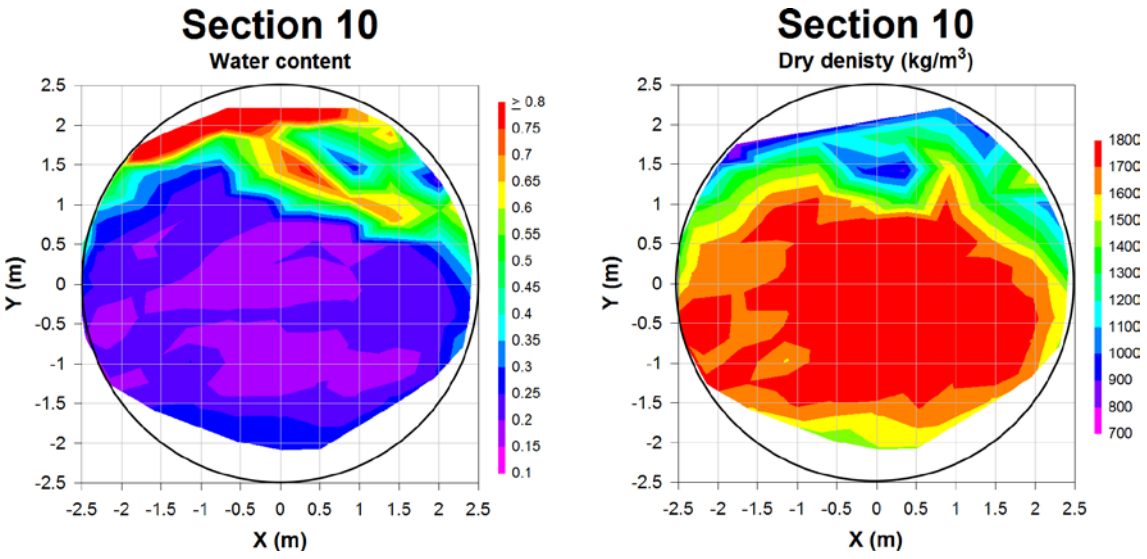


***Figure 1-9.*** *The water content and dry density of the backfill material in Section 10 approximately 2 m from the inner concrete plug (from Johannesson 2013).*

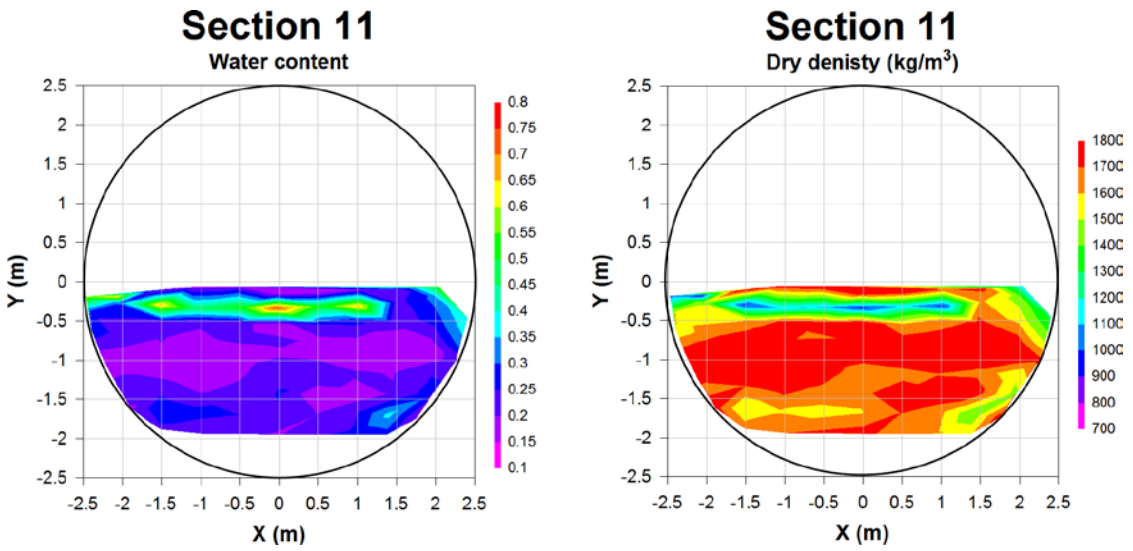


***Figure 1-10.*** *The water content and dry density of the backfill material in Section 11 at the inner concrete plug (from Johannesson 2013).*

**Table 1-1. Main composition of the groundwater in bore hole HG0038B01 in 2002, 2006, 2007, 2008, and 2010.**

| Date | Na mM | K mM | Ca mM | Mg mM | $HCO_3$ mM | Cl mM | $SO_4$ mM | Br mM | F mM | Si mM | pH | E.C. mS/m |
|---|---|---|---|---|---|---|---|---|---|---|---|---|
| 2002-09-17 | 92.6 | 0.26 | 49.9 | 2.00 | 0.63 | 195.0 | 4.78 | 0.554 | 0.08 | 0.18 | 7.42 | 1,907 |
| 2006-05-19 | 106.1 | 0.27 | 58.9 | 1.89 | 0.24 | 213.8 | 5.28 | 0.621 | 0.08 | 0.16 | 7.62 | 2,110 |
| 2006-10-02 | 98.7 | 0.26 | 56.6 | 1.90 | 0.21 | 219.2 | 5.57 | 0.617 | 0.08 | 0.21 | 7.62 | 2,170 |
| 2007-10-03 | 114.8 | 0.26 | 69.1 | 2.06 | 0.18 | 249.9 | 5.70 | 0.741 | 0.07 | 0.20 | 7.64 | 2,380 |
| 2008-09-16 | – | – | – | – | 0.19 | 225.9 | 5.54 | 0.582 | 0.09 | 0.00 | 7.79 | 2,230 |
| 2010-11-30 | 106.1 | 0.23 | 63.9 | 1.76 | 0.16 | 231.6 | 5.60 | 0.703 | 0.10 | 0.20 | 7.40 | 2,261 |

## 1.2 The bentonite buffers

### 1.2.1 Test philosophy

The main goal of the laboratory analyses has been to investigate if any significant differences could be observed between samples taken from field conditions with high temperature and high thermal gradient (i.e. *exposed* material) on one hand, and *reference* material on the other. Reference material of unexposed MX-80 bentonite and buffer material from different positions in deposition hole 5 and 6 in the outer section, have been tested, and the results compared with respect to physical properties, mineralogy and chemistry. The following physical properties have been determined for the material (test technique within brackets):

- Hydraulic conductivity (swelling pressure device).
- Swelling pressure (swelling pressure device).
- Unconfined compression strength (mechanical press).
- Shear strength (triaxial cell).

And the following chemical-mineralogical parameters (methods within brackets):

- Water-soluble salts (ion chromatography, IC).
- Chemical composition of the bulk bentonite and the < 0.5 µm fraction (ICP/AES+ICP/MS, evolved gas analysis).

- Cation exchange capacity (CEC) of the bulk bentonite and the < 0.5 µm fraction (Cu-trien method).
- Exchangeable cations (exchange with $NH_4$, ICP-AES).
- Mineralogical composition of the bulk material and the < 0.5 µm fraction (XRD and FTIR).
- Spot, line and area analyses of selected elements (SEM-EDX).
- Iron and copper oxidation state (Mössbauer spectroscopy, XANES).

Three large sectors were saved of each of the excavated buffer blocks and samples for the laboratory analysis were taken from these (Figure 1-11).

The buffer from each of the two deposition holes 5 and 6 was analyzed according to the following strategy:

- Analyses were made of bentonite from two profiles, which were selected so that they represented areas with either good access to water, or areas with dry conditions. The temperature, to which the bentonite had been exposed, was another factor considered in the selection.
- Material from **one** of the selected profiles was analyzed for hydro-mechanical properties according to the "Basic package–HM" (see Table 1-2). This work was made by Clay Technology AB.
- Material from **two** selected profiles from each of the deposition holes was analyzed for mineralogy and chemical composition according to the "Basic package–C" (see Table 1-2). One profile was analyzed by Clay Technology AB and one was analyzed by B+Tech except for the FTIR analyses, which were all made at B+Tech.
- Material from the same profile as was analysed according to the "Basic package-HM" was also analyzed according to the "Extended package". The Mössbauer analyses were made by Johan Lindén at Åbo Academy, and the triaxial tests and the scanning electron microscopy were made by Clay Technology AB.
- Determination of the iron and copper redox chemistry with XANES and mineralogy with synchrotron XRD were performed by Daniel Svensson, SKB. This was done outside of the planned project work, and the results were added to the report at a late stage as supplementary data.

### 1.2.2 Sampling

The main part of the analyses (especially the chemical/mineralogical analyses) was performed on samples obtained by dividing selected *large sectors,* which were sawn horizontally in five, approximately 10 cm thick parts, labeled A (at the top) to E (at the bottom). These pieces were thereafter cut along the block radius into approximately 2 cm thick samples (Figure 1-11 and Figure 1-12a), which were marked and recorded. In order to increase the resolution, samples proximal to the canister were divided into thinner subsamples.

Block material for Mössbauer and XANES-analyses required handling and sampling under oxygen-free conditions and was packed in vacuum-sealed aluminum-polymer bags as rapidly as possible after the retrieval. Further sampling was done in inert atmosphere in a glove box, where the exposed block surfaces were removed before the specimens for analyses were taken.

Specimens for the hydro-mechanical tests were cored from the large sectors (Figure 1-12b). Most of these samples had a diameter of 35 mm but samples taken close to the canister had a diameter of 20 mm.

**Table 1-2. Summary of analyses of the buffer from the two deposition holes 5 and 6.**

| Analyses | | Tests and analyses | Made by |
|---|---|---|---|
| Bentonite | Basic package – HM | Swelling pressure, hydraulic conductivity, unconfined compression test | Clay Tech |
| | Basic package – C | Soluble salts, chemical composition, exchangeable cations, CEC, mineralogy (XRD+FTIR) | Clay Tech/ B+Tech |
| | Extended package | Shear strength, spot/area analyses of selected elements (SEM-EDX), iron oxidation state (Mössbauer), | Clay Tech/ Åbo Academy |
| | Supplementary analyses | Iron and copper oxidation state (XANES); synchrotron XRD | SKB |

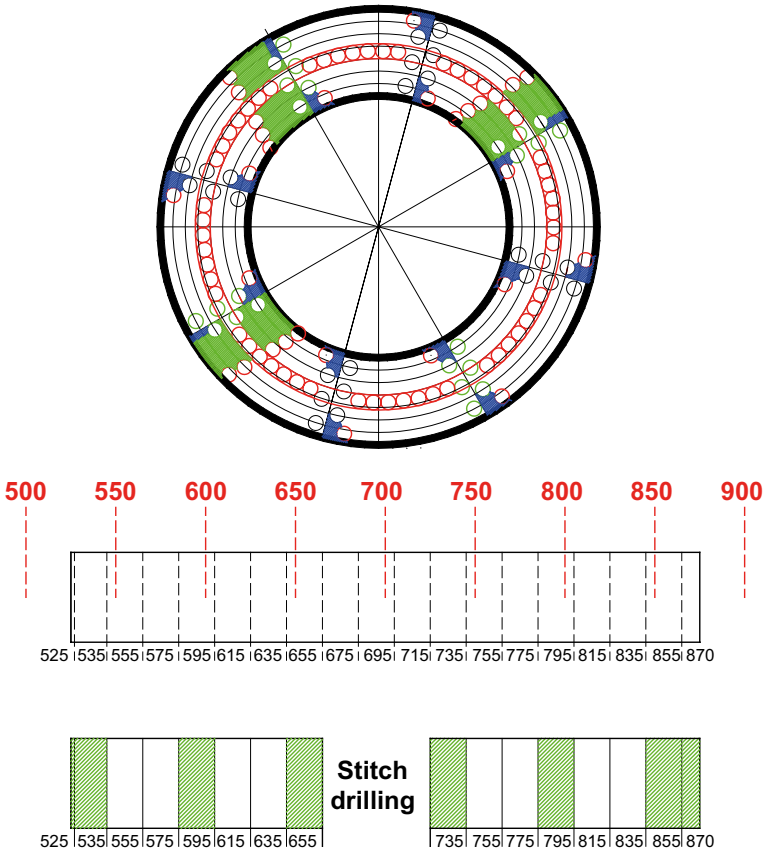


***Figure 1-11.*** *Upper: Schematic drawing of a ring-shaped block after retrieval by stitch drilling (red circles). The green areas represent the big sectors sampled for laboratory tests. Lower: Principle of the radial partition of big sectors of the buffer blocks. Distance is given in millimeters from the center of the canister.*


***Figure 1-12.*** *a) The upper part (A) of a big sector (355) of a buffer block before the sampling for laboratory analyses. b) Sampling of a sector of a buffer block by core drilling.*

The denomination of a sample (center of a volume) was according to the following example:

P5R06 032A 535b where

P5 material from Prototype Repository deposition hole 5.

R06 block number (R for ring-shaped blocks, C for massive cylinders).

032 azimuth direction (0/360 degrees is in the direction towards the end of the tunnel, i.e. almost towards west).

A vertical level in the block (A at the top, E at the bottom).

535 radial distance in millimeters from the center of the canister.

b bulk material (alt. c = the fine clay fraction).

Reference material (non-compacted bentonite saved at the block manufacturing) for a specific block was labeled according to the following example:

P5R06 Rb where

P5 Prototype Repository deposition hole 5.

R06 block number.

R reference material.

b bulk material (alt. c = the fine clay fraction).

## 1.3 The tunnel backfill material

### 1.3.1 Test philosophy

The main goal of the laboratory analyses of the backfill material was to determine if any significant mineralogical changes could be observed in samples taken close to the concrete plug.

The backfill material was a mixture of bentonite (30% by weight) and crushed rock with grain-sizes ranging from 0 to 20 mm. Since the primary aim of the analyses was to provide mineralogical and chemical data for characterization of the bentonite, it was considered essential that a fairly pure and representative fraction of the bentonite could be extracted from the backfill without changing, for instance, the soluble salt content and the exchangeable cation pool. In order to concentrate the bentonite, particles > 1 mm were removed by dry sieving.

The material < 1 mm and < 0.5 μm extracted from the bulk backfill material from positions close to the inner concrete plug in the tunnel of the outer section was analyzed. The mineralogical and chemical characteristics were compared with those of a sample taken 1 meter from the plug used as reference, because no backfill material was available that had not been exposed to tunnel conditions. The following parameters (methods within brackets) were determined:

- Water-soluble salts (ion chromatography).
- Chemical composition of the “purified” backfill material (< 1 mm) and the fine clay fraction (ICP-AES/MS+evolved gas analysis).
- Cation exchange capacity of the purified backfill material (< 1 mm) and the fine clay fraction (Cu-trien method).
- Exchangeable cations (exchange with $NH_4$, ICP-AES).
- Mineralogical composition of the purified backfill material (< 1 mm) and of the fine clay fraction (XRD).

The analyses were made according to the following plan:

- Material from the selected profile was analyzed for mineralogy and chemical composition according to the "Basic package–C" (Table 1-3).
- "Extended package" was performed on the < 1 mm (SEM-EDX) and the < 0.5 µm fractions (Greene Kelly test) of the same material as the "Basic package-C".

All analyses were performed at Clay Technology AB.

### 1.3.2 Sampling

Large samples with an average length of about 10 cm were taken of the backfill material *in situ* in a profile perpendicular to the inner concrete plug, at mid height in the tunnel (Figure 1-13). Specimens for chemical/mineralogical analyses were obtained by dividing selected 10 cm pieces into samples with a width of 2 cm.

The denomination of a sample (centre of a volume) was according to the following example: PBF_50b where:

PBF material from **P**rototype Repository **B**ack**f**ill

50 distance in millimetres from the inner concrete plug in section II

b bulk bentonite, in this case the < 1 mm fraction (alt. c = the fine clay fraction)

**Table 1-3. Chemical-mineralogical analyses of the backfill.**

| Analyses | | Analyses | Made by |
|---|---|---|---|
| Backfill material | Basic package – C | Soluble salts, chemical composition, exchangeable cations, CEC, mineralogy | Clay Tech |
| | Extended package-C | CEC of fine clay fractions after Li-saturation and heating (Greene Kelly test)<br>SEM-EDX | Clay Tech |

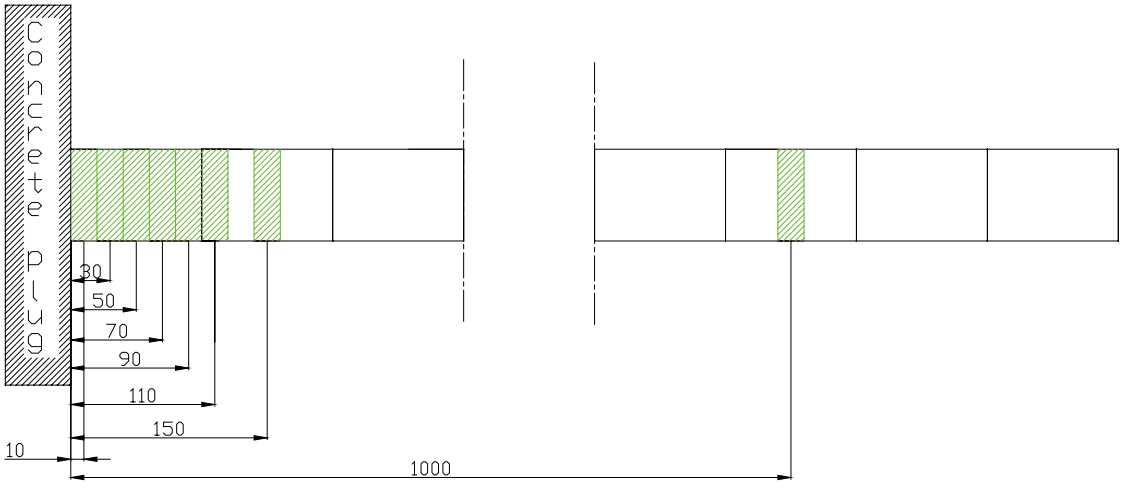


***Figure 1-13.*** *Position (in millimetres) of the samples of the backfill material close to the inner concrete plug in section II. A sample taken at 1,000 mm was used as reference sample.*

# 2 Hydro-mechanical analyses on the buffer material

## 2.1 General

The following hydro-mechanical tests were run and are described in this section:

- Hydraulic conductivity and swelling pressure tests.
- Unconfined compression tests.
- Triaxial tests.

The material used for the hydro-mechanical tests were taken from one profile in each of the two deposition holes. For deposition hole 6, a profile in block No 5 was chosen (direction 165°) and in deposition hole 5 a profile in block No 6 was chosen (direction 50°). The tests were made on both field-exposed material and on reference samples, taken at the manufacturing of the buffer blocks. The purpose of this procedure was to study possible changes in the buffer material after almost 8 years of exposure to elevated temperature and saturation of water from the surrounding rock. The dry density and water content of the bentonite in the investigated buffer profile at the retrieval are shown in Figure 1-6 and Figure 1-7.

### 2.1.1 Basic geotechnical properties

The basic variables water content w (%) and bulk density $\rho_{bulk}$ were determined on the specimens. The dry mass $m_s$ of a specimen was obtained by drying the wet specimen with the total mass $m_{tot}$ at 105˚C for 24h.

The gravimetric water content w is calculated according to Equation 2-1 (Craig 1992).

$$w = 100 \times \frac{m_{tot} - m_s}{m_s} \tag{2-1}$$

The bulk density was calculated from the total mass of the specimen and the volume determined by weighing the specimen in air and submerged into paraffin oil with known density.

From the known bulk density and water content, the dry density $\rho_d$ (kg/m$^3$), void ratio e and degree of saturation $S_r$ (%) were determined according to Equations 2-2, 2-3 and 2-4.

$$\rho_d = \frac{\rho_{bulk}}{1 - w/100} \tag{2-2}$$

$$e = \frac{\rho_s - \rho_d}{\rho_d} \tag{2-3}$$

$$S_r = \frac{\rho_s \times w}{\rho_w \times e} \tag{2-4}$$

where

$m_{tot}$ = total mass of the specimen (kg)

$m_s$ = dry mass of the specimen (kg)

$\rho_s$ = particle density (kg/m$^3$)

$\rho_w$ = density of water (kg/m$^3$)

$\rho_{bulk}$ = bulk density of the specimen (kg/m$^3$)

For determination of void ratio and degree of saturation the particle density $\rho_s$ = 2,780 kg/m$^3$ (Karnland et al. 2006) and water density $\rho_w$ = 1,000 kg/m$^3$ were used.

## 2.2 Hydraulic conductivity and swelling pressure

### 2.2.1 General

A swelling pressure device was used to determine hydraulic conductivity and swelling pressure. The parameters are functions of the density of the sample and the chemical composition of the water and the buffer material (Karnland et al. 2006).

### 2.2.2 Test equipment

The acid-proof stainless steel test equipment used for hydraulic conductivity and swelling pressure determinations is shown in Figure 2-1. The specimens were confined by a cylinder ring with a diameter of 35 mm or 20 mm and stainless steel filters at the top and bottom. The smallest cylinder was used for the specimens taken close to the canister surface in order to get a specimen which is representative of the buffer very close to the canister. The test volume was sealed by o-rings placed between the bottom plate and the cylinder ring and between the piston and the cylinder ring. At test start the height of the test specimen was approximately 15 mm.

A load cell placed between the piston and the upper lid measured the axial force from the samples. The displacement of the piston due to transducer deformation is 25 µm at maximum force, corresponding to 0.17% of the sample height which was considered insignificant.

### 2.2.3 Preparation of specimen and the test procedure

One series of tests from each deposition hole, 5 and 6 respectively, was run. In every series three types of specimens were tested; reference specimens and specimens from the field experiment prepared in two different ways:

- Material saved at the block production was compacted aiming at the saturated densities 1,900, 1,950, 2,000, 2,050, 2,100 and 2,150 kg/m$^3$ at full water saturation (references). These densities correspond to dry densities of 1,410, 1,480, 1,560, 1,640, 1,720 and 1,800 kg/m$^3$ respectively.
- Specimens were drilled and trimmed to fit the sample holders, thus having a density close to the field value.
- Block samples were air-dried and ground to a grain size similar to the original MX-80 powder and re-compacted to a density at saturation of 2,000 kg/m$^3$ which corresponds to a dry density of 1,560 kg/m$^3$. The purpose of this treatment of the material is to investigate whether potential differences between the field-exposed material and the reference samples are related to changes in the bentonite or to changes in the structure in the buffer material (e.g. precipitates).

The specimens were saturated or re-saturated after preparation by introducing water to the bottom and top side simultaneously. Water was added after evacuation of air from filters and tubes by a vacuum pump. Groundwater from the Prototype test site was used for all specimens. The main composition of the water is shown in Table 1-1. During the saturation a minor water pressure of approximately 5 kPa was applied. The swelling pressure was measured continuously.

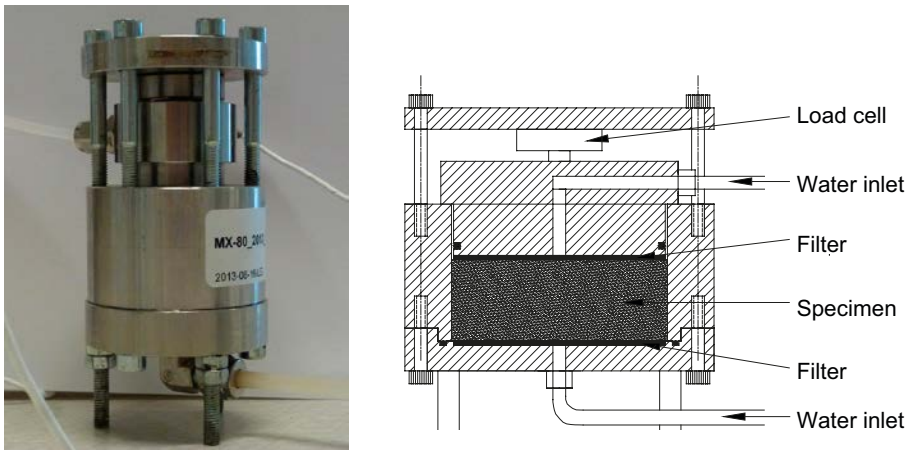


***Figure 2-1.*** *A picture and a schematic drawing of the swelling pressure device.*

After saturation of the specimens, a pore pressure gradient was applied with a Pressure & Volume Controller from GDS instruments. The volume of the out-flowing water was determined by measuring the position of a meniscus in a thin transparent plastic tube, with an inner diameter of 2 mm connected to the top side of the swelling pressure device ( Figure 2-1). The position of the meniscus was measured with an accuracy of about 0.5 mm. This corresponds to a volume of water of about 1.5 $mm^3$. The measurement of the outflow continued until stable rate was observed. The hydraulic conductivity was then calculated according to Darcy´s law. The gradient during the tests was between 2,500 and 10,100 m/m which corresponded to pore pressure differences of 200 kPa and 1,500 kPa across the samples. The applied pore pressures were chosen differently depending on the determined swelling pressure for the samples so that the pore pressure should not exceed half the swelling pressure in order to minimize the risk of piping during the tests. The measurements of the outflow were made during several days in order to get stable values of the evaluated hydraulic conductivity. The water pressure was thereafter reduced to zero and the test was terminated. The swelling pressure was evaluated just before the increase of pore pressure. The water content and density were determined for each specimen after the tests according to Section 2.1.1.

### 2.2.4 Results

The results from measurements of swelling pressure and hydraulic conductivity of samples from deposition hole 5 and 6 are given in Table 2-1 and Table 2-2, respectively, and are plotted as a function of dry density in Figure 2-2, Figure 2-3 and Figure 2-4. In the diagrams the green and red colors denote deposition hole 5 and 6, respectively. In the figures diamonds and squares indicate drilled specimens and triangles and circles represent ground and compacted samples. The references are indicated with black crosses.

**Table 2-1. Results from the measurements of swelling pressure and hydraulic conductivity of samples from deposition hole 5.**

| Sample ID | Preparation | Diameter of specimen | Dry density | Water content | Void ratio | Degree of saturation | Swelling pressure | Gradient | Hydr. cond | Hydr.cond corrected |
|---|---|---|---|---|---|---|---|---|---|---|
| | | D | $\rho_d$ | w | e | $S_r$ | Ps | I | $k_w$ | $k_{w,corr}$ |
| | | mm | $kg/m^3$ | % | – | % | kPa | m/m | $10^{-14}$ m/s | $10^{-14}$ m/s |
| P5R06 50 535B | drilled | 20 | 1,600 | 26.9 | 0.74 | 101*) | 7,600 | 10,000 | 2.8 | 3.9 |
| P5R06 50 625B | drilled | 35 | 1,570 | 27.8 | 0.77 | 100 | 5,000 | 10,000 | 3.9 | 4.3 |
| P5R06 50 735B | drilled | 35 | 1,570 | 27.7 | 0.77 | 100 | 5,600 | 9,900 | 3.6 | 4.0 |
| P5R06 50 775B | drilled | 35 | 1,470 | 32.1 | 0.89 | 100 | 2,900 | 9,600 | 7.0 | 7.4 |
| P5R06 50 815B | drilled | 35 | 1,520 | 29.7 | 0.83 | 100 | 4,700 | 10,100 | 4.3 | 4.7 |
| P5R06 50 535B Rec | ground and compacted | 35 | 1,500**) | 31.0 | 0.86 | 101 | 3,200 | 7,900 | 9.4 | 9.9 |
| P5R06 50 585B Rec | ground and compacted | 35 | 1,470 | 32.3 | 0.89 | 101 | 2,800 | 7,700 | 11.8 | 12.2 |
| P5R06 50 625B Rec | ground and compacted | 35 | 1,490 | 31.4 | 0.86 | 101 | 3,400 | 7,800 | 9.3 | 9.8 |
| P5R06 50 735B Rec | ground and compacted | 35 | 1,470 | 32.0 | 0.89 | 100 | 2,600 | 7,700 | 11.9 | 12.4 |
| P5R06 50 775B Rec | ground and compacted | 35 | 1,500 | 30.9 | 0.85 | 101 | 3,400 | 7,800 | 9.3 | 9.7 |
| P5R06 50 815B Rec | ground and compacted | 35 | 1,510 | 30.1 | 0.84 | 99 | 4,000 | 7,900 | 8.1 | 8.6 |
| P5R06 R 1900 | compacted | 35 | 1,250 | 44.7 | 1.23 | 101 | 700 | 4,500 | 76.6 | 77.4 |
| P5R06 R 1950 | compacted | 35 | 1,430 | 33.9 | 0.94 | 100 | 2,500 | 4,900 | 12.9 | 13.7 |
| P5R06 R 2000 | compacted | 35 | 1,480 | 31.7 | 0.88 | 100 | 3,000 | 9,500 | 8.4 | 8.7 |
| P5R06 R 2050 | compacted | 35 | 1,600 | 26.4 | 0.74 | 100 | 7,300 | 9,700 | 4.0 | 4.3 |
| P5R06 R 2100 | compacted | 35 | 1,620 | 25.7 | 0.71 | 100 | 10,000 | 9,400 | 3.6 | 4.0 |
| P5R06 R 2150 | compacted | 35 | 1,650 | 24.8 | 0.69 | 100 | 11,000 | 9,300 | 3.2 | 3.6 |

*) The degree of saturation is calculated from the measurements of water content and bulk density. Small errors in those parameters may result in an unrealistic calculated degree of saturation larger than 100%.

**) The dry densities for the ground and recompacted samples determined after the performed tests were significantly lower than the planned density of 1,560 $kg/m^3$. There are no reasonable explanations for this at present.

**Table 2-2. Results from the measurements of swelling pressure and hydraulic conductivity of samples from deposition hole 6.**

| Sample ID | Preparation | Diameter of specimen D mm | Dry density $\rho_d$ kg/m$^3$ | Water content w % | Void ratio e – | Degree of saturation $S_r$ % | Swelling pressure $P_s$ kPa | Gradient I m/m | Hydr. cond $k_w$ $10^{-14}$ m/s | Hydr.cond corrected $k_{w,corr}$ $10^{-14}$ m/s |
|---|---|---|---|---|---|---|---|---|---|---|
| P6R05 165C 535 | drilled | 20 | 1,570 | 27.9 | 0.78 | 100 | 6,100 | 9,100 | 3.2 | 4.4 |
| P6R05 165C 580 | drilled | 35 | 1,610 | 26.4 | 0.73 | 101*) | 7,100 | 9,700 | 2.8 | 3.1 |
| P6R05 165C 615 | drilled | 35 | 1,620 | 25.7 | 0.71 | 100 | 8,800 | 8,900 | 2.5 | 3.0 |
| P6R05 165C 725 | drilled | 35 | 1,630 | 26.0 | 0.71 | 102 | 9,000 | 9,500 | 2.5 | 2.9 |
| P6R05 165C 765 | drilled | 35 | 1,620 | 26.2 | 0.72 | 101 | 8,600 | 9,400 | 2.5 | 2.9 |
| P6R05 165C 805 | drilled | 35 | 1,590 | 27.2 | 0.75 | 101 | 6,300 | 9,900 | 3.2 | 3.5 |
| P6R05 165C 535 Rec | ground and compacted | 35 | 1,550**) | 28.5 | 0.80 | 99 | 5,400 | 10,100 | 7.5 | 7.9 |
| P6R05 165C 580 Rec | ground and compacted | 35 | 1,530 | 29.4 | 0.82 | 100 | 4,600 | 10,000 | 9.4 | 9.8 |
| P6R05 165C 615 Rec | ground and compacted | 35 | 1,550 | 28.8 | 0.80 | 100 | 6,000 | 10,000 | 9.0 | 9.4 |
| P6R05 165C 725 Rec | ground and compacted | 35 | 1,510 | 30.7 | 0.84 | 102 | 3,500 | 9,800 | 9.6 | 10.0 |
| P6R05 165C 765 Rec | ground and compacted | 35 | 1,550 | 28.8 | 0.80 | 100 | 4,000 | 10,000 | 8.2 | 8.5 |
| P6R05 165C 805 Rec | ground and compacted | 35 | 1,540 | 29.2 | 0.80 | 101 | 4,900 | 9,900 | 7.0 | 7.4 |
| P6R05 R 1900 | compacted | 35 | 1,320 | 40.4 | 1.11 | 102 | 1,200 | 2,500 | 29.4 | 30.8 |
| P6R05 R 1950 | compacted | 35 | 1,440 | 33.4 | 0.93 | 99 | 2,800 | 2,600 | 11.6 | 12.9 |
| P6R05 R 2000 | compacted | 35 | 1,560 | 28.4 | 0.79 | 100 | 6,000 | 10,100 | 7.0 | 5.5 |
| P6R05 R 2050 | compacted | 35 | 1,600 | 26.6 | 0.74 | 101 | 7,700 | 9,800 | 3.9 | 4.2 |
| P6R05 R 2100 | compacted | 35 | 1,660 | 24.2 | 0.68 | 100 | 14,900 | 9,800 | 2.9 | 3.3 |
| P6R05 R 2150 | compacted | 35 | 1,700 | 22.3 | 0.63 | 98 | 19,800 | 9,600 | 2.2 | 2.5 |

*) The degree of saturation is calculated from the measurements of water content and bulk density. Small errors in those parameters will result in an unrealistic calculated degree of saturation larger than 100%.

**) The dry densities for the ground and recompacted samples determined after the performed tests were significantly lower than the planned density of 1,560 kg/m$^3$. There are no reasonable explanations for this.

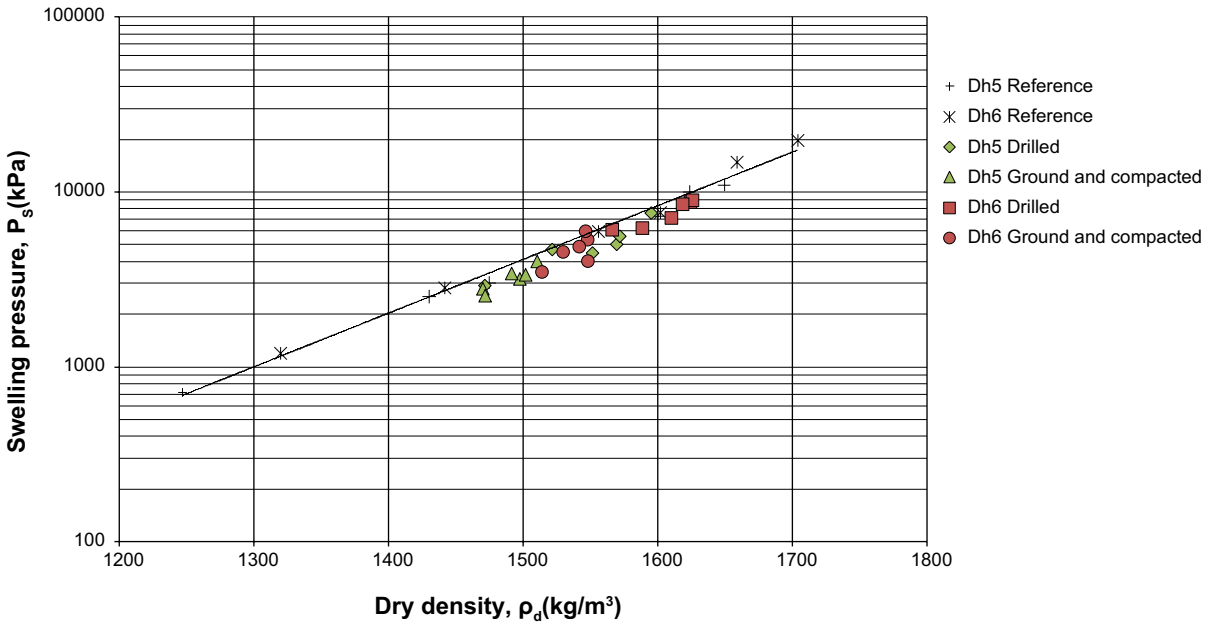


*Figure 2-2. The determined swelling pressure as a function of the dry density of samples from deposition holes 5 and 6. Black points denote results from measurements made on reference samples.*

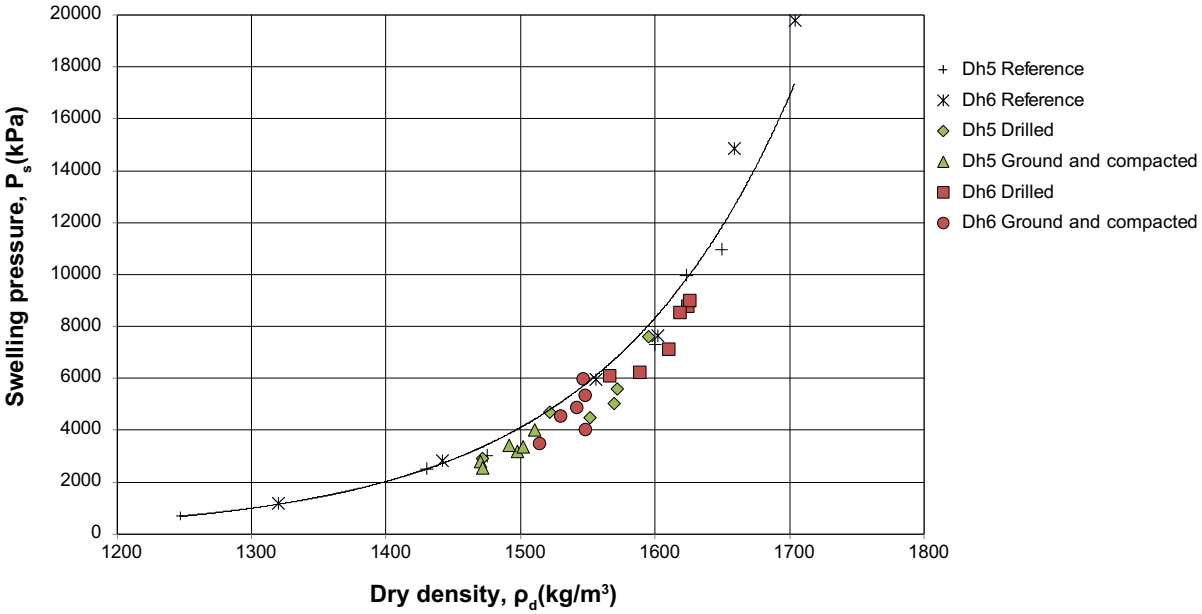


***Figure 2-3.*** *Results as in Figure 2-2 but without log scale on the y axis.*

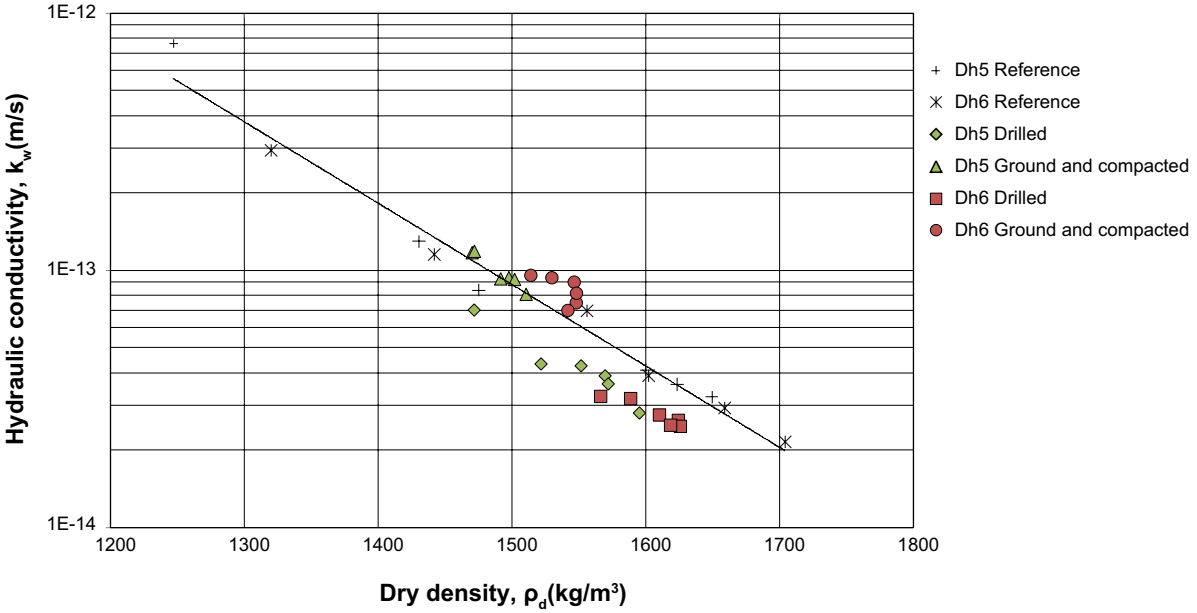


***Figure 2-4.*** *The determined hydraulic conductivity as a function of the dry density. Green and red symbols denote deposition hole 5 and 6, respectively.*

The swelling pressure given in Table 2-1 and Table 2-2 was determined before the measurement of hydraulic conductivity, $P_s$.

For the evaluated hydraulic conductivity ($k_w$) in Table 2-1 and Table 2-2, the evaporation was not taken into account. Evaporation of the outflowing water can be a source of error and therefore the hydraulic conductivity was also evaluated regarding evaporation, $k_{w,corr}$. The tests show that the difference in percentage $(k_{w,corr} - k_w)/k_{w,corr}$ was less than 30% for all measurements, which is in the same range as reported by Åkesson et al. (2012).

### 2.2.5 Discussion

Based on this investigation, in which the swelling pressure and the hydraulic conductivity of material exposed to field conditions for almost 8 years were compared to those of reference material the following conclusions can be drawn:

- There are no large variations in swelling pressure between the reference specimens and the specimens of field-exposed material although there is a small tendency that the swelling pressures of the field-exposed material are somewhat lower, i.e. all the green diamonds and the red squares in Figure 2-2 and Figure 2-3 plot under the solid line representing the swelling pressure of the reference specimens.
- An estimation of the variation in the measurement of the swelling pressure can be made by analyzing the specimen of ground and compacted samples from deposition hole 6 (marked with red circles in Figure 2-2 and Figure 2-3). Five of these samples had similar dry density and the average measured swelling pressure for these specimens was 4,975 kPa with a standard deviation of 747 kPa.
- The hydraulic conductivity of the trimmed specimens taken from the field experiment was somewhat lower than that of the reference specimens, especially at higher densities.
- An estimation of the variation in the measurement of the hydraulic conductivity can be made in the same way as for the swelling pressure (Figure 2-4). The average measured hydraulic conductivity and the standard deviation for the ground and compacted specimens were 8.23 E–14 m/s and 1.00 E–14 m/s, respectively.
- In Figure 2-5 the distance from the "reference line" and the measured swelling pressure and hydraulic conductivity are plotted as function of the position of the specimen relative the canister surface. There is no obvious trend in these plots, which means that the small changes observed between the field-exposed material and the references cannot be correlated to their positions in the buffer and thus the maximum temperature to which the samples have been exposed.

Hypothetically, changes in these parameters would be an expected outcome of, for instance, an alteration of the smectite and/or of the formation of precipitates. Neoformed precipitates were certainly observed but only in the innermost centimeters of the buffer (see Section 3) while the observed changes in hydraulic conductivity and swelling pressure could not be related to a specific position in the buffer. This would leave some other mechanisms to be responsible for the results obtained such as homogenization of the bentonite in the buffer caused by e.g. temperature, pressure and the duration of the exposure.

The conclusions above are consistent with the findings from the investigations of the buffer material in Canister Retrieval Test (CRT), shown in Figure 2-6 and Figure 2-7 (Dueck et al. 2011a). In the Canister Retrieval Test the buffer material had been exposed to similar temperature as the buffer in the Prototype Repository.

In Figure 2-8 the swelling pressure measurements on specimens taken from the Temperature Buffer Test (TBT) are plotted. The temperature in this test was higher compared to the temperature in the Prototype Repository. In general, the measured swelling pressure for the tests made on material from TBT, both the reference specimens and the specimens of the field-exposed material are lower compared to corresponding tests made on material from the Prototype Repository. In the TBT there is a more pronounced decrease in swelling pressure of the samples taken at high temperatures (the specimens marked with red dots in Figure 2-8) compared to the test made on reference material (Åkesson et al. 2012).

The corresponding plot for the evaluated hydraulic conductivity of the specimens taken from the TBT-test is shown in Figure 2-9. In this case all the data are grouped around the line representing the measurements on the reference material (Åkesson et al. 2012) while the data from Prototype Repository indicate a lower hydraulic conductivity for the specimens of field-exposed material, c.f. Figure 2-4.

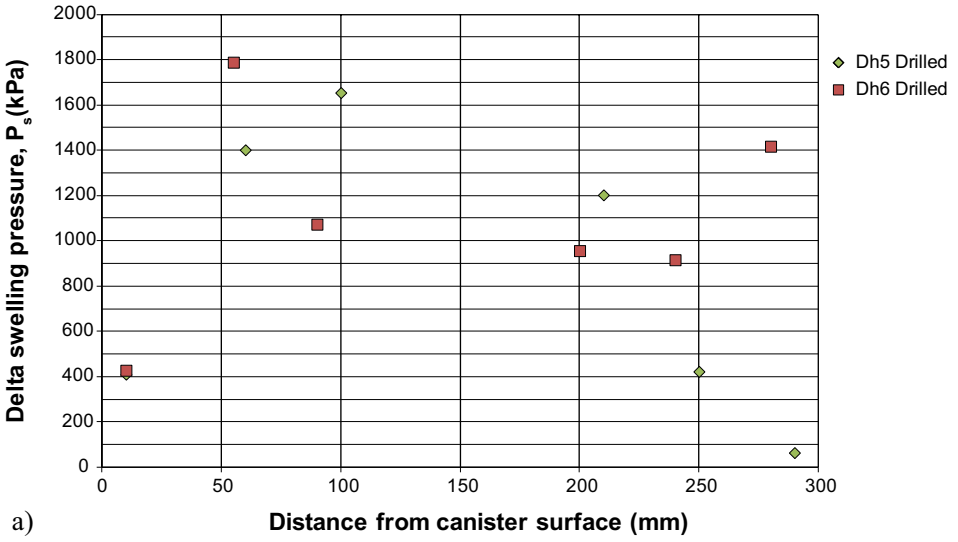


a)

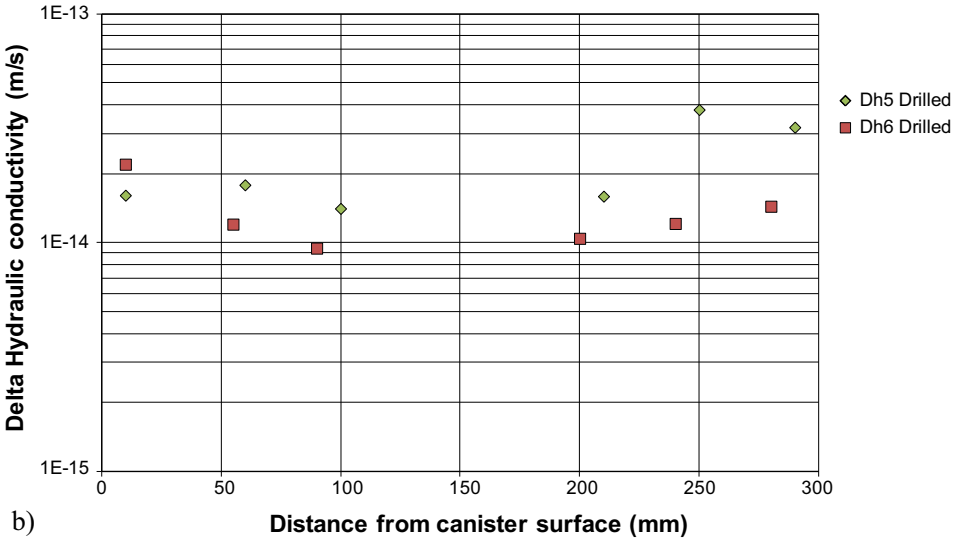


b)

***Figure 2-5.*** *The calculated differences between the "reference line" and the measured swelling pressure (a) and hydraulic conductivity (b) as function of the distance of the specimens relative to the canister surface.*

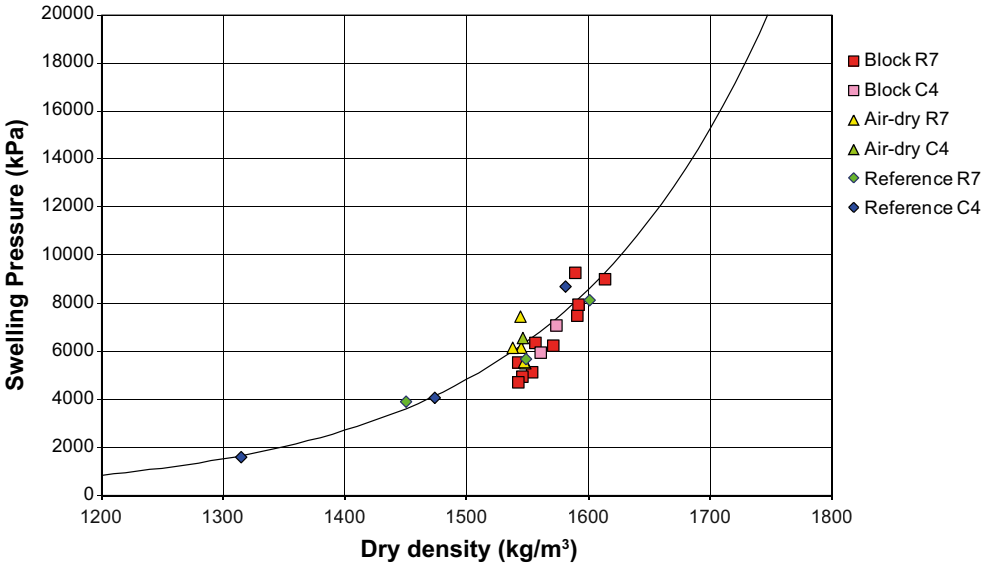


***Figure 2-6.*** *Swelling pressure as a function of dry density from Canister Retrieval Test (from Dueck et al. 2011a).*

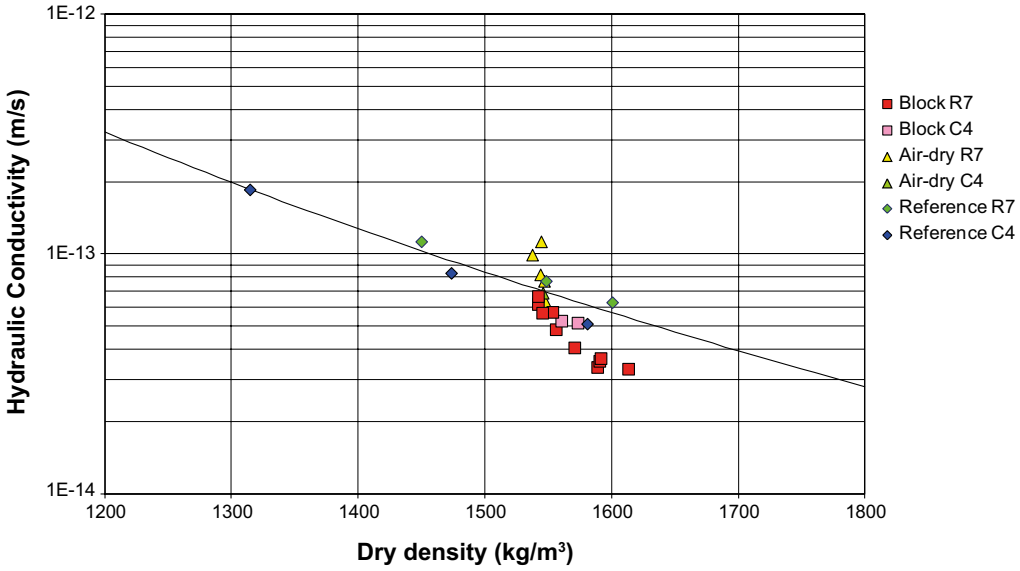


***Figure 2-7.*** *Hydraulic conductivity as a function of the dry density from Canister Retrieval Test (from Dueck et al. 2011a).*

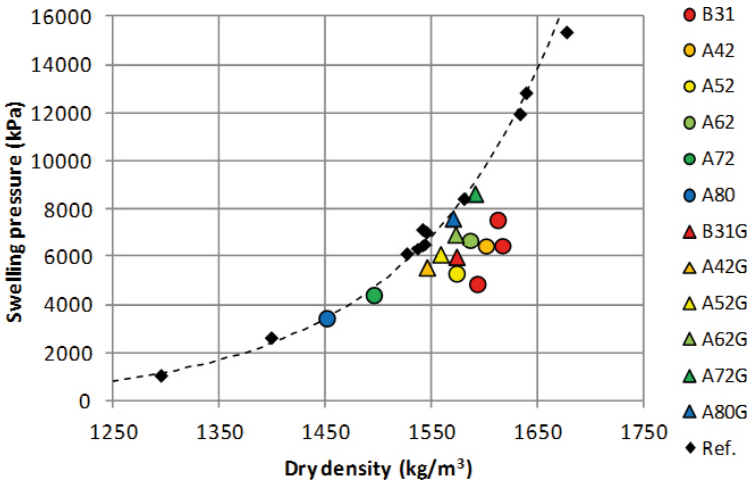


***Figure 2-8.*** *Swelling pressure as a function of dry density from Temperature Buffer Test (from Åkesson et al. 2012).*

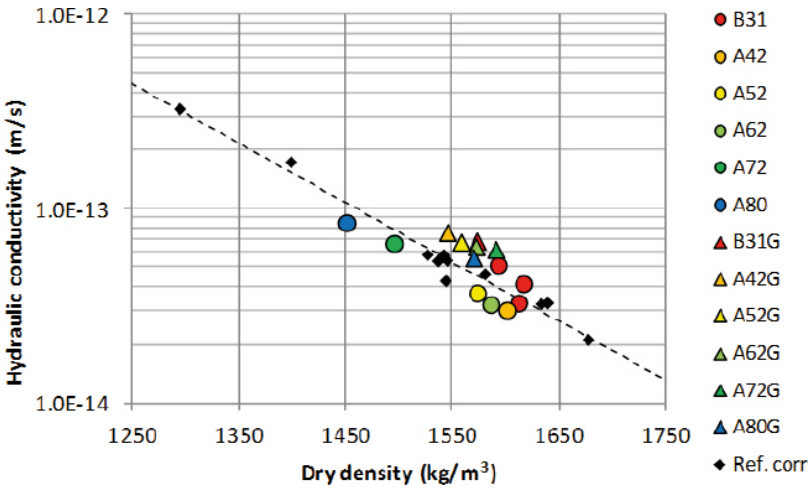


***Figure 2-9.*** *Hydraulic conductivity as a function of the dry density from Temperature Buffer Test (from Åkesson et al. 2012).*

## 2.3 Triaxial tests

### 2.3.1 General

To evaluate the strength of a soil material a triaxial test can be used. A description concerning technique and evaluation was given by Börgesson et al. (1995). Four triaxial tests were made, two on reference material and two on field-exposed material. The purpose of the test is, if possible, to find out if there are any differences in the behavior during the tests (strength and strain) between the two different types of samples. Furthermore the results are also compared with previously made triaxial tests on bentonite to find out if there have been any changes in the material due to the field exposure.

### 2.3.2 Test equipment

The test specimens were pre-saturated in a cylindrical saturation device equipped with a cylindrical steel filter to achieve radial saturation. A piston allowed for measurement of the axial swelling pressure during the saturation. The device was axially divisible in order to enable removal of the specimens without use of axial force.

A high-pressure triaxial cell was used for the tests. The cell was equipped with standard strain gauges, force transducer and pore-pressure transducers according to Figure 2-10.

### 2.3.3 Preparation of specimen and test procedure

The technique requires relatively large test specimens and is resource consuming, both concerning time and active work. The two test series were therefore limited to two specimens each; one from the field experiment and one reference specimen. The field specimens from hole 5 and 6 were sampled from ring 6 and 5, directions 50 and 165 degrees, vertical positions C and A, 545 and 547 mm from the center of the canister which generates sample identifications P5R06 050C 545 and P6R05 165A 547 (cf. denomination in Section 1.2.2).

From the field experiment two specimens were prepared by sawing rough work pieces which were trimmed to cylindrical forms with a diameter of 35 mm and a height of 70 mm. Material that was put aside during the block production was used to compact one reference specimen per deposition hole. The references were given the same dimensions and water saturated in the same device as the field specimens.

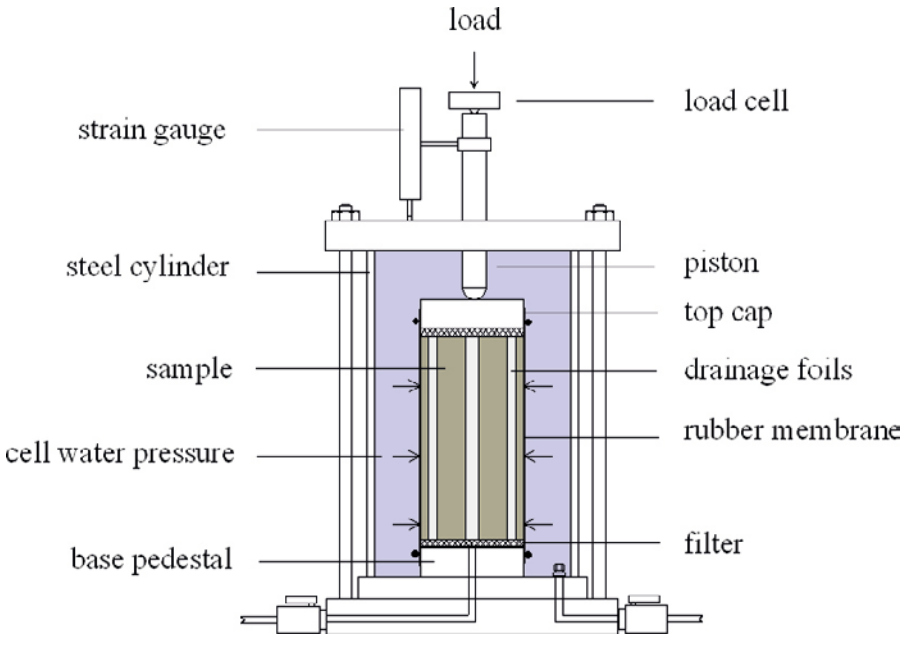


***Figure 2-10.*** *Triaxial test equipment used in combination with a mechanical press.*

The specimens were mounted in the triaxial cell (Figure 2-10) after about four weeks of water saturation. During both saturation and shearing groundwater from the Prototype test site was used. The main composition of the used water is shown in Table 1-1. A cell pressure corresponding to the swelling pressure during the saturation was applied and the pore pressure $u$ of the specimens was measured meanwhile the pedestal valve was kept closed. In order to help equalize the pore pressure in the sample, filter paper drains were attached vertically.

When pressure equilibrium was reached a mechanical press with constant shear rate of 0.0006 mm/min was used for increasing the vertical stress of the specimens. To minimize problems with air in the system the pore pressure was 500 kPa or higher at the start of the shearing. After failure occurred, water content and density of the specimens were determined according to Section 2.1.1.

Cell pressure $\sigma_3$, pore pressure $u$, deformation $\Delta l$, and axial force $F$ were continuously measured during the tests. Any volume change was disregarded and the samples were considered as undrained during shearing. The deviator stress was calculated from:

$$q = \frac{F}{A_0}\left(\frac{l_0 - \Delta l}{l_0}\right) \tag{2-5}$$

where $A_0$ is the specimen initial cross section area and $l_0$ the initial length of the sample. The contact area between load piston and top-cap was considered insignificant.

The vertical total stress $\sigma_1$ was calculated from:

$$\sigma_1 = q + \sigma_3 \tag{2-6}$$

The average effective stress $p$' was calculated from:

$$p' = \frac{1}{3}(\sigma_1 + 2\sigma_3 - 3u) \tag{2-7}$$

The strain $\varepsilon$ was calculated from:

$$\varepsilon = \frac{\Delta l}{l_0} \tag{2-8}$$

### 2.3.4 Results

In Figure 2-11 and Figure 2-12 the deviator stress is plotted versus strain and effective mean stress, respectively. In Table 2-3 the measured and calculated results from the triaxial tests are shown as final water contents, densities, stresses and strains at maximum deviator stress. The swelling pressures measured during water saturation in the saturation device are also shown.

**Table 2-3. Results of the triaxial tests.**

| | After removal from saturation device | | After removal from triaxial cell | | | | At maximum deviator stress | | | | |
|---|---|---|---|---|---|---|---|---|---|---|---|
| Sample ID (Preparation) | Dry density | Swelling pressure | Dry density | Water content | Void ratio | Degree of saturation | Cell pressure | Pore pressure | Effective stress | Deviator stress | Strain at $q_{max}$ |
| | $\rho_d$ kg/m³ | $P_s$ kPa | $\rho_d$ kg/m³ | w % | e – | $S_r$ % | $\sigma_3$ kPa | u kPa | p' kPa | $q_{max}$ kPa | ε % |
| P5R06 050C 545 (trimmed) | 1,574 | 8,000 | 1,559 | 28.3 | 0.78 | 101 | 8,020 | 1,360 | 7,560 | 2,710 | 4.3 |
| P5R06 R (compacted) | 1,573 | 11,900 | 1,548 | 28.6 | 0.80 | 100 | 9,790 | 1,070 | 9,710 | 2,950 | 10.4 |
| P6R05 165A 547 (trimmed) | 1,610 | 10,500 | 1,612 | 26.0 | 0.72 | 100 | 10,910 | 1,510 | 10,680 | 3,841 | 6.2 |
| P6R05 R (compacted) | 1,616 | 10,900 | 1,641 | 25.1 | 0.69 | 100 | 10,630 | 1,380 | 10,390 | 3,400 | 8.9 |

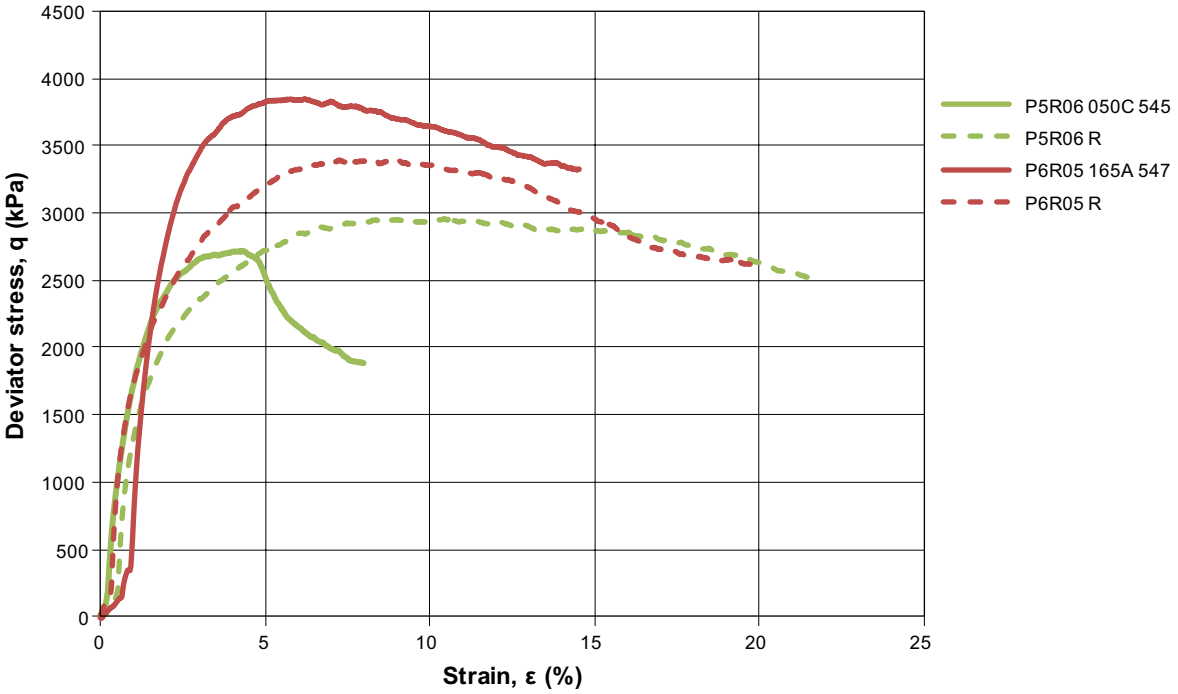


***Figure 2-11.*** *Deviator stress versus strain resulting from the triaxial tests.*

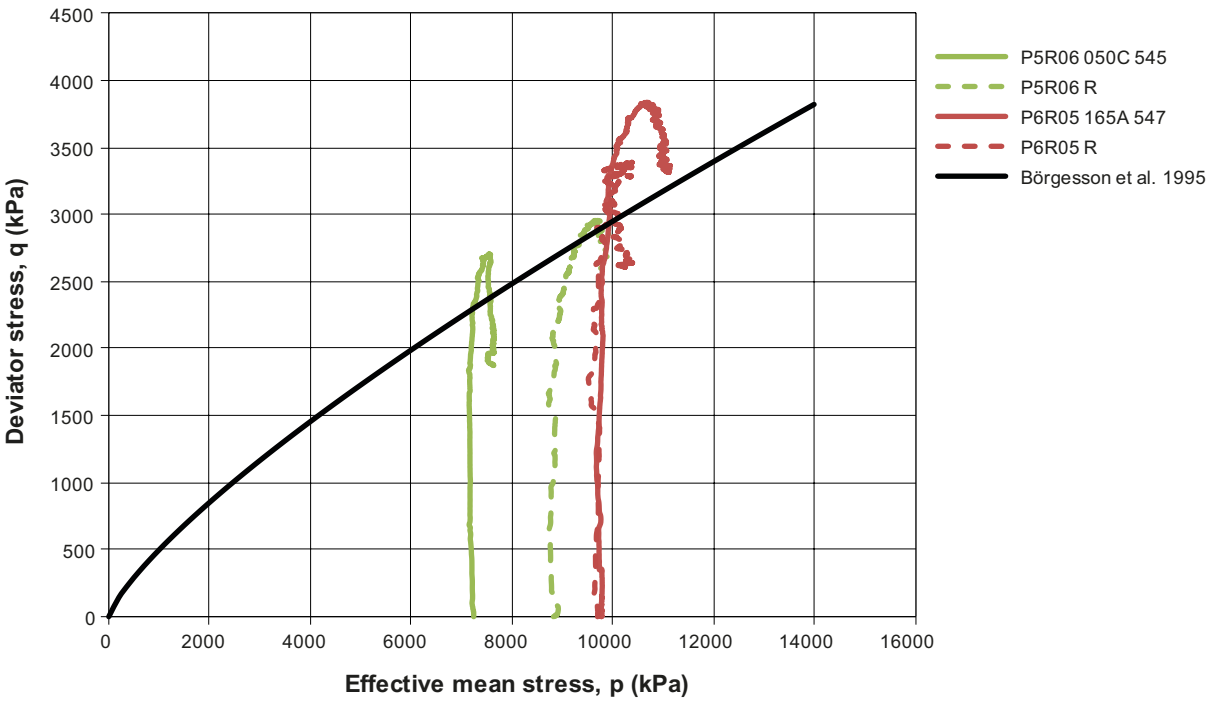


***Figure 2-12.*** *Stress paths plotted as deviator stress versus mean effective stress.*

The stiffness of all the specimens is similar at the beginning of the tests, i.e. up to a strain of about 2% (see Figure 2-11). At failure, however, the strain of the specimens with field-exposed material is smaller compared to the specimens of reference material.

The deviator stresses at failure are larger for all the tests than in previous tests on MX-80 (Börgesson et al. 1995). There is a small tendency that the field-exposed specimens had higher deviator stress at failure compared to the reference specimens (Figure 2-12).

### 2.3.5 Discussion

In Figure 2-13 the results from the triaxial test made in this project are compared with resulst from tests made on material from the TBT-test (Åkesson et al. 2012). The former tests, both on field-exposed material and references, show a larger strength compared to earlier tests (black line in Figure 2-13; Börgesson et al. 1995). This can be explained by the fact that distilled water was used in the latter tests while formation water was used both in the tests with the Prototype and TBT buffer material. Also in the tests with material from the TBT-test the field-exposed material seems to have a smaller strain at failure compared to the test made on reference material (Figure 2-14).

The observed differences in strength and strain between exposed and refrence materials are unlikely related to any of the geochemical alterations which were observed mainly in the innermost centimeters of the buffer (see Section 3). The cause of the diffrences remains to be established.

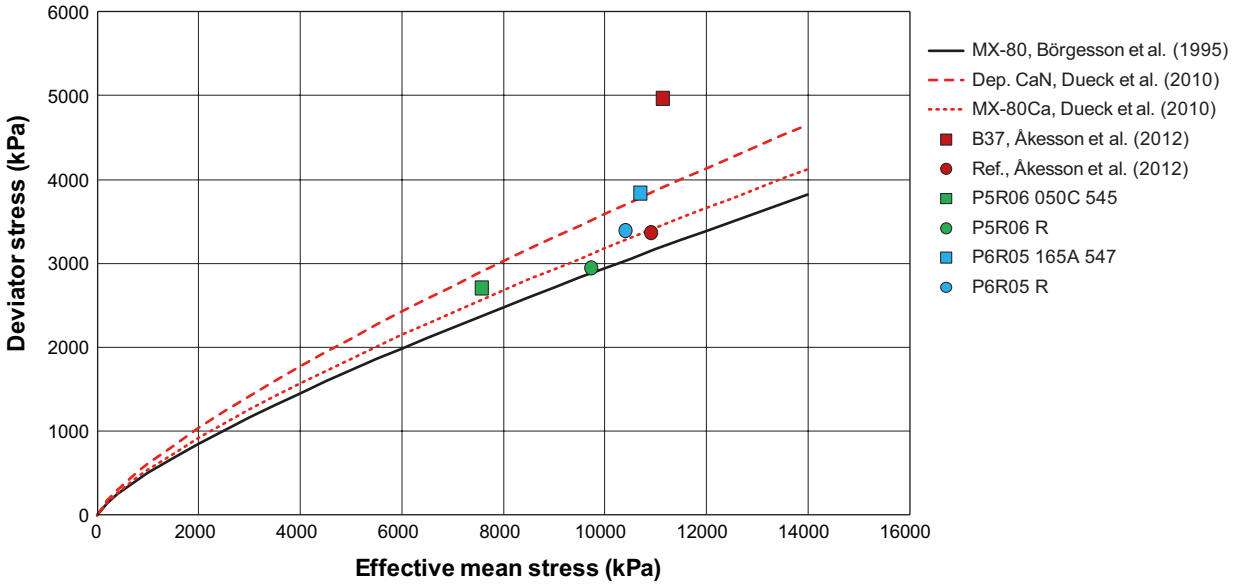


***Figure 2-13.*** *Comparison of results from the triaxial tests on Prototype samples with results from other studies.*

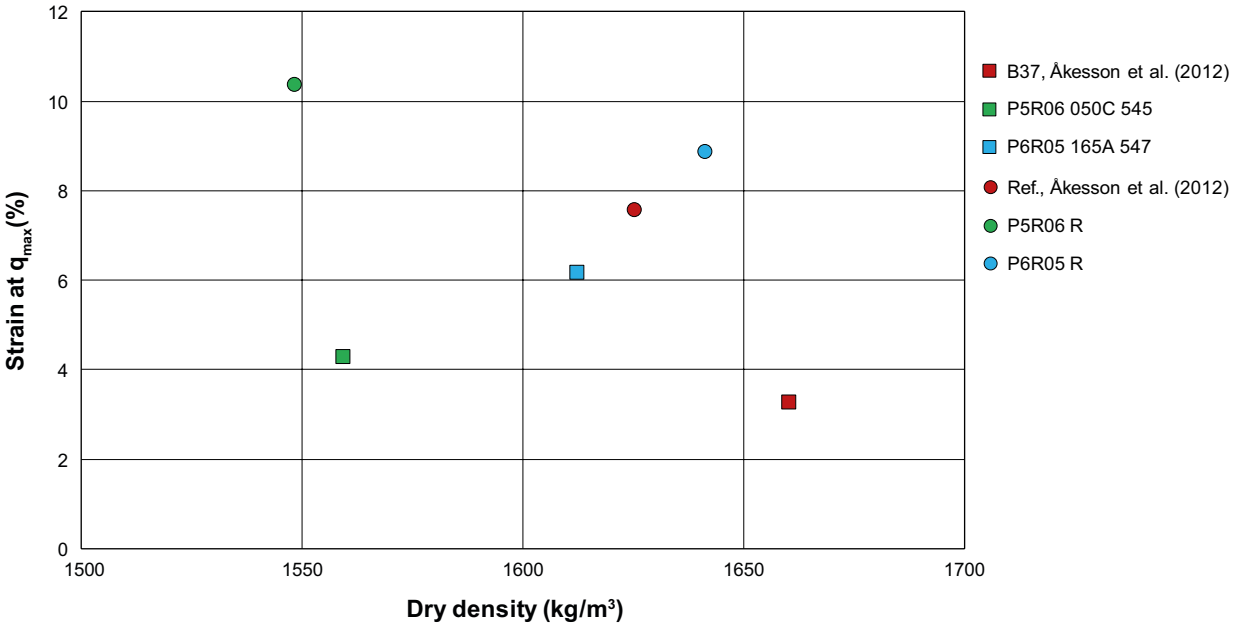


***Figure 2-14.*** *The strain at $q_{max}$ as function of the dry density evaluated from triaxial tests.*

## 2.4 Unconfined compression test

### 2.4.1 General

The unconfined compression test method has been used in several studies reported by Dueck et al. (2010, 2011a), Karnland et al. (2009) and Åkesson et al. (2012).

The unconfined compression test is an experimentally simple method, compared to the triaxial test, for determination of the shear strength of clay specimens. The specimen is compressed axially with a constant rate of strain with, unlike the tiaxial test, no radial confinement or external radial stress. The cylindrical specimen is compressed to shear failure. The test is normally made at a high rate of strain where it is assumed like for the undarined triaxial test that no volume change of the sample occurs at the shearing. The shear strength is commonly determined on tall specimens with a height equal to double the size of the diameter to allow for the shear failure to develop without boundary effects from the end surfaces. The test method was here also used on short specimens with a height equal to the diameter, to study relative changes between different specimens. The tests were made on both field-exposed specimens and on reference specimens. The purpose of the tests is to find out if there are any differences in the behavior between the two types of specimens and if any changes can be related to the distance from the canister surface of the samples in the buffer (i.e. to the temperature).

### 2.4.2 Test equipment

Both short and tall specimens were tested and before the compression test the specimens were saturated in a specially designed saturation device of steel. During the compression test the short specimens were placed in a mechanical press according to Figure 2-15 where a constant rate of strain was applied. The end surfaces were lubricated to minimize the end effects of the short specimens. The same mechanical press was used for the tall specimens, Figure 2-16. During both types of test the deformation and the applied force were measured by means of a load cell and a deformation transducer. All transducers were calibrated prior to the shearing of one series and checked afterwards.

### 2.4.3 Preparation of specimen and test procedure

Three main test series from each deposition hole were run, two series with short specimens and one series with long specimens. The diameters of all specimens were 20 mm and the short ones had equal height as diameter aiming at observing relative changes between specimens. The tall specimens' heights were twice the size of the diameter aiming at determination of shear strength. In addition two replacement series from deposition hole 6 were also run. All specimens were fully saturated, except for two short series which were sheared directly after sampling.

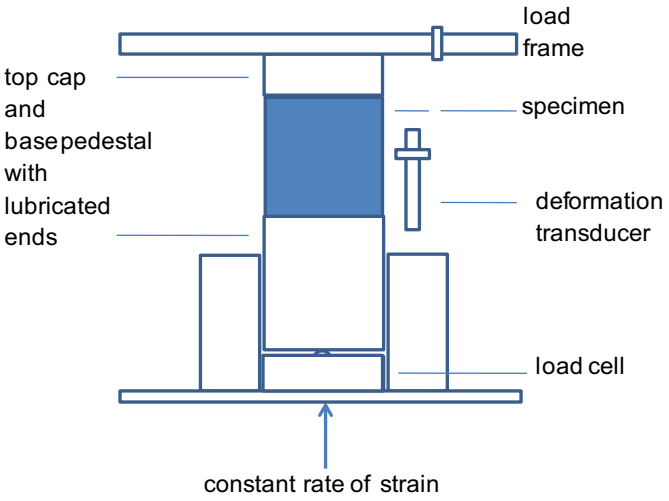


***Figure 2-15.*** *Set-up for the unconfined compression test on short specimens.*

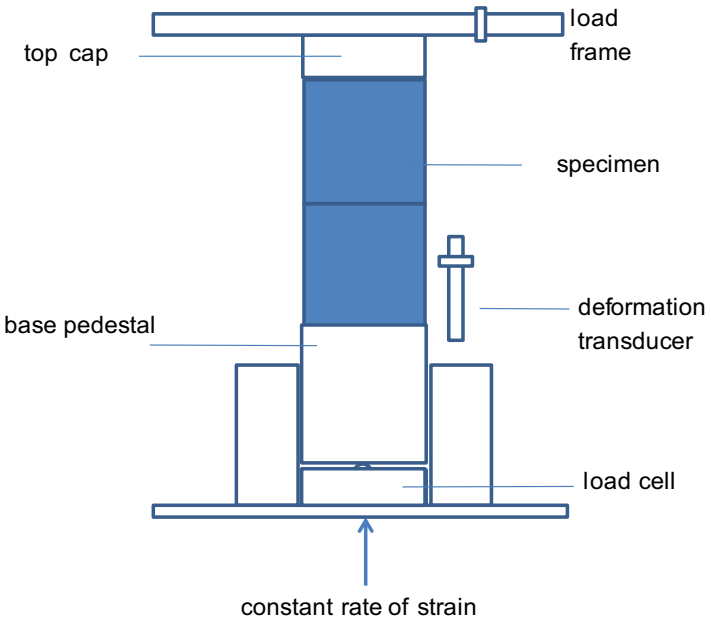


***Figure 2-16.*** *Set-up for the unconfined compression test on tall specimens.*

The specimens of field-exposed material were prepared by drilling and trimming cylindrical specimens while the references were compacted to cylindrical specimens from material saved from the block production. The tall reference specimens were assembled by two short specimens put on top of each other in the saturation device before the saturation. The dimension of the test samples was minimized in order to increase the spatial resolution in the sampling of the block and to ensure full water saturation.

Groundwater from the Prototype test site (composition in Table 1-1) was used for the saturation of the drilled and compacted specimens which was done in a specially designed saturation device where water was applied to the specimens after evacuation of air from the tubes and filters. The short and tall specimens were saturated for 2 and 8 weeks, respectively. After saturation the specimens were removed from the saturation device at least 12 hours before the shearing to homogenize. During this period the specimens were protected from evaporation.

Shearing occurred in the mechanical press with a constant strain rate of 0.16 mm/min for the short specimens and 0.32 mm/min for the tall, i.e. 0.8%/min. During shearing the specimens were surrounded by a protective plastic film to minimize evaporation. After failure the water content and density were determined according to Section 2.1.1.

No volume change was taken into account during shearing and the specimens were considered as undrained. The deviator stress $q$ (kPa) and the strain $\varepsilon$ (%) were derived from Equations (2-5) and (2-8), respectively. The results were adjusted for initial problems with the contact surface. The strain was decreased with the intercept on the x-axis, strain-axis, of the tangent to the stress-strain curve taken at a stress of 500 kPa.

### 2.4.4 Results

The results from the test series are presented in Table 2-4 to Table 2-6, where maximum deviator stress and the corresponding strain for each specimen are presented together with the dry density, water content, void ratio, and degree of saturation. A plot of deviator stress versus strain for all specimens in these series is shown in Figure 2-17 to Figure 2-24. The legends denote the distance from canister center (mm) or the references density (kg/m$^3$).

The results for samples from deposition hole 5 are presented in Table 2-4 and Figure 2-17 to Figure 2-19.

A similar test series was made for samples from deposition hole 6 but it was discovered in the evaluation of these tests that the initial load on the samples was too high resulting in an incorrect strain of the samples at failure. A new series of tests with samples from deposition hole 6 was therefore made, which was denoted series B. The results for the replacement series (B) from deposition hole 6 are shown in Table 2-5 and Figure 2-20 to Figure 2-22. The results for the original series (A) from deposition hole 6 are presented in Table 2-6 and Figure 2-23 and Figure 2-24.

**Table 2-4. Results for the series from deposition hole 5 series.**

| Sample ID | Preparation | Saturated with solution | Dimensions | Dry density $\rho_d$ kg/m$^3$ | Water content w % | Void ratio e – | Degree of saturation $S_r$ % | Maximum deviator stress $q_{max}$ kPa | Strain at $q_{max}$ ε % |
|---|---|---|---|---|---|---|---|---|---|
| P5R06 050B 535 | drilled | unsaturated | H = D | 1,645 | 24.2 | 0.69 | 97 | 3,513 | 3.3 |
| P5R06 050B 575 | drilled | unsaturated | H = D | 1,649 | 24.1 | 0.69 | 97 | 4,981 | 4.8 |
| P5R06 050B 615 | drilled | unsaturated | H = D | 1,653 | 24.1 | 0.68 | 98 | 4,848 | 4.8 |
| P5R06 050B 735 | drilled | unsaturated | H = D | 1,654 | 24.0 | 0.68 | 98 | 5,037 | 5.7 |
| P5R06 050B 775 | drilled | unsaturated | H = D | 1,635 | 25.0 | 0.70 | 99 | 4,382 | 5.8 |
| P5R06 050B 805 | drilled | unsaturated | H = D | 1,623 | 25.5 | 0.71 | 100 | 3,987 | 6.6 |
| P5R06 050B 535 | drilled | Prototype grw | H = D | 1,612 | 26.2 | 0.72 | 101 | 3,332 | 4.6 |
| P5R06 050B 575 | drilled | Prototype grw | H = D | 1,585 | 27.4 | 0.75 | 101 | 2,869 | 6.8 |
| P5R06 050B 615a | drilled | Prototype grw | H = D | 1,560 | 28.3 | 0.78 | 100 | 2,469 | 7.6 |
| P5R06 050B 615b | drilled | Prototype grw | H = D | 1,588 | 27.1 | 0.75 | 100 | 2,905 | 5.6 |
| P5R06 050B 735 | drilled | Prototype grw | H = D | 1,574 | 27.8 | 0.77 | 101 | 2,608 | 7.7 |
| P5R06 050B 775 | drilled | Prototype grw | H = D | 1,580 | 27.5 | 0.76 | 101 | 2,846 | 6.8 |
| P5R06 050B 805 | drilled | Prototype grw | H = D | 1,539 | 29.2 | 0.81 | 101 | 2,282 | 7.5 |
| P5R06 R 1400 | compacted | Prototype grw | H = D | 1,411 | 34.4 | 0.97 | 99 | 1,122 | 10.3 |
| P5R06 R 1550 | compacted | Prototype grw | H = D | 1,537 | 28.6 | 0.81 | 98 | 2,237 | 8.3 |
| P5R06 R 1675 | compacted | Prototype grw | H = D | 1,647 | 24.1 | 0.81 | 97 | 4,133 | 6.1 |
| P5R06 050B 535 | drilled | Prototype grw | H = 2D | 1,599 | 26.6 | 0.74 | 100 | 2,840 | 3.6 |
| P5R06 050B 575 | drilled | Prototype grw | H = 2D | 1,613 | 26.3 | 0.72 | 101 | 3,027 | 3.3 |
| P5R06 050B 615a | drilled | Prototype grw | H = 2D | 1,595 | 26.4 | 0.74 | 99 | 2,958 | 4.7 |
| P5R06 050B 615b | drilled | Prototype grw | H = 2D | 1,614 | 26.1 | 0.72 | 100 | 3,358 | 4.4 |
| P5R06 050B 735 | drilled | Prototype grw | H = 2D | 1,608 | 26.5 | 0.73 | 101 | 3,030 | 4.0 |
| P5R06 050B 775 | drilled | Prototype grw | H = 2D | 1,580 | 27.3 | 0.76 | 100 | 2,732 | 4.6 |
| P5R06 050B 805 | drilled | Prototype grw | H = 2D | 1,562 | 28.4 | 0.78 | 101 | 2,580 | 5.0 |
| P5R06 R 1400 | compacted | Prototype grw | H = 2D | 1,392 | 35.4 | 1.00 | 99 | 1,047 | 7.4 |
| P5R06 R 1550 | compacted | Prototype grw | H = 2D | 1,536 | 28.7 | 0.81 | 99 | 2,028 | 5.9 |
| P5R06 R 1675 | compacted | Prototype grw | H = 2D | 1,632 | 24.7 | 0.70 | 98 | 3,720 | 5.2 |

**Table 2-5. Results for replacement series (B) deposition hole 6.**

| Sample ID | Preparation | Saturated with solution | Dimensions | Dry density $\rho_d$ kg/m$^3$ | Water content w % | Void ratio e – | Degree of saturation $S_r$ % | Maximum deviator stress $q_{max}$ kPa | Strain at $q_{max}$ ε % |
|---|---|---|---|---|---|---|---|---|---|
| P6R05 165C 540 | drilled | unsaturated | H = D | 1,680 | 22.7 | 0.65 | 97 | 4,280 | 3.2 |
| P6R05 165C 565 | drilled | unsaturated | H = D | 1,678 | 23.1 | 0.66 | 98 | 4,170 | 2.4 |
| P6R05 165C 600 | drilled | unsaturated | H = D | 1,691 | 22.7 | 0.64 | 98 | 2,155 | 1.1 |
| P6R05 165C 635 | drilled | unsaturated | H = D | 1,688 | 23.0 | 0.65 | 99 | 5,419 | 2.7 |
| P6R05 165C 740 | drilled | unsaturated | H = D | 1,673 | 22.9 | 0.66 | 96 | 5,987 | 4.1 |
| P6R05 165C 785 | drilled | unsaturated | H = D | 1,672 | 23.0 | 0.66 | 97 | 5,814 | 4.5 |
| P6R05 165C 535 | drilled | Prototype grw | H = D | 1,639 | 25.1 | 0.70 | 100 | 3,375 | 3.6 |
| P6R05 165C 575 | drilled | Prototype grw | H = D | 1,646 | 24.8 | 0.69 | 100 | 3,720 | 4.7 |
| P6R05 165C 615a | drilled | Prototype grw | H = D | 1,650 | 24.4 | 0.68 | 99 | 4,354 | 5.5 |
| P6R05 165C 615b | drilled | Prototype grw | H = D | 1,647 | 24.9 | 0.69 | 100 | 3,917 | 4.1 |
| P6R05 165C 735 | drilled | Prototype grw | H = D | 1,640 | 24.6 | 0.70 | 98 | 4,169 | 5.9 |
| P6R05 165C 775 | drilled | Prototype grw | H = D | 1,638 | 24.8 | 0.70 | 99 | 4,078 | 6.4 |
| P6R05 R 1400 | compacted | Prototype grw | H = D | 1,398 | 34.9 | 0.99 | 98 | 1,075 | 10.6 |
| P6R05 R 1550 | compacted | Prototype grw | H = D | 1,537 | 28.5 | 0.81 | 98 | 2,204 | 8.6 |
| P6R05 R 1675 | compacted | Prototype grw | H = D | 1,641 | 24.1 | 0.69 | 96 | 4,328 | 6.6 |
| P6R05_165_C535 | drilled | Prototype grw | H = 2D | 1649 | 24.7 | 0.69 | 100 | 3,032 | 1.5 |
| P6R05 165C 575 | drilled | Prototype grw | H = 2D | 1,651 | 24.5 | 0.68 | 99 | 3,532 | 1.6 |
| P6R05 165C 615 | drilled | Prototype grw | H = 2D | 1,673 | 23.8 | 0.66 | 100 | 4,388 | 2.3 |
| P6R05 165C 735 | drilled | Prototype grw | H = 2D | 1,682 | 23.3 | 0.65 | 99 | 5,520 | 3.2 |
| P6R05 165C 775 | drilled | Prototype grw | H = 2D | 1,639 | 25.1 | 0.70 | 100 | 4,052 | 3.7 |
| P6R05 165C 805 | drilled | Prototype grw | H = 2D | 1,634 | 25.3 | 0.70 | 100 | 3,700 | 3.7 |
| P6R05 R 1400 | compacted | Prototype grw | H = 2D | 1,403 | 34.7 | 0.98 | 98 | 1,110 | 6.5 |
| P6R05 R 1550 | compacted | Prototype grw | H = 2D | 1,544 | 27.8 | 0.80 | 97 | 2,298 | 5.1 |
| P6R05 R 1675 | compacted | Prototype grw | H = 2D | 1,664 | 23.7 | 0.67 | 98 | 4,592 | 4.6 |

**Table 2-6 Results for the original series (A) from deposition hole 6.**

| Sample ID | Preparation | Saturated with solution | Dimensions | Dry density $\rho_d$ kg/m$^3$ | Water content w % | Void ratio e – | Degree of saturation $S_r$ % | Maximum deviator stress $q_{max}$ kPa | Strain at $q_{max}$ ε % |
|---|---|---|---|---|---|---|---|---|---|
| P6R05 165B 535a | drilled | Prototype grw | H = D | 1,578 | 26.5 | 0.76 | 97 | 2,561 | 4.8 |
| P6R05 165B 535b | drilled | Prototype grw | H = D | 1,614 | 25.4 | 0.72 | 98 | 2,703 | 3.0 |
| P6R05 165B 575 | drilled | Prototype grw | H = D | 1,607 | 25.8 | 0.73 | 98 | 2,601 | 3.9 |
| P6R05 165B 615 | drilled | Prototype grw | H = D | 1,607 | 25.7 | 0.73 | 98 | 2,965 | 5.2 |
| P6R05 165B 735 | drilled | Prototype grw | H = D | 1,611 | 26.0 | 0.73 | 100 | 3,138 | 6.3 |
| P6R05 165B 775 | drilled | Prototype grw | H = D | 1,593 | 26.6 | 0.75 | 99 | 2,855 | 7.3 |
| P6R05 165B 805 | drilled | Prototype grw | H = D | 1,601 | 26.0 | 0.74 | 98 | 2,382 | 2.9 |
| P6R05 R 1400 | compacted | Prototype grw | H = D | 1,385 | 35.0 | 1.01 | 97 | 959 | 6.7 |
| P6R05 R 1550 | compacted | Prototype grw | H = D | 1,527 | 28.6 | 0.82 | 97 | 2,147 | 8.2 |
| P6R05 R 1675 | compacted | Prototype grw | H = D | 1,632 | 24.7 | 0.70 | 98 | 3,873 | 7.1 |
| P6R05 165B 535a | drilled | Prototype grw | H = 2D | 1,644 | 24.8 | 0.69 | 100 | 3,384 | 2.3 |
| P6R05 165B 535b | drilled | Prototype grw | H = 2D | 1,634 | 25.5 | 0.70 | 101 | 3,006 | 1.7 |
| P6R05 165B 575 | drilled | Prototype grw | H = 2D | 1,613 | 25.8 | 0.72 | 99 | 3,590 | 4.6 |
| P6R05 165B 615 | drilled | Prototype grw | H = 2D | 1,623 | 25.6 | 0.71 | 100 | 3,650 | 4.1 |
| P6R05 165B 735 | drilled | Prototype grw | H = 2D | 1,622 | 25.6 | 0.71 | 100 | 3,725 | 5.0 |
| P6R05 165B 775 | drilled | Prototype grw | H = 2D | 1,614 | 26.0 | 0.72 | 100 | 2,028 | 1.2 |
| P6R05 165B 805 | drilled | Prototype grw | H = 2D | 1,614 | 26.0 | 0.72 | 100 | 3,532 | 4.0 |
| P6R05 R 1400 | compacted | Prototype grw | H = 2D | 1,352 | 34.7 | 1.06 | 91 | 976 | 6.0 |
| P6R05 R 1550 | compacted | Prototype grw | H = 2D | 1,532 | 28.1 | 0.82 | 96 | 2,175 | 5.0 |
| P6R05 R 1675 | compacted | Prototype grw | H = 2D | 1,623 | 23.9 | 0.71 | 93 | 4,347 | 3.7 |

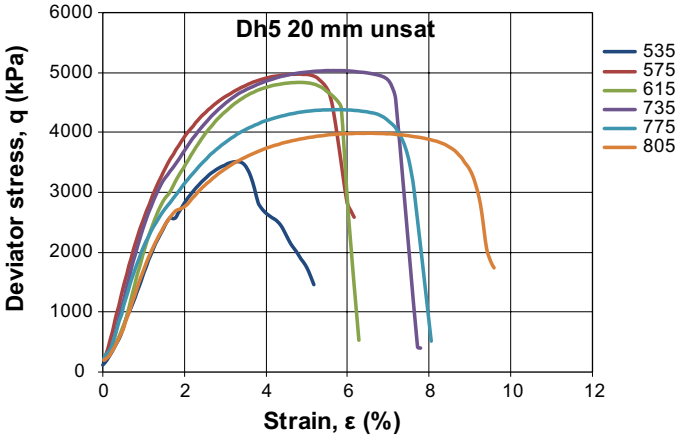


***Figure 2-17.*** *Deviator stress versus strain for short, unsaturated specimens from deposition hole 5. The labels show the position (mm) from canister center.*

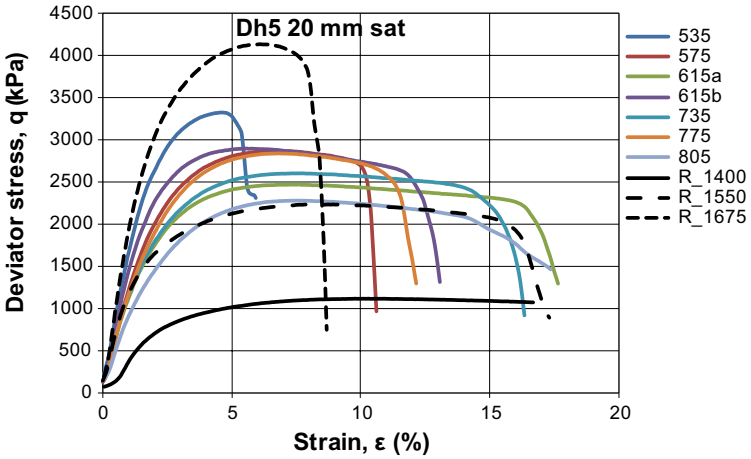


***Figure 2-18.*** *Deviator stress versus strain for short, saturated specimens from deposition hole 5. The labels show the position (mm) from canister center or the references initial dry density (kg/m$^3$) of the references.*

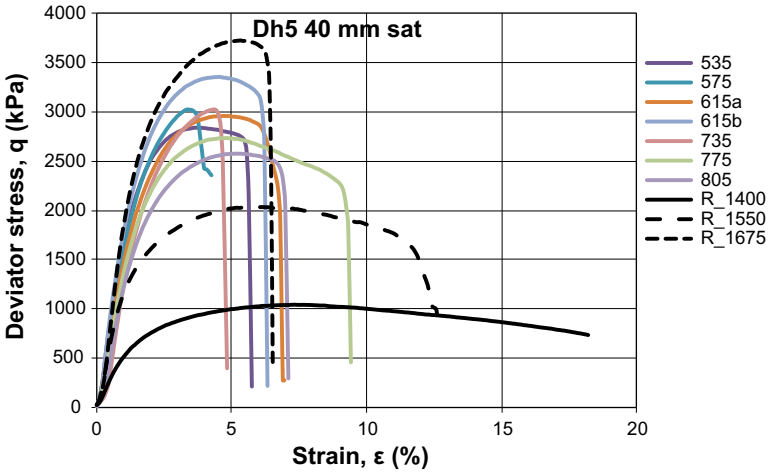


***Figure 2-19.*** *Deviator stress versus strain for tall, saturated specimens from deposition hole 5. The labels show the position (mm) from canister center or the references initial dry density (kg/m$^3$) of the references.*

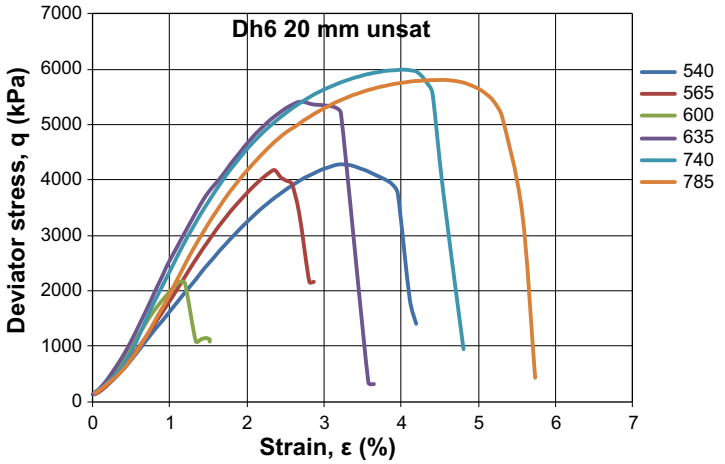


***Figure 2-20.*** *Deviator stress versus strain for short, unsaturated specimens from deposition hole 6. The labels show the position (mm) from canister center.*

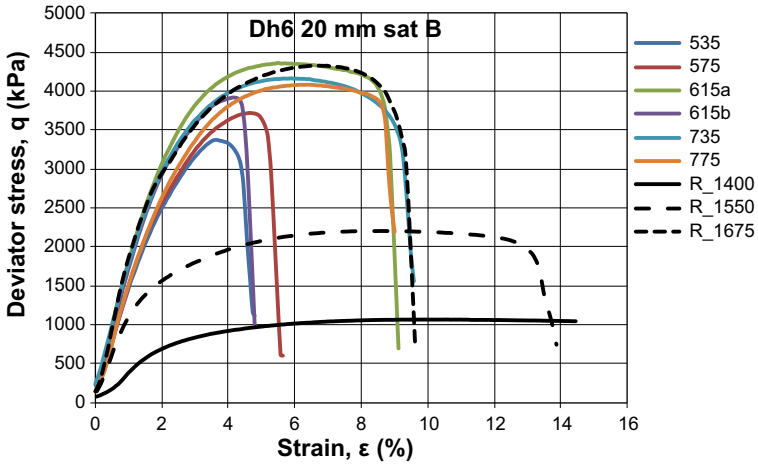


***Figure 2-21.*** *Deviator stress versus strain for short, saturated replacement specimens from deposition hole 6. The labels show the position (mm) from canister center or the references initial dry density (kg/m$^3$) of the references.*

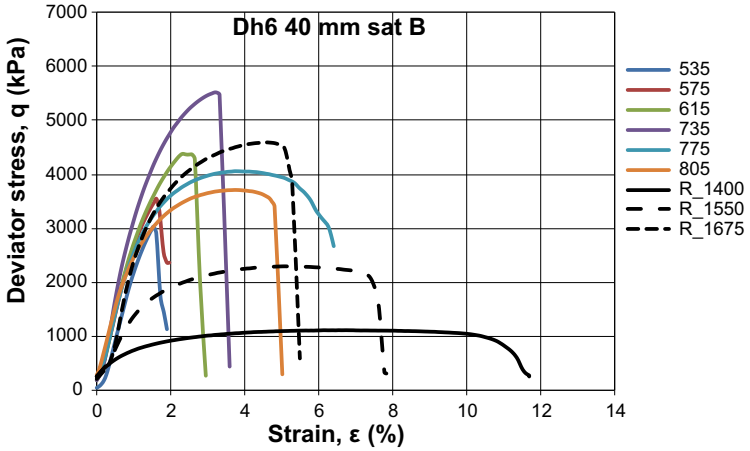


***Figure 2-22.*** *Deviator stress versus strain for tall, saturated replacement specimens from deposition hole 6. The labels show the position (mm) from canister center or the references initial dry density (kg/m$^3$) of the references.*

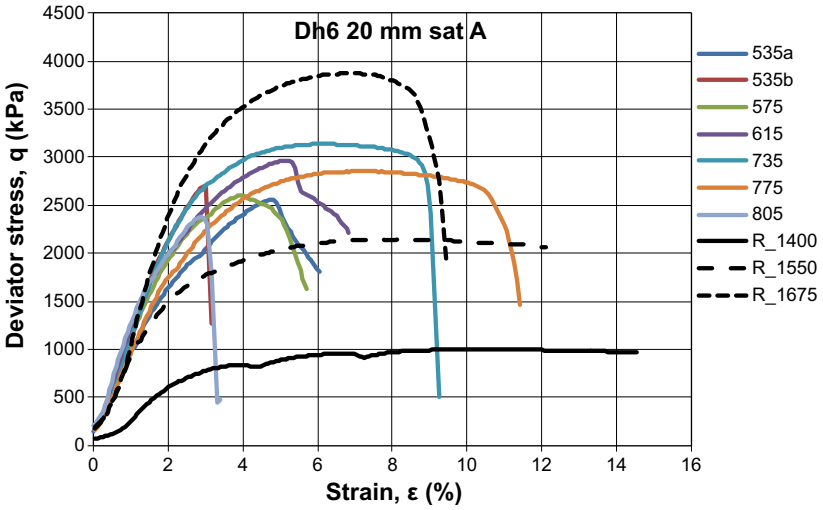


***Figure 2-23.*** *Deviator stress versus strain for short, saturated specimens from deposition hole 6. The labels show the position (mm) from canister center or the references initial dry density (kg/m³) of the references.*

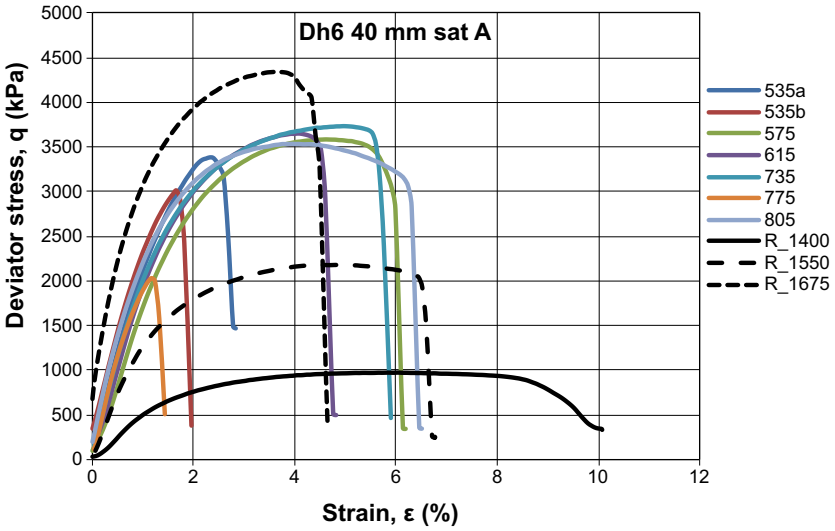


***Figure 2-24.*** *Deviator stress versus strain for tall, saturated specimens from deposition hole 6. The labels show the position (mm) from canister center or the references initial dry density (kg/m³) of the references.*

The results, plotted as maximum deviator stress $q_{max}$ and corresponding strain ε versus dry density, are shown in Figure 2-25 and Figure 2-26. Samples from deposition hole 5 are marked with green symbols whereas red symbols denote samples from deposition hole 6. Only series B from deposition hole 6 is plotted in Figure 2-25 and Figure 2-26. The lines in the figures are calculated from the tests made on the reference samples.

### 2.4.5 Discussion

The stress at failure increased for the reference specimen as well as for the specimens of field-exposed material with increasing dry density. Although the scatter in strength is large, especially at higher densities, no large differences in strength can be seen between the reference specimens and the specimens with field-exposed material (Figure 2-25). The strength is also independent on the height of the specimens.

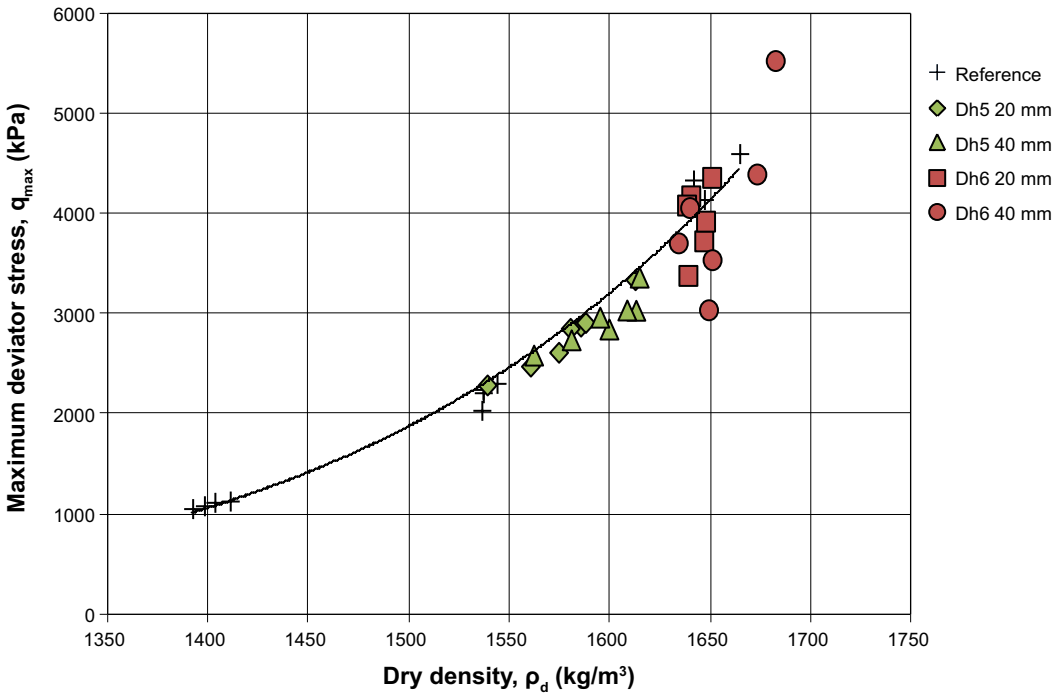


***Figure 2-25.*** *Maximum deviator stress versus dry density for test series with short and tall, saturated specimens.*

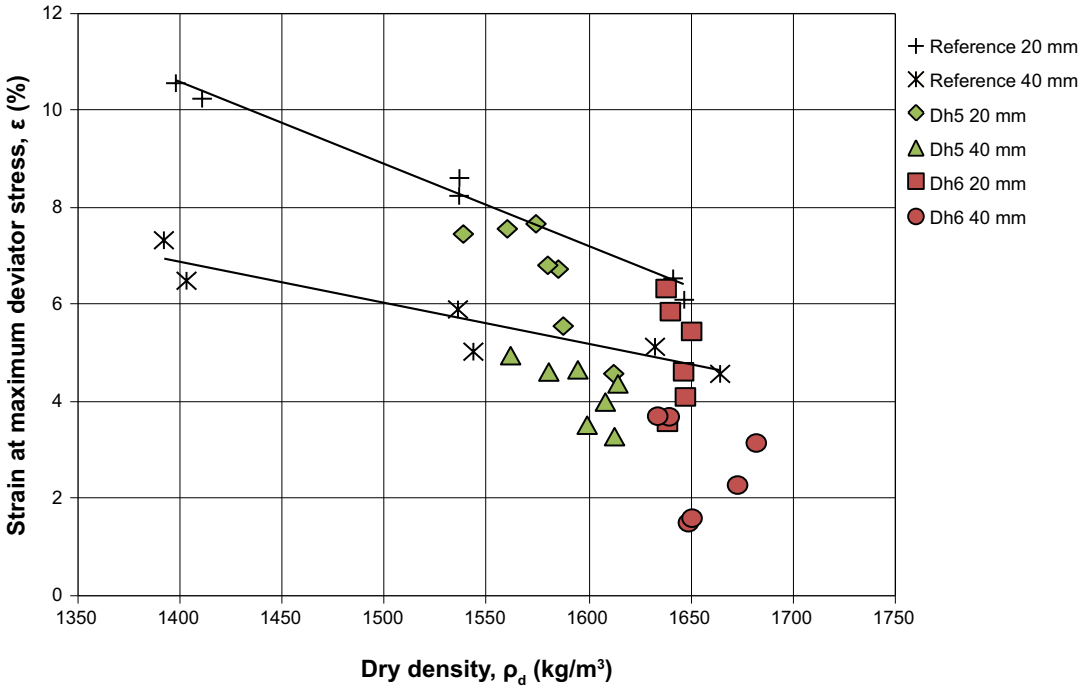


***Figure 2-26.*** *Strain at maximum deviator stress versus dry density for test series with short and tall, saturated specimens.*

The strain at failure of the specimens is primarily dependent on the dry density (Figure 2-26). A higher density results, as expected, in lower strain at failure, i.e. a more brittle behavior. The strain at failure is also depending on the height of the samples, i.e. the higher samples have smaller strain at failure. Although there is large scatter in the evaluated strain at failure for the specimens with field-exposed material, especially at higher densities, the differences between the reference specimens and the field-exposed specimens are small. All the samples of the field-exposed material plot, however, below the lines representing the strain for the reference specimens, implying that field-exposed material is somewhat more brittle than the reference specimens. In Figure 2-27 the distance from the lines evaluated from the reference samples and the measured strain at maximum deviator stress from Figure 2-26 are plotted as function of the position of the samples relative the canister surface. There seems to be at trend in the plot indicating that the deviation from the reference line is increasing with decreasing distance from the canister, i.e. the higher the temperature the greater the brittleness of the field-exposed material.

The observed differences in strain between exposed and reference materials might be related to some of the geochemical alterations which were observed in the innermost centimeters of the buffer (see Section 3). Figure 2-27 is, however, indicating a trend of decreasing strain up to a distance of 100 mm from the canister and this would leave some other mechanisms to be responsible for the results obtained.

The data from the unconfined compression tests performed in the investigation of the field experiment Canister Retrieval Test (CRT) are plotted in Figure 2-28. The strength of the samples is similar to that of the samples tested within the Prototype project. The strain at maximum deviator stress is also similar although the effect of the temperature on this parameter is more pronounced in the CRT test.

The data from the unconfined compression tests performed in the investigation of the field experiment Temperature Buffer Test (TBT) are plotted in Figure 2-29. Also in this experiment the strength of the samples is similar to that of the samples tested within the Prototype project. Exceptions are those samples which were exposed to the highest temperatures (the red dots in Figure 2-29), which have a lower maximum deviator stress compared to the rest of the tested material. This has been explained by the fact that these specimens were very difficult to take out from the buffer block without getting fractures which have affected the strength even after saturation (Åkesson et al. 2012). The strain at maximum deviator stress for the field-exposed material in TBT is significantly lower than that of the reference specimens which is also valid for the specimens taken close to the canister in the Prototype repository (cf. Figure 2-27). It should be pointed out that the maximum temperature in the buffer of the TBT was much higher than in the Prototype Repository buffers.

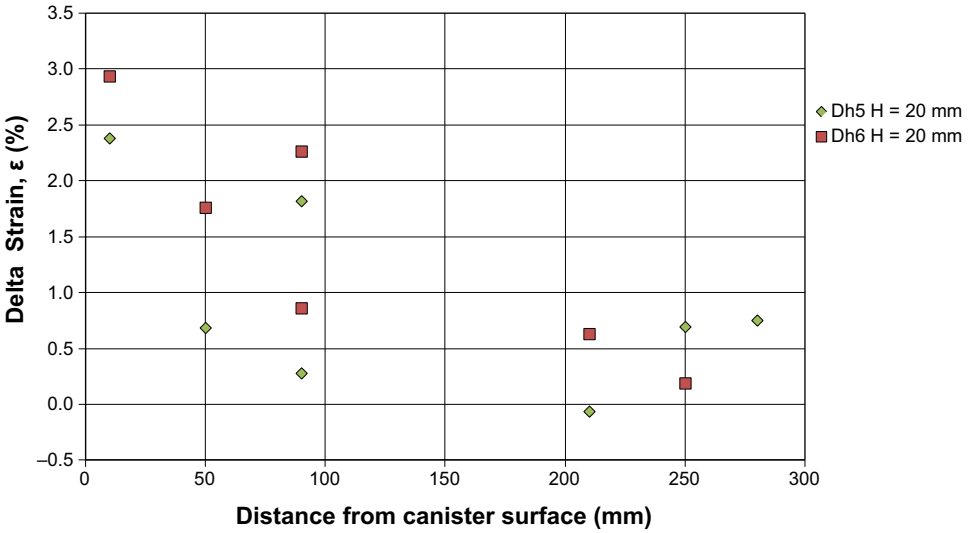


***Figure 2-27.*** *The calculated differences between the "reference line" and the measured strain at maximum deviator stress as function of the distance for the specimens to the canister surface.*

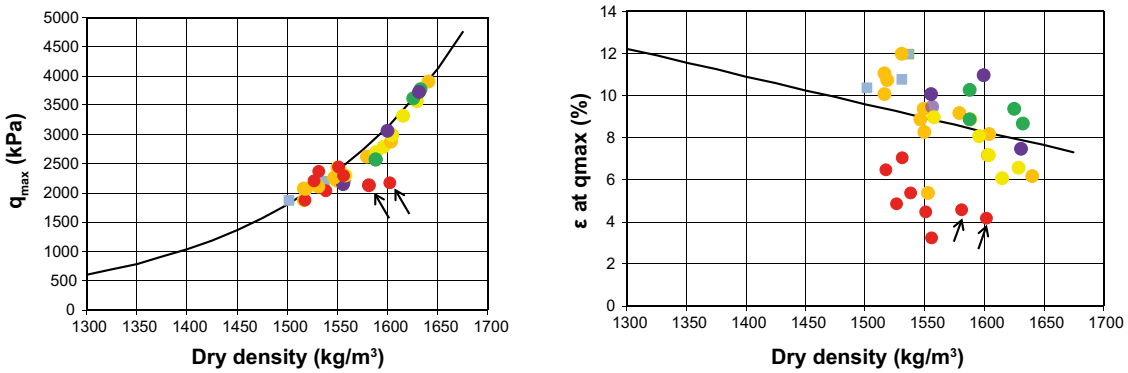


***Figure 2-28.*** *Maximum deviator stress and strain versus dry density for specimens taken from the CRT. Test results for the short specimens (series CRTUC) with the colors red, orange, yellow, green, dark blue, purple and light blue representing the temperatures 93˚C, 87˚C, 83˚C, 78˚C, 74˚C, 69˚C and 28˚C, respectively. The trend-lines represent a best fit line from the reference tests. The arrows indicate specimens with a pronounced crack at sampling (from Dueck et al. 2011a).*

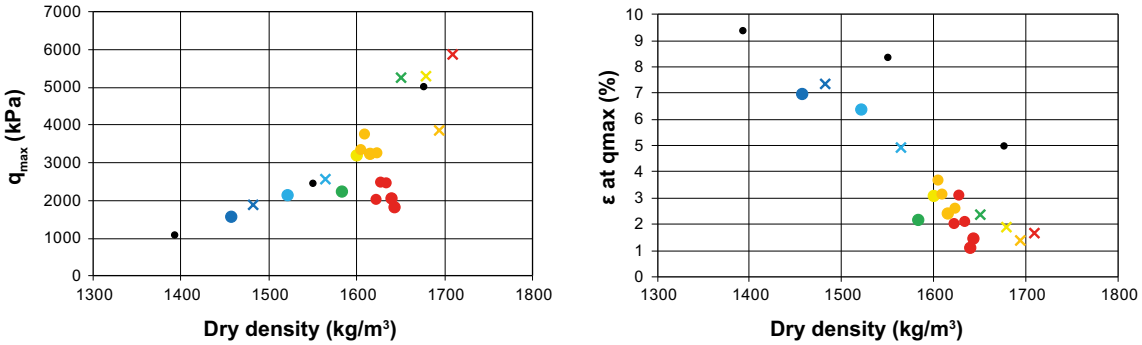


***Figure 2-29.*** *Maximum deviator stress and strain versus dry density for test series with short saturated specimens and specimens sheared directly after drilling (crosses) taken from the TBT. From the warmest to the coldest the colors red, orange, yellow, green, and blue are used. Black points denote references. (from Åkesson et al. 2012)*

## 2.5 Summary of the hydro-mechanical analyses

Based on this investigation, where properties of bentonite exposed to repository-like conditions were compared to those of reference material, the following observations were made in the determination of swelling pressure and hydraulic conductivity;

- No large differences in swelling pressure between the reference specimens and the specimens with field-exposed material were observed, although there was a small tendency that the swelling pressures of the field-exposed material were somewhat lower.
- The hydraulic conductivity of the trimmed specimens taken from the field experiment was somewhat lower than that of the reference specimens, especially at higher densities.
- The small differences observed between the tests of field-exposed material and the reference tests cannot be correlated to the positions in the buffer and thus, to the maximum temperature the samples have been exposed to.

And the following in the triaxial tests;

- The stiffness of all the specimens was similar at the beginning of the tests, i.e. up to a strain of about 2%. At failure however, the strain of the specimens with field-exposed material was smaller compared to the specimens of reference material.
- The field-exposed specimens tended to have higher deviator stress at failure than the reference specimens.

And finally in the unconfined compression tests the following was observed;

- The stress at failure increased with increasing dry density but no large differences in strength between the reference specimens and the specimens with field-exposed material were seen.
- The strain at failure of the specimens depends on the dry density and a higher density results in lower strain at failure, i.e. a more brittle behavior. The field-exposed material was somewhat more brittle than the reference specimens.

The results are consistent with findings from the analyses made on the material from the Canister Retrieval Test. The CRT was running at similar temperature as the Prototype Repository, although for shorter time, five years.

The findings from the Temperature Buffer Test are not in all respects comparable to the results from the Prototype Repository. The explanation for this might be that the TBT was running at higher temperature than the Prototype Repository.

# 3 Chemical and mineralogical analyses of the bentonite buffer

## 3.1 Introduction

The stability of the bentonite, and of its predominant mineral smectite, when subjected to elevated temperatures and hydration by saline water from the host rock is of vital importance for the long-term performance of the buffer. Previous field tests at different scales, of different design and duration have highlighted mainly thermo-hydraulic processes and effects of water and solute transports under the thermal and hydration gradients that prevail during the initial operational stage of a repository (e.g. Dueck et al. 2011b, Olsson and Karnland 2011, Åkesson et al. 2012). The objective of the present study was to determine chemical and mineralogical properties of the buffer material before and after the field experiment in order to assess how the bentonite was affected by a 8-year-long exposure to hydrothermal conditions.

At the retrieval in 2011 the bentonite buffers in deposition hole 5 and 6 had been subjected to elevated temperature and wetting by groundwater for almost eight years. The design criteria for the KBS-3 repository stipulate that the temperature should never exceed 100ºC at any position in the buffer. The recorded temperature evolution at mid height in the buffers in deposition hole 5 and 6 (cf. Figure 1-3 to Figure 1-5) shows that the maximum temperature (80–85ºC) had been below the stipulated maximum temperature during the entire test period, and also that higher temperature had been maintained for longer time in deposition hole 5 than in deposition hole 6. The outer parts of both buffers were never heated above ~ 60ºC.

The state of the buffers in terms of water content, dry density, and degree of water saturation at the time of excavation shows that none of the buffers was homogeneous after almost 8 years of wetting with groundwater. Moreover, large variations existed, both between the deposition holes and between blocks from the same hole, and also within one and the same block (cf. Figure 1-6 to Figure 1-8).

Bentonite from altogether five different blocks from the buffers in deposition hole 5 and 6 has been analyzed either at Clay Technology AB, Lund, B+Tech Oy, Helsinki, or by SKB at MAX-lab, Lund University, for a chemical and mineralogical characterization. All results obtained by the three laboratories are presented in this joint report, where Section 3.3 contains the results reported by Clay Technology AB, Section 3.4 the results reported by B+Tech Oy, and Section 3.5 the results reported by SKB.

## 3.2 Materials and methods

The buffers surrounding the copper canisters consisted of compacted Wyoming bentonite with the commercial name Volclay MX80, which is a sodium-dominated bentonite produced by American Colloid Co.

The bentonite blocks for the buffers had been compacted by a tentative method in which a lubricant had been applied to the walls of the mold used in the block manufacturing. In the investigation of the buffer from the Canister Retrieval Test (Dueck et al. 2011b), which was compacted using the same method, it was observed that those block surfaces that had been in contact with lubricated mold walls were contaminated. According to the material safety data sheet from the producer (Dow Corning) the lubricant is based on hydrotreated heavy naphtalenic petroleum distillate, solvent dewaxed heavy paraffinic petroleum distillate and 12-hydroxy lithium stearate, with additives of $MoS_2$, Zn-dialkyldithiophosphate and graphite. In order to discriminate chemical artifacts caused by contamination of the bentonite with grease, an analysis of the lubricant, Molycote® BR2+, was included in the laboratory tests of the Prototype project and performed at a laboratory accredited for analyses of petroleum products (Saybolt Sweden AB). The result is given in Table 3-1.

**Table 3-1. Chemical analysis of selected elements in Molykote® BR2+ (excl. C).**

| Analysis | Unit | Method | Result | Uncertainty |
|---|---|---|---|---|
| Sulfur | % mass | ASTM D4294-10 | 1.800 | 0.078 |
| Metals by ICP: | | ASTM D5185-95m | | |
| Mo | mg/kg | | 928 | |
| Zn | mg/kg | | 6,754 | |
| Li | mg/kg | | 780 | |
| P | mg/kg | | 3,560 | |
| Mg | mg/kg | | 1 | |
| Cu | mg/kg | | 2 | |
| Ni | mg/kg | | 1 | |

### 3.2.1 Sampling

The laboratories at Clay Technology, Lund, and B+Tech, Helsinki, used similar sampling strategies and the same analytical methods unless otherwise stated. When differences exist in the procedures, this is indicated in the following descriptions: e.g. use of different sample mass is indicated as 0.8/0.5 g, where the order is Clay Technology/B+Tech. The investigation performed at SKB´s laboratory focused on the innermost ~ 50 mm of one of the top blocks (P6R10), which was analyzed primarily for determination of the oxidation state of iron and copper (XANES-analyses).

Dismantling of the test packages from deposition hole 5 and 6 was completed during 2011 and, awaiting the laboratory tests, large sectors of the bentonite rings were stored in evacuated and welded bags of aluminum laminate. Selected sectors of the bentonite rings were sawn horizontally in five parts with a thickness of approximately 10 cm, which were labeled A (at the top) to E (at the bottom).

Laboratory samples were taken along the radius of two sectors of block R06 from deposition hole 5 – a “wet” profile in sector 050 (analyzed by Clay Technology AB) and a “dry” profile in sector 250 (analyzed by B+Tech Oy). The position of the blocks in the buffer is shown in Figure 3-1 and the sampled profiles in Figure 1-6 to Figure 1-8. Two blocks from deposition hole 6 have been analyzed, sector 165 of block R05 (Clay Technology AB) and sector 355 of block R08 (B+Tech Oy; Figure 3-1 and Figure 1-6 to Figure 1-8). The latter block was sampled at B+Tech, while the rest of the sampling was made at Clay Technology. Before sampling, a few millimeters were removed from the top and bottom of the blocks to avoid possible contamination that may have occurred during handling and transport.

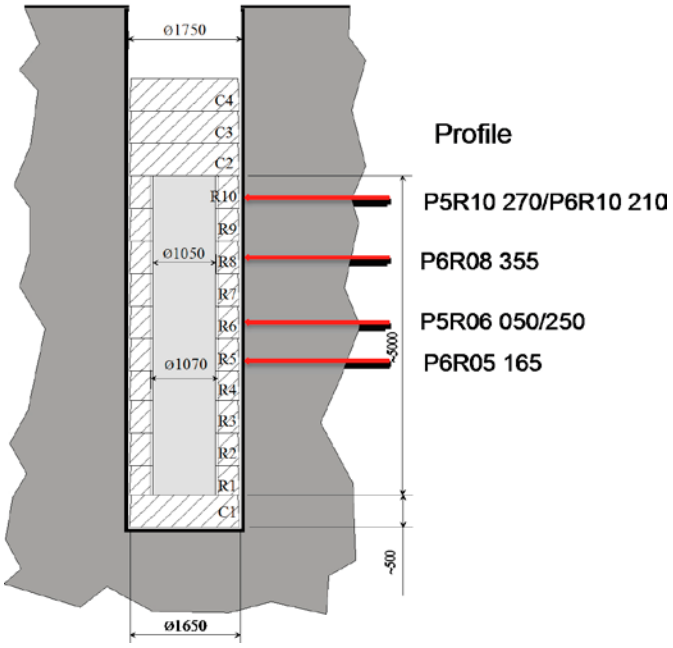


*Figure 3-1. Dimensions (in mm) of the buffer/canister and the vertical position of the sampled bentonite blocks in deposition hole 5 (P5) and 6 (P6), respectively.*

In general, samples were cut into ~ 20/~ 17 mm thick slices with a wire saw, but the spatial resolution was increased at the canister. The canister/bentonite interface was sampled by scraping off a 1–2 mm thick layer from the bentonite surface with a surgical knife.

In addition, samples for chemical analysis with increased spatial resolution were taken of the innermost 3 cm of the profiles P5R06 050, P5R10 270, and P6R05 165, which were sliced by use of a knife in 1 to 5 mm thick, contiguous samples (Clay Technology AB).

Separate samples of profiles P6R05 165 and P5R10 270 for Mössbauer analysis and of profile P6R10 210 for XANES analysis, respectively, were taken under inert atmosphere in a glove box, but for the rest, sampling was made under normal laboratory conditions without any precautions to avoid oxidation of the samples.

All samples and analyses have been compiled in Table 3-2 and Table 3-3.

**Table 3-2. Test matrix for Prototype, deposition hole 5, block R06 profile 050, block R06 profile 250, and block R10 profile 270. b = bulk bentonite; c = fraction < 0.5 µm.**

| Sample id | Thickness (mm) | Aqueous leaching | EC | CEC | Chemical analysis | XRD | SEM | FTIR | Mössbauer |
|---|---|---|---|---|---|---|---|---|---|
| P5R06 050A 525 | < 1 | b | b | b | b | b | b | b | |
| P5R06 050A 530 | 10 | b | b | b/c | b/c | b/c | | b/c | |
| P5R06 050A 545 | 20 | b | b | b/c | b/c | b/c | | b/c | |
| P5R06 050A 585 | 20 | b | b | b/c | b/c | b/c | | b/c | |
| P5R06 050A 630 | 20 | b | b | b/c | b/c | b/c | | b/c | |
| P5R06 050A 725 | 20 | b | b | b/c | b/c | b/c | | b/c | |
| P5R06 050A 765 | 20 | b | b | b/c | b/c | b/c | | b/c | |
| P5R06 050A 825 | 20 | b | b | b/c | b/c | b/c | | b/c | |
| P5R06 R-1 | ref | b | b | b/c | b/c | b/c | | b/c | |
| P5R06 R-2 | ref | b | b | b/c | b/c | b/c | | b/c | |
| P5R06 R-3 | ref | b | b | b/c | b/c | b/c | | b/c | |
| P5R06 050A 526 | 1 | | | | b | | | | |
| P5R06 050A 528 | 2 | | | | b | | | | |
| P5R06 050A 530 | 2 | | | | b | | | | |
| P5R06 050A 532 | 2 | | | | b | | | | |
| P5R06 050A 534 | 2 | | | | b | | | | |
| P5R06 050A 536 | 2 | | | | b | | | | |
| P5R06 050A 538 | 2 | | | | b | | | | |
| P5R06 050A 541 | 5 | | | | b | | | | |
| P5R06 050A 547 | 5 | | | | b | | | | |
| P5R06 050A 551 | 5 | | | | b | | | | |
| P5R06 250B 525 | < 1 | b | b | b | b | b | | b | |
| P5R06 250B 530 | 10 | b | b | b/c | b/c | b/c | | b/c | |
| P5R06 250B 545 | 20 | b | b | b/c | b/c | b/c | | b/c | |
| P5R06 250B 600 | 20 | b | b | b/c | b/c | b/c | | b/c | |
| P5R06 250B 640 | 20 | b | b | b/c | b/c | b/c | | b/c | |
| P5R06 250B 730 | 20 | b | b | b/c | b/c | b/c | | b/c | |
| P5R06 250B 770 | 20 | b | b | b/c | b/c | b/c | | b/c | |
| P5R06 250B 830 | 20 | b | b | b/c | b/c | b/c | | b/c | |
| P5R06 R-1 | ref | b | b | b/c | b/c | b/c | | b/c | |
| P5R06 R-2 | ref | b | b | b/c | b/c | b/c | | b/c | |
| P5R10 270C 525 | 1 | | | | b | | | | b |
| P5R10 270C 527 | 2 | | | | b | | | | |
| P5R10 270C 530 | 2 | | | | b | | | | |
| P5R10 270C 532 | 2 | | | | b | | | | |
| P5R10 270C 534 | 2 | | | | b | | | | |
| P5R10 270C 536 | 2 | | | | b | | | | |
| P5R10 270C 538 | 2 | | | | b | | | | |
| P5R10 270C 542 | 5 | | | | b | | | | |
| P5R10 270C 547 | 5 | | | | b | | | | |
| P5R10 270C 552 | 5 | | | | b | | | | |
| P5R10 R | ref | | | | b | | | | |

**Table 3-3. Test matrix for Prototype, deposition hole 6, block R05 profile 165 (A, B, and D), block R08 profile 355 and block R10 profile 210. b = bulk bentonite; c = fraction < 0.5 µm.**

| Sample id | Thickness (mm) | Aqueous leaching | EC | CEC | Chemical analysis | XRD | SEM | FTIR | Mössbauer | XANES |
|---|---|---|---|---|---|---|---|---|---|---|
| P6R05 165B 525 | < 1 | b | b | b/c | b/c | b | b | b/c | | |
| P6R05 165B 530 | 10 | b | b | b/c | b/c | b/c | | b/c | | |
| P6R05 165B 540 | 20 | b | b | b/c | b/c | b/c | | b/c | | |
| P6R05 165B 555 | 20 | | | | b | | | | | |
| P6R05 165B 575 | 20 | b | b | b/c | b/c | b/c | | b/c | | |
| P6R05 165B 615 | 20 | b | b | b/c | b/c | b/c | | b/c | | |
| P6R05 165B 645 | 20 | b | b | b/c | b/c | b/c | | b/c | | |
| P6R05 165B 735 | 20 | b | b | b/c | b/c | b/c | | b/c | | |
| P6R05 165B 775 | 20 | b | b | b/c | b/c | b/c | | b/c | | |
| P6R05 165B 825 | 20 | b | b | b/c | b/c | b/c | | b/c | | |
| P6R05 165B 835 | < 1 | | | | b | | | | | |
| P6R05 R-1 | ref | b | b | b/c | b/c | b/c | | b/c | b | |
| P6R05 R-2 | ref | b | b | b/c | b/c | b/c | | b/c | b | |
| P6R05 R-3 | ref | b | b | b/c | b/c | b/c | | b/c | | |
| P6R05 165A 525 | < 1 | | | | b | | | | | |
| P6R05 165A 526 | 1 | | | | b | | | | | |
| P6R05 165A 528 | 2 | | | | b | | | | | |
| P6R05 165A 530 | 2 | | | | b | | | | | |
| P6R05 165A 532 | 2 | | | | b | | | | | |
| P6R05 165A 534 | 2 | | | | b | | | | | |
| P6R05 165A 536 | 2 | | | | b | | | | | |
| P6R05 165A 538 | 2 | | | | b | | | | | |
| P6R05 165A 542 | 5 | | | | b | | | | | |
| P6R05 165A 547 | 5 | | | | b | | | | | |
| P6R05 165A 552 | 5 | | | | b | | | | | |
| P6R05 165D 535 | 10 | | | | | | | | b | |
| P6R05 165D 555 | 10 | | | | | | | | b | |
| P6R05 165D 575 | 10 | | | | | | | | b | |
| P6R05 165D 615 | 10 | | | | | | | | b | |
| P6R08 355A 525 | < 2 | b | b | b/c | b/c | b/c | | b/c | | |
| P6R08 355A 527 | 16 | b | b | b/c | b/c | b/c | | b/c | | |
| P6R08 355A 574 | 16 | b | b | b/c | b/c | b/c | | b/c | | |
| P6R08 355A 620 | 16 | b | b | b/c | b/c | b/c | | b/c | | |
| P6R08 355A 735 | 17 | b | b | b/c | b/c | b/c | | b/c | | |
| P6R08 355A 786 | 17 | b | b | b/c | b/c | b/c | | b/c | | |
| P6R08 355A 837 | 17 | b | b | b/c | b/c | b/c | | b/c | | |
| P6R08 355A 846 | 8 | b | b | b/c | b/c | b/c | | b/c | | |
| P6R05 R-1 | ref | b | b | b/c | b/c | b/c | | b/c | | |
| P6R05 R-2 | ref | b | b | b/c | b/c | b/c | | b/c | | |
| P6R10 210 525 | < 1 | | | | | b | | | | b |
| P6R10 210 532 | 6 | | | | | b | | | | b |
| P6R10 210 544 | 6 | | | | | b | | | | b |
| P6R10 210 558 | 6 | | | | | b | | | | b |
| P6R10 R | ref | | | | | b | | | | b |

Samples were labeled according to the general nomenclature (Section 1.2.2), i.e. with the number of the deposition hole, the block number (R for ring-shaped blocks), the compass direction in the deposition hole, the vertical level in the block (A-E), and the distance (in millimeters) from the center of the canister. A suffix **b** or **c** indicates wether the sample consists of the bulk material or the clay fraction (in this case the fraction < 0.5 µm). Uncompacted MX-80 bentonite stored since the manufacturing of each of the blocks was used as reference samples, which were labeled with deposition hole and block number plus R (and b or c).

### 3.2.2 Sample preparation

In general, both the bulk samples and the Na-converted < 0.5 μm fractions of the bentonite were analyzed for mineralogy, cation exchange properties, and chemical composition (cf. Tables 3-2 and 3-3). The bulk material was not subject to any pre-treatments prior to the analyses, apart from drying at 60ºC and grinding in a ball mill/crushing in an agate mortar.

In order to get as pure a smectite fraction as possible, thereby making element allocations in formula calculations less ambiguous, the < 0.5μm fraction, instead of the conventional < 2μm clay fraction, was chosen. Furthermore, the clay was saturated with one single, non-structural cation – in this case sodium- to make the allocation of cations to exchange and structural sites, respectively, less ambiguous. In order to facilitate separation of the < 0.5 μm fraction, the bentonite (~ 20 g) was first suspended in deionized water and the clay was converted to Na-clay by addition of NaCl p.a. (final concentration 1M), followed by centrifugation and decantation of the clear supernatant. The procedure was repeated twice. Excess salt was thereafter removed by centrifuge-washings followed by dialysis (Spectrapore 3, 3,500 MWCO dialysis membrane) against deionized water until the electrical conductivity of the external water remained < 10 μS/cm for five days. After completed dialysis the slurry was dispersed in deionized water and centrifuged with a centrifugation time/speed calculated by use of Stokes´ Law to correspond to a particle separation at an equivalent diameter of 0.5 μm. The supernatant was thereafter withdrawn with a pipette. The sediment was re-suspended, centrifuged and the supernatant collected repeatedly until the supernatant was transparent. The fine clay fraction was thereafter subjected to two more cycles of salt treatment, washing and dialysis. Further details on the purification and homo-ionisation procedure can be found in e.g. Kiviranta and Kumpulainen (2011).

Part of the Na-converted clay suspension was exchanged to Mg-form for XRD analysis, and the rest was dried at 60ºC, ground with an oscillating mill to approximately 10 μm, and used for the other analyses (cf. Tables 3-2, 3-3).

### 3.2.3 Aqueous leachates

Aqueous leaching of the bulk samples was performed to obtain information about the composition of solutes and soluble salts in the bentonite. The dried (105ºC) and ground bentonite was dispersed in deionized water (solid:liquid ratio 1:100) by ultrasonic treatment for 30 minutes and stirring overnight. The suspension was left for 5 days at room temperature to allow equilibration and sedimentation. After phase separation by centrifugation and stepwise ultra-filtration using filters of decreasing pore size (from 2 to 0.2 μm syringe filters Acrodisc PF), major anions and inorganic C were determined by use of ion chromatography (IC) and a C/N analyzer, respectively, at the Department of Biology, Lund University.

The parallel analyses performed by B+Tech included dispersion of bulk sample in deionized water (solid:liquid ratio 1:30), two hours of shaking, centrifugation and determination of dissolved sulfate and chloride in the clear supernatant by ion chromatography at Labtium Oy, Finland.

### 3.2.4 Chemical analysis of bentonite and purified, homoionic Na-clay

The chemical composition of the bulk material and of the Na-converted < 0.5μm fraction of the bentonite was determined at a certified laboratory (ACME Analytical Laboratories, Canada). Major and refractory elements, and rare earths were determined by ICP emission or mass spectroscopy using standard techniques for silicate analysis ($LiBO_2/Li_2B_4O$ fusion followed by nitric acid digestion). Precious metals and base metals (Mo, Cu, Pb, Zn, Ni, As, Cd, Sb, Bi, Ag, Au, Hg, Tl, Se) were determined by ICP mass spectroscopy in leachates of aqua regia. Loss on ignition (LOI) was determined as the difference in weight of the dried (at 105/60ºC) and the ignited sample (at 1,000ºC). Total carbon and sulfur were determined by evolved gas analysis (EGA) at the same laboratory by combustion of the samples in a Leco furnace, equipped with IR-detectors. Carbonate carbon was determined as $CO_2$ evolved on treatment of a sub-sample with hot 15% HCl. Sulfate was determined on separate samples pre-ignited at 550ºC. The concentration of sulfide-S may be estimated by subtracting the sulfate-S concentration from the total concentration of S. Similarly, the concentration of organic C can be estimated by subtracting inorganic C from the total concentration of C.

The concentration of $Fe^{2+}$ was determined titrimetrically (at ACME Analytical Laboratories, Canada) in the samples from blocks P5 R06 250 and P6 R08 355 (B+Tech). First, samples were digested with sulfuric acid, followed by digestion with hydrofluoric acid. Then indicator solution, consisting of distilled water, sulfuric acid, phosphoric acid, boric acid and diphenylamine sulfonate, was added to every sample solution. Solutions were titrated using a dichromate ($K_2Cr_2O_7$) solution. Concentration of $Fe^{3+}$ was determined by subtracting the ferrous iron concentration from the total concentration of Fe.

### 3.2.5 Cation exchange capacity (CEC) and exchangeable cations (EC)

The cation exchange capacity (CEC) of bulk materials and of fine clay fractions (< 0.5 μm) was determined by exchange with copper(II)triethylenetetramine following the procedure of Meier and Kahr (1999), modified according to Ammann et al. (2005) to ensure complete exchange.

The ground sample (~ 400/200 mg) was dispersed in 50/25 ml deionized water by ultrasonic treatment and shaking until complete dispersion. 20/10 ml of ~ 15 mM Cu(II)-triethylenetetramine solution was added to the suspension, which was left to react for 30 minutes on a vibrating table. After centrifugation, the absorbance at 620 nm of the supernatant was measured using a spectrophotometer (Shimadzu UV-Vis/Thermo Scientific Genesys 10S UV-Vis, respectively) and deionized water as blank solution. CEC was calculated on the basis of the uptake of Cu by the clay. The water content of the clay was determined gravimetrically for a separate sample dried at 105º C for 24 h. All CEC determinations were done in duplicate.

The exchangeable cations of the bulk bentonite were determined by extraction into alcoholic ammonium chloride solution according to a procedure originally recommended for CEC determinations of gypsiferous/calcareous soils (e.g. Belyayeva 1967, Jackson 1975). An alcoholic solution was used to minimize dissolution of gypsum and calcite, which are soluble in aqueous solutions. Ideally, i.e. when there is a minimum of easily soluble salts, such as chlorides and carbonates of alkali metals, the sum of extracted cations should be equivalent to the CEC of the sample.

0.8/0.5 g of the ground bulk sample was shaken for 30 minutes in approximately one third of a total volume of 50/25 ml of the extractant (0.15/0.5 M $NH_4Cl$ in ~ 80% ethanol). After centrifugation the supernatant was collected. This treatment was repeated twice. After evaporation of the alcohol and adjustment of the volume with deionized water, the concentration of Ca, Mg, Na and K was determined by use of an ICP-AES equipment (at the Department of Biology, Lund University/Labtium Oy, Finland). Cu was included in the analyses of the samples from block P6 R05 165. The water content of the bentonite was determined for a separate sample as described above. The results are reported as milliequivalents/100 g dry weight.

### 3.2.6 X-ray diffraction analysis (XRD)

Two of the laboratories determined the mineralogical composition by X-ray diffraction analysis of both randomly oriented powders of bulk samples, and of oriented samples of purified and homoionic Mg-clay samples. The third laboratory performed X-ray diffraction on randomly oriented powders in capillaries with a synchrotron source. The procedures differ in many respects, which motivates that separate descriptions are given:

Clay Technology AB:

Random powders of bulk samples are needed for a general characterization of the bentonite, for quantitative evaluations and for the distinction between di- and trioctahedral types of clay minerals by measurements of d(060). These specimens were prepared after grinding the bulk material by use of an agate mortar and pestle to a grain-size < 10 μm. Samples were stored at room temperature at ambient relative humidity. The powders were scanned in the 2θ interval 2–66° with a step size of 0.05º 2θ and a counting time of 5 s.

The < 0.5μm fractions of the samples were X-ray scanned as oriented specimens, which give strongly enhanced basal (*00l*) reflections, and little or no evidence of the hk reflections of clay minerals. This type of preparation is used for clay mineral identification and is necessary for tests of the swelling properties and identification of interstratified structures. In order to give unambiguous diffraction characteristics, the samples were suspended in deionized water and saturated with magnesium by

addition of $MgCl_2$ (0.5M). After removal of excess salt by centrifuge-washings, oriented aggregates were prepared of the clay slurry according to the "smear-on-glass" method" (Moore and Reynolds 1989) and dried at room temperature. The oriented mounts were X-ray scanned with a step size of 0.06º 2θ and a counting time of 5 s in the interval 2–36° 2θ. In order to test the swelling properties, the samples were re-scanned after solvation with ethylene glycol (EG) at 60ºC for 48 hours.

A Seifert 3000 TT X-ray diffractometer with CuKα radiation and automatic divergence slit was used for the X-ray diffraction analyses.

B+Tech Oy:

Bulk sample was ground in agate mortar with pestle to a particle size < 10 µm. Approximately 10 mg of ground bulk material was mixed with acetone on a glass slide. Sample mount was put into a desiccator that contained saturated $Mg(NO_3)_2$ solution in order to achieve standard relative humidity (54% RH at 20º C), and kept there at least 5 days. Sample mount was then transferred to a rotating sample holder, scanned with Philips X'Pert MPD diffractometer equipped with Cu anode tube and monochromator, a variable divergence slit, using wavelength of $K\alpha_1$ = 1.54060 Å; $K\alpha_2$ = 1.54443 Å; and Kβ = 1.39225 Å; voltage of 40 kV and current of 55 mA, from 2 to 70º 2θ with 0.02º counting steps and 1s/step counting time at the Geological Survey of Finland. The XRD mount was scanned three times and the mean pattern calculated in order to decrease the background noise for more efficient detection of accessory minerals. The XRD pattern was first used for identification of minerals. The low angle intensity aberrations produced by the auto-slit geometry were corrected with the HighScore Plus for the full pattern fitting (quantification) with Siroquant. The position of the d(060) line of the clay minerals was assessed.

To identify clay minerals, oriented XRD mounts were prepared from purified clay fractions (< 0.5 µm) that had been converted to Mg-forms. The filter-membrane peel-off technique (Drever 1973, Moore and Reynolds 1989) was used for preparation of the mounts. A concentrated suspension containing approximately 600 mg of purified clay in 10 ml of deionized water was vacuum filtered onto 0.45 µm pore size cellulose filter and transferred to a glass slide. Sample mounts were dried in air and X-ray scanned from 2 to 35º 2θ with 0.02º counting steps and a counting time of 1s/step. Then, oriented sample mounts were placed on a platform in a desiccator containing EG and put into an oven at 60ºC for 20 h. Mounts were scanned immediately after solvation from 2 to 35º 2θ with 0.02º counting steps and a counting time of 1s/step to identify smectites. All determinations were done at the Geological Survey of Finland, except the scanning of oriented mounts of four samples from profile P5:R06 250B (640c, 730c, 770c, and 830c), and all scans of EG solvated oriented clay fractions from profile P5:R06 250B, which were done at the University of Helsinki, Department of Inorganic Chemistry, using Philips X'Pert PRO MPD diffractometer equipped with Cu tube (wavelength 1.5419 Å, voltage of 45 kV and current of 40 mA), variable divergence slit set to 8 mm constant irradiated length, and PIXcel1D detector, from 2 to 35º 2θ with 0.053º counting steps.

The mineralogical composition was determined from randomly oriented XRD patterns of bulk samples using a full-profile Rietveld refinement by the Siroquant software. Only minerals identified by XRD or by optical microscopy were included in the analysis. First, background was subtracted. Refinement was done in several subsequent steps until no major improvement in pattern fit was achieved. Instrument zero, phase scales, half-widths, unit cell dimensions, and preferred orientation were refined. Mineralogical composition was validated by comparison with the normative composition calculated from the chemical data.

SKB´s laboratory at Äspö:

Synchrotron X-ray diffraction studies of samples from the short profile P6R10 210 were carried out and reported by Daniel Svensson, SKB and Staffan Hansen, Lund University. X-ray powder diffraction data were collected at beam-line I711 at the MAX-lab synchrotron, Lund University, Sweden (Cerenius et al. 2000) using a Mar system with a flat CCD detector (Mar 165, 2,048 × 2,048 pixels). The X-ray beam had a wavelength of 0.994 Å, as refined using a $LaB_6$ reference sample, and a size of 0.9 mm × 0.9 mm. Data collection was done for 30 s. The data were evaluated using the software Fit2d (version V12.077, A.P. Hammersley, ESRF). The sampling was done in ambient atmosphere and a capillary was filled with ground clay (agate mortar) and was sealed with modelling clay. The samples used were thus essentially unoriented.

### 3.2.7 Optical microscopy of coarse fractions

Optical microscopy was performed by B+Tech on samples from profiles P5R06 250 and P6R08 355 in order to identify accessory minerals in the coarse fraction (> 0.5 µm), which was separated from the clay material by gravity sedimentation. A small amount of sample was gently ground in agate mortar, placed on a glass slide and a drop of glycerol (with refractive index of 1.47) was added. Cover glass was placed on top. Sample mounts were observed with plane- and cross-polarized light. Among others, color, pleochroism, birefringence, particle size, morphology, and isotropicity of mineral particles were examined.

### 3.2.8 Scanning Electron Microsopy (SEM)

Bentonite from positions close to the canister/bentonite interface in block P6R05 and block P5R06 was analysed by SEM/EDX analyses in order to give a more detailed picture of the distribution of elements. Centimeter-sized samples from the copper/bentonite contact zone were vacuum dried, mounted on glass sample holders by use of carbon tape, and finally placed in a SEM Hitachi S-3400N microscope. Morphology was mainly studied in low vacuum mode (80 Pa) by use of a quad-type semiconductor backscattered electron detector, and element analyses were performed with an Oxford energy dispersive spectrometer with a Si detector (Inka X-sight mod 7021 EDX). An acceleration voltage of 15 kV, a sample current about 1 nA and a counting live-time of 50 s were used. Cobalt was used to monitor drift of the instrument.

Detailed element analyses in points, along lines and on areas (mapping) were performed. Generally, there is a significant scatter in this kind of SEM/EDX analyses due to true local variation in the element distribution in the original MX-80 bulk material, and to steric artefacts related to the sample preparation. In order to capture general trends, area mean analyses (typically 50 µm × 50 µm) were also performed at increasing distances from the copper/bentonite interface.

The penetration depth of the excitation electrons is only a few µm at the maximum, and the results consequently only represent this depth. Analyses were therefore made both on the bentonite surface that had been in direct contact with the copper canister, and on prepared surfaces in the bentonite perpendicular to the copper/bentonite interface. The latter surfaces were prepared by breaking the samples without further processing, in order not to redistribute any material. Special focus was on the radial distribution of elements, minerals and substances, e.g precipitates, copper, and the lubricant used in the production of the bentonite blocks. These analyses were performed by Clay Technology AB.

### 3.2.9 Fourier transform infrared spectroscopy (FTIR)

All FTIR analyses were performed and evaluated by B+Tech, Helsinki.

FTIR was used to study changes in composition of clay minerals, and identify poorly crystalline phases such as silica and opal, minor or trace minerals such as carbonates, and organic material. 2 mg of dry and ground sample material was ground with 200 mg of KBr powder in agate mortar and pressed to 13 mm diameter discs. The spectrum was recorded immediately after preparation and after drying the KBr discs at 150° C for 20 h to remove adsorbed water. Infrared spectrum was recorded in triplicate using transmission mode in a range from 4,000 to 300 (or 200) $cm^{-1}$ with Perkin Elmer Spectrum One FTIR spectrometer at the Department of Geosciences and Geography, University of Helsinki. Resolution of scans was 4 $cm^{-1}$. In order to avoid misunderstandings in comparisons of FTIR patterns, a sharp band at wavelength 1,384 $cm^{-1}$ arising from plain KBr pellet was removed from all patterns.

During the fractionation of sample P6R08 355A 525b, a black, non-polaric, light material separated from the sample and floated on top of the suspension. This material was assumed to be lubricant used in the block production and was collected and analyzed with FTIR (sample P6R08 355A 525b_black) in order to separate FTIR bands arising from lubricant from the ones in the bentonite.

### 3.2.10 Mössbauer analysis

The Mössbauer analysis was carried out and reported by Johan Lindén, Åbo Akademi, Department of Physics (Appendix 1). The analyses were performed on selected samples to identify potential changes in iron-bearing minerals, and to quantify changes in iron oxidation state. Samples were dried in $N_2$-atmosphere inside a glove box, ground to a fine powder and thereafter sent under $N_2$-atmosphere to Åbo Akademi, where the samples immediately were placed in a glove box (concentration of $O_2/H_2O$ less than 4 ppm). Each sample was prepared at maximum a few days before the measurement was started. 55 mg of sample powder was mixed with epoxy glue in an Al-cup in $N_2$-atmosphere. The mixture was spread evenly on the bottom of an Al-cup (area of ~ 3 $cm^2$), air bubbles (if present) were pierced with a needle and the samples were allowed to dry in a glove box in $N_2$-atmosphere. Just before the measurement, the epoxy protected absorbers were exposed to ambient air for approximately 30 minutes when transferred to the vacuum chamber of the cryostat used for cooling the samples to 77 K.

All spectra were collected at 77 K in transmission mode using a sinusoidal velocity scale with a maximum Doppler velocity of 10.1 mm/s. The velocity was chosen to allow detection of the magnetic lines of Fe oxides and hydroxides. For paramagnetic samples this scale was a bit too large, but weak magnetic lines were anticipated to be present (Kumpulainen et al. 2011), hence this velocity scale was chosen. The 77 K temperature prevents the oxidation of the samples during the long measurement. The geometry, i.e. source-to-detector distance, absorber area and collimation, was the same for all samples, as well as the settings for the gamma-ray window. Data were collected for seven days for each sample. The reference sample R-1 was measured first and sample R-2 was measured after all other samples were measured.

Sample cooling was achieved using an Oxford ITC-4 continuous-flow cryostat operated with liquid nitrogen. The 14.4-keV Mössbauer quanta were produced by a Cyclotron Co. $^{57}$Co:*Rh* (25 mCi April 2009) source and detected using a LND 4546 proportional counter with a beryllium window. A Fast ComTec MA-250 velocity transducer was used for moving the source. It was equipped with a Halder MR-351 drive unit. The data was gathered using a Fast ComTec MCA-3 multichannel-analyzer PCI card in an ordinary desktop PC. The measurements were done in a multiscaling mode. The spectra were fitted using a homemade, nonlinear least-square fit program, utilizing spectral components corresponding to four paramagnetic doublets and one magnetic sextet (all components were not found in every spectrum). For the paramagnetic components, fit parameters were quadrupole splitting ($\Delta$ in mm/s), isomer shift ($\delta$ with respect to $\alpha$-Fe in mm/s) and spectral intensities (I in %). For the magnetic component, the internal field (B in T) and its gaussian distribution ($\Delta$B in T) were included as fit parameters as well. All components were constrained to have a common line width ($\Gamma$ in mm/s).

### 3.2.11 XANES analysis

XANES studies on samples from profile P6R10 210 were carried out and reported by Daniel Svensson, SKB and Staffan Hansen, Lund University. Natural $FeCO_3$ (siderite from Ivigtut, Greenland; Fe(II) in octahedral coordination; freshly ground) was used as Fe(II) standard and synthetic $Fe_2O_3$ (Fe(III) in octahedral coordination) was used as Fe(III) standard. In order to assure the reliability of the XANES measurements, these standards were routinely re-measured.

When the bentonite blocks were removed from the deposition hole their surface was exposed to air. The blocks were as rapidly as possible packaged in vacuum-sealed aluminum-polymer bags. The total time from sampling in the hole to the packaging was approximately 5 minutes. Further sampling was done under argon atmosphere in a glove box. The surface of the samples was removed by scraping and the specimens for the XANES measurements were taken from the inner part along the length of the sample. After a couple of minutes the bentonite in the argon box ($O_2$ < 0.1 ppm, $H_2O$ = 0.6 ppm) showed some cracking caused by dehydration. The total time between the uptake of the samples and the XANES measurements at the synchrotron was 4 days.

The samples were mounted between sulfur free XRF tapes in a polypropylene sample holder. The thickness of the sample holder was 1 mm and the size of the X-ray beam was in the order of 0.5 mm × 0.5 mm. X-ray absorption data was recorded at beam line I811 at the MAX-lab synchrotron, Lund University, Sweden. The beamline is based on a super-conducting multi-pole wiggler that pro-

vides a high-flux X-ray beam. The design is based on vertical collimation of the beam by a cylindrical mirror before a double-crystal monochromator in Si(111) direction (approximately 0.7 eV in energy resolution). The second crystal is bendable for horizontal focusing, and the vertical focusing on the sample is done by a second cylindrical mirror. The horizontal focus is obtained by sagittal bending of the second monochromator crystal (Carlson et al. 2006). Three consecutive scans were recorded in the range –150 to +500 eV (relative to the absorption edge) and merged. The scans were of quick-scan type (approximately 2,200 steps in about 120 seconds; 0.33 eV step size). The Lytle detector was used (fluorescence mode) due to the rather low iron content in some of the clays. Metallic iron foil was used for energy calibration, and a manganese filter was added to remove X-rays with lower energies.

The free software Athena (version 0.8.059; Bruce Ravel, Brookhaven National Laboratory) was used. Athena is a graphical front end to IFEFFIT (version 1.2.5; Matt Newville, Consortium for Advanced Radiation Sources, University of Chicago). The first inflection point of the iron foil was adjusted to 7,112.0 eV. The data was normalized in three steps: (i) the spectral region from –150 to –30 eV was fitted to a pre-edge straight line, which was subtracted from the data, (ii) a post-edge straight line was fitted of the spectral region from +150 to approximately +400 eV, which was subtracted from the data, and (iii) an average value of an interval in the post-edge range was used for scaling the data to achieve a step height of unity at the absorption edge. Due to the long spectral region before and after the K edge the automatic normalization routine of the software worked well in all cases. The semi-quantitative determination of the Fe(II) content was done by linear combination fitting of standards in the Athena software, using the default interval –20 to +30 eV relative to the absorption edge. The strategy was to do the linear combination fit in an interval as small and close to the edge as possible to exclude or minimize the effect from the differences in the absorption spectra in the pre- and post-edge regions.

## 3.3 Results for profiles P6R05 165, P5R06 050 and P5R10 270

### 3.3.1 Aqueous leachates

The concentration of anions extracted by dispersion of the bulk samples in deionized water (s:l ratio 1:100) are listed in Table 3-4 and the radial distribution of the major anions chloride, sulfate (as $SO_4$–S) and carbonate (as inorganic C) is plotted in Figure 3-2.

**Table 3-4. Major anions and inorganic carbon (mg/g dry clay) extracted by leaching the bentonite in deionized water in a solid:liquid ratio of 1:100. The water ratio w is listed in the right column.**

| Sample id | F | Cl | $NO_3$–N | $PO_4$–P | $SO_4$–S | inorg. C | w |
|---|---|---|---|---|---|---|---|
| | mg/g dry clay | | | | | | |
| P6R05 165B 525b | 0.040 | 0.679 | 0.018 | 0.007 | 2.76 | 1.93 | 0.236 |
| P6R05 165B 530b | 0.004 | 0.591 | 0.023 | 0.004 | 1.50 | 1.47 | 0.236 |
| P6R05 165B 540b | 0.003 | 0.663 | 0.034 | 0.006 | 1.44 | 1.59 | 0.239 |
| P6R05 165B 575b | 0.002 | 0.990 | 0.048 | 0.007 | 1.41 | 1.33 | 0.251 |
| P6R05 165B 615b | 0.002 | 0.582 | 0.023 | 0.005 | 1.36 | 1.40 | 0.240 |
| P6R05 165B 645b | 0.002 | 0.503 | 0.021 | 0.006 | 1.37 | 1.37 | 0.242 |
| P6R05 165B 735b | 0.002 | 0.665 | 0.027 | 0.007 | 1.35 | 1.52 | 0.242 |
| P6R05 165B 775b | 0.000 | 0.505 | 0.026 | 0.008 | 1.32 | 1.68 | 0.244 |
| P6R05 165B 825b | 0.002 | 1.062 | 0.020 | 0.008 | 1.25 | 1.36 | 0.244 |
| P6R05 Rb-1 | 0.006 | 0.140 | 0.048 | 0.006 | 1.22 | 1.70 | 0.180 |
| P6R05 Rb-2 | 0.015 | 0.181 | 0.033 | 0.006 | 1.24 | 1.67 | 0.180 |
| P6R05 Rb-3 | 0.003 | 0.164 | 0.032 | 0.006 | 1.15 | 1.61 | 0.180 |
| P5R06 050A 525b | 0.016 | 0.393 | 0.004 | 0.014 | 1.34 | 2.11 | 0.260 |
| P5R06 050A 530b | 0.004 | 0.816 | 0.031 | 0.006 | 1.69 | 1.24 | |
| P5R06 050A 545b | 0.001 | 0.492 | 0.005 | 0.000 | 1.00 | 1.14 | |
| P5R06 050A 585b | 0.003 | 0.603 | 0.004 | 0.000 | 1.18 | 1.17 | 0.253 |
| P5R06 050A 630b | 0.003 | 0.639 | 0.006 | 0.000 | 1.17 | 1.21 | 0.256 |
| P5R06 050A 725b | 0.003 | 0.611 | 0.005 | 0.000 | 1.14 | 1.22 | 0.260 |
| P5R06 050A 765b | 0.004 | 0.617 | 0.003 | 0.000 | 1.35 | 1.34 | 0.283 |
| P5R06 050A 825b | 0.003 | 0.584 | 0.003 | 0.000 | 1.07 | 1.32 | |
| P5R06 Rb-1 | 0.008 | 0.115 | 0.032 | 0.000 | 0.99 | 1.57 | 0.175 |
| P5R06 Rb-2 | 0.006 | 0.088 | 0.011 | 0.000 | 1.01 | 1.41 | 0.175 |
| P5R06 Rb-3 | 0.006 | 0.117 | 0.024 | 0.000 | 1.02 | 1.41 | 0.175 |

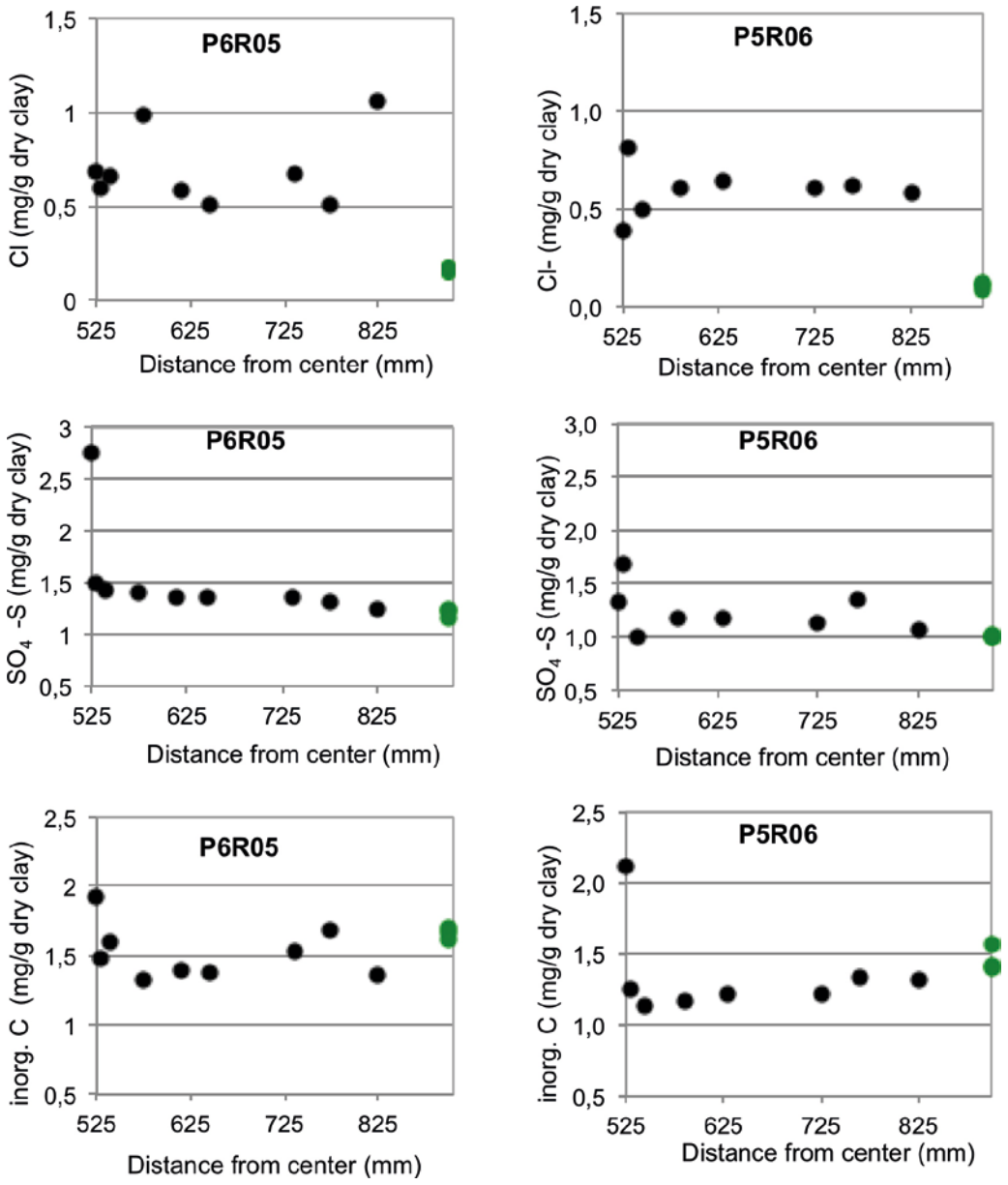


***Figure 3-2.*** *Radial distribution of Cl, $SO_4$–S and inorganic carbon in profiles P5R06 050 and P6R05 165. Reference samples are plotted in green on the right axis.*

The Na-Ca-Cl type groundwater (~ 8,100 mg Cl/L) used for wetting the bentonite buffer is the primary source of chloride (the groundwater composition is given in Table 1-1). Except for the innermost part of the sampled sector 165 from block P6R05, which had a saturation value below 0.95, the sampled sectors of blocks P6R05 165 and P5R06 050 were more or less fully water saturated at the excavation (cf. Figure 1-6 and Figure 1-7). The saturation had resulted in an approximately six-fold increase in the chloride concentration in both blocks, but the chloride distribution is clearly more irregular in block P6R05 (Table 3-4; Figure 3-2).

The sulfate concentration in the contact sample of block P6R05 is more than doubled in relation to the reference samples of the block and slightly elevated in the innermost part of the buffer. Somewhat elevated sulfate concentrations are seen also in the two innermost samples of block P5R06, while the rest of the samples have similar concentrations as the references. Since sulfate is a minor anion in the groundwater, the inventory of gypsum in MX80 bentonite is probably the primary sulfate source, but the distribution gives no clear evidence of a sulfate transport along the thermal/hydration gradients. It is an open question whether the lubricant, which has a total sulfur content of 1.8% S (Table 3-1), might have contributed some sulfur for the sulfate formation.

The inorganic carbon originates from carbonates, which dissolved more or less completely during the leaching with water. Consequently, inorganic carbon is strongly correlated to the acid soluble carbon content of the bentonite (cf. Section 3.3.3) and both parameters indicate carbonate precipitation in the contact samples and depletion in the bentonite some centimeters away from the canister. This pattern is most clear in block P5R06 and calcite in amounts exceeding the detection limit of XRD occurs only in the innermost sample of this block.

### 3.3.2 Exchangeable cations (EC) and cation exchange capacity (CEC)

Data on the cations extracted by exchange against ammonium in alcoholic solution are given in Table 3-5 and the radial distribution of the major cations has been plotted in Figure 3-3.

Exchangeable sodium and potassium both display a minimum at the canister, but all values for the contact samples, which were contaminated by grease in the block production (cf. Section 3.3.3), must be considered uncertain because of the "dilution effect" in the analysis, among other things.

**Table 3-5. Exchangeable cations, extracted by exchange against $NH_4^+$ in 80% alcohol solution. n.d. = not determined.**

| Sample id | Ca | | Cu | K | | Mg | | Na | | Sum |
|---|---|---|---|---|---|---|---|---|---|---|
| | meq/100 g | % | meq/100 g | meq/100 g | % | meq/100 g | % | meq/100 g | % | meq/100 g |
| P5R06 050A 525b | 21.9 | 27 | n.d. | 1.4 | 2 | 5.1 | 6 | 51 | 64 | 80 |
| P5R06 050A 530b | 21.0 | 26 | n.d. | 1.5 | 2 | 5.4 | 7 | 53 | 66 | 81 |
| P5R06 050A 545b | 19.7 | 25 | n.d. | 1.6 | 2 | 5.2 | 7 | 54 | 67 | 80 |
| P5R06 050A 585b | 20.8 | 25 | n.d. | 1.6 | 2 | 5.1 | 6 | 54 | 66 | 82 |
| P5R06 050A 630b | 21.0 | 25 | n.d. | 1.8 | 2 | 5.4 | 7 | 55 | 66 | 83 |
| P5R06 050A 725b | 20.3 | 25 | n.d. | 1.7 | 2 | 5.8 | 7 | 55 | 66 | 83 |
| P5R06 050A 765b | 20.3 | 25 | n.d. | 1.6 | 2 | 5.9 | 7 | 55 | 66 | 83 |
| P5R06 050A 825b | 20.8 | 24 | n.d. | 1.7 | 2 | 6.4 | 8 | 56 | 66 | 85 |
| P5R06 Rb-1 | 21.6 | 25 | n.d. | 1.7 | 2 | 7.0 | 8 | 56 | 65 | 86 |
| P5R06 Rb-2 | 21.8 | 26 | n.d. | 1.6 | 2 | 6.8 | 8 | 55 | 65 | 86 |
| P5R06 Rb-3 | 21.5 | 25 | n.d. | 1.6 | 2 | 7.0 | 8 | 55 | 65 | 85 |
| P6R05 165B 525b | 21.8 | 27 | 0.09 | 1.5 | 2 | 6.6 | 8 | 51 | 63 | 81 |
| P6R05 165B 530b | 19.5 | 24 | 0.03 | 1.7 | 2 | 6.7 | 8 | 55 | 66 | 82 |
| P6R05 165B 540b | 18.5 | 23 | 0.01 | 2.0 | 2 | 5.5 | 7 | 56 | 68 | 82 |
| P6R05 165B 575b | 19.3 | 23 | 0.00 | 2.1 | 3 | 6.4 | 8 | 56 | 67 | 84 |
| P6R05 165B 615b | 19.1 | 23 | 0.01 | 1.9 | 2 | 5.5 | 6 | 58 | 69 | 85 |
| P6R05 165B 645b | 19.2 | 23 | 0.02 | 2.2 | 3 | 5.1 | 6 | 57 | 68 | 83 |
| P6R05 165B 735b | 19.2 | 22 | 0.01 | 1.7 | 2 | 5.7 | 7 | 59 | 69 | 85 |
| P6R05 165B 775b | 18.4 | 22 | 0.03 | 1.9 | 2 | 5.5 | 7 | 59 | 69 | 84 |
| P6R05 165B 820b | 18.6 | 23 | 0.02 | 1.7 | 2 | 6.1 | 8 | 54 | 67 | 80 |
| P6R05 Rb-1 | 19.0 | 23 | 0.03 | 1.6 | 2 | 8.3 | 10 | 53 | 65 | 82 |
| P6R05 Rb-2 | 19.9 | 23 | 0.01 | 1.9 | 2 | 9.1 | 11 | 54 | 63 | 85 |
| P6R05 Rb-3 | 19.4 | 23 | 0.01 | 2.1 | 3 | 8.6 | 10 | 53 | 64 | 83 |

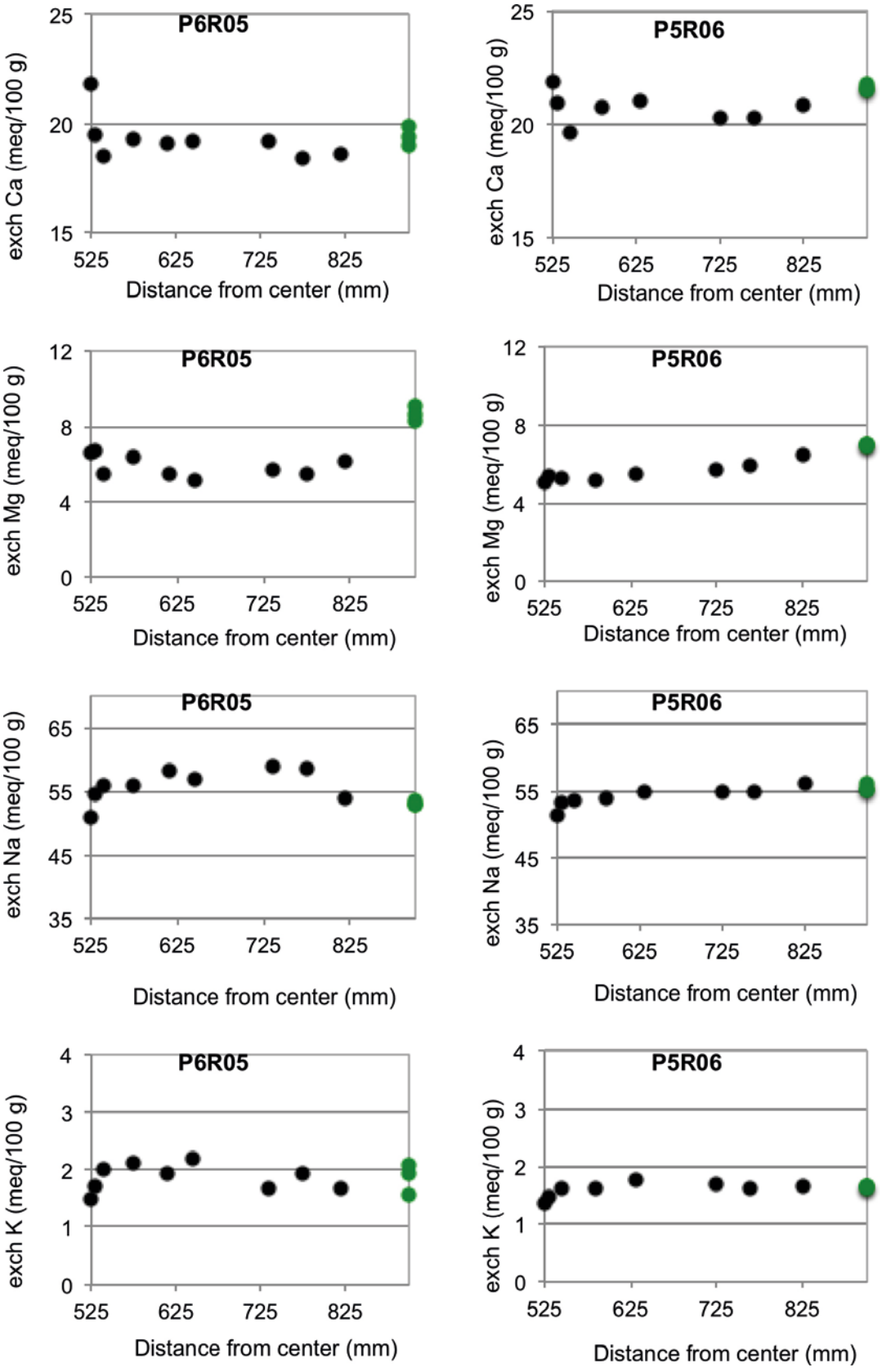


***Figure 3-3.*** *Distribution of exchangeable Ca, Mg, Na and K in profiles P5R06 050 and P6R05 165. Reference samples are plotted in green on the right axis*

There is no clear trend in the distribution of exchangeable calcium, apart from a minor maximum at the canister/bentonite interface in both blocks. Some calcium may be derived from dissolution of calcium sulfate and/or carbonate that precipitated at the canister but the solubility of these phases in the extractant is very low.

In contrast, exchangeable magnesium has decreased -by up to 3 milliequivalents- compared to the references in most parts of the block profiles, suggesting a minor but general desorption of magnesium from exchange sites. In the inner parts calcium is the main replacing cation, while sodium has increased in the middle and outer parts, particularily in block P6R05.

The relative proportion of the extracted cations in the mean reference sample is: sodium 65%, calcium 24%, magnesium 9% and potassium 2%. The proportions have shifted somewhat after the field test, the most significant change being the reduced proportion of magnesium in a large part of both blocks and an increased proportion of calcium at the canister (Figure 3-4).

Copper was included in the analysis of the samples from block P6R05, which showed that copper in clear excess of the concentration in the reference samples was extracted only from the material of the bentonite/canister interface. The extractable amount of Cu was less than 0.5% of the total exchangeable cation pool, and made up approximately one third of the total available amount of Cu (80 ppm), suggesting that most of the copper in the bentonite exists in a form that is not readily accessible for cation exchange.

The cation exchange capacity of bulk samples and of fractions < 0.5 µm are compiled in Table 3-6 and the mean values are plotted versus the position of the samples in the buffer in Figure 3-5. CEC values written in italics in Table 3-6 are for the contaminated samples of the inner block surfaces, in which the total carbon content alone amounts to 2.5–3% C (cf. Section 3.3.3). These CEC-values must be considered uncertain because of the dilution effect, and also because the contaminant itself may produce artifacts in the CEC determination. While no clear trend can be seen in CEC of the bulk bentonite from block P5R06, CEC of the bentonite from the less warm block P6R05 tend to be lower – by up to 4 meq/100 g- than the reference bentonite. The variation in CEC of the reference samples (mean CEC 84.8, st.dev. 0.8 meq/100 g) gives some idea about the repeatability in CEC determinations on MX80 by the Cu-trien method (cf. also Dohrmann et al. 2012), and suggests that an actual difference in CEC might exist between the block and the reference bentonite. The pattern is, however, not reproduced in the CEC-values of the < 0.5 µm fractions of the block, which have essentially the same CEC (mean CEC 94.9, st.dev. 1.2 meq/100 g) as the references for the block (mean CEC 95.3, st.dev. 0.6 meq/100 g). Hence, there are no indications that CEC of the smectite has changed. The fact that at least one of the blocks that was investigated in parallel has given similar, somewhat contradictory CEC results (Section 3.4.3) calls for further investigations to firmly establish whether an actual difference exists in the exchange behaviour of the exposed and the unexposed bulk bentonite in some blocks.

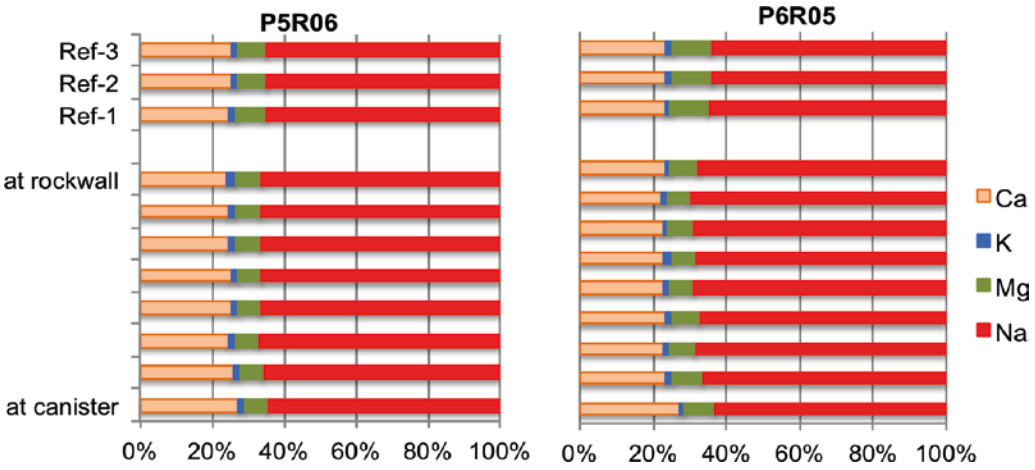


***Figure 3-4.*** *Relative distribution of exchangeable Ca, K, Mg and Na in profiles P5R06 050 and P6R05 165.*

**Table 3-6. Cation exchange capacity (CEC) of bulk samples and of < 0.5 µm fractions from blocks P5R06 and P6R05. Values in italics discussed in the text. n.d. = not determined (fractionation was not possible).**

| Sample id | bulk samples | | | < 0.5 µm | | |
|---|---|---|---|---|---|---|
| | CEC-1 | CEC-2 | CEC-mean | CEC-1 | CEC-2 | CEC-mean |
| | meq/100 g | | | meq/100 g | | |
| P5R06 050A 525 | *80* | *79* | *79* | n.d. | n.d. | |
| P5R06 050A 530 | 83 | 83 | 83 | 90 | 91 | 91 |
| P5R06 050A 545 | 83 | 83 | 83 | 90 | 91 | 90 |
| P5R06 050A 585 | 83 | 83 | 83 | 91 | 92 | 91 |
| P5R06 050A 630 | 82 | 82 | 82 | 89 | 90 | 89 |
| P5R06 050A 725 | 84 | 82 | 83 | 89 | 89 | 89 |
| P5R06 050A 765 | 83 | 82 | 82 | 89 | 89 | 89 |
| P5R06 050A 825 | 82 | 83 | 82 | 90 | 90 | 90 |
| P5R06 R-1 | 85 | 85 | 85 | 89 | 90 | 89 |
| P5R06 R-2 | 84 | 84 | 84 | 90 | 90 | 90 |
| P5R06 R-3 | 82 | 82 | 82 | 89 | 89 | 89 |
| P6R05 165B 525 | *84* | *84* | *84* | *93* | *94* | *93* |
| P6R05 165B 530 | 81 | 81 | 81 | 93 | 94 | 93 |
| P6R05 165B 540 | 81 | 81 | 81 | 96 | 98 | 97 |
| P6R05 165B 575 | 81 | 82 | 81 | 94 | 95 | 95 |
| P6R05 165B 615 | 82 | 83 | 83 | 95 | 96 | 95 |
| P6R05 165B 645 | 82 | 84 | 83 | 95 | 95 | 95 |
| P6R05 165B 735 | 83 | 85 | 84 | 96 | 96 | 96 |
| P6R05 165B 775 | 83 | 83 | 83 | 95 | 94 | 94 |
| P6R05 165B 825 | 83 | 82 | 82 | 94 | 94 | 94 |
| P6R05 R-1 | 85 | 86 | 85 | 95 | 96 | 95 |
| P6R05 R-2 | 85 | 85 | 85 | 95 | 95 | 95 |
| P6R05 R-3 | 84 | 84 | 84 | 96 | 95 | 96 |

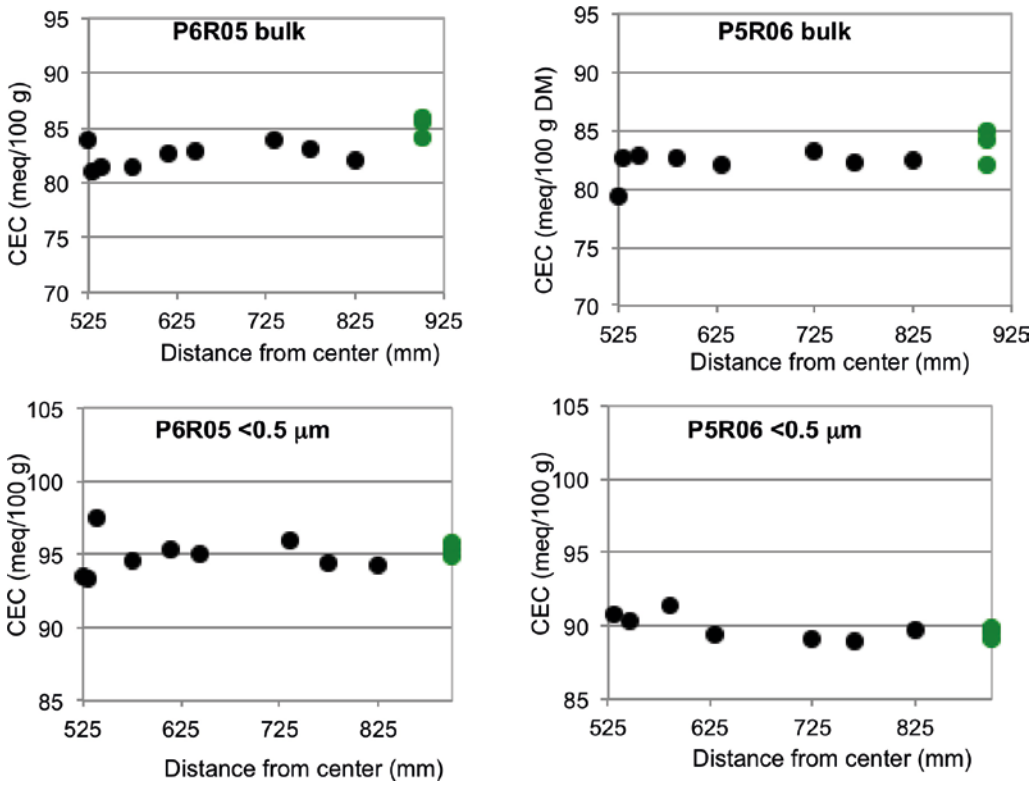


***Figure 3-5.*** *The CEC of bulk samples and of < 0.5 µm fractions in profiles P5R06 050 and P6R05 165.*

The < 0.5 µm fractions of block P5R06 have systematically lower CEC than the < 0.5 µm fractions of block P6R05. Chemical as well as XRD-and FITR-data indicate that the quartz content of the fine clay fractions of block P5R06 is higher than that of the samples from block P6R05, possibly due to an inadequate fractionation procedure. This difference in the amounts of "impurities" with no or insignificant cation exchange capacity will likely be reflected also in CEC.

### 3.3.3 Chemical composition of the bulk bentonite and the fraction < 0.5 µm

The chemical compositions are given in Table 3-7 (bulk samples and < 0.5 µm fractions of block P5R06), Table 3-8 (bulk samples of block P5R10) and Table 3-9 (bulk samples and < 0.5 µm fractions of block P6R05) at the end of this chapter.

The samples of the inner surface of the blocks investigated had conspicuously high contents of "organic carbon" along with higher than average concentrations of Mo, Zn, and P (Figure 3-6), which are the main "indicator" elements of the lubricant used in the block manufacturing (cf. Table 3-1; Li was not included in the analysis of the bentonite because Li-borates were used for the sample digestion). Elevated concentrations of these elements were found also in a sample taken of the outer surface of block P6R05 (Figure 3-6 left), which indicated adsorption of the lubricant on those block surfaces that had been in contact with the greased mold walls. The chemical composition of the fine clay fraction showed that the fractionation by size did hardly reduce the organic carbon content (Figure 3-6) suggesting that the lubricant adhered preferentially to clay particles. Apart from causing inflated concentration values for the indicator elements and dilution effects in the analyses of the contaminated samples, the lubricant affected the dispersion properties of the clay. As a consequence, the yield of the fraction < 0.5 µm of the contact sample 525 from block P6R05 was significantly lower than for other samples from the same profile and the representativeness of the extracted fine clay fraction may therefore be poor. All efforts to disperse the contact sample of block P5R06 were negative and this sample was therefore not possible to fractionate by size.

The three series of contiguous samples taken with increased spatial resolution at the canister suggested that the bentonite was contaminated to a depth of about 5 mm (Figure 3-7).

The radial distribution of copper within the blocks (Figure 3-8) showed that copper had been incorporated into the bentonite immediately adjacent to the canister in concentrations ranging from ~ 80 (block P6R05) to 670 ppm (block P5R06). The latter block had the maximum Cu-concentration of all blocks analyzed by digestion of whole samples (cf. Section 3.4). However, parallel area analyses on a micrometer-scale (50 µm × 50 µm) of the bentonite/canister interface by use of SEM-EDX (Section 3.3.6) showed that the copper content ranged from background concentrations in some areas up to a few weight % in other, nearby areas, suggesting that the copper distribution was much more irregular and random than indicated in the ICP-analyses, which provide the average concentrations of the entire, ~ 1 mm thick contact samples.

The high-resolution series of the innermost 3 cm of the blocks show that the concentration gradient is steep in the innermost millimeters at the canister/bentonite interface in block P5R06 and P6R05, while appear smoothed in the innermost 10 mm in block P5R10 (Figure 3-8 lower diagram). The latter block from the top of the package and the corresponding part of the canister were detached from the package in one piece by sawing, and sawdust might have contaminated the bentonite.

The Na-converted, purified < 0.5 µm fraction of the contact sample from block P6R05 had almost the same copper concentration as the bulk sample (the contact sample from block P5R06 was not fractionated due to poor dispersion), again suggesting that most copper existed in an insoluble, non-exchangeable form (cf. Section 3.3.2).

Sulfate and carbonate minerals are trace constituents in MX-80, but attention is paid to these minerals because of their temperature-dependent solubility – hence, the solubility of gypsum and calcite decreases with increasing temperature. Previous field tests (e.g. Karnland et al. 2011, Olsson and Karnland 2011, Åkesson et al. 2012) demonstrated that these phases tend to be redistributed along thermal and/or hydration gradients and accumulate in the warmer parts of the buffer and also that the dissolution/precipitation reactions involved exerted control on the porewater chemistry.

The mean concentration of total sulfur in the reference MX-80 bentonite is 0.27% S (std. dev. 0.013; N=6; detection limit=0.02%). According to the data on water-soluble salts, approximately 40% of the total sulfur content is derived from soluble minerals, mainly gypsum ($CaSO_4*2H_2O$). Sulfide minerals,

such as pyrite, are the primary source of the remaining sulfur fraction. The sulfur values plotted in Figure 3-9 were calculated on a $CO_2$-free basis to minimize artifacts that arise due to the large variations in the carbon content among the samples. The high-resolution series of contiguous samples show that total sulfur has increased in all three blocks in the vicinity of the canister, where the lubricant, which contains 1.8% S, is a candidate source of sulfur. The peak values are, however, not always found in samples of the canister/bentonite interface (e.g. P6R05) and the results of the aqueous leachates (Section 3.3.1) suggest that also sulfate precipitation has contributed to the increase in total sulfur at the canister in blocks P5R06 and P6R05 (P5R10 was not analyzed).

The purification/fractionation of the < 0.5 µm fraction has effectively removed/dissolved the sulfur-bearing constituents, and the sulfur content of this fraction is generally below the detection limit of the analytical method (0.02%; Tables 3-7 and 3-9).

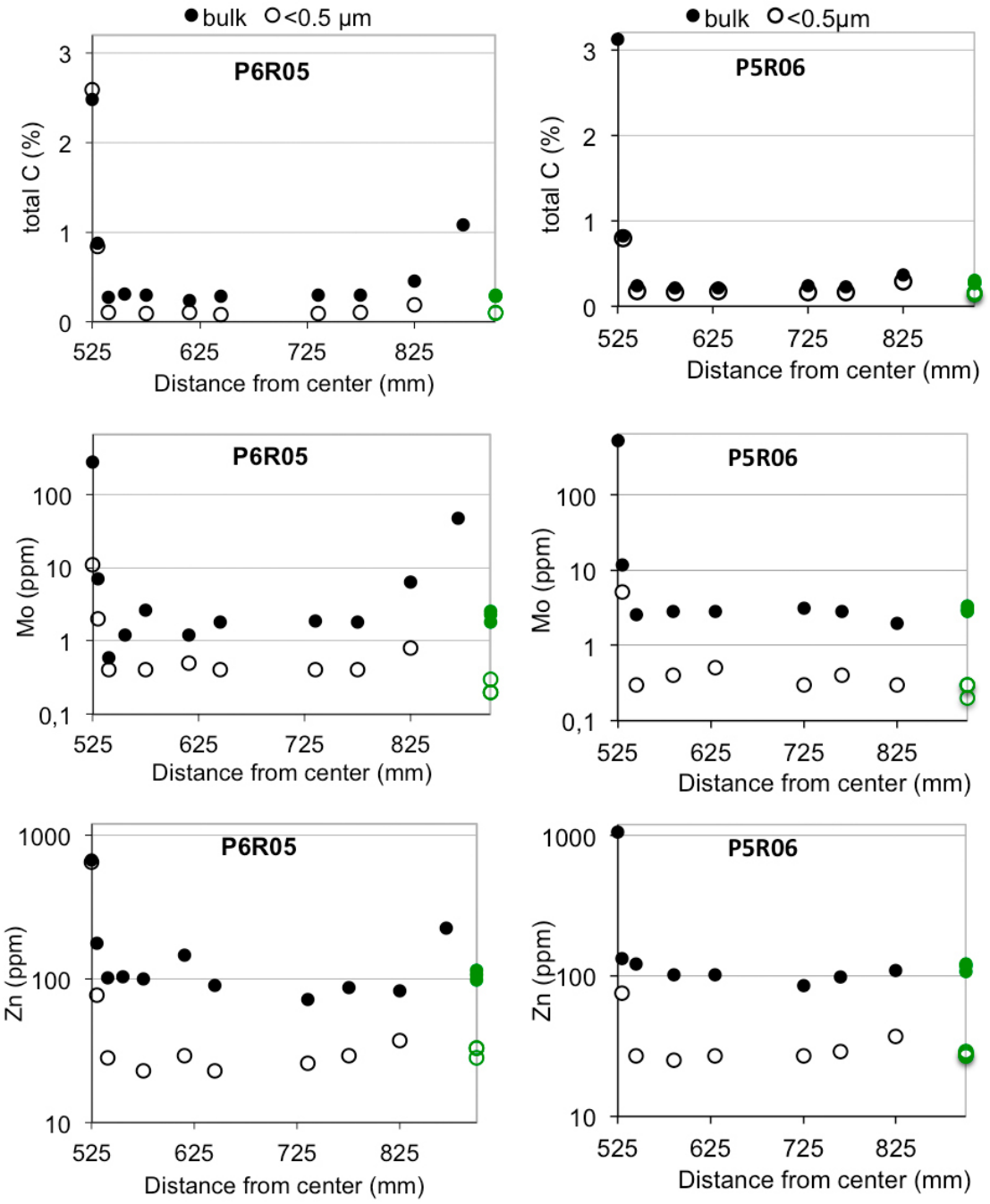


***Figure 3-6.*** *Radial distribution of lubricant "indicator" elements in bulk samples and < 0.5 µm fractions of profiles P5R06 050 and P6R05 165 (< 0.5 µm fraction of P5R06 525 missing). Bulk samples were taken of both the inner and outer surface of block P6R05. Reference samples plotted in green on the right axis.*

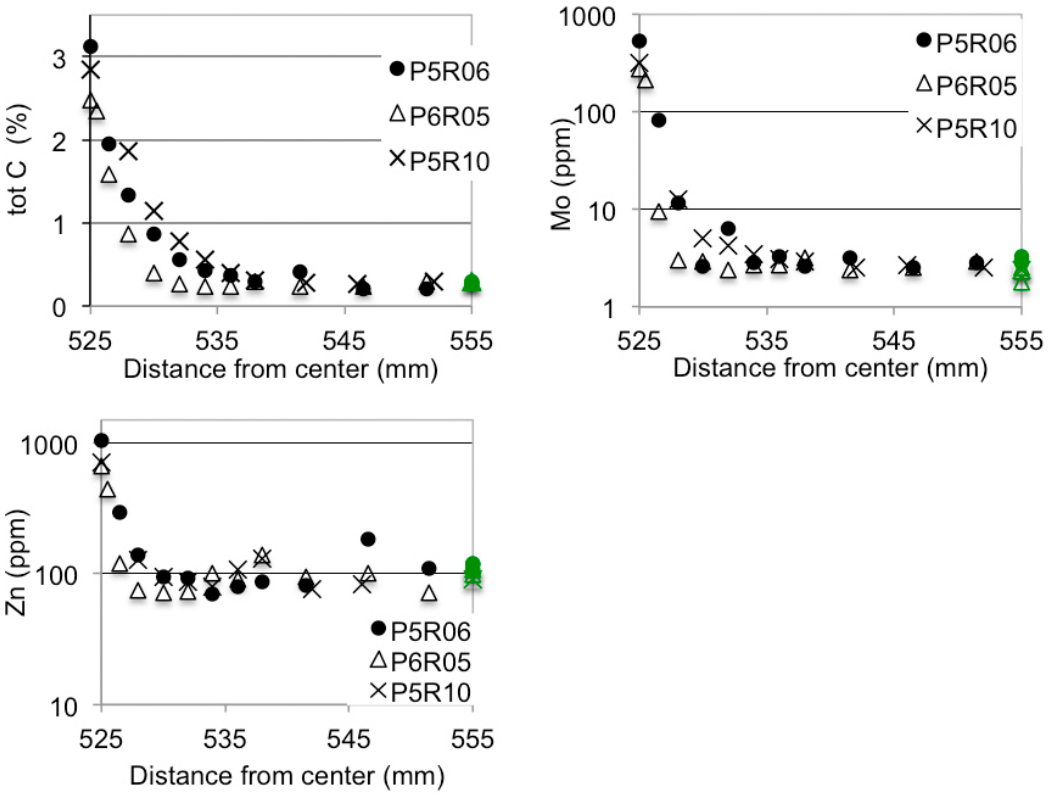


***Figure 3-7.*** *Distribution of lubricant "indicator" elements in the innermost ~ 3 cm of blocks P5R06, P6R05 and P5R10. Reference samples plotted in green on the right axis.*

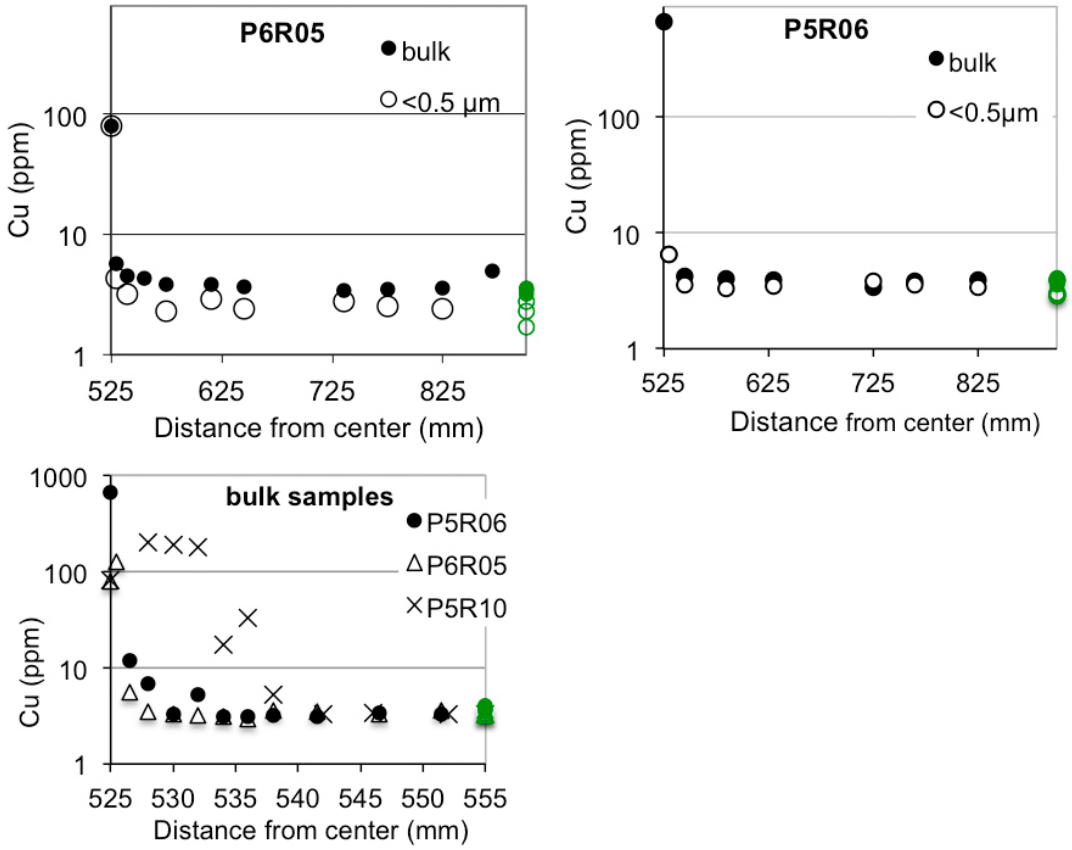


***Figure 3-8. Upper diagrams****: Radial distribution of copper in bulk and < 0.5 µm fractions of profiles P5R06 050 and P6R05 165 (< 0.5 µm fraction P5R06 525 missing). Bulk samples were taken of both the inner and outer block surface of P6R05.* ***Lower diagram****: Distribution of copper in bulk samples from the innermost 3 cm of blocks P5R06, P6R05 and P5R10. Reference samples plotted in green on the right axis.*

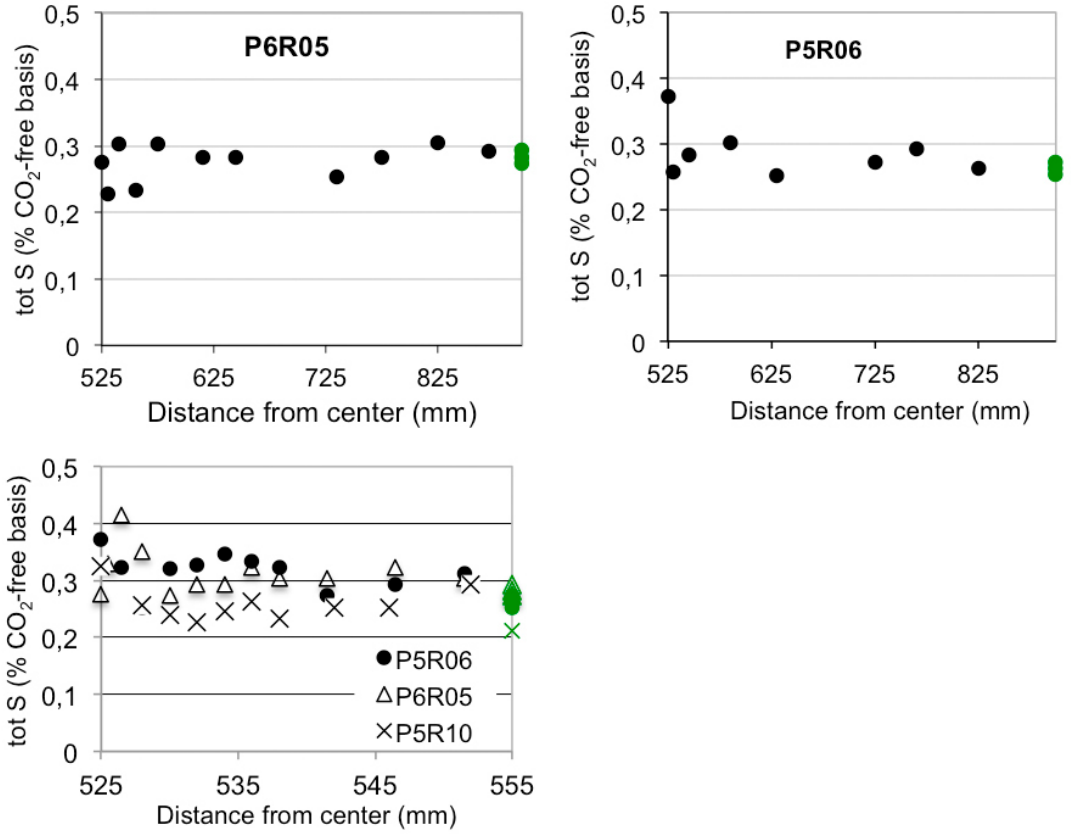


***Figure 3-9. Upper diagrams**: Radial distribution of total sulfur (on $CO_2$-free basis) in bulk samples of profiles P5R06 050 and P6R05 165. **Lower diagram**: Distribution of total sulfur in bulk samples from the innermost 3 cm of blocks P5R06, P6R05 and P5R10. Reference samples plotted in green on the right axis.*

The mean concentration of total carbon in the reference bentonite is 0.29% C (std.dev. 0.014; N=6; detection limit=0.02%). The acid-insoluble carbon fraction (0.16% C) is primarily organic. As already shown (Figure 3-6 and Figure 3-7), the total carbon values are highly inflated in those parts of the blocks that were contaminated by grease, which contains a multitude of carbon compounds as well as graphite.

The mean content of acid-soluble carbon in the reference samples is 0.13% C. This carbon fraction is derived primarily from carbonates, and corresponds to 1.1% $CaCO_3$ if all carbon is allocated to calcium carbonate. In the high-resolution series of the innermost 3 cm of the blocks, the acid-soluble carbon in the two blocks from deposition hole 5 displays a distinct maximum at the canister (Figure 3-10), which is paralleled by an increase in calcium (Figure 3-11), indicating precipitation of calcium carbonate. At some distance from the canister, the bentonite appears depleted in carbonate compared to the references.

In contrast, the distribution of carbonate carbon is fairly constant in the block from deposition hole 6 and calcium correlates better to sulfate than to carbonate carbon in the inner millimeters of this block. The distribution patterns thus match the patterns of the water-soluble inorganic carbon and are consistent with XRD-data indicating an increase in calcite in the innermost sample of the "warmest" block P5R06, whereas as no calcite peaks are detectable in block P6R05 (Section 3.3.5).

The chemical data for the < 0.5 µm fraction (Tables 3-7 and 3-9) indicate that the calcium-bearing phases were effectively removed/dissolved in the purification/fractionation procedure and CaO data for this fraction (range 0.03–0.12% CaO) were omitted in the plots of Figure 3-11.

Also magnesium displays a gradient in the innermost centimeter(s) of all three blocks investigated, with a maximum at the canister. The pattern is particularly distinct in the hottest block P5R06, where the MgO content has increased by 0.8% MgO (ignited basis) compared to the mean of the reference samples (Figure 3-12). While the separation, homo-ionisation and dialysis of the fine clay fraction removed soluble phases, such as sulfates and carbonates of calcium, more or less completely, the magnesium content of the < 0.5 µm fraction of the innermost samples in blocks P6R05 and P5R06 still exceeds that of the reference samples, which suggests that magnesium exists in a phase of low solubility.

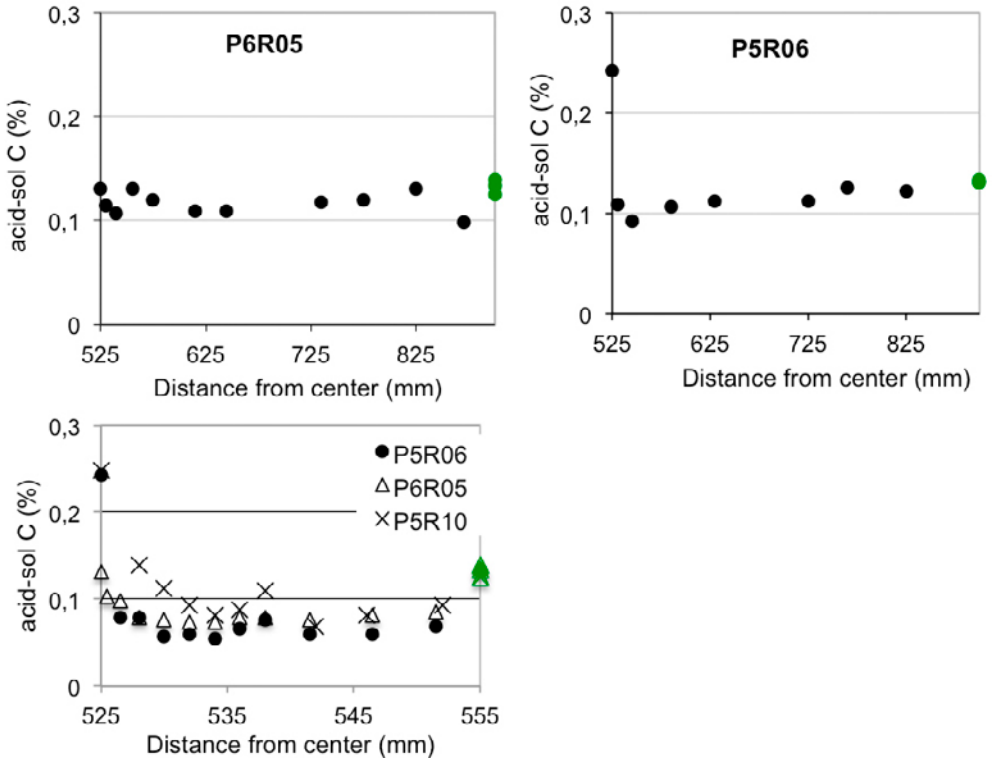


***Figure 3-10. Upper diagrams**: Radial distribution of acid-soluble carbon in bulk samples of profiles P5R06 050 and P6R05 165. Samples were taken of both the inner and outer block surface of P6R05.*
***Lower diagram**: Distribution of acid-soluble carbon in bulk samples from the innermost 3 cm of blocks P5R06, P6R05 and P5R10. Reference samples plotted in green on the right axis.*

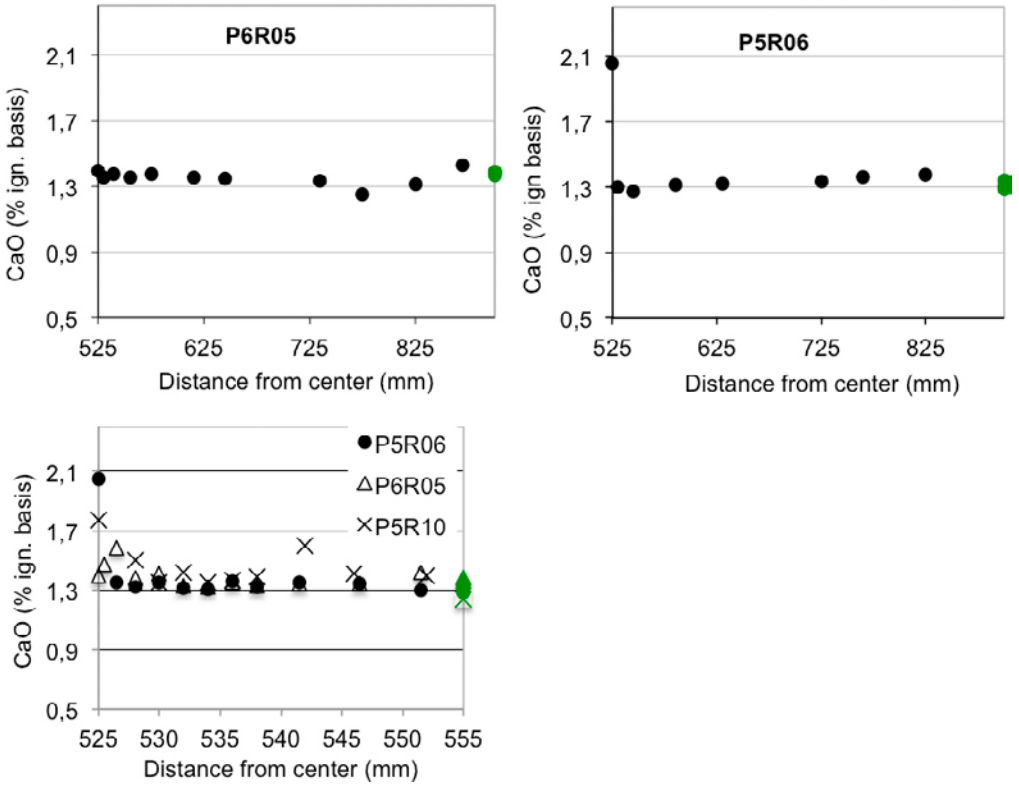


***Figure 3-11. Upper diagrams**: Radial distribution of CaO (ignited basis) in bulk samples in profiles P5R06 050 and P6R05 165. Bulk samples were taken of both the inner and outer block surface of P6R05.*
***Lower diagram**: Distribution of CaO in bulk samples from the innermost 3 cm of blocks P5R06, P6R05 and P5R10. Reference samples plotted in green on the right axis.*

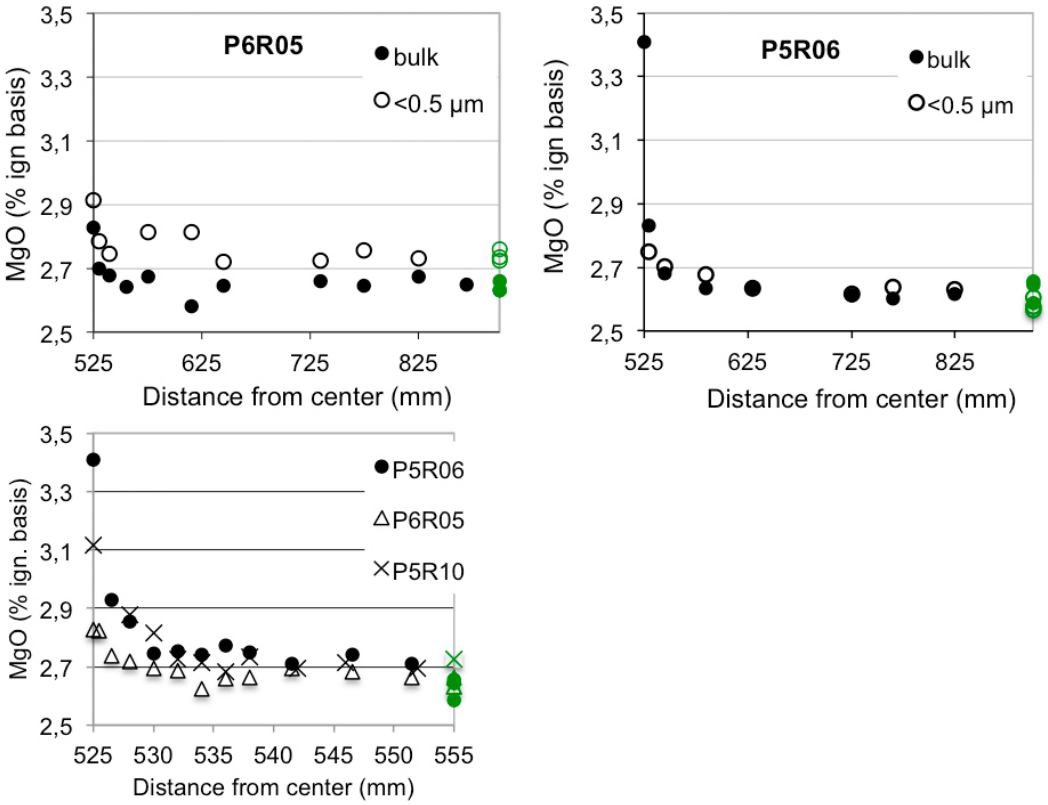


***Figure 3-12. Upper diagrams**: Radial distribution of magnesium (on ignited basis) in bulk samples and < 0.5 µm fractions of profiles P5R06 050 and P6R05 165 (< 0.5 µm fraction of P5R06 525 is missing). Bulk samples were taken of both the inner and outer block surface of P6R05. **Lower diagram**: Distribution of magnesium in bulk samples from the innermost 3 cm of blocks P5R06, P6R05 and P5R10. Reference samples plotted in green on the right axis.*

An analogous distribution pattern of magnesium was observed in the parallel investigation of block P5R06 (cf. Section 3.4.5) and has been reported in several previous field tests with MX-80 buffers and of varying duration, maximum temperatures and temperature gradients (e.g. LOT A0 in Karnland et al. 2011, LOT A2 in Olsson and Karnland 2011, TBT in Åkesson et al. 2012), and also small-scale laboratory tests with MX80 bentonite have demonstrated a migration of magnesium in response to thermal gradients (e.g. Jodin-Caumon et al. 2010).

The distribution pattern of the major oxides $SiO_2$, $Al_2O_3$ and $Fe_2O_3$ displays a more or less distinct decrease towards the canister, which fully or partially is caused by the inherent correlations in constant-sum weight percentages data, i.e. an increase in one component (CaO, C and MgO in this case) results in an apparent decrease in other, major components. Comparisons of the major oxide composition are therefore based on ratios of the oxides rather than percentage values. The ratios $SiO_2/Al_2O_3$ and $Al_2O_3/Fe_2O_3$ (Figure 3-13 and Figure 3-14) display very little changes along the radius of the blocks and the variation is in the same range as in the "repeatability test" performed on the reference bentonite. Except for the $SiO_2/Al_2O_3$ ratio of the fine clay fractions from block P5R06, both ratios are numerically similar also to those of the other blocks investigated in parallel (cf. Section 3.4.5).

The systematically higher $SiO_2/Al_2O_3$ ratio of the fine clay fractions from block P5R06 and the corresponding reference samples reflects the higher content of free silica (quartz) in these samples, which is reflected also in the CEC-values and seen in the XRD- and FTIR profiles of the fine clay fractions. The higher quartz content in this series of samples is probably caused by an inadequate fractionation procedure.

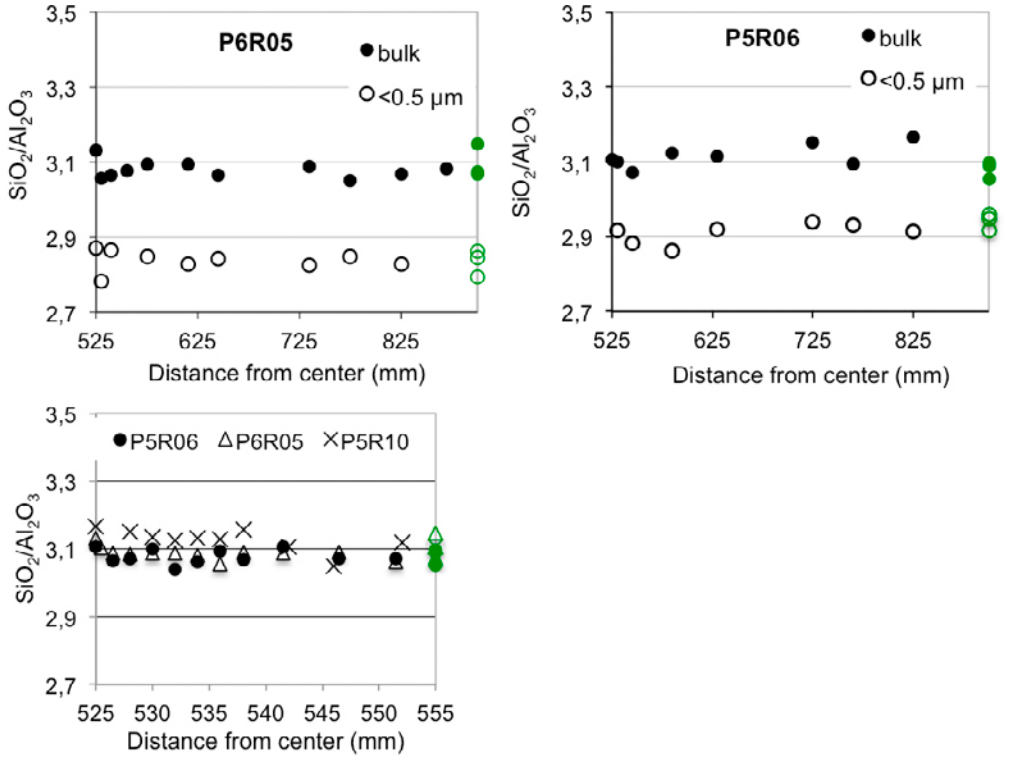


***Figure 3-13. Upper diagrams**: Plot the ratio $SiO_2/Al_2O_3$ of bulk samples and < 0.5 µm fractions of profiles P5R06 050 and P6R05 165 (< 0.5 fraction of P5R06 525 is missing). Bulk samples were taken of both the inner and outer block surface of P6R05. **Lower diagram**: the ratio $SiO_2/Al_2O_3$ of bulk samples from the innermost 3 cm of blocks P5R06, P6R05 and P5R10. Reference samples plotted in green on the right axis.*

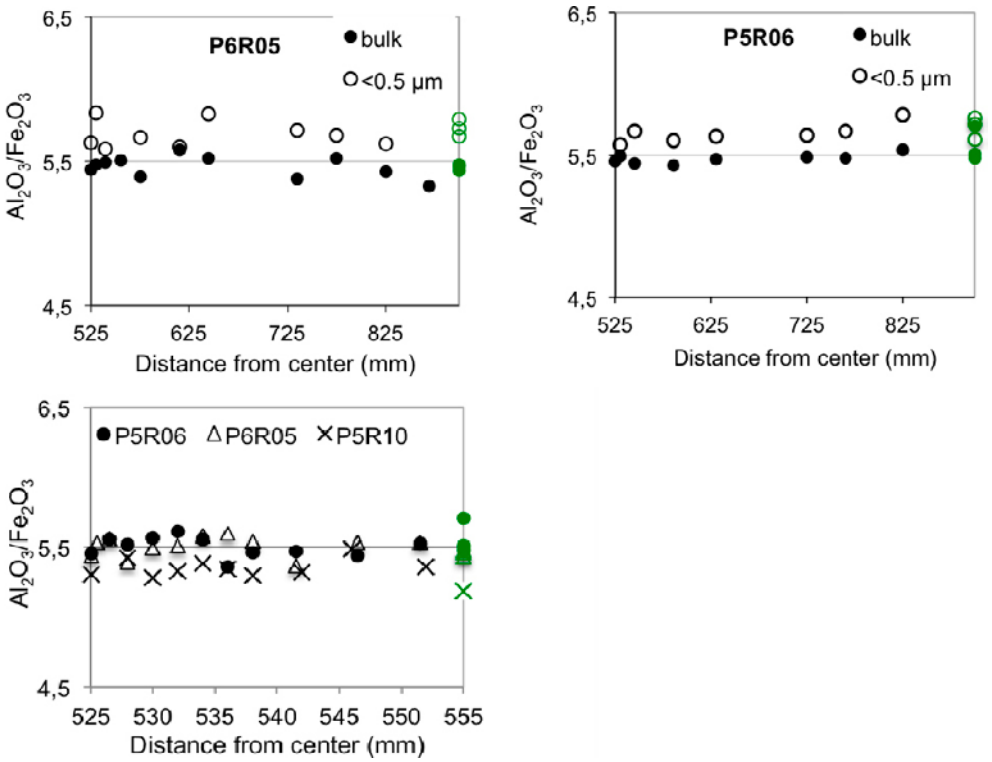


***Figure 3-14. Upper diagrams**: Plot the ratio $Al_2O_3/Fe_2O_3$ of bulk samples and < 0.5 µm fractions of profiles P5R06 050 and P6R05 165 (< 0.5 µm fraction of P5R06 525 is missing). Bulk samples were taken of both the inner and outer block surface of P6R05. **Lower diagram**: Plot of the ratio $Al_2O_3/Fe_2O_3$ of bulk samples from the innermost 3 cm of blocks P5R06, P6R05 and P5R10.*

**Table 3-7. Chemical composition of the bulk bentonite samples (b) and Na-converted < 0.5 μm fractions (c) from profile P5R06 050A. $CO_2$=acid-soluble carbon as $CO_2$; DL=detection limit. Sample P5R06 050A 525 was not fractionated due to poor sample dispersion.**

| Sample id | $SiO_2$ | $Al_2O_3$ | $Fe_2O_3$ | MgO | CaO | $Na_2O$ | $K_2O$ | $TiO_2$ | $P_2O_5$ | MnO | $Cr_2O_3$ | LOI | Sum | TOT/C | TOT/S | $CO_2$ | Ba | Be | Co | Cs | Ga | Hf | Nb | Rb |
|---|---|---|---|---|---|---|---|---|---|---|---|---|---|---|---|---|---|---|---|---|---|---|---|---|
| | % | % | % | % | % | % | % | % | % | % | % | % | % | % | % | % | ppm | ppm | ppm | ppm | ppm | ppm | ppm | ppm |
| DL | 0.01 | 0.01 | 0.04 | 0.01 | 0.01 | 0.01 | 0.01 | 0.01 | 0.01 | 0.01 | 0.002 | –5.1 | 0.01 | 0.02 | 0.02 | 0.02 | 1 | 1 | 0.2 | 0.1 | 0.5 | 0.1 | 0.1 | 0.1 |
| P5R06 050A 525b | 59.33 | 19.1 | 3.5 | 3.07 | 1.85 | 2.06 | 0.49 | 0.14 | 0.07 | 0.02 | < 0.002 | 9.9 | 99.55 | 3.12 | 0.33 | 0.89 | 232 | 2 | 1.4 | 0.2 | 26.7 | 7.7 | 26.4 | 11.5 |
| P5R06 050A 526b | 60.61 | 19.78 | 3.56 | 2.66 | 1.23 | 2.13 | 0.49 | 0.14 | 0.06 | < 0.01 | < 0.002 | 9.1 | 99.78 | 1.95 | 0.3 | 0.29 | 253 | 3 | 1.5 | 0.3 | 28.5 | 8.3 | 27.9 | 11.8 |
| P5R06 050A 528b | 61.15 | 19.92 | 3.61 | 2.61 | 1.21 | 2.11 | 0.5 | 0.14 | 0.06 | < 0.01 | < 0.002 | 8.5 | 99.81 | 1.34 | 0.24 | 0.29 | 286 | 3 | 1.3 | 0.4 | 27.2 | 8.2 | 29.7 | 12.2 |
| P5R06 050A 530b-1 | 61.76 | 19.93 | 3.63 | 2.61 | 1.20 | 2.13 | 0.54 | 0.15 | 0.06 | < 0.01 | 0.002 | 7.8 | 99.81 | 0.82 | 0.25 | 0.40 | 307 | 4 | 1.7 | 0.4 | 29.8 | 7.7 | 29.3 | 12.6 |
| P5R06 050A 530b-2 | 61.55 | 19.86 | 3.57 | 2.52 | 1.24 | 2.14 | 0.53 | 0.14 | 0.05 | < 0.01 | < 0.002 | 8.2 | 99.81 | 0.86 | 0.31 | 0.21 | 295 | < 1 | 1.3 | 0.3 | 28.2 | 8.6 | 28.6 | 12.8 |
| P5R06 050A 532b | 61.34 | 20.19 | 3.6 | 2.53 | 1.21 | 2.13 | 0.52 | 0.14 | 0.05 | < 0.01 | < 0.002 | 8.1 | 99.81 | 0.56 | 0.32 | 0.22 | 315 | < 1 | 1.0 | 0.3 | 28.1 | 7.5 | 29.1 | 12.0 |
| P5R06 050A 534b | 61.54 | 20.10 | 3.62 | 2.52 | 1.20 | 2.14 | 0.52 | 0.14 | 0.06 | < 0.01 | < 0.002 | 8.0 | 99.81 | 0.43 | 0.34 | 0.2 | 382 | 4 | 1.1 | 0.3 | 28.2 | 9.4 | 29.4 | 12.6 |
| P5R06 050A 536b | 61.79 | 19.98 | 3.73 | 2.56 | 1.26 | 2.16 | 0.55 | 0.14 | 0.05 | < 0.01 | 0.002 | 7.6 | 99.82 | 0.37 | 0.33 | 0.24 | 337 | < 1 | 1.1 | 0.4 | 29.9 | 8.4 | 28.7 | 13.2 |
| P5R06 050A 538b | 61.78 | 20.14 | 3.69 | 2.54 | 1.22 | 2.15 | 0.54 | 0.15 | 0.06 | < 0.01 | 0.003 | 7.6 | 99.82 | 0.3 | 0.32 | 0.28 | 316 | 2 | 1.2 | 0.4 | 29.0 | 7.4 | 29.4 | 12.7 |
| P5R06 050A 542b | 61.84 | 19.91 | 3.64 | 2.50 | 1.25 | 2.14 | 0.53 | 0.15 | 0.05 | < 0.01 | < 0.002 | 7.8 | 99.80 | 0.41 | 0.27 | 0.22 | 472 | 5 | 1.2 | 0.3 | 31.0 | 8.8 | 28.1 | 13.1 |
| P5R06 050A 545b | 62.39 | 20.31 | 3.73 | 2.50 | 1.19 | 2.23 | 0.59 | 0.16 | 0.04 | 0.01 | < 0.002 | 6.7 | 99.81 | 0.24 | 0.28 | 0.34 | 349 | < 1 | 1 | 0.3 | 25.6 | 9.5 | 32.8 | 12.7 |
| P5R06 050A 547b | 61.67 | 20.07 | 3.69 | 2.53 | 1.24 | 2.21 | 0.54 | 0.15 | 0.05 | < 0.01 | < 0.002 | 7.7 | 99.83 | 0.21 | 0.29 | 0.22 | 306 | < 1 | 1.2 | 0.3 | 27.6 | 7.8 | 29.2 | 12.6 |
| P5R06 050A 552b | 61.76 | 20.10 | 3.64 | 2.50 | 1.20 | 2.15 | 0.55 | 0.15 | 0.05 | < 0.01 | < 0.002 | 7.7 | 99.83 | 0.21 | 0.31 | 0.25 | 338 | < 1 | 1.3 | 0.4 | 29.4 | 8.2 | 28.6 | 13.3 |
| P5R06 050A 585b | 62.58 | 20.03 | 3.69 | 2.45 | 1.22 | 2.14 | 0.53 | 0.15 | 0.06 | < 0.01 | < 0.002 | 7.0 | 99.83 | 0.21 | 0.30 | 0.39 | 291 | 2 | 1.5 | 0.5 | 29.0 | 7.5 | 27.3 | 12.2 |
| P5R06 050A 630b | 62.56 | 20.08 | 3.67 | 2.45 | 1.23 | 2.10 | 0.54 | 0.14 | 0.06 | < 0.01 | < 0.002 | 7.0 | 99.82 | 0.22 | 0.25 | 0.41 | 332 | 3 | 1.3 | 0.5 | 30.1 | 8.8 | 29.5 | 12.7 |
| P5R06 050A 725b | 62.76 | 19.92 | 3.63 | 2.43 | 1.24 | 2.11 | 0.53 | 0.14 | 0.05 | < 0.01 | < 0.002 | 7.0 | 99.82 | 0.24 | 0.27 | 0.41 | 305 | 3 | 1.4 | 0.3 | 31.0 | 8.4 | 30.7 | 13.6 |
| P5R06 050A 765b | 62.69 | 20.26 | 3.70 | 2.43 | 1.27 | 2.17 | 0.54 | 0.14 | 0.05 | < 0.01 | < 0.002 | 6.6 | 99.82 | 0.23 | 0.29 | 0.46 | 325 | < 1 | 1.3 | 0.5 | 28.9 | 8.5 | 28.7 | 12.4 |
| P5R06 050A 825b | 62.73 | 19.81 | 3.58 | 2.43 | 1.28 | 2.13 | 0.52 | 0.15 | 0.05 | < 0.01 | < 0.002 | 7.1 | 99.82 | 0.37 | 0.26 | 0.45 | 264 | 4 | 1.4 | 0.5 | 30.7 | 8.0 | 29.9 | 13.7 |
| P5R06 Rb-1 | 62.28 | 20.16 | 3.68 | 2.47 | 1.25 | 2.17 | 0.56 | 0.15 | 0.05 | 0.01 | < 0.002 | 7.0 | 99.80 | 0.26 | 0.27 | 0.48 | 337 | 1 | 0.5 | 0.3 | 27.0 | 9.7 | 31.0 | 11.7 |
| P5R06 Rb-2 | 62.59 | 20.21 | 3.67 | 2.47 | 1.22 | 2.20 | 0.59 | 0.16 | 0.05 | 0.01 | < 0.002 | 6.6 | 99.81 | 0.30 | 0.25 | 0.48 | 361 | < 1 | 1.2 | 0.3 | 28.9 | 7.4 | 28.1 | 13.2 |
| P5R06 Rb-3 | 62.38 | 20.43 | 3.58 | 2.41 | 1.20 | 2.19 | 0.58 | 0.16 | 0.03 | < 0.01 | < 0.002 | 6.8 | 99.81 | 0.28 | 0.26 | 0.49 | 315 | < 1 | < 0.2 | 0.4 | 26.6 | 9.4 | 34.1 | 12.6 |
| P5R06 050A 530c | 61.41 | 21.06 | 3.78 | 2.52 | 0.08 | 2.52 | 0.09 | 0.13 | < 0.01 | < 0.01 | < 0.002 | 8.3 | 99.87 | 0.79 | < 0.02 | < 0.02 | 43 | 4 | 1.0 | 0.2 | 29.3 | 8.8 | 26 | 2.9 |
| P5R06 050A 545c | 61.56 | 21.36 | 3.77 | 2.49 | 0.07 | 2.59 | 0.08 | 0.13 | 0.02 | < 0.01 | < 0.002 | 7.8 | 99.87 | 0.18 | < 0.02 | 0.02 | 36 | 2 | 0.9 | 0.2 | 29.3 | 8.4 | 26.1 | 2.9 |
| P5R06 050A 585c | 61.56 | 21.50 | 3.84 | 2.47 | 0.04 | 2.60 | 0.06 | 0.13 | < 0.01 | < 0.01 | < 0.002 | 7.7 | 99.87 | 0.17 | < 0.02 | 0.02 | 26 | 7 | 0.8 | 0.1 | 29.3 | 8.1 | 24.1 | 2.2 |
| P5R06 050A 630c | 61.97 | 21.23 | 3.77 | 2.43 | 0.09 | 2.46 | 0.11 | 0.13 | 0.03 | < 0.01 | < 0.002 | 7.7 | 99.88 | 0.18 | 0.02 | < 0.02 | 51 | 2 | 0.8 | 0.2 | 29.6 | 7.9 | 26.7 | 3.7 |
| P5R06 050A 725c | 61.94 | 21.08 | 3.74 | 2.41 | 0.12 | 2.43 | 0.12 | 0.13 | 0.02 | < 0.01 | < 0.002 | 7.9 | 99.88 | 0.17 | < 0.02 | < 0.02 | 54 | 2 | 0.9 | 0.2 | 29.5 | 8.5 | 28.8 | 3.8 |
| P5R06 050A 765c | 62.18 | 21.21 | 3.74 | 2.44 | 0.07 | 2.45 | 0.09 | 0.13 | 0.03 | < 0.01 | < 0.002 | 7.5 | 99.88 | 0.17 | < 0.02 | 0.03 | 43 | < 1 | 0.5 | 0.1 | 29.8 | 8.5 | 27.2 | 3.0 |
| P5R06 050A 825c | 61.8 | 21.22 | 3.67 | 2.42 | 0.13 | 2.37 | 0.10 | 0.13 | 0.02 | < 0.01 | < 0.002 | 8.0 | 99.89 | 0.29 | < 0.02 | 0.03 | 38 | 2 | 0.8 | 0.2 | 29.4 | 8.3 | 26.8 | 3.1 |
| P5R06 Rc-1 | 62.61 | 21.16 | 3.70 | 2.39 | 0.06 | 2.54 | 0.08 | 0.13 | 0.03 | < 0.01 | < 0.002 | 7.2 | 99.88 | 0.16 | < 0.02 | 0.03 | 37 | 2 | 0.5 | 0.1 | 29.7 | 8.1 | 27.7 | 2.8 |
| P5R06 Rc-2 | 62.17 | 21.31 | 3.70 | 2.41 | 0.05 | 2.57 | 0.06 | 0.13 | 0.02 | < 0.01 | < 0.002 | 7.5 | 99.90 | 0.14 | < 0.02 | < 0.02 | 28 | 2 | 0.5 | 0.2 | 29.8 | 8.7 | 26.8 | 2.4 |
| P5R06 Rc-3 | 62.14 | 21.08 | 3.76 | 2.37 | 0.06 | 2.61 | 0.10 | 0.13 | 0.02 | < 0.01 | < 0.002 | 7.6 | 99.88 | 0.15 | < 0.02 | 0.02 | 41 | 2 | 0.9 | 0.1 | 30.6 | 7.7 | 26.7 | 3.2 |

**Table 3-7 continued.**

| Sample id | Sc | Sn | Sr | Ta | Th | U | V | W | Zr | Y | La | Ce | Pr | Nd | Sm | Eu | Gd | Tb | Dy | Ho | Er | Tm | Yb | Lu |
|---|---|---|---|---|---|---|---|---|---|---|---|---|---|---|---|---|---|---|---|---|---|---|---|---|
| | ppm | ppm | ppm | ppm | ppm | ppm | ppm | ppm | ppm | ppm | ppm | ppm | ppm | ppm | ppm | ppm | ppm | ppm | ppm | ppm | ppm | ppm | ppm | ppm |
| DL | 1 | 1 | 0.5 | 0.1 | 0.2 | 0.1 | 8 | 0.5 | 0.1 | 0.1 | 0.1 | 0.1 | 0.02 | 0.3 | 0.05 | 0.02 | 0.05 | 0.01 | 0.05 | 0.02 | 0.03 | 0.01 | 0.05 | 0.01 |
| P5R06 050A 525b | 5 | 7 | 276.1 | 3.0 | 40.9 | 15.0 | < 8 | < 0.5 | 177.3 | 39.7 | 51.7 | 112.9 | 12.92 | 46.3 | 10.03 | 0.62 | 8.76 | 1.55 | 7.92 | 1.72 | 4.73 | 0.69 | 4.64 | 0.57 |
| P5R06 050A 526b | 6 | 10 | 291.5 | 3.2 | 41.6 | 13.8 | < 8 | < 0.5 | 198.0 | 40.1 | 56.8 | 117.9 | 13.21 | 48.8 | 10.50 | 0.68 | 9.55 | 1.51 | 8.46 | 1.63 | 4.46 | 0.64 | 3.88 | 0.57 |
| P5R06 050A 528b | 5 | 9 | 319.8 | 3.1 | 43.3 | 14.2 | < 8 | < 0.5 | 200.5 | 39.9 | 57.8 | 120.4 | 13.57 | 51.4 | 10.80 | 0.62 | 9.51 | 1.57 | 8.73 | 1.67 | 4.55 | 0.63 | 4.08 | 0.58 |
| P5R06 050A 530b-1 | 6 | 9 | 315.3 | 2.8 | 39.1 | 14.2 | 17 | < 0.5 | 195.9 | 41.4 | 54.4 | 114.0 | 13.04 | 47.7 | 10.15 | 0.66 | 9.55 | 1.66 | 8.91 | 1.68 | 4.76 | 0.72 | 4.69 | 0.57 |
| P5R06 050A 530b-2 | 5 | 9 | 348.6 | 3.0 | 42.9 | 14.8 | < 8 | < 0.5 | 197.5 | 40.5 | 56.6 | 117.6 | 13.41 | 45.7 | 10.41 | 0.64 | 9.43 | 1.56 | 8.62 | 1.70 | 4.52 | 0.63 | 4.12 | 0.54 |
| P5R06 050A 532b | 6 | 8 | 316.2 | 3.1 | 40.7 | 13.9 | < 8 | < 0.5 | 213.2 | 41.4 | 57.1 | 118.0 | 13.29 | 48.0 | 10.43 | 0.66 | 9.28 | 1.56 | 8.57 | 1.68 | 4.40 | 0.66 | 4.09 | 0.55 |
| P5R06 050A 534b | 6 | 9 | 310.7 | 3.0 | 40.6 | 14.0 | < 8 | < 0.5 | 206.3 | 41.0 | 58.5 | 120.0 | 13.43 | 49.5 | 10.73 | 0.67 | 9.61 | 1.54 | 9.32 | 1.66 | 4.38 | 0.67 | 4.33 | 0.57 |
| P5R06 050A 536b | 6 | 11 | 330.8 | 2.9 | 41.3 | 14.3 | < 8 | < 0.5 | 211.5 | 42.7 | 57.1 | 117.8 | 13.54 | 50.0 | 10.60 | 0.70 | 9.50 | 1.58 | 8.18 | 1.58 | 4.63 | 0.67 | 4.04 | 0.57 |
| P5R06 050A 538b | 6 | 9 | 305.8 | 3.1 | 42.6 | 13.8 | < 8 | < 0.5 | 192.5 | 41.3 | 56.6 | 115.6 | 13.48 | 48.8 | 9.94 | 0.68 | 9.52 | 1.55 | 8.47 | 1.65 | 4.64 | 0.63 | 4.20 | 0.56 |
| P5R06 050A 542b | 5 | 11 | 313.5 | 3.0 | 42.1 | 15.0 | < 8 | < 0.5 | 206.1 | 42.3 | 58.5 | 118.9 | 13.87 | 51.4 | 10.39 | 0.68 | 9.45 | 1.59 | 8.95 | 1.63 | 4.51 | 0.67 | 4.11 | 0.59 |
| P5R06 050A 545b | 6 | 10 | 308.6 | 3.1 | 43.2 | 14.6 | 9 | < 0.5 | 206.7 | 43.7 | 58.8 | 131.5 | 14.51 | 55.7 | 11.70 | 0.78 | 10.94 | 1.65 | 9.83 | 1.67 | 4.56 | 0.72 | 4.30 | 0.56 |
| P5R06 050A 547b | 6 | 10 | 285.3 | 2.8 | 42.4 | 14.7 | < 8 | < 0.5 | 194.9 | 40.1 | 58.0 | 120.7 | 13.82 | 52.7 | 10.75 | 0.69 | 9.22 | 1.55 | 8.91 | 1.77 | 4.62 | 0.67 | 4.37 | 0.56 |
| P5R06 050A 552b | 6 | 10 | 313.6 | 3.0 | 41.7 | 14.7 | < 8 | < 0.5 | 203.8 | 42.1 | 54.8 | 115.6 | 13.37 | 49.3 | 10.66 | 0.67 | 9.25 | 1.55 | 8.54 | 1.62 | 4.56 | 0.67 | 4.02 | 0.59 |
| P5R06 050A 585b | 6 | 9 | 291.1 | 2.9 | 40.3 | 14.6 | 10 | < 0.5 | 192.9 | 41.8 | 56.4 | 114.2 | 13.25 | 52.0 | 10.19 | 0.71 | 9.25 | 1.61 | 8.06 | 1.68 | 4.63 | 0.72 | 4.24 | 0.57 |
| P5R06 050A 630b | 6 | 9 | 327.2 | 3.0 | 42.4 | 15.3 | 11 | < 0.5 | 201.1 | 44.9 | 58.5 | 121.2 | 14.07 | 52.2 | 10.31 | 0.75 | 9.89 | 1.74 | 8.77 | 1.74 | 4.9 | 0.73 | 4.55 | 0.63 |
| P5R06 050A 725b | 6 | 10 | 316.3 | 3.1 | 42.4 | 14.8 | 14 | < 0.5 | 203.3 | 43.8 | 57.2 | 124.9 | 14.18 | 51.4 | 10.71 | 0.70 | 9.52 | 1.69 | 9.04 | 1.93 | 5.02 | 0.78 | 4.47 | 0.59 |
| P5R06 050A 765b | 6 | 9 | 293.1 | 3.3 | 39.9 | 14.1 | 13 | < 0.5 | 206.1 | 42.6 | 56.1 | 118.9 | 13.12 | 49.9 | 10.33 | 0.73 | 9.23 | 1.66 | 8.76 | 1.64 | 4.75 | 0.75 | 4.52 | 0.59 |
| P5R06 050A 825b | 6 | 9 | 297.0 | 3.0 | 41.4 | 14.7 | 15 | < 0.5 | 190.2 | 41.4 | 55.0 | 114.7 | 13.78 | 51.1 | 10.09 | 0.73 | 9.67 | 1.68 | 8.49 | 1.84 | 5.18 | 0.71 | 4.74 | 0.57 |
| P5R06 Rb-1 | 6 | 11 | 287.1 | 3.3 | 43.5 | 14.3 | < 8 | < 0.5 | 209.8 | 46.7 | 61.7 | 132.7 | 14.59 | 53.1 | 11.97 | 0.71 | 11.04 | 1.66 | 9.73 | 1.66 | 4.95 | 0.73 | 4.18 | 0.66 |
| P5R06 Rb-2 | 6 | 9 | 282.6 | 3.2 | 41.6 | 14.1 | 8 | < 0.5 | 190.0 | 43.8 | 59.2 | 129.0 | 14.13 | 49.3 | 11.74 | 0.72 | 10.03 | 1.68 | 9.35 | 1.61 | 4.62 | 0.74 | 3.91 | 0.61 |
| P5R06 Rb-3 | 6 | 8 | 286.1 | 3.2 | 43.9 | 14.2 | < 8 | < 0.5 | 205.4 | 43.0 | 60.5 | 126.7 | 14.27 | 55.9 | 11.39 | 0.75 | 10.51 | 1.65 | 9.05 | 1.66 | 4.49 | 0.70 | 3.88 | 0.54 |
| P5R06 050A 530c | 6 | 9 | 14.6 | 3.2 | 40.1 | 14.0 | 39 | < 0.5 | 151.8 | 35.4 | 54.2 | 113.3 | 13.34 | 48.2 | 10.06 | 0.57 | 9.26 | 1.50 | 7.92 | 1.52 | 4.02 | 0.57 | 3.31 | 0.45 |
| P5R06 050A 545c | 6 | 10 | 13.4 | 3.5 | 39.7 | 13.0 | 54 | < 0.5 | 153.3 | 35.5 | 53.4 | 113.0 | 13.12 | 50.1 | 10.42 | 0.55 | 9.16 | 1.49 | 8.24 | 1.53 | 3.99 | 0.59 | 3.28 | 0.50 |
| P5R06 050A 585c | 6 | 10 | 10.8 | 3.3 | 37.3 | 12.2 | 60 | < 0.5 | 147.4 | 30.7 | 48.9 | 100.5 | 12.04 | 40.7 | 9.20 | 0.52 | 8.18 | 1.36 | 7.64 | 1.30 | 3.52 | 0.52 | 3.08 | 0.41 |
| P5R06 050A 630c | 6 | 9 | 14.9 | 3.4 | 39.6 | 13.8 | 71 | < 0.5 | 153.8 | 34.8 | 53.9 | 114.1 | 13.14 | 47.3 | 10.33 | 0.58 | 9.30 | 1.50 | 8.27 | 1.44 | 3.73 | 0.59 | 3.31 | 0.48 |
| P5R06 050A 725c | 6 | 10 | 17.2 | 3.7 | 42.6 | 13.9 | 25 | < 0.5 | 163.1 | 39.1 | 57.2 | 119.7 | 13.85 | 49.9 | 10.82 | 0.56 | 10.06 | 1.58 | 9.10 | 1.62 | 4.15 | 0.61 | 3.79 | 0.5 |
| P5R06 050A 765c | 6 | 10 | 14.8 | 3.6 | 40.1 | 14.2 | 32 | < 0.5 | 158.3 | 37.7 | 55.5 | 114.6 | 13.39 | 48.6 | 10.28 | 0.57 | 9.71 | 1.53 | 8.70 | 1.56 | 3.98 | 0.60 | 3.65 | 0.47 |
| P5R06 050A 825c | 6 | 10 | 13.0 | 3.2 | 41.1 | 13.8 | 42 | < 0.5 | 151.5 | 36.8 | 54.4 | 113.7 | 13.52 | 47.6 | 10.60 | 0.56 | 9.23 | 1.52 | 8.79 | 1.55 | 4.29 | 0.59 | 3.32 | 0.48 |
| P5R06 Rc-1 | 6 | 10 | 12.9 | 3.4 | 41.0 | 14.3 | 26 | < 0.5 | 155.5 | 36.5 | 54.8 | 113.6 | 13.28 | 50.3 | 10.23 | 0.54 | 9.47 | 1.50 | 8.44 | 1.53 | 3.96 | 0.58 | 3.57 | 0.45 |
| P5R06 Rc-2 | 6 | 11 | 11.3 | 3.4 | 39.9 | 13.9 | 18 | < 0.5 | 155.2 | 34.2 | 53.5 | 109.6 | 12.90 | 48.0 | 10.01 | 0.54 | 9.13 | 1.44 | 7.59 | 1.40 | 3.74 | 0.53 | 3.04 | 0.42 |
| P5R06 Rc-3 | 6 | 10 | 11.8 | 3.5 | 41.1 | 14.4 | 16 | < 0.5 | 157.5 | 36.7 | 56.8 | 117.2 | 13.8 | 50.7 | 11.09 | 0.58 | 9.66 | 1.53 | 8.67 | 1.54 | 4.06 | 0.60 | 3.71 | 0.47 |

**Table 3-7 continued.**

| Sample id | Mo | Cu | Pb | Zn | Ni | As | Cd | Sb | Bi | Ag | Au | Hg | Tl | Se |
|---|---|---|---|---|---|---|---|---|---|---|---|---|---|---|
| | ppm | ppm | ppm | ppm | ppm | ppm | ppm | ppm | ppm | ppm | ppb | ppm | ppm | ppm |
| DL | 0.1 | 0.1 | 0.1 | 1 | 0.1 | 0.5 | 0.1 | 0.1 | 0.1 | 0.1 | 0.5 | 0.01 | 0.1 | 0.5 |
| P5R06 050A 525b | 528.6 | 669.7 | 63.1 | 1,051 | 6.3 | 16.2 | 0.9 | 0.3 | 1.0 | 0.2 | < 0.5 | < 0.01 | 0.6 | < 0.5 |
| P5R06 050A 526b | 82.4 | 12.0 | 39.7 | 297 | 3.1 | 10.7 | 0.5 | 0.8 | 1.1 | 0.2 | < 0.5 | 0.02 | 0.4 | 1.2 |
| P5R06 050A 528b | 11.6 | 6.8 | 37.2 | 139 | 2.8 | 9.5 | 0.3 | 0.6 | 0.9 | 0.2 | < 0.5 | < 0.01 | 0.3 | 1.0 |
| P5R06 050A 530b-1 | 11.7 | 6.6 | 48.6 | 133 | 4.6 | 13 | 0.3 | 0.3 | 1.1 | 0.1 | < 0.5 | < 0.01 | 0.4 | < 0.5 |
| P5R06 050A 530b-2 | 2.6 | 3.3 | 39.1 | 94 | 2.8 | 9.9 | 0.3 | 0.5 | 0.9 | 0.2 | 1.4 | < 0.01 | 0.3 | 0.8 |
| P5R06 050A 532b | 6.4 | 5.2 | 40.8 | 93 | 3.0 | 9.9 | 0.3 | 0.5 | 0.9 | 0.1 | < 0.5 | 0.02 | 0.3 | 0.7 |
| P5R06 050A 534b | 2.8 | 3.1 | 45.6 | 70 | 2.9 | 10.1 | 0.2 | 0.7 | 0.9 | 0.2 | 0.9 | 0.02 | 0.3 | 0.8 |
| P5R06 050A 536b | 3.3 | 3.1 | 40.9 | 79 | 2.7 | 10.0 | 0.2 | 0.7 | 0.9 | 0.1 | 1.1 | 0.02 | 0.3 | 0.9 |
| P5R06 050A 538b | 2.6 | 3.2 | 43.7 | 87 | 2.7 | 10.5 | 0.3 | 0.8 | 1.0 | 0.2 | < 0.5 | 0.01 | 0.3 | 0.8 |
| P5R06 050A 542b | 3.2 | 3.1 | 40.4 | 81 | 3.0 | 9.8 | 0.2 | 0.5 | 0.9 | 0.2 | < 0.5 | 0.02 | 0.3 | 0.6 |
| P5R06 050A 545b | 2.6 | 4.2 | 52.7 | 122 | 3.6 | 14.6 | 0.4 | 0.1 | 1.2 | 0.2 | < 0.5 | 0.02 | 0.4 | < 0.5 |
| P5R06 050A 547b | 2.5 | 3.4 | 41.2 | 184 | 3.0 | 11.1 | 0.4 | 0.7 | 1.0 | 0.2 | < 0.5 | 0.01 | 0.3 | 0.8 |
| P5R06 050A 552b | 2.8 | 3.3 | 43.2 | 109 | 3.0 | 10.8 | 0.3 | 0.6 | 1.0 | 0.2 | < 0.5 | 0.01 | 0.3 | < 0.5 |
| P5R06 050A 585b | 2.8 | 4.0 | 52.4 | 102 | 3.5 | 13.8 | 0.3 | 0.1 | 1.2 | 0.2 | < 0.5 | 0.01 | 0.3 | < 0.5 |
| P5R06 050A 630b | 2.8 | 3.9 | 50.3 | 102 | 3.1 | 12.9 | 0.4 | 0.2 | 1.2 | 0.2 | 0.7 | 0.03 | 0.4 | < 0.5 |
| P5R06 050A 725b | 3.1 | 3.4 | 48.0 | 85 | 3.3 | 12.9 | 0.4 | 0.2 | 1.2 | 0.2 | < 0.5 | 0.01 | 0.4 | < 0.5 |
| P5R06 050A 765b | 2.8 | 3.8 | 49.5 | 99 | 3.2 | 13.6 | 0.4 | 0.2 | 1.2 | 0.2 | < 0.5 | < 0.01 | 0.4 | < 0.5 |
| P5R06 050A 825b | 2.0 | 3.9 | 49.6 | 110 | 3.4 | 11.7 | 0.2 | 0.2 | 1.2 | 0.2 | < 0.5 | < 0.01 | 0.4 | < 0.5 |
| P5R06 Rb-1 | 3.0 | 3.7 | 47.4 | 107 | 3.3 | 12.9 | 0.4 | 0.4 | 1.2 | 0.2 | < 0.5 | 0.01 | 0.3 | < 0.5 |
| P5R06 Rb-2 | 3.3 | 4.1 | 51.0 | 118 | 3.6 | 13.6 | 0.3 | 0.3 | 1.2 | 0.2 | < 0.5 | 0.01 | 0.4 | < 0.5 |
| P5R06 Rb-3 | 2.8 | 3.6 | 51.1 | 121 | 3.3 | 14.0 | 0.4 | 0.2 | 1.2 | 0.2 | < 0.5 | < 0.01 | 0.3 | < 0.5 |
| P5R06 050A 530c | 5.1 | 6.6 | 26.1 | 76 | 3.1 | 1.9 | < 0.1 | < 0.1 | 0.7 | < 0.1 | 3.2 | 0.04 | < 0.1 | < 0.5 |
| P5R06 050A 545c | 0.3 | 3.6 | 26.8 | 27 | 2.9 | 2.5 | < 0.1 | < 0.1 | 0.7 | < 0.1 | < 0.5 | 0.05 | < 0.1 | < 0.5 |
| P5R06 050A 585c | 0.4 | 3.3 | 21.5 | 25 | 2.2 | 2.2 | < 0.1 | < 0.1 | 0.6 | < 0.1 | < 0.5 | 0.07 | < 0.1 | < 0.5 |
| P5R06 050A 630c | 0.5 | 3.5 | 26.4 | 27 | 2.7 | 2.8 | < 0.1 | < 0.1 | 0.6 | < 0.1 | < 0.5 | 0.05 | < 0.1 | < 0.5 |
| P5R06 050A 725c | 0.3 | 3.8 | 27.5 | 27 | 2.6 | 2.7 | 0.1 | < 0.1 | 0.7 | < 0.1 | 0.8 | 0.04 | < 0.1 | < 0.5 |
| P5R06 050A 765c | 0.4 | 3.6 | 26.5 | 29 | 2.7 | 2.1 | < 0.1 | < 0.1 | 0.7 | < 0.1 | 2.2 | 0.04 | < 0.1 | < 0.5 |
| P5R06 050A 825c | 0.3 | 3.4 | 26.0 | 37 | 2.3 | 2.2 | < 0.1 | < 0.1 | 0.7 | < 0.1 | < 0.5 | 0.04 | 0.1 | < 0.5 |
| P5R06 Rc-1 | 0.3 | 3.9 | 22.2 | 28 | 1.9 | 1.8 | < 0.1 | < 0.1 | 0.6 | < 0.1 | 1.5 | 0.04 | < 0.1 | < 0.5 |
| P5R06 Rc-2 | 0.2 | 2.9 | 21.6 | 29 | 2.1 | 1.7 | < 0.1 | < 0.1 | 0.5 | < 0.1 | < 0.5 | 0.04 | < 0.1 | < 0.5 |
| P5R06 Rc-3 | 0.3 | 3.0 | 25.7 | 27 | 2.0 | 2.6 | < 0.1 | < 0.1 | 0.6 | < 0.1 | < 0.5 | 0.06 | < 0.1 | < 0.5 |

**Table 3-8. Chemical composition of the bulk bentonite samples (b) from profile P5R10 270C. $CO_2$=acid-soluble carbon as $CO_2$; DL=detection limit.**

| Sample id | $SiO_2$ | $Al_2O_3$ | $Fe_2O_3$ | MgO | CaO | $Na_2O$ | $K_2O$ | $TiO_2$ | $P_2O_5$ | MnO | $Cr_2O_3$ | LOI | Sum | TOT/C | TOT/S | $CO_2$ | Ba | Be | Co | Cs | Ga | Hf | Nb | Rb |
|---|---|---|---|---|---|---|---|---|---|---|---|---|---|---|---|---|---|---|---|---|---|---|---|---|
| | % | % | % | % | % | % | % | % | % | % | % | % | % | % | % | % | ppm | ppm | ppm | ppm | ppm | ppm | ppm | ppm |
| DL | 0.01 | 0.01 | 0.04 | 0.01 | 0.01 | 0.01 | 0.01 | 0.01 | 0.01 | 0.01 | 0.002 | –5.1 | 0.01 | 0.02 | 0.02 | 0.02 | 1 | 1 | 0.2 | 0.1 | 0.5 | 0.1 | 0.1 | 0.1 |
| P5R10 270C 525b | 59.59 | 18.82 | 3.55 | 2.78 | 1.58 | 1.97 | 0.50 | 0.14 | 0.07 | < 0.01 | < 0.002 | 10.7 | 99.68 | 2.85 | 0.29 | 0.91 | 274 | < 1 | 1.0 | 0.3 | 25.7 | 8.0 | 27.6 | 11.7 |
| P5R10 270C 528b | 60.68 | 19.26 | 3.55 | 2.60 | 1.36 | 2.01 | 0.50 | 0.14 | 0.06 | < 0.01 | < 0.002 | 9.6 | 99.78 | 1.86 | 0.24 | 0.51 | 376 | 1 | 0.8 | 0.4 | 26.9 | 8.0 | 30.8 | 12.2 |
| P5R10 270C 530b | 61.05 | 19.47 | 3.69 | 2.56 | 1.23 | 2.00 | 0.54 | 0.14 | 0.05 | < 0.01 | < 0.002 | 9.1 | 99.80 | 1.14 | 0.23 | 0.41 | 290 | 1 | 0.7 | 0.3 | 26.3 | 8.7 | 28.9 | 11.7 |
| P5R10 270C 532b | 61.09 | 19.55 | 3.67 | 2.48 | 1.29 | 1.99 | 0.55 | 0.14 | 0.07 | 0.01 | < 0.002 | 9.0 | 99.80 | 0.78 | 0.22 | 0.34 | 304 | 2 | 0.8 | 0.3 | 28.1 | 8.4 | 28.0 | 12.6 |
| P5R10 270C 534b | 60.96 | 19.47 | 3.62 | 2.46 | 1.23 | 1.99 | 0.56 | 0.14 | 0.06 | < 0.01 | < 0.002 | 9.3 | 99.81 | 0.56 | 0.24 | 0.30 | 336 | < 1 | 0.9 | 0.5 | 26.9 | 8.3 | 26.1 | 12.7 |
| P5R10 270C 536b | 61.33 | 19.60 | 3.67 | 2.45 | 1.25 | 2.02 | 0.57 | 0.14 | 0.06 | < 0.01 | < 0.002 | 8.7 | 99.82 | 0.40 | 0.26 | 0.32 | 316 | 1 | 0.9 | 0.4 | 27.4 | 7.9 | 28.0 | 12.9 |
| P5R10 270C 538b | 61.55 | 19.50 | 3.68 | 2.50 | 1.27 | 2.01 | 0.58 | 0.14 | 0.06 | < 0.01 | < 0.002 | 8.5 | 99.81 | 0.31 | 0.23 | 0.40 | 325 | 1 | 1.0 | 0.5 | 26.3 | 8.4 | 29.3 | 13.0 |
| P5R10 270C 542b | 61.02 | 19.64 | 3.69 | 2.46 | 1.46 | 2.02 | 0.58 | 0.14 | 0.05 | < 0.01 | < 0.002 | 8.7 | 99.81 | 0.28 | 0.25 | 0.25 | 445 | < 1 | 0.9 | 0.3 | 26.8 | 8.4 | 29.2 | 13.2 |
| P5R10 270C 546b | 61.03 | 20.02 | 3.65 | 2.48 | 1.29 | 2.01 | 0.57 | 0.14 | 0.05 | < 0.01 | < 0.002 | 8.6 | 99.82 | 0.26 | 0.25 | 0.30 | 307 | < 1 | 0.7 | 0.3 | 27.0 | 8.3 | 27.9 | 12.3 |
| P5R10 270C 552b | 61.51 | 19.73 | 3.68 | 2.47 | 1.28 | 2.03 | 0.56 | 0.14 | 0.05 | < 0.01 | < 0.002 | 8.3 | 99.80 | 0.29 | 0.29 | 0.34 | 367 | 2 | 1.2 | 0.4 | 25.1 | 8.8 | 29.2 | 12.6 |
| P5R10 Rb | 61.71 | 19.87 | 3.83 | 2.51 | 1.14 | 2.10 | 0.51 | 0.14 | 0.05 | 0.01 | 0.005 | 7.9 | 99.82 | 0.29 | 0.21 | 0.46 | 250 | < 1 | 1.0 | 0.4 | 27.2 | 8.7 | 27.7 | 11.4 |

| Sample id | Sc | Sn | Sr | Ta | Th | U | V | W | Zr | Y | La | Ce | Pr | Nd | Sm | Eu | Gd | Tb | Dy | Ho | Er | Tm | Yb | Lu |
|---|---|---|---|---|---|---|---|---|---|---|---|---|---|---|---|---|---|---|---|---|---|---|---|---|
| | ppm | ppm | ppm | ppm | ppm | ppm | ppm | ppm | ppm | ppm | ppm | ppm | ppm | ppm | ppm | ppm | ppm | ppm | ppm | ppm | ppm | ppm | ppm | ppm |
| DL | 1 | 1 | 0.5 | 0.1 | 0.2 | 0.1 | 8 | 0.5 | 0.1 | 0.1 | 0.1 | 0.1 | 0.02 | 0.3 | 0.05 | 0.02 | 0.05 | 0.01 | 0.05 | 0.02 | 0.03 | 0.01 | 0.05 | 0.01 |
| P5R10 270C 525b | 6 | 10 | 332.0 | 2.9 | 40.1 | 13.4 | < 8 | 0.5 | 190.9 | 42.8 | 55.5 | 115.9 | 13.63 | 48.5 | 10.04 | 0.69 | 9.27 | 1.52 | 8.52 | 1.60 | 4.54 | 0.66 | 3.63 | 0.53 |
| P5R10 270C 528b | 6 | 10 | 347.7 | 3.4 | 43.2 | 14.7 | < 8 | < 0.5 | 213.1 | 44.0 | 56.1 | 117.9 | 13.85 | 48.3 | 10.82 | 0.67 | 9.49 | 1.58 | 9.06 | 1.58 | 4.47 | 0.64 | 4.09 | 0.56 |
| P5R10 270C 530b | 6 | 9 | 333.9 | 2.9 | 42.6 | 14.4 | < 8 | < 0.5 | 204.7 | 42.1 | 57.4 | 120.1 | 14.22 | 54.1 | 10.70 | 0.72 | 9.78 | 1.55 | 9.20 | 1.74 | 4.45 | 0.69 | 4.19 | 0.56 |
| P5R10 270C 532b | 6 | 9 | 309.7 | 2.9 | 41.2 | 13.8 | < 8 | < 0.5 | 200.7 | 43.0 | 55.1 | 114.4 | 13.55 | 51.9 | 10.18 | 0.69 | 9.36 | 1.51 | 8.78 | 1.63 | 4.32 | 0.67 | 3.81 | 0.54 |
| P5R10 270C 534b | 6 | 8 | 320.7 | 2.8 | 41.0 | 14.2 | < 8 | < 0.5 | 195.1 | 43.2 | 53.8 | 112.8 | 13.52 | 49.1 | 10.83 | 0.68 | 9.35 | 1.55 | 8.61 | 1.56 | 4.44 | 0.63 | 4.11 | 0.56 |
| P5R10 270C 536b | 6 | 8 | 304.5 | 3.0 | 40.2 | 14.0 | < 8 | 0.6 | 196.3 | 41.8 | 54.4 | 113.3 | 13.47 | 48.4 | 10.24 | 0.68 | 9.22 | 1.48 | 8.47 | 1.63 | 4.42 | 0.66 | 3.93 | 0.55 |
| P5R10 270C 538b | 6 | 9 | 315.7 | 3.1 | 40.8 | 14.3 | < 8 | < 0.5 | 213.3 | 43.4 | 57.6 | 121.5 | 13.84 | 53.0 | 10.91 | 0.66 | 9.60 | 1.60 | 8.57 | 1.62 | 4.81 | 0.68 | 4.22 | 0.59 |
| P5R10 270C 542b | 6 | 9 | 310.2 | 3.5 | 40.3 | 13.9 | < 8 | 0.7 | 202.7 | 42.3 | 56.5 | 114.6 | 13.77 | 51.6 | 10.50 | 0.73 | 9.21 | 1.49 | 8.59 | 1.61 | 4.35 | 0.64 | 4.07 | 0.54 |
| P5R10 270C 546b | 6 | 10 | 291.1 | 3.0 | 41.0 | 14.0 | < 8 | < 0.5 | 195.7 | 43.5 | 56.7 | 118.0 | 14.09 | 51.7 | 10.84 | 0.68 | 9.60 | 1.54 | 8.96 | 1.71 | 4.52 | 0.70 | 4.52 | 0.57 |
| P5R10 270C 552b | 6 | 9 | 323.7 | 3.1 | 42.1 | 14.8 | < 8 | < 0.5 | 195.6 | 44.4 | 59.9 | 123.2 | 14.30 | 50.6 | 11.29 | 0.68 | 9.77 | 1.59 | 8.88 | 1.71 | 4.62 | 0.69 | 4.44 | 0.56 |
| P5R10 Rb | 6 | 8 | 274.3 | 3.1 | 42.6 | 14.9 | < 8 | 0.6 | 192.6 | 43.4 | 57.7 | 119.5 | 14.14 | 54.8 | 11.24 | 0.68 | 9.69 | 1.59 | 8.93 | 1.63 | 4.55 | 0.67 | 4.23 | 0.58 |

**Table 3-8 continued.**

| Sample id | Mo | Cu | Pb | Zn | Ni | As | Cd | Sb | Bi | Ag | Au | Hg | Tl | Se |
|---|---|---|---|---|---|---|---|---|---|---|---|---|---|---|
| | ppm | ppm | ppm | ppm | ppm | ppm | ppm | ppm | ppm | ppm | ppb | ppm | ppm | ppm |
| DL | 0.1 | 0.1 | 0.1 | 1 | 0.1 | 0.5 | 0.1 | 0.1 | 0.1 | 0.1 | 0.5 | 0.01 | 0.1 | 0.5 |
| P5R10 270C 525b | 316.2 | 80.7 | 42.2 | 715 | 4.7 | 15.1 | 0.2 | 0.2 | 0.9 | 0.2 | < 0.5 | 0.02 | 0.4 | < 0.5 |
| P5R10 270C 528b | 12.6 | 198.5 | 40.2 | 128 | 2.9 | 11.2 | 0.3 | 0.2 | 0.7 | 0.2 | < 0.5 | 0.02 | 0.4 | 0.7 |
| P5R10 270C 530b | 5.0 | 187.2 | 41.7 | 94 | 4.0 | 12.0 | 0.2 | 0.1 | 0.8 | 0.1 | < 0.5 | 0.02 | 0.3 | < 0.5 |
| P5R10 270C 532b | 4.2 | 180.2 | 41.4 | 86 | 2.9 | 11.9 | 0.2 | 0.2 | 0.8 | 0.2 | < 0.5 | 0.02 | 0.3 | 0.8 |
| P5R10 270C 534b | 3.5 | 17.5 | 39.7 | 80 | 3.4 | 11.8 | 0.3 | 0.2 | 0.8 | 0.2 | < 0.5 | 0.03 | 0.3 | < 0.5 |
| P5R10 270C 536b | 3.1 | 32.8 | 43.0 | 108 | 3.3 | 13.0 | 0.4 | 0.2 | 0.8 | 0.1 | < 0.5 | 0.02 | 0.3 | < 0.5 |
| P5R10 270C 538b | 2.9 | 5.2 | 40.6 | 131 | 2.8 | 11.4 | 0.4 | 0.3 | 0.8 | 0.2 | < 0.5 | 0.01 | 0.3 | < 0.5 |
| P5R10 270C 542b | 2.5 | 3.3 | 41.7 | 77 | 2.8 | 16.1 | 0.3 | 0.2 | 0.7 | 0.2 | 0.7 | 0.03 | 0.4 | < 0.5 |
| P5R10 270C 546b | 2.7 | 3.4 | 45.1 | 84 | 3.0 | 12.9 | 0.2 | 0.3 | 0.8 | 0.2 | < 0.5 | 0.02 | 0.3 | < 0.5 |
| P5R10 270C 552b | 2.5 | 3.3 | 38.4 | 79 | 2.7 | 13.5 | 0.3 | 0.2 | 0.8 | 0.2 | 0.7 | 0.02 | 0.4 | 0.9 |
| P5R10 Rb | 2.4 | 3.3 | 44 | 91 | 2.9 | 12 | 0.4 | 0.3 | 0.9 | 0.2 | < 0.5 | 0.02 | 0.3 | < 0.5 |

**Table 3-9. Chemical composition of the bulk bentonite samples (b) from profiles P6R5 165B and 165A and of Na-converted < 0.5 µm fractions (c) from profile P6R5 165B. $CO_2$=acid-soluble carbon as $CO_2$; DL=detection limit; n.d=not determined.**

| Sample id | $SiO_2$ | $Al_2O_3$ | $Fe_2O_3$ | MgO | CaO | $Na_2O$ | $K_2O$ | $TiO_2$ | $P_2O_5$ | MnO | $Cr_2O_3$ | LOI | Sum | TOT/C | TOT/S | $CO_2$ | Ba | Be | Co | Cs | Ga | Hf | Nb | Rb | Sc |
|---|---|---|---|---|---|---|---|---|---|---|---|---|---|---|---|---|---|---|---|---|---|---|---|---|---|
| | % | % | % | % | % | % | % | % | % | % | % | % | % | % | % | % | ppm | ppm | ppm | ppm | ppm | ppm | ppm | ppm | ppm |
| DL | 0.01 | 0.01 | 0.04 | 0.01 | 0.01 | 0.01 | 0.01 | 0.01 | 0.01 | 0.01 | 0.002 | –5.1 | 0.01 | 0.02 | 0.02 | 0.02 | 1 | 1 | 0.2 | 0.1 | 0.5 | 0.1 | 0.1 | 0.1 | 1 |
| P6R5 165B 525b | 60.94 | 19.47 | 3.58 | 2.57 | 1.27 | 2.09 | 0.50 | 0.14 | 0.08 | < 0.01 | < 0.002 | 9.1 | 99.70 | 2.48 | 0.25 | 0.48 | 295 | 2 | 1.9 | 0.3 | 27.8 | 8.4 | 30.0 | 12.4 | 5 |
| P6R5 165B 530b | 61.60 | 20.15 | 3.68 | 2.49 | 1.25 | 2.15 | 0.53 | 0.15 | 0.05 | 0.01 | < 0.002 | 7.7 | 99.81 | 0.88 | 0.22 | 0.42 | 345 | 2 | 1.0 | 0.4 | 28.9 | 8.3 | 29.3 | 13.1 | 6 |
| P6R5 165B 540b | 62.13 | 20.27 | 3.69 | 2.49 | 1.28 | 2.16 | 0.56 | 0.14 | 0.06 | < 0.01 | < 0.002 | 7.0 | 99.83 | 0.27 | 0.30 | 0.39 | 358 | 1 | 1.0 | 0.4 | 29.4 | 8.6 | 29.1 | 13.2 | 6 |
| P6R5 165B 555b | 62.36 | 20.27 | 3.68 | 2.46 | 1.26 | 2.15 | 0.55 | 0.15 | 0.06 | < 0.01 | < 0.002 | 6.9 | 99.81 | 0.31 | 0.23 | 0.48 | 342 | 1 | 1.2 | 0.4 | 29.6 | 8.7 | 30.7 | 13.9 | 6 |
| P6R5 165B 575b | 62.38 | 20.16 | 3.74 | 2.49 | 1.28 | 2.14 | 0.54 | 0.15 | 0.05 | < 0.01 | < 0.002 | 6.9 | 99.81 | 0.30 | 0.30 | 0.44 | 320 | 3 | 1.1 | 0.4 | 30.1 | 8.8 | 31.4 | 14.0 | 5 |
| P6R5 165B 615b | 62.44 | 20.18 | 3.62 | 2.40 | 1.26 | 2.15 | 0.54 | 0.14 | 0.06 | < 0.01 | < 0.002 | 7.0 | 99.83 | 0.24 | 0.28 | 0.40 | 316 | 2 | 1.2 | 0.4 | 29.7 | 8.7 | 30.6 | 13.8 | 6 |
| P6R5 165B 645b | 62.72 | 20.47 | 3.71 | 2.48 | 1.26 | 2.16 | 0.56 | 0.15 | 0.05 | < 0.01 | < 0.002 | 6.2 | 99.80 | 0.28 | 0.28 | 0.40 | 416 | 2 | 1.1 | 0.4 | 30.2 | 8.7 | 31.6 | 14.9 | 6 |
| P6R5 165B 735b | 62.65 | 20.28 | 3.77 | 2.49 | 1.25 | 2.17 | 0.55 | 0.15 | 0.05 | < 0.01 | < 0.002 | 6.4 | 99.81 | 0.30 | 0.25 | 0.43 | 335 | 3 | 1.2 | 0.5 | 30.2 | 8.6 | 31.6 | 14.4 | 6 |
| P6R5 165B 775b | 62.52 | 20.49 | 3.71 | 2.47 | 1.17 | 2.16 | 0.51 | 0.14 | 0.05 | < 0.01 | < 0.002 | 6.6 | 99.82 | 0.30 | 0.28 | 0.44 | 294 | 3 | 1.1 | 0.4 | 28.2 | 8.0 | 30.7 | 13.1 | 6 |
| P6R5 165B 825b | 62.26 | 20.29 | 3.74 | 2.49 | 1.22 | 2.13 | 0.54 | 0.15 | 0.05 | < 0.01 | < 0.002 | 6.9 | 99.79 | 0.45 | 0.30 | 0.48 | 312 | 3 | 1.0 | 0.5 | 29.8 | 8.2 | 33.9 | 14.1 | 6 |
| P6R5 165B 835b | 61.77 | 20.04 | 3.76 | 2.45 | 1.32 | 2.16 | 0.55 | 0.15 | 0.06 | < 0.01 | < 0.002 | 7.5 | 99.78 | 1.08 | 0.28 | 0.36 | 321 | 3 | 1.5 | 0.5 | 29.0 | 8.7 | 31.3 | 13.9 | 6 |
| P6R5 Rb-1 | 62.26 | 20.26 | 3.70 | 2.45 | 1.29 | 2.15 | 0.57 | 0.15 | 0.05 | < 0.01 | < 0.002 | 6.9 | 99.80 | 0.30 | 0.29 | 0.51 | 398 | 2 | 1.0 | 0.4 | 29.0 | 8.5 | 31.0 | 14.4 | 6 |
| P6R5 Rb-2 | 62.76 | 19.94 | 3.67 | 2.45 | 1.27 | 2.12 | 0.54 | 0.15 | 0.05 | < 0.01 | < 0.002 | 6.9 | 99.81 | 0.29 | 0.27 | 0.46 | 310 | 2 | 1.1 | 0.4 | 29.5 | 8.6 | 31.2 | 14.2 | 6 |
| P6R5 Rb-3 | 62.30 | 20.31 | 3.72 | 2.48 | 1.29 | 2.13 | 0.54 | 0.15 | 0.05 | 0.01 | < 0.002 | 6.8 | 99.82 | 0.29 | 0.28 | 0.49 | 346 | 3 | 1.7 | 0.3 | 29.1 | 8.6 | 31.2 | 13.9 | 6 |
| P6R5 165A 525b | 60.42 | 19.48 | 3.52 | 2.55 | 1.33 | 2.03 | 0.48 | 0.14 | 0.07 | < 0.01 | < 0.002 | 9.7 | 99.75 | 2.34 | 0.30 | 0.38 | 274 | 3 | 1.2 | 0.2 | 27.6 | 7.2 | 25.8 | 11.1 | 5 |
| P6R5 165A 526b | 60.82 | 19.71 | 3.55 | 2.49 | 1.44 | 2.10 | 0.50 | 0.15 | 0.05 | < 0.01 | < 0.002 | 9.0 | 99.82 | 1.59 | 0.39 | 0.36 | 265 | < 1 | 1.5 | 0.3 | 28.8 | 8.3 | 29.5 | 12.2 | 6 |
| P6R5 165A 528b | 61.30 | 19.88 | 3.69 | 2.49 | 1.27 | 2.07 | 0.49 | 0.14 | 0.05 | < 0.01 | 0.005 | 8.4 | 99.78 | 0.86 | 0.34 | 0.29 | 452 | < 1 | 1.5 | 0.3 | 26.1 | 8.3 | 28.4 | 11.7 | 5 |
| P6R5 165A 530b | 61.65 | 19.98 | 3.64 | 2.48 | 1.30 | 2.10 | 0.52 | 0.14 | 0.05 | 0.01 | < 0.002 | 7.9 | 99.81 | 0.40 | 0.27 | 0.28 | 383 | < 1 | 1.3 | 0.2 | 28.9 | 8.2 | 29.4 | 13.3 | 6 |
| P6R5 165A 532b | 61.91 | 20.06 | 3.64 | 2.48 | 1.23 | 2.10 | 0.53 | 0.14 | 0.06 | < 0.01 | < 0.002 | 7.7 | 99.83 | 0.27 | 0.29 | 0.27 | 305 | 2 | 1.2 | 0.4 | 29.5 | 9.2 | 29.3 | 12.8 | 6 |
| P6R5 165A534b | 61.90 | 20.09 | 3.60 | 2.42 | 1.22 | 2.12 | 0.55 | 0.15 | 0.06 | < 0.01 | 0.005 | 7.7 | 99.80 | 0.23 | 0.29 | 0.27 | 443 | < 1 | 1.3 | 0.3 | 28.3 | 8.6 | 31.4 | 13.8 | 5 |
| P6R5 165A 536b | 61.73 | 20.20 | 3.61 | 2.45 | 1.25 | 2.10 | 0.53 | 0.14 | 0.05 | < 0.01 | < 0.002 | 7.8 | 99.82 | 0.24 | 0.32 | 0.29 | 437 | < 1 | 0.8 | 0.3 | 27.8 | 7.5 | 27.6 | 12.8 | 5 |
| P6R5 165A 538b | 62.01 | 20.06 | 3.62 | 2.46 | 1.23 | 2.13 | 0.53 | 0.14 | 0.05 | < 0.01 | < 0.002 | 7.6 | 99.82 | 0.29 | 0.30 | 0.29 | 315 | 2 | 1.3 | 0.3 | 29.1 | 7.5 | 28.9 | 13.2 | 5 |
| P6R5 165 A 542b | 61.68 | 19.97 | 3.72 | 2.48 | 1.24 | 2.10 | 0.55 | 0.15 | 0.05 | < 0.01 | < 0.002 | 7.9 | 99.81 | 0.23 | 0.30 | 0.28 | 386 | < 1 | 1.3 | 0.4 | 28.5 | 8.5 | 27.7 | 13.1 | 6 |
| P6R5 165A 547b | 61.75 | 19.98 | 3.61 | 2.47 | 1.24 | 2.10 | 0.54 | 0.14 | 0.05 | < 0.01 | < 0.002 | 7.9 | 99.82 | 0.23 | 0.32 | 0.30 | 317 | 3 | 0.9 | 0.4 | 28.7 | 8.7 | 28.1 | 12.8 | 6 |
| P6R5 165A 552b | 61.49 | 20.09 | 3.63 | 2.45 | 1.31 | 2.12 | 0.55 | 0.14 | 0.06 | < 0.01 | < 0.002 | 8.0 | 99.82 | 0.30 | 0.30 | 0.31 | 370 | 2 | 1.3 | 0.2 | 27.0 | 8.2 | 26.5 | 12.4 | 5 |
| P6R5 165B 525c | 59.78 | 20.82 | 3.70 | 2.62 | 0.04 | 2.61 | < 0.01 | 0.12 | 0.02 | < 0.01 | < 0.002 | 10.1 | 99.83 | 2.59 | 0.04 | n.d. | 9 | 4 | 1.8 | 0.2 | 27.0 | 6.6 | 19.6 | 1.1 | 6 |
| P6R5 165B 530c | 60.55 | 21.76 | 3.73 | 2.55 | 0.04 | 2.71 | 0.03 | 0.13 | 0.02 | < 0.01 | < 0.002 | 8.4 | 99.92 | 0.84 | < 0.02 | n.d. | 12 | < 1 | 0.9 | < 0.1 | 30.0 | 7.6 | 20.9 | 1.1 | 6 |
| P6R5 165B 540c | 61.42 | 21.44 | 3.84 | 2.53 | 0.03 | 2.64 | 0.01 | 0.12 | 0.02 | < 0.01 | < 0.002 | 7.8 | 99.91 | 0.10 | < 0.02 | n.d. | 17 | < 1 | 1.4 | 0.1 | 28.1 | 8.9 | 20.5 | 1.1 | 6 |
| P6R5 165B 575c | 61.23 | 21.51 | 3.80 | 2.59 | 0.04 | 2.66 | < 0.01 | 0.12 | 0.03 | < 0.01 | < 0.002 | 7.9 | 99.92 | 0.09 | < 0.02 | n.d. | 16 | < 1 | 1.1 | < 0.1 | 28.3 | 7.5 | 22.7 | 0.9 | 6 |
| P6R5 165B 615c | 61.09 | 21.61 | 3.86 | 2.59 | 0.05 | 2.67 | 0.03 | 0.13 | 0.03 | < 0.01 | < 0.002 | 7.9 | 99.93 | 0.10 | 0.08 | n.d. | 16 | < 1 | 0.8 | < 0.1 | 30.5 | 7.2 | 21.3 | 1.3 | 6 |
| P6R5 16B5 645c | 61.42 | 21.61 | 3.71 | 2.51 | 0.03 | 2.72 | < 0.01 | 0.12 | 0.02 | < 0.01 | 0.002 | 7.7 | 99.90 | 0.08 | 0.05 | n.d. | 20 | 2 | 1.8 | < 0.1 | 28.9 | 8.3 | 21.8 | 1.1 | 6 |
| P6R5 165B 735c | 60.51 | 21.41 | 3.75 | 2.48 | 0.04 | 2.70 | 0.01 | 0.12 | 0.02 | < 0.01 | < 0.002 | 8.9 | 99.90 | 0.09 | < 0.02 | n.d. | 14 | 4 | 2.2 | 0.1 | 28.6 | 8.2 | 20.9 | 1.4 | 6 |
| P6R5 165B 775c | 61.07 | 21.45 | 3.78 | 2.53 | 0.04 | 2.69 | 0.03 | 0.13 | 0.03 | < 0.01 | < 0.002 | 8.2 | 99.91 | 0.11 | 0.03 | n.d. | 14 | 1 | 0.9 | < 0.1 | 30.3 | 7.1 | 21.1 | 1.3 | 6 |
| P6R5 165B 825c | 61.00 | 21.58 | 3.84 | 2.51 | 0.05 | 2.64 | < 0.01 | 0.12 | 0.01 | < 0.01 | 0.002 | 8.1 | 99.90 | 0.19 | < 0.02 | n.d. | 14 | < 1 | 1.3 | < 0.1 | 29.5 | 6.9 | 20.9 | 1.2 | 6 |
| P6R5 Rc-1 | 61.17 | 21.37 | 3.73 | 2.50 | 0.03 | 2.75 | 0.02 | 0.12 | 0.02 | < 0.01 | < 0.002 | 8.2 | 99.92 | 0.11 | 0.06 | n.d. | 13 | 1 | 0.6 | < 0.1 | 30.2 | 8.1 | 21.2 | 1.0 | 6 |
| P6R5 Rc-2 | 60.98 | 21.83 | 3.77 | 2.52 | 0.03 | 2.76 | < 0.01 | 0.12 | 0.02 | < 0.01 | < 0.002 | 7.9 | 99.93 | 0.10 | 0.09 | n.d. | 9 | < 1 | 1.4 | < 0.1 | 28.9 | 7.4 | 20.8 | 1.0 | 6 |
| P6R5 Rc-3 | 61.14 | 21.5 | 3.79 | 2.54 | 0.04 | 2.75 | 0.01 | 0.12 | 0.02 | < 0.01 | < 0.002 | 8.0 | 99.93 | 0.09 | 0.04 | n.d. | 11 | < 1 | 0.7 | < 0.1 | 30.7 | 7.5 | 19.3 | 0.7 | 6 |

**Table 3-9 continued.**

| Sample id | Sn | Sr | Ta | Th | U | V | W | Zr | Y | La | Ce | Pr | Nd | Sm | Eu | Gd | Tb | Dy | Ho | Er | Tm | Yb | Lu | Mo |
|---|---|---|---|---|---|---|---|---|---|---|---|---|---|---|---|---|---|---|---|---|---|---|---|---|
| | ppm | ppm | ppm | ppm | ppm | ppm | ppm | ppm | ppm | ppm | ppm | ppm | ppm | ppm | ppm | ppm | ppm | ppm | ppm | ppm | ppm | ppm | ppm | ppm |
| DL | 1 | 0.5 | 0.1 | 0.2 | 0.1 | 8 | 0.5 | 0.1 | 0.1 | 0.1 | 0.1 | 0.02 | 0.3 | 0.05 | 0.02 | 0.05 | 0.01 | 0.05 | 0.02 | 0.03 | 0.01 | 0.05 | 0.01 | 0.1 |
| P6R5 165B 525b | 10 | 190.5 | 3.1 | 39.5 | 14.0 | < 8 | < 0.5 | 215.3 | 42.2 | 56.5 | 115.6 | 13.38 | 48.9 | 10.22 | 0.65 | 8.85 | 1.57 | 8.29 | 1.64 | 4.74 | 0.72 | 4.27 | 0.61 | 274.7 |
| P6R5 165B 530b | 9 | 292.2 | 3.1 | 39.3 | 13.6 | < 8 | < 0.5 | 210.7 | 41.7 | 57.1 | 117.4 | 13.53 | 49.6 | 10.55 | 0.63 | 8.95 | 1.60 | 8.35 | 1.64 | 4.51 | 0.68 | 4.17 | 0.57 | 7.0 |
| P6R5 165B 540b | 9 | 290.2 | 3.0 | 41.0 | 14.5 | < 8 | < 0.5 | 212.8 | 41.0 | 54.1 | 111.2 | 12.97 | 48.2 | 9.68 | 0.66 | 8.33 | 1.55 | 8.12 | 1.63 | 4.55 | 0.69 | 4.13 | 0.57 | 0.6 |
| P6R5 165B 555b | 10 | 291.3 | 3.3 | 42.5 | 14.7 | < 8 | < 0.5 | 221.3 | 43.1 | 59.5 | 121.0 | 14.04 | 51.6 | 10.53 | 0.71 | 9.35 | 1.65 | 8.69 | 1.74 | 4.71 | 0.73 | 4.34 | 0.57 | 1.2 |
| P6R5 165B 575b | 9 | 312.1 | 3.3 | 44.3 | 15.2 | < 8 | < 0.5 | 241.4 | 43.7 | 61.1 | 128.2 | 14.55 | 53.4 | 11.37 | 0.73 | 9.74 | 1.68 | 8.94 | 1.76 | 5.02 | 0.74 | 4.51 | 0.64 | 2.6 |
| P6R5 165B 615b | 10 | 299.6 | 3.2 | 42.0 | 14.2 | < 8 | < 0.5 | 206.1 | 43.3 | 59.4 | 122.2 | 14.19 | 50.7 | 10.66 | 0.70 | 9.29 | 1.63 | 8.26 | 1.64 | 4.63 | 0.69 | 4.30 | 0.58 | 1.2 |
| P6R5 165B 645b | 10 | 316.0 | 3.2 | 43.1 | 15.3 | < 8 | < 0.5 | 226.4 | 46.2 | 62.4 | 126.6 | 14.33 | 49.4 | 10.93 | 0.75 | 10.03 | 1.74 | 9.04 | 1.74 | 4.86 | 0.73 | 4.37 | 0.62 | 1.8 |
| P6R5 165B 735b | 10 | 299.7 | 3.2 | 43.5 | 15.8 | < 8 | < 0.5 | 223.1 | 42.6 | 59.6 | 122.3 | 13.81 | 50.1 | 10.62 | 0.72 | 9.52 | 1.64 | 8.80 | 1.69 | 4.86 | 0.75 | 4.51 | 0.61 | 1.9 |
| P6R5 165B 775b | 10 | 290.6 | 3.2 | 42.8 | 15.2 | 9 | < 0.5 | 213.9 | 43.4 | 60.4 | 122.3 | 13.91 | 49.2 | 10.79 | 0.68 | 9.41 | 1.65 | 8.69 | 1.71 | 4.82 | 0.71 | 4.34 | 0.56 | 1.8 |
| P6R5 165B 825b | 11 | 298.2 | 3.3 | 44.4 | 15.6 | < 8 | < 0.5 | 224.8 | 46.0 | 62.6 | 126.3 | 14.43 | 53.2 | 11.13 | 0.73 | 9.61 | 1.70 | 9.18 | 1.69 | 4.90 | 0.73 | 4.59 | 0.61 | 6.4 |
| P6R5 165B 840b | 10 | 304.9 | 3.1 | 42.8 | 15.0 | 20 | < 0.5 | 233.7 | 43.0 | 62.2 | 122.1 | 14.11 | 51.8 | 10.82 | 0.68 | 9.27 | 1.67 | 9.01 | 1.69 | 4.69 | 0.73 | 4.47 | 0.62 | 46.4 |
| P6R5 Rb-1 | 10 | 303.1 | 3.2 | 42.5 | 14.6 | < 8 | < 0.5 | 229.6 | 43.5 | 58.8 | 118.8 | 13.89 | 51.3 | 10.86 | 0.71 | 9.48 | 1.65 | 8.78 | 1.69 | 4.65 | 0.73 | 4.58 | 0.63 | 1.8 |
| P6R5 Rb-2 | 9 | 295.3 | 3.2 | 42.5 | 14.9 | < 8 | 0.6 | 222.3 | 43.9 | 58.1 | 120.2 | 13.62 | 50.0 | 10.83 | 0.70 | 9.47 | 1.66 | 8.91 | 1.69 | 4.90 | 0.73 | 4.52 | 0.62 | 2.3 |
| P6R5 Rb-3 | 9 | 295.9 | 3.2 | 42.4 | 15.1 | 8 | < 0.5 | 228.3 | 42.4 | 59.2 | 122.3 | 13.53 | 50.1 | 10.44 | 0.69 | 9.21 | 1.64 | 8.59 | 1.65 | 4.65 | 0.75 | 4.23 | 0.57 | 2.5 |
| P6R5 165A 525b | 9 | 212.1 | 2.8 | 38.8 | 13.6 | < 8 | < 0.5 | 189.1 | 39.9 | 53.4 | 109.8 | 13.13 | 50.6 | 9.94 | 0.64 | 9.19 | 1.46 | 8.14 | 1.51 | 4.39 | 0.64 | 3.81 | 0.52 | 210.5 |
| P6R5 165A 526b | 9 | 297.5 | 3.1 | 41.8 | 13.8 | < 8 | < 0.5 | 197.7 | 40.6 | 58.1 | 119.9 | 13.35 | 50.0 | 10.11 | 0.68 | 9.22 | 1.51 | 8.84 | 1.64 | 4.56 | 0.66 | 3.86 | 0.60 | 9.6 |
| P6R5 165A 528b | 10 | 342.8 | 3.3 | 41.7 | 14.3 | 16 | < 0.5 | 210.1 | 43.0 | 57.9 | 121.6 | 13.69 | 48.9 | 10.73 | 0.65 | 9.66 | 1.58 | 8.57 | 1.61 | 4.54 | 0.71 | 4.12 | 0.54 | 3.0 |
| P6R5 165A 530b | 10 | 330.9 | 3.1 | 45.8 | 15.1 | < 8 | < 0.5 | 192.4 | 42.6 | 58.4 | 122.0 | 14.23 | 51.1 | 11.05 | 0.68 | 9.85 | 1.61 | 9.03 | 1.74 | 4.85 | 0.66 | 4.29 | 0.57 | 2.9 |
| P6R5 165A 532b | 9 | 295.0 | 2.9 | 42.8 | 14.7 | < 8 | < 0.5 | 204.5 | 43.5 | 59.8 | 121.7 | 13.94 | 55.0 | 10.45 | 0.67 | 9.79 | 1.58 | 9.46 | 1.63 | 4.57 | 0.68 | 4.00 | 0.59 | 2.4 |
| P6R5 165A534b | 10 | 303.5 | 3.1 | 45.2 | 15.3 | < 8 | < 0.5 | 214.6 | 42.7 | 58.6 | 123.0 | 14.19 | 51.6 | 11.09 | 0.72 | 9.78 | 1.61 | 8.96 | 1.81 | 5.03 | 0.68 | 4.29 | 0.59 | 2.7 |
| P6R5 165A 536b | 9 | 310.5 | 3.1 | 42.4 | 14.3 | < 8 | < 0.5 | 188.7 | 40.6 | 55.1 | 116.0 | 13.41 | 48.9 | 10.16 | 0.66 | 9.38 | 1.52 | 8.51 | 1.67 | 4.50 | 0.63 | 4.06 | 0.56 | 2.7 |
| P6R5 165A 538b | 10 | 286.0 | 3.1 | 41.9 | 14.6 | < 8 | < 0.5 | 195.3 | 41.6 | 58.4 | 121.6 | 13.50 | 50.8 | 10.73 | 0.71 | 9.47 | 1.58 | 8.72 | 1.72 | 4.60 | 0.65 | 4.40 | 0.55 | 3.2 |
| P6R5 165 A 542b | 9 | 300.3 | 2.9 | 43.3 | 15.2 | < 8 | < 0.5 | 203.0 | 42.0 | 57.7 | 117.1 | 13.83 | 50.3 | 10.31 | 0.70 | 9.30 | 1.53 | 8.69 | 1.71 | 4.68 | 0.66 | 4.03 | 0.58 | 2.4 |
| P6R5 165A 547b | 9 | 290.7 | 2.9 | 42.9 | 14.4 | < 8 | < 0.5 | 201.7 | 41.2 | 57.0 | 117.3 | 13.57 | 49.0 | 10.16 | 0.63 | 9.33 | 1.51 | 8.37 | 1.66 | 4.68 | 0.67 | 4.40 | 0.52 | 2.5 |
| P6R5 165A 552b | 7 | 279.3 | 3.1 | 41.3 | 15.0 | < 8 | 2.4 | 193.4 | 44.3 | 64.1 | 134.8 | 15.03 | 55.2 | 11.24 | 0.79 | 10.36 | 1.64 | 9.94 | 1.75 | 4.66 | 0.68 | 4.41 | 0.58 | 2.9 |
| P6R5 165B 525c | 10 | 8.1 | 2.6 | 29.0 | 9.3 | < 8 | < 0.5 | 131.8 | 21.9 | 41.3 | 83.2 | 9.55 | 31.6 | 7.12 | 0.36 | 5.84 | 0.99 | 5.35 | 0.86 | 2.08 | 0.30 | 2.02 | 0.20 | 11.0 |
| P6R5 165B 530c | 10 | 7.4 | 3.2 | 31.4 | 10.6 | < 8 | < 0.5 | 135.6 | 23.0 | 43.5 | 88.7 | 9.93 | 36.7 | 7.37 | 0.37 | 6.41 | 0.99 | 5.54 | 0.95 | 2.53 | 0.32 | 2.04 | 0.24 | 2.0 |
| P6R5 165B 540c | 10 | 9.7 | 3.4 | 34.7 | 11.4 | < 8 | 0.7 | 143.6 | 27.9 | 45.9 | 95.6 | 10.67 | 40.2 | 7.76 | 0.38 | 7.14 | 1.08 | 6.13 | 1.03 | 2.69 | 0.35 | 2.17 | 0.29 | 0.4 |
| P6R5 165B 575c | 10 | 10.0 | 3.3 | 34.0 | 10.8 | < 8 | < 0.5 | 144.7 | 26.4 | 46.9 | 93.5 | 10.72 | 40.0 | 8.32 | 0.36 | 7.10 | 1.10 | 5.22 | 1.03 | 2.58 | 0.34 | 2.44 | 0.25 | 0.4 |
| P6R5 165B 615c | 10 | 9.4 | 3.0 | 33.3 | 11.3 | < 8 | < 0.5 | 132.7 | 25.0 | 42.6 | 89.0 | 10.17 | 36.3 | 7.78 | 0.39 | 6.67 | 1.04 | 5.37 | 1.08 | 2.69 | 0.34 | 2.18 | 0.26 | 0.5 |
| P6R5 16B5 645c | 9 | 9.3 | 2.9 | 32.5 | 11.0 | < 8 | < 0.5 | 144.8 | 27.0 | 46.8 | 95.9 | 10.80 | 42.1 | 8.31 | 0.34 | 6.85 | 1.11 | 5.81 | 0.98 | 2.61 | 0.35 | 2.11 | 0.28 | 0.4 |
| P6R5 165B 735c | 9 | 9.3 | 2.8 | 30.3 | 10.5 | 9 | < 0.5 | 139.0 | 23.1 | 42.8 | 83.8 | 9.83 | 34.8 | 7.55 | 0.35 | 5.97 | 1.03 | 5.36 | 0.97 | 2.18 | 0.30 | 2.02 | 0.22 | 0.4 |
| P6R5 165B 775c | 9 | 8.8 | 2.9 | 33.6 | 11.2 | < 8 | < 0.5 | 135.9 | 26.2 | 43.2 | 90.5 | 10.60 | 40.2 | 8.10 | 0.42 | 6.94 | 1.07 | 5.97 | 1.06 | 2.91 | 0.36 | 2.15 | 0.28 | 0.4 |
| P6R5 165B 825c | 10 | 9.3 | 3.2 | 29.8 | 10.0 | 9 | < 0.5 | 138.0 | 22.6 | 42.5 | 86.7 | 9.61 | 35.7 | 7.35 | 0.43 | 6.42 | 0.97 | 5.36 | 0.9 | 2.6 | 0.28 | 1.79 | 0.20 | 0.8 |
| P6R5 Rc-1 | 9 | 8.4 | 3.0 | 32.3 | 10.2 | < 8 | < 0.5 | 137.9 | 24.6 | 44.4 | 90.8 | 10.17 | 36.7 | 7.47 | 0.39 | 6.82 | 0.99 | 5.98 | 0.95 | 2.63 | 0.34 | 2.20 | 0.25 | 0.3 |
| P6R5 Rc-2 | 12 | 8.0 | 3.1 | 31.1 | 10.4 | 10 | < 0.5 | 141.3 | 23.5 | 43.4 | 90.6 | 10.24 | 39.4 | 7.60 | 0.34 | 6.02 | 0.97 | 4.81 | 0.88 | 2.10 | 0.29 | 2.15 | 0.22 | 0.2 |
| P6R5 Rc-3 | 9 | 7.5 | 3.1 | 29.8 | 9.8 | < 8 | < 0.5 | 131.1 | 21.3 | 39.5 | 81.8 | 9.27 | 36.0 | 7.02 | 0.33 | 6.11 | 0.90. | 5.46 | 0.80 | 2.13 | 0.29 | 1.87 | 0.21 | 0.2 |

**Table 3-9 continued.**

| Sample id | Cu | Pb | Zn | Ni | As | Cd | Sb | Bi | Ag | Au | Hg | Tl | Se |
|---|---|---|---|---|---|---|---|---|---|---|---|---|---|
| | ppm | ppm | ppm | ppm | ppm | ppm | ppm | ppm | ppm | ppb | ppm | ppm | ppm |
| DL | 0.1 | 0.1 | 1 | 0.1 | 0.5 | 0.1 | 0.1 | 0.1 | 0.1 | 0.5 | 0.01 | 0.1 | 0.5 |
| P6R5 165B 525b | 79.6 | 38.6 | 667 | 6.6 | 10.8 | 0.3 | < 0.1 | 0.9 | 0.2 | < 0.5 | 0.03 | 0.4 | < 0.5 |
| P6R5 165B 530b | 5.7 | 40.9 | 177 | 3.9 | 11.0 | 0.4 | < 0.1 | 0.9 | 0.2 | 3.8 | 0.02 | 0.4 | < 0.5 |
| P6R5 165B 540b | 4.5 | 47.4 | 102 | 3.9 | 12.9 | 0.3 | < 0.1 | 1.0 | 0.2 | 0.7 | 0.04 | 0.5 | 0.7 |
| P6R5 165B 555b | 4.3 | 48.6 | 104 | 4.0 | 13.3 | 0.3 | < 0.1 | 0.9 | 0.2 | < 0.5 | 0.03 | 0.4 | < 0.5 |
| P6R5 165B 575b | 3.8 | 45.3 | 100 | 4.0 | 12.5 | 0.3 | 0.1 | 1.0 | 0.2 | < 0.5 | < 0.01 | 0.4 | 0.8 |
| P6R5 165B 615b | 3.8 | 45.6 | 147 | 3.6 | 12.9 | 0.3 | < 0.1 | 0.8 | 0.2 | < 0.5 | 0.02 | 0.4 | 1.0 |
| P6R5 165B 645b | 3.7 | 47.4 | 90 | 3.7 | 12.8 | 0.3 | < 0.1 | 0.9 | 0.1 | 1.0 | 0.02 | 0.4 | 1.6 |
| P6R5 165B 735b | 3.4 | 44.3 | 72 | 4.0 | 12.4 | 0.3 | < 0.1 | 0.9 | 0.2 | < 0.5 | 0.02 | 0.4 | < 0.5 |
| P6R5 165B 775b | 3.5 | 42.2 | 87 | 3.5 | 12.6 | 0.3 | < 0.1 | 1.0 | 0.2 | < 0.5 | 0.01 | 0.3 | 0.5 |
| P6R5 165B 825b | 3.6 | 43.2 | 83 | 4.1 | 11.7 | 0.3 | 0.1 | 0.8 | 0.2 | < 0.5 | 0.02 | 0.4 | 0.7 |
| P6R5 165B 840b | 5.0 | 43.8 | 227 | 8.5 | 11.6 | 0.3 | < 0.1 | 0.9 | 0.2 | < 0.5 | 0.03 | 0.4 | 1.0 |
| P6R5 Rb-1 | 3.2 | 43.4 | 107 | 3.1 | 13.0 | 0.3 | 0.1 | 0.9 | 0.2 | < 0.5 | 0.02 | 0.4 | 0.8 |
| P6R5 Rb-2 | 3.6 | 43.2 | 99 | 3.4 | 12.4 | 0.3 | 0.2 | 0.9 | 0.2 | < 0.5 | 0.03 | 0.4 | 1.3 |
| P6R5 Rb-3 | 3.4 | 48.0 | 115 | 3.9 | 13.5 | 0.3 | 0.2 | 1.0 | 0.2 | < 0.5 | 0.02 | 0.4 | 0.8 |
| P6R5 165A 525b | 124.7 | 33.9 | 447 | 4.0 | 9.4 | 0.5 | 0.5 | 0.9 | 0.2 | < 0.5 | 0.01 | 0.3 | 0.6 |
| P6R5 165A 526b | 5.5 | 37.4 | 121 | 3.0 | 10.1 | 0.3 | 0.6 | 1.0 | 0.2 | < 0.5 | 0.01 | 0.3 | 0.6 |
| P6R5 165A 528b | 3.5 | 40.5 | 75 | 3.0 | 11.5 | 0.2 | 0.7 | 1.0 | 0.2 | < 0.5 | 0.01 | 0.3 | 0.7 |
| P6R5 165A 530b | 3.3 | 44.1 | 71 | 3.1 | 10.3 | 0.3 | 0.7 | 0.9 | 0.2 | < 0.5 | < 0.01 | 0.3 | 0.7 |
| P6R5 165A 532b | 3.2 | 43.2 | 74 | 2.8 | 10.4 | 0.2 | 0.5 | 1.0 | 0.2 | < 0.5 | < 0.01 | 0.3 | < 0.5 |
| P6R5 165A534b | 3.1 | 43.8 | 101 | 2.7 | 11.1 | 0.3 | 0.7 | 1.0 | 0.2 | < 0.5 | 0.01 | 0.3 | 0.5 |
| P6R5 165A 536b | 2.9 | 41.7 | 91 | 2.8 | 11.8 | 0.3 | 0.7 | 1.0 | 0.2 | < 0.5 | < 0.01 | 0.3 | < 0.5 |
| P6R5 165A 538b | 3.6 | 45.2 | 139 | 3.6 | 13.9 | 0.4 | 0.8 | 1.1 | 0.2 | < 0.5 | 0.02 | 0.4 | 0.5 |
| P6R5 165 A 542b | 3.5 | 44.8 | 94 | 2.9 | 11.7 | 0.4 | 0.6 | 1.1 | 0.2 | < 0.5 | 0.01 | 0.4 | 1.0 |
| P6R5 165A 547b | 3.3 | 44.8 | 102 | 3.0 | 11.9 | 0.3 | 0.8 | 1.0 | 0.2 | < 0.5 | 0.01 | 0.3 | 1.0 |
| P6R5 165A 552b | 3.6 | 40.3 | 71 | 3.3 | 15.6 | 0.1 | 0.7 | 1.0 | 0.2 | < 0.5 | 0.01 | 0.4 | 0.7 |
| P6R5 165B 525c | 80.4 | 15.4 | 647 | 5.6 | 1.2 | 0.1 | 0.2 | 0.4 | < 0.1 | < 0.5 | 0.02 | < 0.1 | < 0.5 |
| P6R5 165B 530c | 4.3 | 22.0 | 77 | 3.5 | 1.8 | < 0.1 | 0.1 | 0.6 | < 0.1 | 0.7 | 0.01 | < 0.1 | < 0.5 |
| P6R5 165B 540c | 3.2 | 25.6 | 28 | 3.1 | 1.8 | < 0.1 | 0.2 | 0.6 | < 0.1 | < 0.5 | 0.01 | < 0.1 | < 0.5 |
| P6R5 165B 575c | 2.3 | 24.7 | 23 | 3.1 | 1.2 | < 0.1 | 0.1 | 0.6 | < 0.1 | < 0.5 | 0.02 | < 0.1 | < 0.5 |
| P6R5 165B 615c | 2.9 | 27.0 | 29 | 3.6 | 2.0 | < 0.1 | 0.2 | 0.6 | < 0.1 | < 0.5 | 0.02 | < 0.1 | < 0.5 |
| P6R5 16B5 645c | 2.4 | 24.2 | 23 | 2.8 | 1.6 | < 0.1 | 0.2 | 0.6 | < 0.1 | 0.6 | < 0.01 | < 0.1 | < 0.5 |
| P6R5 165B 735c | 2.8 | 25.4 | 26 | 4.2 | 1.8 | < 0.1 | 0.2 | 0.6 | < 0.1 | < 0.5 | 0.01 | < 0.1 | < 0.5 |
| P6R5 165B 775c | 2.5 | 27.6 | 29 | 3.3 | 2.1 | < 0.1 | 0.2 | 0.6 | < 0.1 | < 0.5 | 0.02 | < 0.1 | < 0.5 |
| P6R5 165B 825c | 2.4 | 19.1 | 37 | 2.9 | 1.3 | < 0.1 | 0.1 | 0.6 | < 0.1 | < 0.5 | 0.01 | < 0.1 | < 0.5 |
| P6R5 Rc-1 | 2.3 | 23.2 | 33 | 2.9 | 1.4 | < 0.1 | 0.1 | 0.4 | < 0.1 | < 0.5 | 0.01 | < 0.1 | < 0.5 |
| P6R5 Rc-2 | 1.7 | 19.2 | 28 | 2.5 | 1.0 | < 0.1 | < 0.1 | 0.3 | < 0.1 | < 0.5 | 0.01 | < 0.1 | < 0.5 |
| P6R5 Rc-3 | 2.8 | 21.4 | 33 | 2.5 | 1.0 | < 0.1 | < 0.1 | 0.3 | < 0.1 | < 0.5 | < 0.01 | < 0.1 | < 0.5 |

### 3.3.4 Structural formula of the smectite

The chemical composition of the Na-converted < 0.5 µm fraction of the samples (Table 3-9) was used for calculations of the average structural formula of the smectite. The samples of block P5 R06 were omitted in these calculations because the XRD- and FTIR-data clearly showed that these samples were not pure smectite but also contained "impurities" of quartz and cristobalite, which would inevitably result in erroneous formulae.

The calculations for the samples of block P6 R05 were based on the structures of 2:1 layer silicates, assuming an anionic charge of –44, in addition to the following assumptions and approximations:

**Iron** was assigned to the octahedral sheet and was assumed to be trivalent. According to the Mössbauer analysis (Section 3.3.7) iron in the bulk samples from the inner part of the blocks (sampled in $N_2$-atmosphere) was more reduced than in the references but corresponding data on the oxidation state of iron were not available for the < 0.5 µm fraction. The assumption that all iron is present only in the ferric state in the purified smectite may underestimate the octahedral charge.

**Titanium** (range 0.12–0.13% $TiO_2$) in the < 0.5 µm fractions was allocated to the octahedral sheet, according to common practice in formula calculations of clay minerals when no discrete titanium phase is detectable (Newman and Brown 1987).

**Potassium** (range < 0.01–0.03% $K_2O$) in the Na-converted clay was considered non-exchangeable and was allocated to illite, the amount of which (0.3% at a maximum) is too small for detection in the XRD analysis. Based on the potassium content, the amount of illite was calculated using the ideal illite formula $K_{1.5}(Si_7Al)(Al_{3.5}Mg_{0.5})O_{20}(OH)_4$ (i.e. K-content 7.6%). The $SiO_2$, $Al_2O_3$ and MgO contents were adjusted accordingly.

All of the remaining **magnesium** was assigned to the octahedral sheet because the clay had been saturated with sodium and dialyzed prior to the chemical analysis. The interlayer charge would be underestimated if some of the magnesium found by chemical analysis of the fine clay was exchangeable.

All of the remaining **silica** was allocated to the tetrahedral sheet of the smectite, although the XRD-data indicate that traces of cristobalite exist in all the fine clay samples. Quantitative estimations based on the diffraction profiles of oriented mounts were considered too uncertain and no correction was made. An occurrence of free silica in the samples necessarily adds an error in the structural formulae.

Any **calcium** that existed after the dialysis of the Na-converted clay (range 0.03–0.05% CaO) was assigned to the pool of interlayer cations.

The results of the calculations (Table 3-10) suggest that the charge of the smectite varies from 0.67 to 0.70 per formula unit, which is within the uncertainty of the method, although it may be noticed that the maximum charge is found in the reference samples. According to the formulae, between 18 and 26% of the charge is located in the tetrahedral sheet, but no systematic trend can be seen in this rather large variation. Based on the charge distribution, the smectite of all samples should be classified as montmorillonite (e.g. Brindley and Brown 1980). Mg exceeds Fe in the octahedral sheet in all samples and is at a maximum in the contact sample. The total octahedral site occupancy in the formula is close to 4 per $O_{20}(OH)_4$, which is the normal value in dioctahedral smectites, but it remains to be established whether the allocation of all magnesium to the octahedral sites of the smectite has a true structural foundation, or whether a neoformed phase of low solubility is the sink for magnesium.

The average formulae of the montmorillonite from block P6R05 and the references, respectively, are similar in almost every detail (cf. also Section 3.4.6):

References: $Ca_{0.005}\ Na_{0.69}(Al_{3.12}\ Fe_{0.36}\ Mg_{0.48}\ Ti_{0.01})(Si_{7.85}\ Al_{0.15})\ O_{20}\ (OH)_4$

Block P6R05: $Ca_{0.006}\ Na_{0.67}(Al_{3.11}\ Fe_{0.37}\ Mg_{0.49}\ Ti_{0.01})(Si_{7.85}\ Al_{0.15})\ O_{20}\ (OH)_4$

**Table 3-10. Calculated mean structural formula of the smectite from profile P6R05 165A. Calculations are based on the chemical composition of the purified Na-saturated < 0.5 µm fraction (Table 3-9).**

| | P6R05 165A | | | | | | | | | | | |
|---|---|---|---|---|---|---|---|---|---|---|---|---|
| | **525c** | **530c** | **540c** | **575c** | **615c** | **645c** | **735c** | **775c** | **825c** | **R-1c** | **R-2c** | **R-3c** |
| Si | 7.87 | 7.82 | 7.87 | 7.86 | 7.84 | 7.86 | 7.85 | 7.86 | 7.85 | 7.87 | 7.83 | 7.86 |
| Al | 0.13 | 0.18 | 0.13 | 0.14 | 0.16 | 0.14 | 0.15 | 0.14 | 0.15 | 0.13 | 0.17 | 0.14 |
| **Σ tetrahedral** | 8.00 | 8.00 | 8.00 | 8.00 | 8.00 | 8.00 | 8.00 | 8.00 | 8.00 | 8.00 | 8.00 | 8.00 |
| Al okt | 3.09 | 3.12 | 3.11 | 3.11 | 3.11 | 3.12 | 3.12 | 3.11 | 3.12 | 3.11 | 3.13 | 3.11 |
| Ti | 0.01 | 0.01 | 0.01 | 0.01 | 0.01 | 0.01 | 0.01 | 0.01 | 0.01 | 0.01 | 0.01 | 0.01 |
| $Fe^{3+}$ | 0.37 | 0.36 | 0.37 | 0.37 | 0.37 | 0.36 | 0.37 | 0.37 | 0.37 | 0.36 | 0.36 | 0.37 |
| Mg | 0.51 | 0.49 | 0.48 | 0.50 | 0.50 | 0.48 | 0.48 | 0.49 | 0.48 | 0.48 | 0.48 | 0.49 |
| **Σ octahedral** | 3.99 | 3.99 | 3.98 | 3.98 | 3.99 | 3.97 | 3.98 | 3.98 | 3.98 | 3.97 | 3.98 | 3.97 |
| Ca | 0.006 | 0.006 | 0.004 | 0.006 | 0.007 | 0.004 | 0.006 | 0.006 | 0.007 | 0.004 | 0.004 | 0.006 |
| Na | 0.667 | 0.680 | 0.657 | 0.663 | 0.666 | 0.676 | 0.680 | 0.673 | 0.659 | 0.688 | 0.687 | 0.686 |
| **interlayer charge** | 0.68 | 0.69 | 0.67 | 0.67 | 0.68 | 0.68 | 0.69 | 0.68 | 0.67 | 0.70 | 0.70 | 0.70 |
| % tet. charge | 20 | 26 | 19 | 21 | 23 | 20 | 22 | 20 | 23 | 18 | 25 | 21 |
| molar weight | 745 | 745 | 745 | 745 | 745 | 745 | 745 | 745 | 745 | 745 | 745 | 745 |
| CEC calculated | 91 | 93 | 89 | 90 | 91 | 92 | 93 | 92 | 90 | 93 | 93 | 93 |
| CEC measured | 93 | 93 | 97 | 95 | 95 | 95 | 96 | 94 | 94 | 95 | 95 | 96 |

### 3.3.5 Mineralogical composition – XRD-analysis

XRD-profiles of the bulk bentonite samples from profiles P5R06 050 and P6R05 165 are shown in Figure 3-15, where the strongest peaks of the major accessory minerals are indicated. The previously dried samples were equilibrated at ambient relative humidity (RH 50 ± 10%) prior to X-ray scanning, but the smectite is still more or less dehydrated in many of the samples, which affects the shape, width and position of its basal reflections.

The two-dimensional (060) hk-peak of smectite is also indicated in Figure 3-15. This reflection is useful for distinguishing di- and trioctahedral sub-groups of clay minerals because it includes the *b* cell dimension, which is more sensitive to the size of the cations and to site occupancy in the octahedral sheet than are the *a* or *c* cell dimensions. Without exceptions, the d-value of the (060) peak falls within the range 1.497 to1.500 Å, which is typical of the dioctahedral sub-group of smectites, to which montmorillonite belongs.

Some variation is seen in the intensities of the strongest peaks of quartz and feldspars, probably as an effect of variations in particles size, orientation and/or inhomogeneous mixing of the samples, which are factors of major importance in the diffraction of X–rays by mixed powders.

Traces of gypsum are generally found in MX80 bentonite, but according to the chemical data the maximum amount of gypsum that can exist in the reference samples (i.e. if all sulfur is allocated to $CaSO_4*2H_2O$) is < 1.5%, which is close to the detection limit of the XRD-analysis. Nevertheless, the strongest gypsum peak can be seen in most of the samples (Figure 3-15) and its intensity is variable but the variation lacks correlation to the chemical data for sulfate, which indicate a maximum close to the canister. However, a peak appears in sample 530b from both block at the position (25.5°2θ) where dehydrated calcium sulfate (anhydrite) has its strongest reflection, but based on one single reflection the identification must be considered uncertain.

Also calcite is found in MX80, and is indicated in the chemical data for the reference samples, but, again, the quantity, ~ 1% (if all carbonate carbon is allocated to $CaCO_3$), is close to the detection limit of the XRD-method. The appearance of a distinct, although weak, calcite peak in the contact sample of block P5R06 is, however, consistent with the chemical data for carbonate carbon and calcium, which suggest that the calcium carbonate content has increased to 2% in this sample.

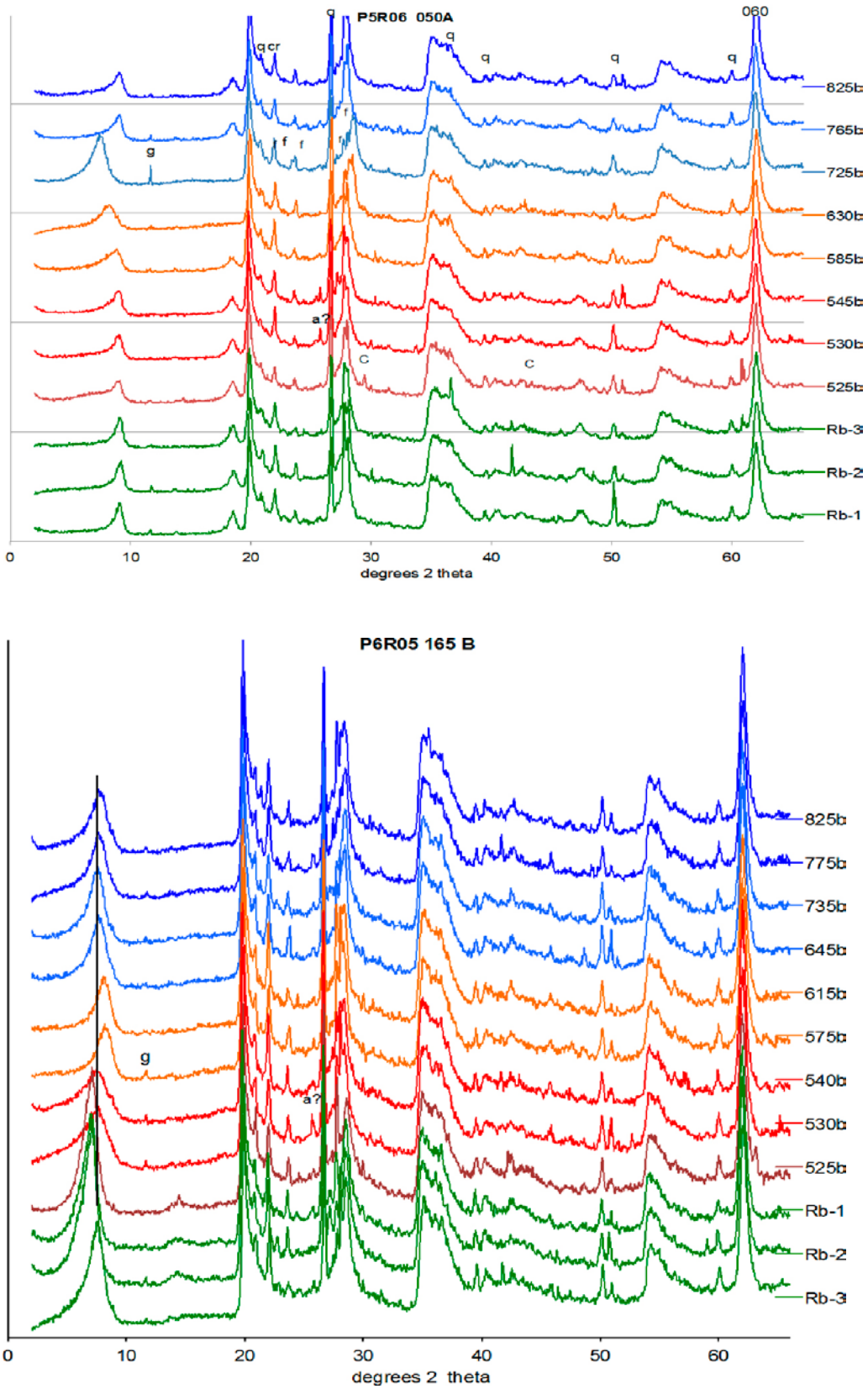


***Figure 3-15.*** *XRD-profiles of random powders of the bulk bentonite samples from profiles P5R06 050 and P6R05 165. a? = possibly anhydrite; c = calcite; cr = cristobalite; g = gypsum; f = feldspars; q = quartz. CuKα radiation.*

XRD-profiles of Mg-exchanged < 0.5 µm fractions in an air-dried and EG-solvated state are shown in Figure 3-16 to Figure 3-19. Data for the samples of the inner contact surface of both blocks are missing, because the contact sample of block P5R06 was not possible to fractionate by size, and the fine clay fraction of sample P6R05 525 was too poorly re-dispersed after the fractionation for preparation of a mount with acceptable preferred orientation of the clay minerals. The relative peak intensities are anomalous and peaks displaced also in the air-dried samples 530c in both blocks, suggesting that the preferred orientation of the clay mineral is poor, probably due to poor dispersion caused by the grease.

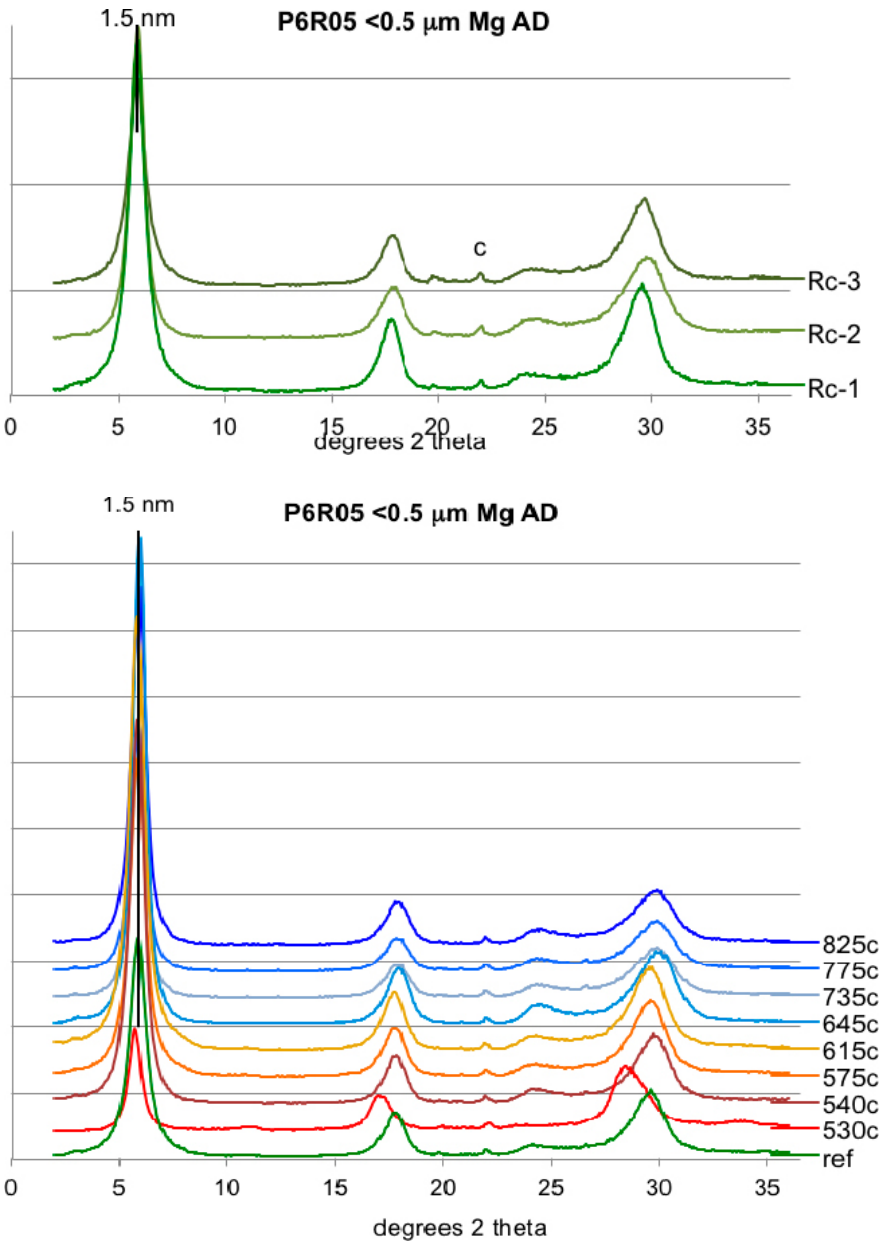


***Figure 3-16.*** *Upper graph: XRD-profiles of oriented mounts of the < 0.5 µm fraction of the reference samples for block P6R05. Lower graph: XRD-profiles of oriented mounts of the < 0.5 mm fraction of the samples from profile P6R05 165. Green curve: mean profile of three reference samples. c = cristobalite. Air-dried, Mg-saturated samples. CuKα radiation.*

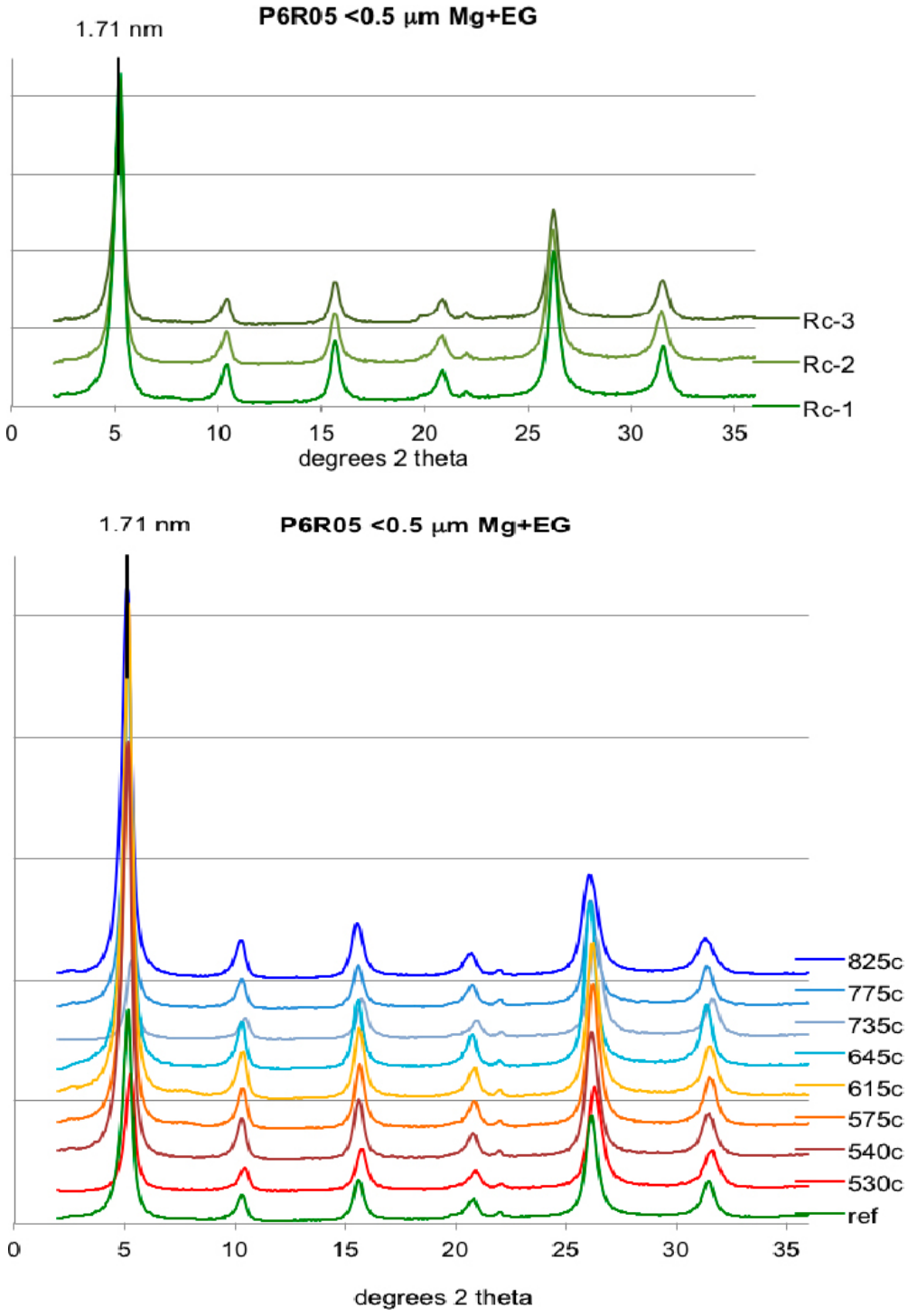


***Figure 3-17. Upper graph**: XRD-profiles of oriented mounts of the < 0.5 µm fraction of the reference samples for block P6R05. **Lower graph**: XRD-profiles of oriented mounts of the < 0.5 µm fraction of the samples from block P6R05. Green curve: mean profile of three reference samples. EG-solvated, Mg-saturated samples. CuKα radiation.*

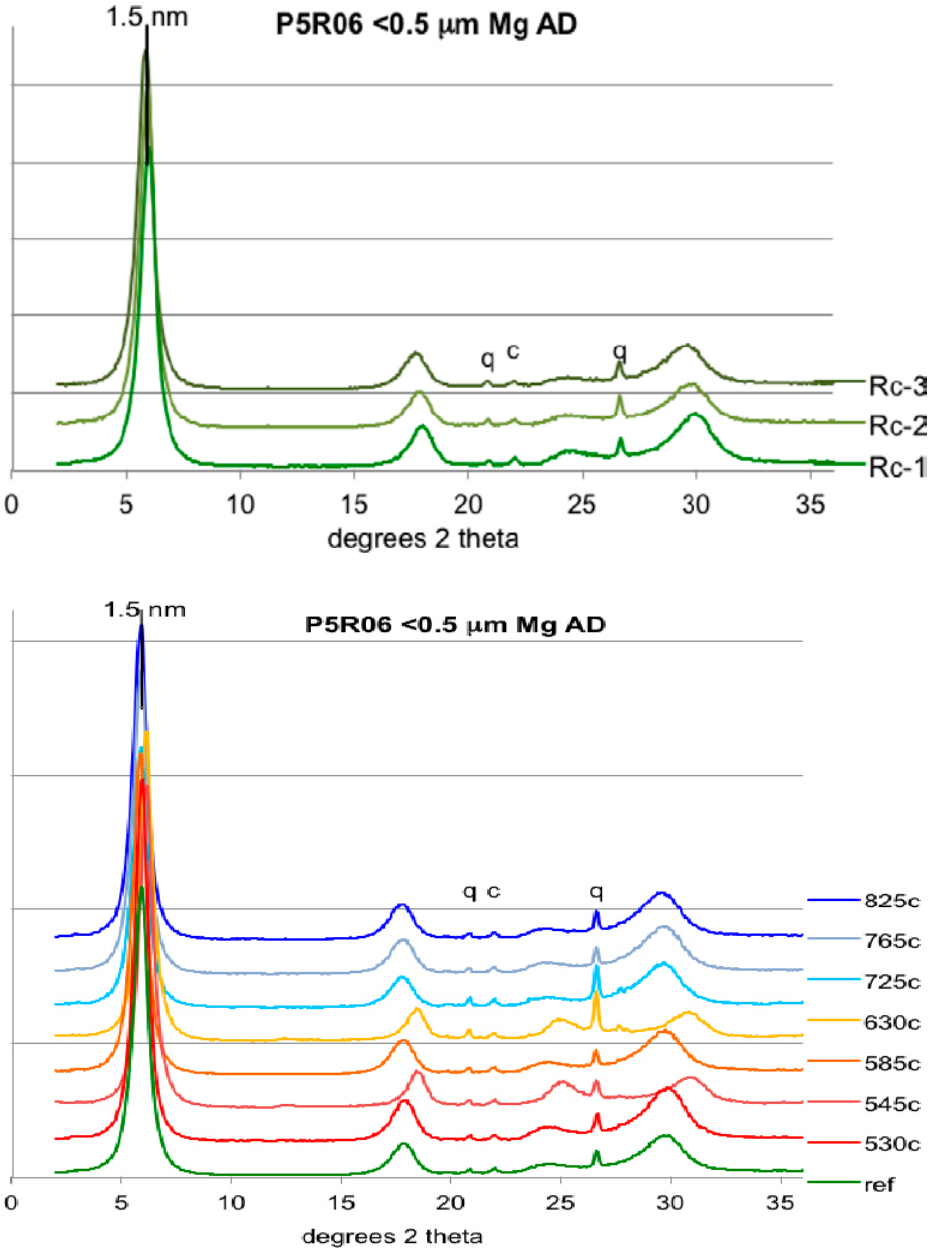


***Figure 3-18. Upper graph**: XRD-profiles of oriented mounts of the < 0.5 µm fraction of the reference samples for block P5R06. **Lower graph**: XRD-profiles of oriented mounts of the < 0.5 µm fraction of the samples from block P5R06. Green curve: mean profile of three reference samples. c = cristobalite; q = quartz. Air-dried, Mg-saturated samples. CuKα radiation.*

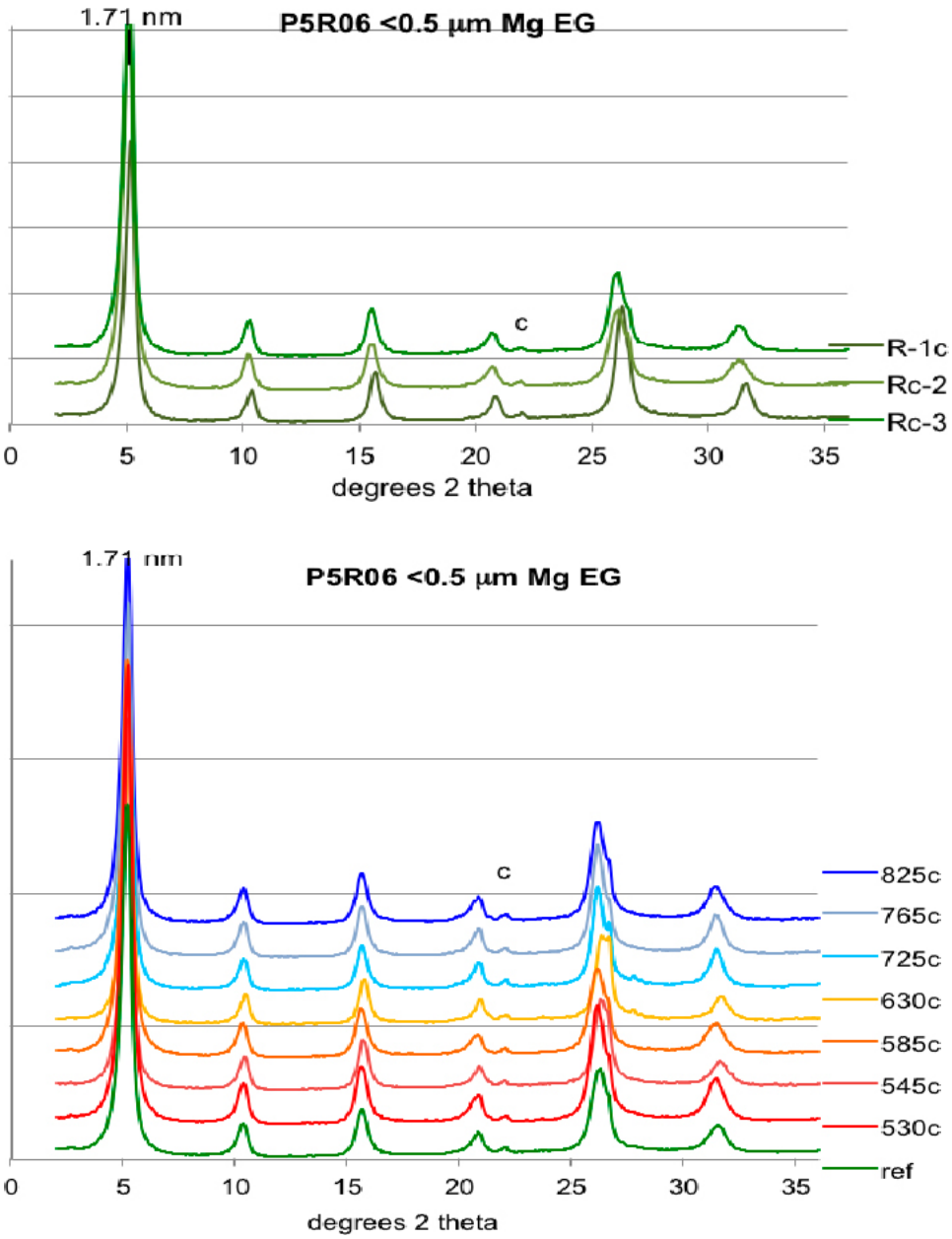


***Figure 3-19. Upper graph****: XRD-profiles of oriented mounts of the < 0.5 µm fraction of the reference samples for block P5R06.* ***Lower graph****: XRD-profiles of oriented mounts of the < 0.5 µm fraction of the samples from block P5R06. Green curve: mean profile of three reference samples. c = cristobalite. EG-solvated, Mg-saturated samples. CuKα radiation.*

However, the EG-solvated samples produce a rational series of basal reflections and the expansion and d-values are essentially the same in all block samples as those of the references.

Traces of cristobalite occur in the fine clay fractions of all samples, and all samples of block P5R06 and the references also contain some quartz. Apart from these minerals, the fine clay fractions appear to be pure montmorillonite.

In the air-dried, Mg-saturated state, the smectite has a basal spacing of 1.5 nm (relative humidity 50 ± 10%). No difference is seen in the expansion behaviour of the smectite, which expands to ~ 1.7 nm upon EG-solvation in all samples, producing a complete rational series of basal reflections. The expansion behaviour is indicative of well-ordered stacking sequences of smectite with insignificant interstratification. Similarly, the value of $\Delta 2\theta_{002/003}$ (the angular difference between the (002) and (003) peaks in degrees 2θ) is in the same range (5.30 ± 0.03) as that of the reference samples and typical of a well-defined montmorillonite phase (Moore and Reynolds 1989). Small amounts of non-exchangeable potassium in the < 0.5 µm fractions (< 0.01 – 0.12% $K_2O$) suggest, however, that some illitic layers may exist in the smectite but in proportions too small for detection by use of routine XRD-analysis.

In summary, the available XRD-data provide no evidence of any structural change in the montmorillonite of blocks P6R05 and P5R06, but the resolution of the XRD-technique is inadequate for detecting subtle structural changes.

### 3.3.6 Scanning electron microscopy (SEM)

#### *Analyses of the inner surface of the blocks*

A tiny fracture pattern was visible with the naked eye on the relatively smooth, inner surface of block P06R05 that had been in contact with the copper canister. Previous observations in other bentonite field tests indicate that the fractures are due to drying and/or stress release in conjunction with the retrieval (Karnland et al. 2009).

Back-scatter images at relatively low magnification revealed clusters of granular particles (ellipse in Figure 3-20 upper left) and bright spots of a size of up to 10 µm (arrow in Figure 3-20 upper left, and Figure 3-21). Calcium and sulfur were frequently present and to a large extent correlated in the granules, while the spots were strongly dominated by sulfur (Figure 3-21).

Copper was found in some areas in concentrations up to a few weight %, and at background concentration in other areas. Characteristic elements in bentonite, such as Si, Al, and K, were present in a distribution typical of the original MX-80 bentonite. No correlation was found between the element distribution and the fracture pattern.

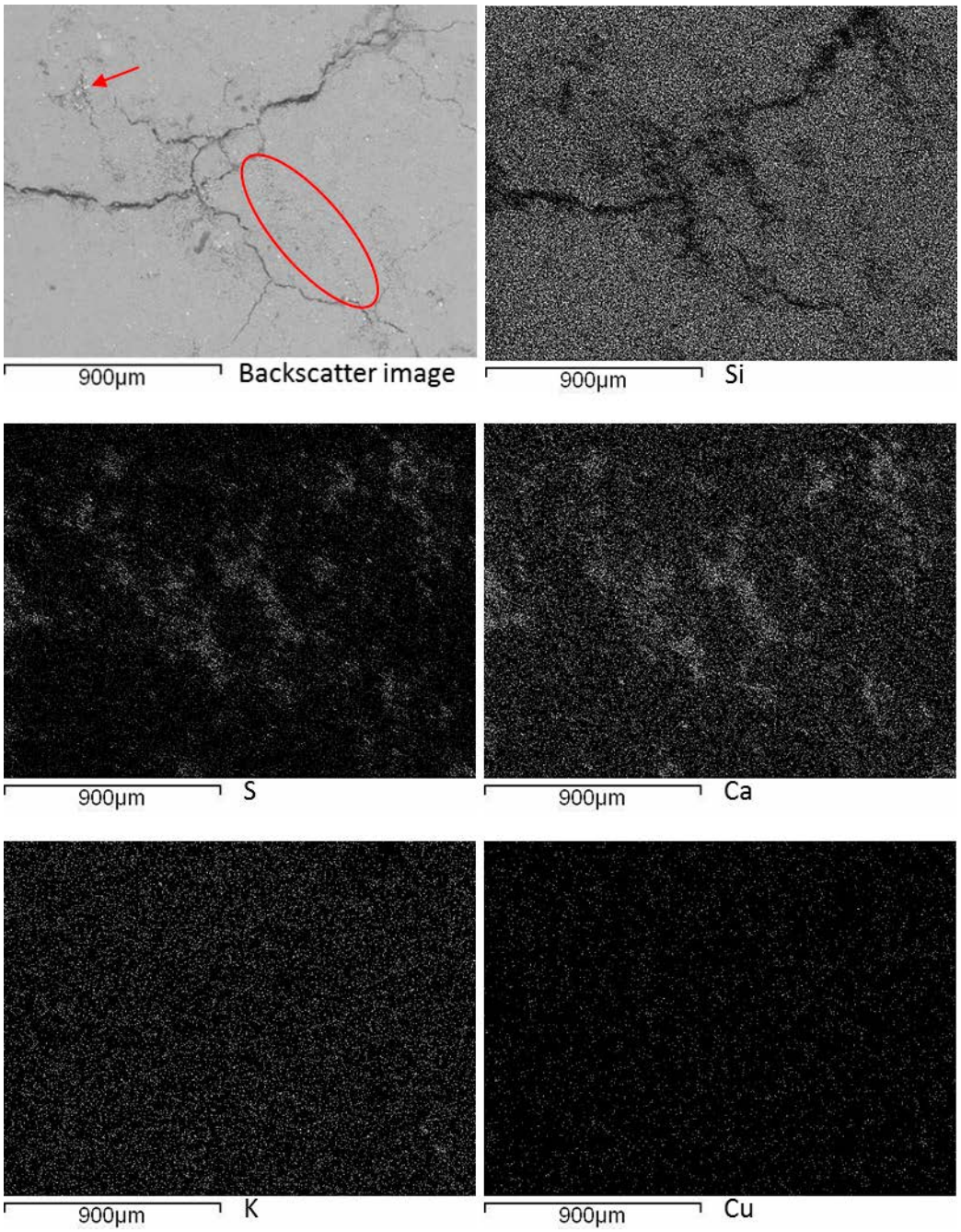


***Figure 3-20.*** *Upper left: Backscatter image of the inner surface of the bentonite block P6R05 previously in contact with the copper canister. The rest of the photos show the results of the element mapping of the same area by use of EDX.*

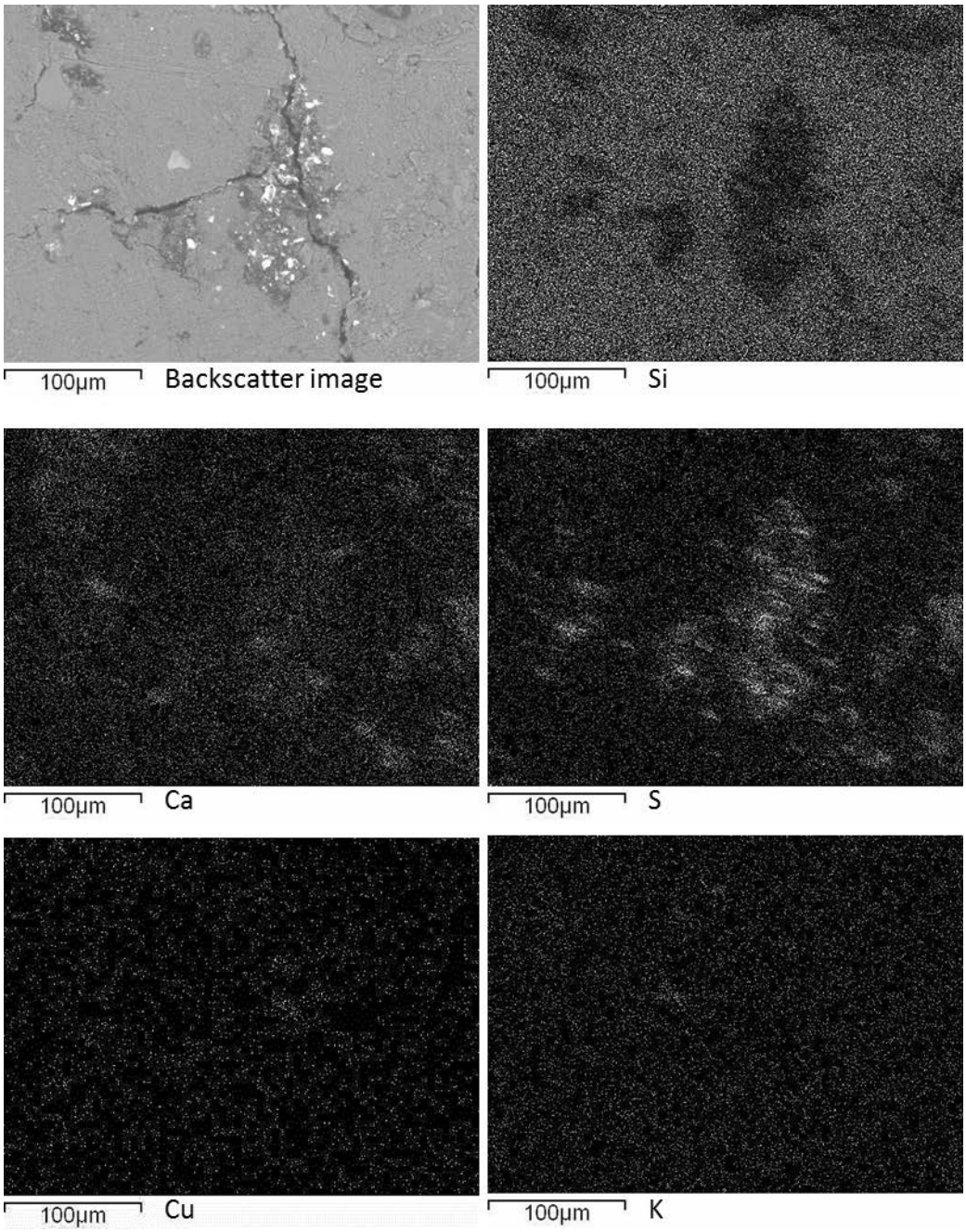


***Figure 3-21.*** *Close-up of the upper left corner, marked by an arrow in Figure 3-20. The rest of the photos show the results of an element mapping of the area by EDX. Note the bright spots, which are dominated by sulfur and not correlated to calcium.*

### *Analyses of the bentonite matrix*

Back-scatter images, supported by element analyses, showed areas in which sulfur-dominated spots were frequent. The size of the spots was up to 20 µm and in general similar to those found on the inner surface of the bentonite block. The areas with these sulfur-dominated spots were unevenly distributed up to a depth of approximately 500 µm in the bentonite, and relatively large areas with no spots were present, also on the canister/bentonite interface (Figure 3-22 and Figure 3-23).

Sulfur was also present in areas without these spots, but at significantly lower concentrations and then in combination with calcium (Figure 3-23 a).

Increased levels of copper were found to a depth of up to approximately 400 µm in the bentonite in some areas (Figure 3-23 b and Figure 3-24). Other areas, also on the previous canister/bentonite interface, showed no increase in copper concentrations compared to the original bentonite (Figure 3-23 a). In order to calibrate line-scan results, successive areas of 50 µm × 50 µm were analyzed quantitatively (Table 3-11). Concentrations ranging from 1.1 to 3.4 weight % copper were found in the innermost positions with a mean value of 1.9 weight % for the first 200 µm. Analyses performed at distances of 1 mm and beyond showed no increase compared to the reference material. The area analyses are consequently in qualitative agreement with the line scan analyses in Figure 3-23 and Figure 3-24.

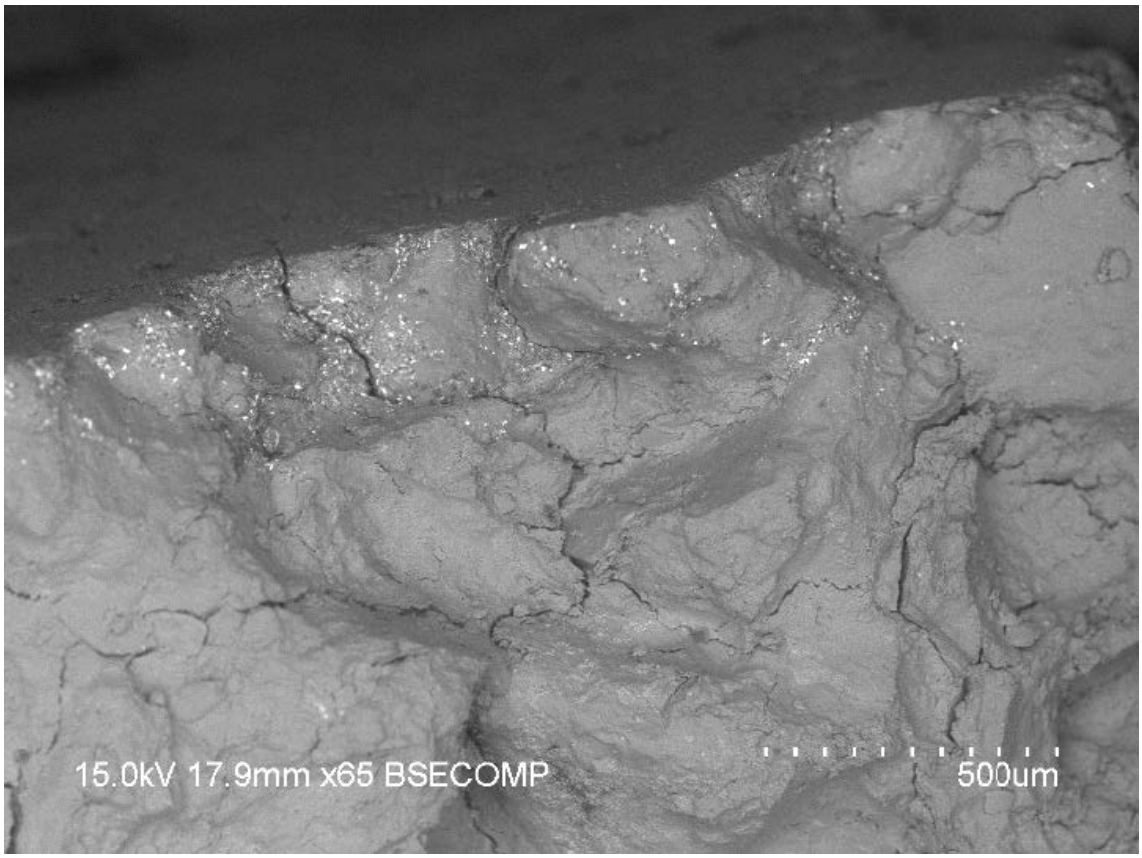


***Figure 3-22.*** *Backscatter over-view image of the innermost part of bentonite from block P6R05 165. The dark area at the top represents the former position of the copper canister. Note the bright spots in the upper part of the bentonite.*

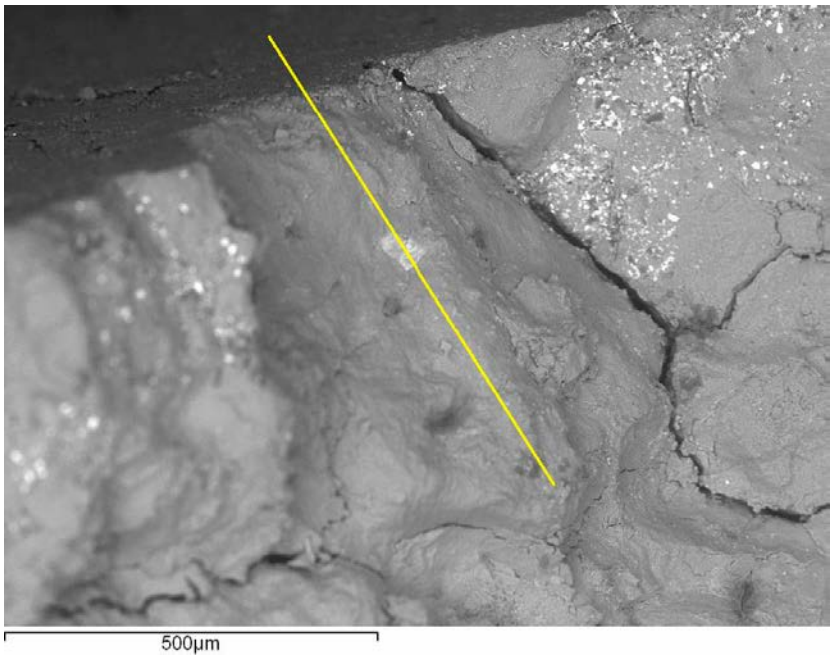
500µm

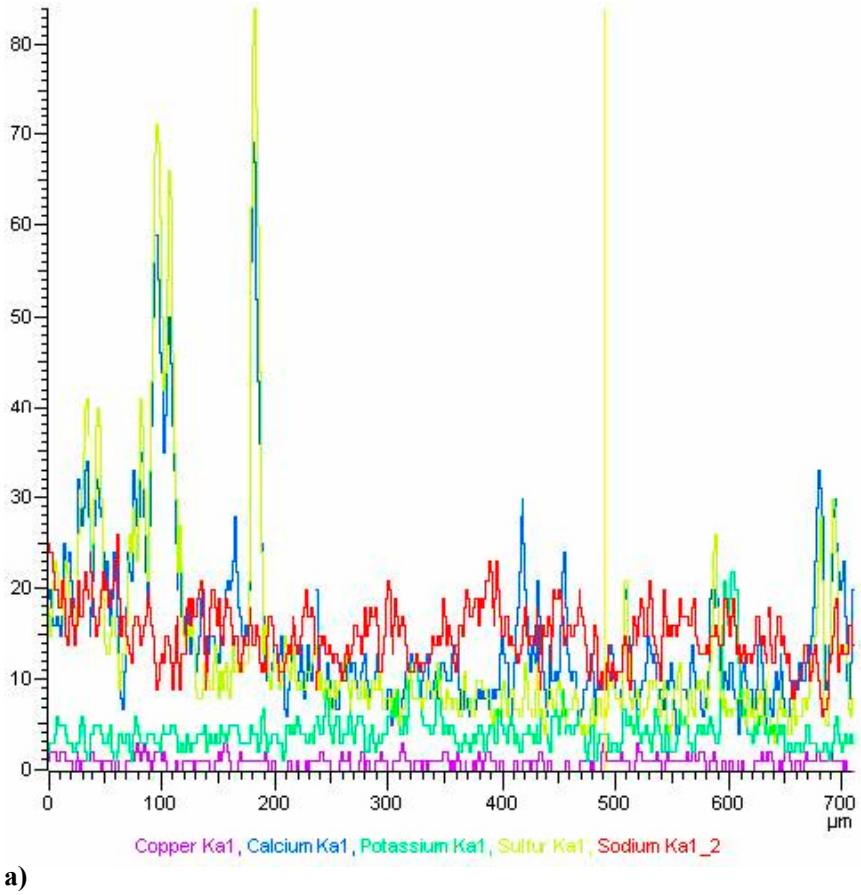
80
70
60
50
40
30
20
10
0
0
100
200
300
400
500
600
700
µm
Copper Ka1, Calcium Ka1, Potassium Ka1, Sulfur Ka1, Sodium Ka1_2

**a)**

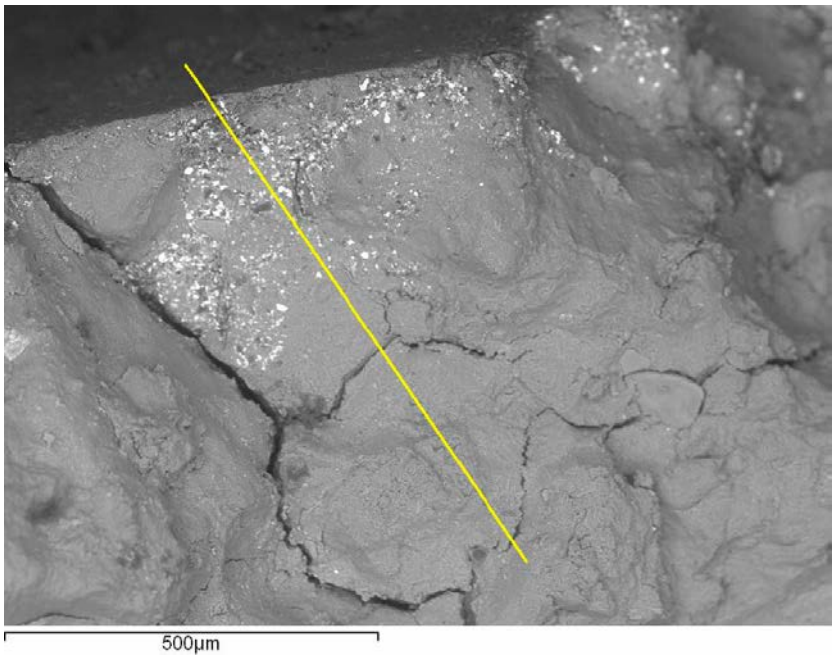


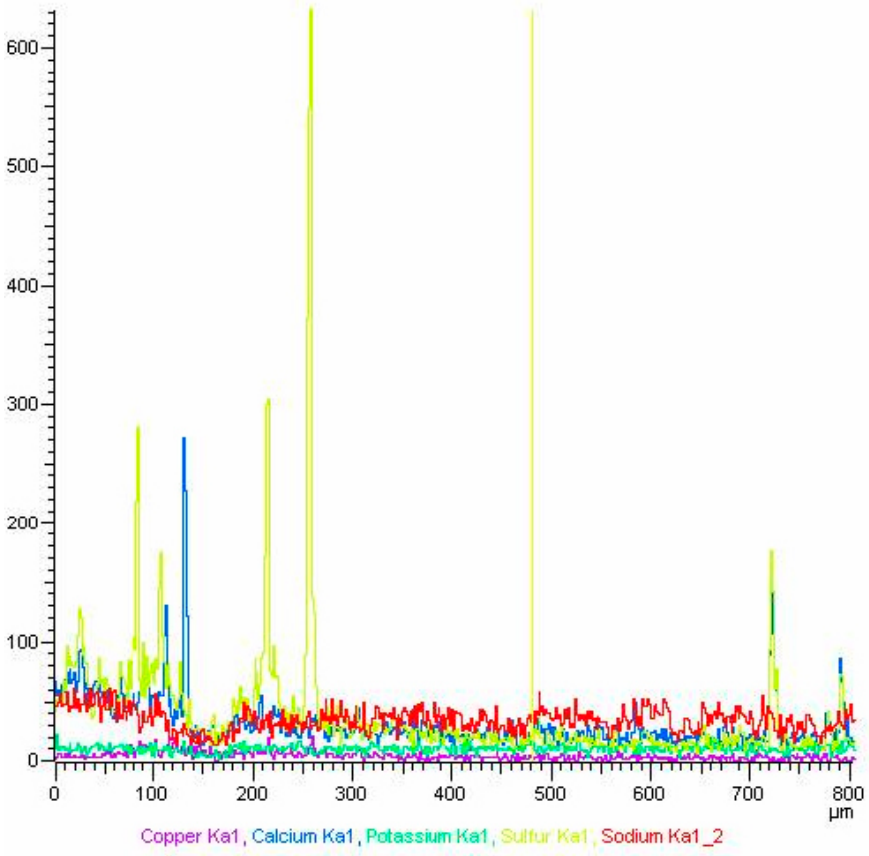


**b)**

***Figure 3-23 a and b.*** *Upper picture: Back-scatter image of the innermost part of the bentonite block P6R05 165. The dark area at the top represents the inner surface of the block. The yellow line indicates the path of the performed element line-scan. Lower diagram: the result of the line scan for some elements of interest. Note the large difference in scale of the ordinate axes.*

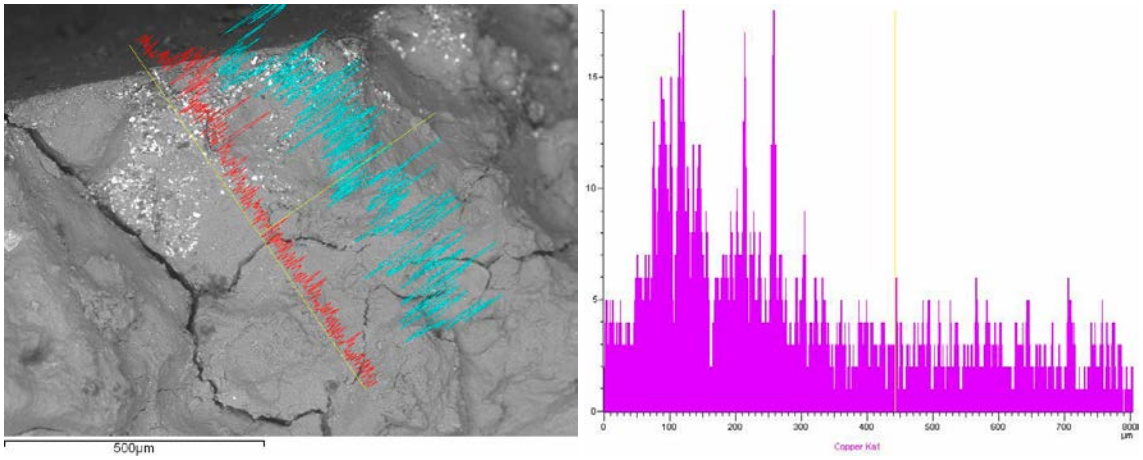


***Figure 3-24.*** *Left: Detailed results of an element line-scan along the yellow line. Red indicates copper content and turquoise represents sodium content as a reference. The scatter in sodium content is largely due to the topography of the surface and does not represent actual variation in the bentonite. Right: Plot of the copper concentration versus distance from the canister/bentonite interface.*

**Table 3-11. Results of area analyses (50 × 50 µm) at different distances from the former bentonite/ copper interface. Distance is the distance from the interface to the center of the analyzed area. Two analyses were made of the innermost area at the canister (25 A and 25 B). Contents in weight percent. Mean σ indicates the mean standard deviation of individual area analyses.**

| Distance, µm | 25 A | 25 B | 75 | 125 | 175 | mean | mean σ |
|---|---|---|---|---|---|---|---|
| **Element** | | | | | | | |
| Na | 1.7 | 1.5 | 1.7 | 1.7 | 1.9 | 1.7 | 0.20 |
| Mg | 2.3 | 2.4 | 2.7 | 2.6 | 2.6 | 2.5 | 0.16 |
| Al | 10.3 | 8.8 | 10.3 | 10.4 | 9.8 | 9.9 | 0.23 |
| Si | 28.3 | 25.5 | 28.9 | 29.2 | 27.2 | 27.8 | 0.35 |
| S | 1.8 | 4.1 | 1.6 | 1.3 | 1.8 | 2.1 | 0.15 |
| K | 0.5 | 0.2 | 0.2 | 0.3 | 0.4 | 0.3 | 0.11 |
| Ca | 1.8 | 2.9 | 1.7 | 1.6 | 2.0 | 2.0 | 0.15 |
| Ti | 0.2 | 0.1 | 0.1 | 0.1 | 0.1 | 0.1 | 0.14 |
| Fe | 3.4 | 2.7 | 3.1 | 3.0 | 4.3 | 3.3 | 0.39 |
| Cu | 1.4 | 3.4 | 1.1 | 1.1 | 2.3 | 1.9 | 0.49 |
| O | 48.4 | 48.2 | 48.7 | 48.7 | 47.6 | 48.3 | 0.62 |

### 3.3.7 FTIR

All FTIR-analyses and evaluations were performed by B+Tech, Helsinki.

FTIR patterns for bulk samples from profile P5R06 050A are shown in Figure 3-25 and for clay fractions in Figure 3-26. Band positions and the corresponding band assignments are shown in Table 3-12 and Table 3-13.

Based on the FTIR analysis, the bulk samples consist mainly of montmorillonite, which appears at wavenumbers at 3,637, 1,049, 919, 882, 851, 621, and 527 $cm^{-1}$ (Madejová and Komadel 2001, Farmer and Russell 1967, Farmer 1974). The samples 525b and 530b at the canister in profile P5R06 050A contain organic impurities appearing at wavenumbers 2,930 $cm^{-1}$ and 2,855 $cm^{-1}$. Furthermore it seems as there is a decrease in the intensity of the carbonate band at approximately 1,420 $cm^{-1}$ (Russell 1987) in samples 530b and 545b, which would be consistent with the chemical data for the inorganic carbon distribution in this block.

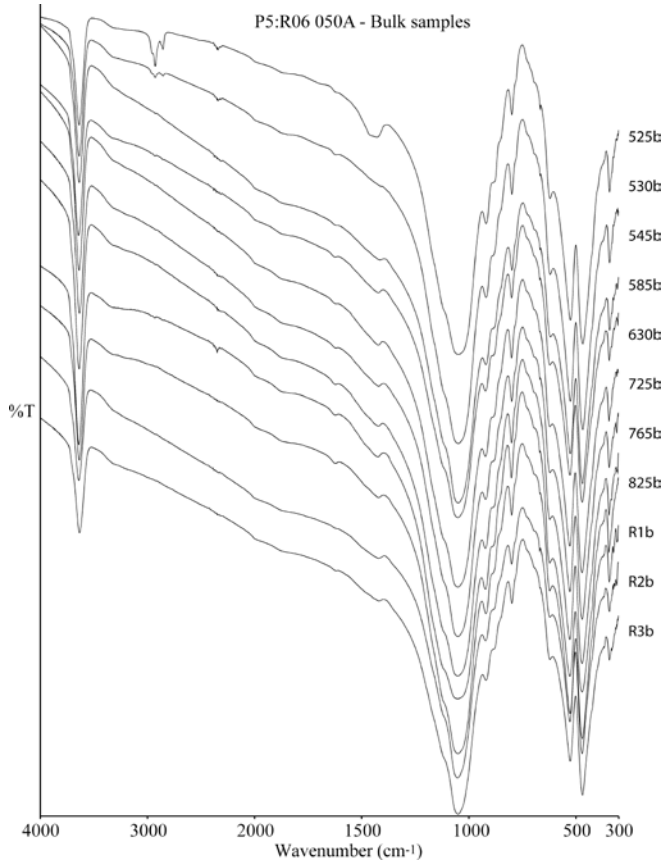


***Figure 3-25.*** *The FTIR patterns of bulk samples from block P5:R06 050A.*

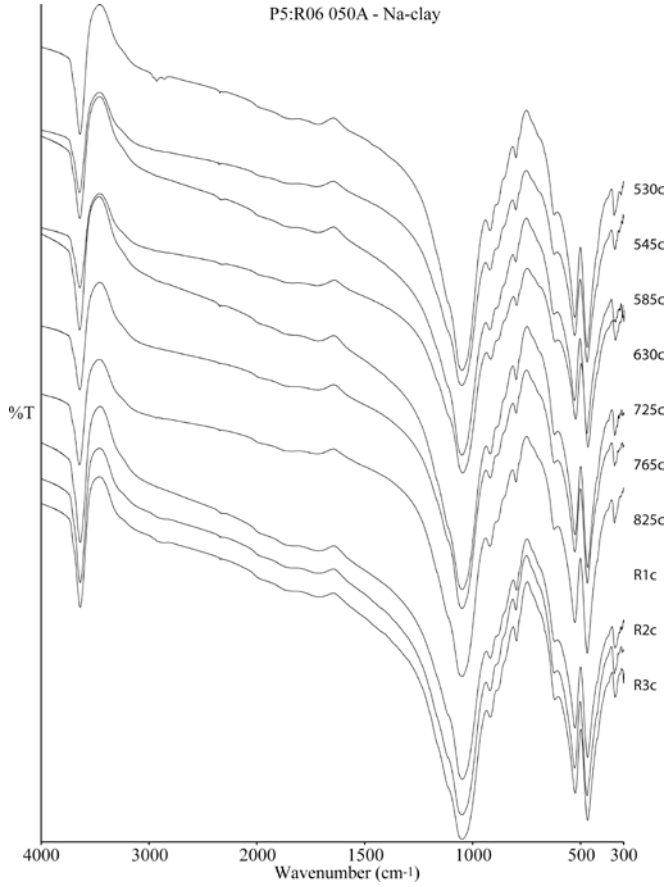


***Figure 3-26.*** *The FTIR patterns of clay fractions from profile P5R06 050A.*

**Table 3-12. The position of FTIR absorption bands of bulk samples from block P5R06 050A, and band assignments (S = smectite, Q = quartz).**

| | OH-stretching bands (S) | $H_2O$-stretching | (Organic impurities) | (Organic impurities) | $H_2O$-bending | $CO_3^{2-}$ (Carbonates) | Si-O stretching, Si-O-Si | Si-O stretching, Tetrahedral Si (S, Q) | OH-bending, AlAlOH (S) | OH-bending, AlFeOH (S), $CO_3^{2-}$ (Calcite) | OH-bending, AlMgOH (S) | Si-O stretching (Q, free Si-O) | Si-O (Q) | Si-O (Feldspars) | Si-O (S) | Coupled Al-O+Si-O bending | Si-O bending (S) | Si-O bending (S) |
|---|---|---|---|---|---|---|---|---|---|---|---|---|---|---|---|---|---|---|
| 525b | 3,638 | 3,315 | 2,927 | 2,856 | 1,620 | 1,420 | 1,119 | 1,046 | 919 | 880 | 855 | 799 | 779 | 728 | 695 | 622 | 525 | 468 |
| 530b | 3,638 | 3,338 | 2,927 | 2,857 | 1,624 | 1,413 | 1,120 | 1,048 | 919 | 885 | 851 | 799 | 780 | 729 | 696 | 621 | 526 | 468 |
| 545b | 3,637 | 3,318 | – | – | 1,622 | 1,414 | 1,119 | 1,051 | 919 | 881 | 851 | 798 | 779 | 728 | 696 | 620 | 527 | 470 |
| 585b | 3,637 | 3,324 | – | – | 1,622 | 1,420 | 1,119 | 1,048 | 920 | 883 | 850 | 798 | 779 | 728 | 695 | 621 | 526 | 469 |
| 630b | 3,637 | 3,338 | – | – | 1,624 | 1,420 | 1,120 | 1,048 | 920 | 881 | 852 | 798 | 779 | 727 | 695 | 620 | 527 | 469 |
| 725b | 3,636 | 3,320 | – | – | 1,622 | 1,420 | 1,118 | 1,050 | 920 | 881 | 851 | 798 | 779 | 728 | 695 | 622 | 527 | 469 |
| 765b | 3,636 | 3,324 | – | – | 1,622 | 1,421 | 1,119 | 1,048 | 920 | 881 | 851 | 798 | 779 | 729 | 696 | 622 | 527 | 469 |
| 825b | 3,637 | 3,329 | – | – | 1,622 | 1,422 | 1,120 | 1,051 | 920 | 884 | 853 | 799 | 779 | 729 | 696 | 620 | 527 | 469 |
| R1b | 3,635 | 3,338 | – | – | 1,624 | 1,420 | 1,119 | 1,048 | 919 | 883 | 850 | 798 | 780 | 728 | 695 | 621 | 526 | 469 |
| R2b | 3,637 | 3,320 | – | – | 1,620 | 1,420 | 1,118 | 1,051 | 919 | 881 | 850 | 798 | 779 | 728 | 696 | 621 | 527 | 469 |
| R3b | 3,638 | 3,333 | – | – | 1,622 | 1,420 | 1,119 | 1,048 | 918 | 879 | 850 | 798 | 779 | 728 | 696 | 622 | 526 | 468 |

**Table 3-13. The position of FTIR absorption bands of clay fractions from block P5R06 050A, and band assignments. S = smectite, Q = quartz, nd = not determined (sample missing).**

| | OH-stretching bands (S) | $H_2O$-stretching | (Organic impurities) | (Organic impurities) | $H_2O$-bending | $CO_3^{2-}$ (Carbonates) | Quartz, Cristobalite, Plagioclase | Si-O stretching, Si-O-Si | Si-O stretching, Tetrahedral Si (S, Q) | OH-bending, AlAlOH (S) | OH-bending, AlFeOH (S) | OH-bending, AlMgOH (S) | Si-O stretching (Q, free Si-O) | Si-O (Q) | Si-O (Feldspars) | Si-O (S) | Coupled AlO+Si-O bending | Si-O bending (S) | Si-O bending (S) |
|---|---|---|---|---|---|---|---|---|---|---|---|---|---|---|---|---|---|---|---|
| 525c | nd | nd | nd | nd | nd | nd | nd | nd | nd | nd | nd | nd | nd | nd | nd | nd | nd | nd | nd |
| 530c | 3,640 | – | 2,927 | 2,845 | – | – | – | 1,117 | 1,046 | 919 | 883 | 848 | 799 | 779 | 729 | 696 | 623 | 526 | 469 |
| 545c | 3,641 | – | – | – | – | – | – | 1,122 | 1,049 | 919 | 880 | 846 | 799 | 779 | 730 | 694 | 621 | 526 | 469 |
| 585c | 3,641 | – | – | – | – | – | – | 1,119 | 1,046 | 919 | 878 | 846 | 799 | – | – | – | 625 | 526 | 468 |
| 630c | 3,642 | – | – | – | – | – | – | 1,122 | 1,049 | 919 | 878 | 853 | 799 | 780 | 730 | 691 | 623 | 526 | 469 |
| 725c | 3,640 | – | – | – | – | – | – | 1,119 | 1,049 | 919 | 880 | 848 | 799 | 778 | 727 | 691 | 623 | 526 | 469 |
| 765c | 3,641 | – | – | – | – | – | – | 1,117 | 1,046 | 919 | 880 | 841 | 799 | 779 | 727 | 696 | 623 | 526 | 468 |
| 825c | 3,640 | – | – | – | – | – | – | 1,115 | 1,048 | 920 | 878 | 846 | 799 | 779 | 728 | 701 | 621 | 526 | 469 |
| R1c | 3,640 | – | – | – | – | – | – | 1,119 | 1,046 | 920 | 880 | 848 | 799 | 776 | 726 | 697 | 623 | 527 | 469 |
| R2c | 3,640 | – | – | – | – | – | – | 1,119 | 1,046 | 919 | 880 | 846 | 799 | 779 | 728 | 696 | 621 | 526 | 468 |
| R3c | 3,640 | – | – | – | – | – | – | 1,119 | 1,046 | 920 | 880 | 848 | 799 | 780 | 727 | 689 | 619 | 526 | 469 |

The clay fractions of P5R06 050A consist mainly of montmorillonite, which appear at wavenumbers at 3,640, 1,047, 919, 880, 847, 622, and 526 $cm^{-1}$ (Madejová and Komadel 2001, Farmer and Russell 1967, Farmer 1974). No differences were noted in smectite FTIR band intensities or positions in the clay fractions (Figure 3-26, Table 3-13). Thus, no change in clay mineralogy or smectite composition was noted. However, in almost all clay fractions of profile P5R06 050A, the quartz bands at wavenumber 780 and 799 $cm^{-1}$ are visible indicating that some quartz is present despite of the purification process (Madejová and Komadel 2001, Russell 1987). The different shape of the FTIR patterns (at approximate wavenumbers 3,400 $cm^{-1}$ and 1,600 $cm^{-1}$) of clay fractions compared to the FTIR patterns of bulk samples is due to an erroneous background calibration for the clay fractions with moist KBr disc.

FTIR patterns of bulk samples from block P6R05 165B are shown in Figure 3-27 and of clay fractions in Figure 3-28. Band positions and the corresponding band assignments are shown in Tables 3-14 and 3-15.

The bulk samples from P6R05 165B consist mainly of montmorillonite, which has bands at wavenumbers 3,636, 1,049, 917, 879, 848, 618, and 525 $cm^{-1}$ (Madejová and Komadel 2001, Farmer and Russell 1967, Farmer 1974). As before, bulk samples of block P6R05 165B show an increase in the intensity of organic impurities in samples 525b, 530b, and maybe also in 825b, which correspond to the inner and outer parts of the profile. These parts of the block were contaminated by the lubricant used in the block production. The organic impurities appear at wavenumbers of 2,930 $cm^{-1}$ and 2,850 $cm^{-1}$. The smaller transmissivity of the R2b sample in the region 4,000–2,000 $cm^{-1}$ (shape of FTIR pattern different from the rest of the samples) is caused by a preparation error of the KBr disc. The disc of R2b was clearly less transparent than other sample discs.

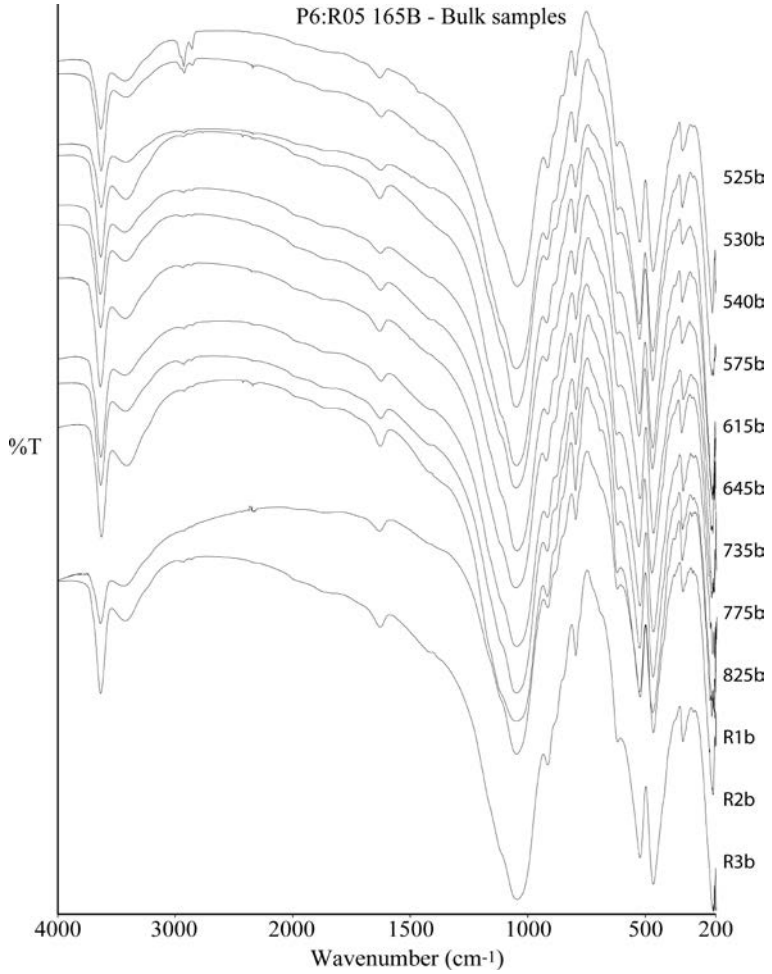


***Figure 3-27.*** *The FTIR patterns of bulk samples from block P6R05 165B.*

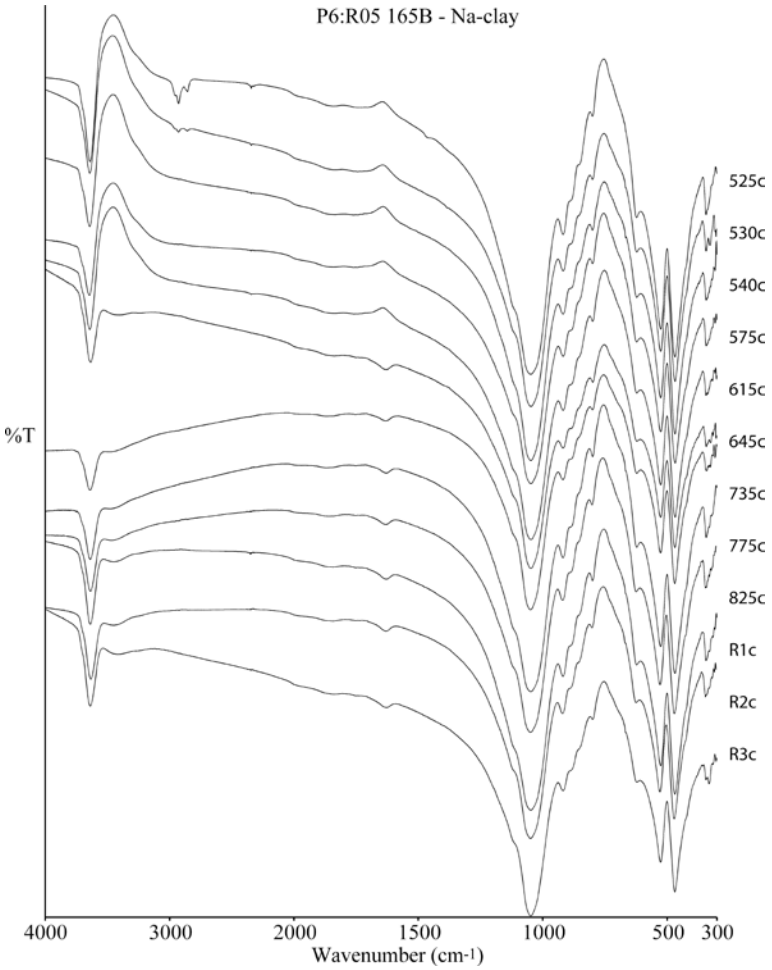


***Figure 3-28.*** *The FTIR patterns of clay fractions from block P6R05 165B.*

**Table 3-14. The position of FTIR absorption bands of bulk samples from block P6:R05 165B, and band assignments (S = smectite).**

| | OH-stretching bands (S) | $H_2O$-stretching | (Organic impurities) | (Organic impurities) | $H_2O$-bending | $CO_3^{2-}$ (Carbonates) | Si-O stretching, Si-O-Si | Si-O stretching, Tetrahedral Si (S, Q) | OH-bending, AlAlOH (S) | OH-bending, AlFeOH (S), $CO_3^{2-}$ (Calcite) | OH-bending, AlMgOH (S) | Si-O stretching (Quartz, Cristobalite, free Si-O) | Si-O (Quartz) | Si-O (Feldspars) | Si-O (S) | Coupled AlO+Si-O bending | Si-O bending (S) | Si-O bending (S) |
|---|---|---|---|---|---|---|---|---|---|---|---|---|---|---|---|---|---|---|
| 525b | 3,634 | 3,414 | 2,928 | 2,855 | 1,627 | 1,464 | 1,117 | 1,044 | 915 | 880 | 845 | 798 | 776 | 729 | 691 | 618 | 523 | 467 |
| 530b | 3,637 | 3,404 | 2,930 | 2,851 | 1,624 | 1,419 | 1,112 | 1,051 | 916 | 876 | 849 | 798 | 778 | 717 | 688 | 618 | 526 | 469 |
| 540b | 3,636 | 3,414 | 2,927 | 2,865 | 1,627 | 1,417 | 1,114 | 1,051 | 916 | 880 | 849 | 798 | 776 | 724 | 696 | 620 | 526 | 468 |
| 575b | 3,636 | 3,419 | 2,927 | 2,851 | 1,631 | 1,431 | 1,114 | 1,047 | 918 | 883 | 849 | 798 | 776 | 728 | 691 | 615 | 525 | 468 |
| 615b | 3,637 | 3,404 | 2,917 | 2,846 | 1,624 | 1,421 | 1,114 | 1,048 | 916 | 880 | 846 | 798 | 778 | 729 | 694 | 620 | 525 | 468 |
| 645b | 3,636 | 3,418 | 2,931 | 2,851 | 1,629 | 1,414 | 1,112 | 1,048 | 916 | 876 | 840 | 798 | 776 | 727 | 689 | 620 | 525 | 468 |
| 735b | 3,634 | 3,429 | 2,927 | 2,856 | 1,628 | 1,424 | 1,116 | 1,048 | 911 | 876 | 847 | 798 | 776 | 727 | 694 | 620 | 525 | 468 |
| 775b | 3,637 | 3,433 | 2,927 | 2,851 | 1,627 | 1,424 | 1,114 | 1,051 | 916 | 878 | 847 | 798 | 776 | 729 | 691 | 616 | 526 | 469 |
| 825b | 3,636 | 3,435 | 2,921 | 2,856 | 1,629 | 1,421 | 1,117 | 1,048 | 918 | 878 | 847 | 798 | 776 | 727 | 696 | 616 | 526 | 468 |
| R1b | 3,634 | 3,419 | 2,927 | 2,851 | 1,630 | 1,428 | 1,116 | 1,047 | 917 | 880 | 843 | 798 | 774 | 729 | 689 | 618 | 524 | 468 |
| R2b | 3,636 | 3,423 | 2,917 | 2,851 | 1,631 | 1,426 | 1,121 | 1,048 | 913 | 878 | 845 | 798 | 776 | 724 | 696 | 620 | 524 | 467 |
| R3b | 3,634 | 3,429 | 2,927 | 2,851 | 1,630 | 1,421 | 1,114 | 1,047 | 917 | 878 | 850 | 798 | 774 | 727 | 689 | 616 | 524 | 468 |

**Table 3-15. The position of FTIR absorption bands of studied clay fractions from block P6:R05 165B, and band assignments (S = smectite).**

| | OH-stretching bands (S) | $H_2O$-stretching | (Organic impurities) | (Organic impurities) | $H_2O$-bending | $CO_3^{2-}$ (Carbonates) | Si-O stretching, Si-O-Si | Si-O stretching, Tetrahedral Si (S, Q) | OH-bending, AlAlOH (S) | OH-bending, AlFeOH (S), | OH-bending, AlMgOH (S) | Si-O stretching (Cristobalite, free Si-O) | Si-O (Quartz) | Si-O (S) | Coupled Al-O+Si-O bending (S) Si-O Cristobalite | Si-O bending (S) | Si-O bending (S) |
|---|---|---|---|---|---|---|---|---|---|---|---|---|---|---|---|---|---|
| 525c | 3,639 | – | 2,927 | 2,849 | – | – | 1,119 | 1,047 | 918 | 880 | 846 | 796 | – | – | 619 | 525 | 468 |
| 530c | 3,641 | – | 2,927 | 2,856 | – | – | 1,124 | 1,046 | 917 | 878 | 848 | 799 | – | – | 621 | 525 | 468 |
| 540c | 3,641 | – | – | – | – | – | 1,117 | 1,044 | 918 | 878 | 846 | 796 | – | – | 623 | 526 | 468 |
| 575c | 3,642 | – | – | – | – | – | 1,122 | 1,044 | 918 | 876 | 846 | 796 | – | – | 621 | 525 | 468 |
| 615c | 3,641 | – | – | – | – | – | 1,119 | 1,046 | 918 | 883 | 846 | 794 | – | – | 623 | 526 | 468 |
| 645c | 3,635 | 3,420 | – | – | 1,627 | – | 1,117 | 1,047 | 914 | 876 | 848 | 796 | – | – | 623 | 526 | 468 |
| 735c | 3,636 | 3,425 | – | – | 1,627 | – | 1,119 | 1,048 | 917 | 880 | 848 | 796 | – | – | 621 | 526 | 469 |
| 775c | 3,637 | 3,447 | – | – | 1,622 | – | 1,119 | 1,048 | 918 | 880 | 848 | 799 | – | – | 621 | 526 | 468 |
| 825c | 3,637 | 3,425 | – | – | 1,634 | – | 1,119 | 1,047 | 918 | 880 | 844 | 796 | – | – | 621 | 526 | 468 |
| R1c | 3,636 | 3,445 | – | – | 1,625 | – | 1,117 | 1,047 | 918 | 878 | 851 | 799 | – | – | 621 | 525 | 468 |
| R2c | 3,636 | 3,438 | – | – | 1,631 | – | 1,119 | 1,047 | 917 | 883 | 846 | 796 | – | – | 621 | 526 | 468 |
| R3c | 3,635 | 3,438 | – | – | 1,631 | – | 1,115 | 1,047 | 918 | 880 | 851 | 794 | – | – | 623 | 526 | 469 |

The clay fractions of P6R05 165B consist mainly of montmorillonite, which appear at wavenumbers at 3,637, 1,047, 918, 880, 846, 621, and 526 $cm^{-1}$. In addition to montmorillonite, also amorphous silica or cristobalite is present, appearing at wavenumber 798 $cm^{-1}$ (Madejová and Komadel 2001). Compared to the reference samples, the only difference that was noted in FTIR patterns of clay fractions from block P6R05 165B, was that the two samples 525c and 530c closest to the canister contact contained the same 2,930 $cm^{-1}$, and at 2,850 $cm^{-1}$ bands as the bulk samples, arising from organic impurities (Figure 3-28, Table 3-15). No change in clay mineralogy or smectite composition was noted. The difference in shape of FTIR patterns of samples 525c–615c compared to the FTIR patterns of samples 645c–Rc3 is due to the erroneous calibration of background of the first 5 samples (525c–615c) with moist KBr disc.

### 3.3.8 Mössbauer spectroscopy

The fitted Mössbauer spectra for samples from P6:R05 165D and P5:R10 270C profiles are displayed in Figure 3-29. Johan Lindén, Åbo Akademi, whose complete report is presented in Appendix 1, provided the fittings and the major part of the discussion. The five components used for the analysis, all corresponding to various Fe species, are shown in the spectra. The magnetic sextet (Component 4) and the paramagnetic Component 5 were not visible in all spectra and hence, were included only when possible to fit to the data. The parameters of the fits are presented in Table 3-16.

The largest components in the measured Mössbauer spectra, i.e. Components 1, 2 and 3, were assigned to iron in clay minerals, Component 1 for $Fe^{2+}$ and Components 2 and 3 for $Fe^{3+}$ (Hogarth et al. 1970, Wagner and Wagner 2004). $Fe^{3+}$ and $Fe^{2+}$ in clay minerals can easily be distinguished by their isomer shifts and quadrupole splittings (Wagner and Wagner 2004). Tetrahedral and octahedral $Fe^{3+}$ also differs slightly in isomer shifts (Wagner and Wagner 2004). However, due to several possible locations/environments, where $Fe^{3+}$ or $Fe^{2+}$ can be located in clay minerals and because clay minerals occur commonly as mixtures, usually a distribution of ill resolved quadrupole doublets can be observed for both trivalent and divalent iron in clay minerals (Wagner and Wagner 2004).

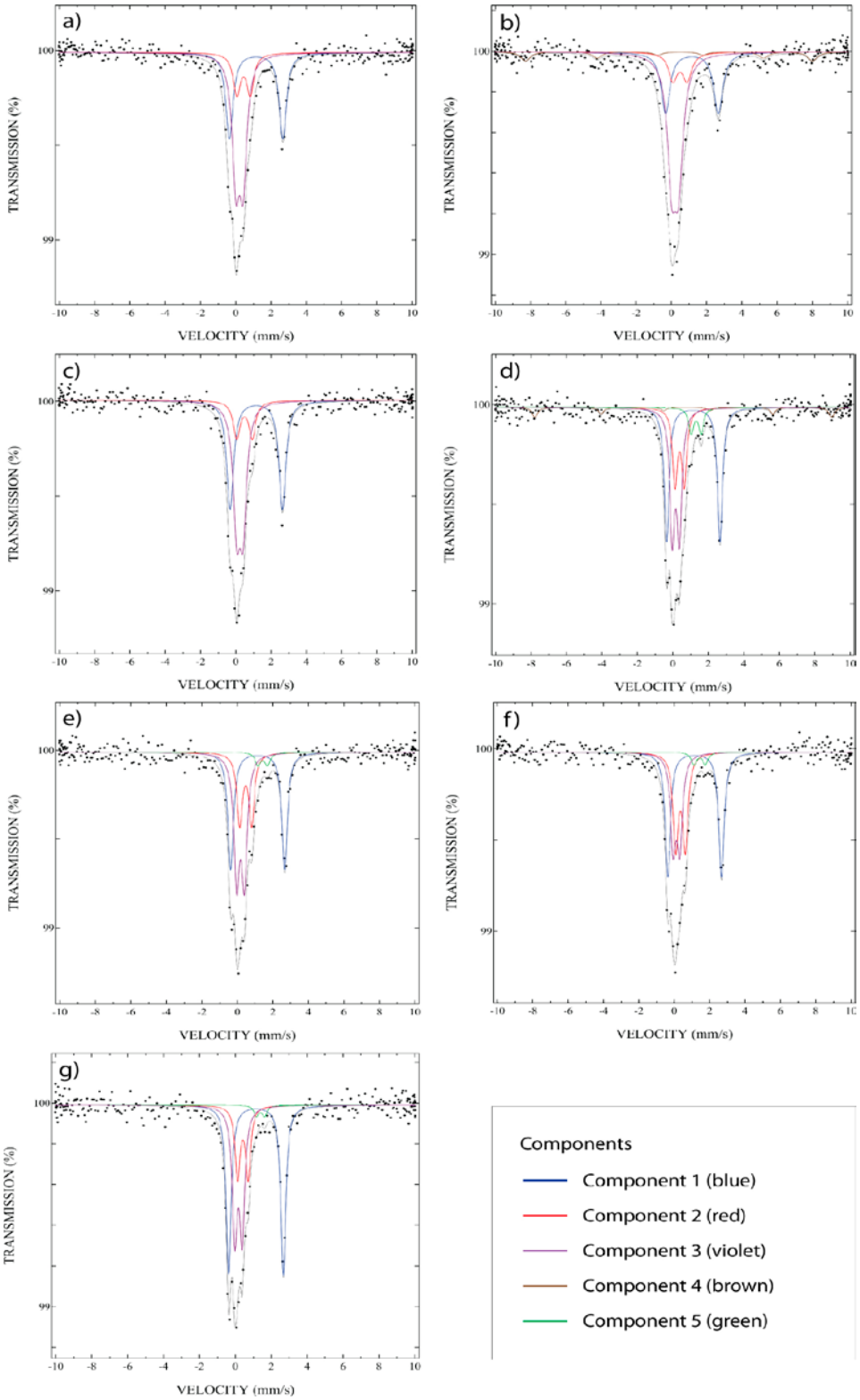


***Figure 3-29.*** *Mössbauer spectrum recorded from sample a) P6R05 R1b, b) P6R05 R2b, c) P6R05165D 535b, d) P6R05 165D 555b, e) P6R05 165D 575b, f) P6R05 165D 615b, and g) P5R10 270C 525b at 77 K. Components of the fit are displayed above the spectrum.*

**Table 3-16. Hyperfine parameters.**

| Sample | Component | I (%) | Δ (mm/s) | δ (mm/s) | B (T) | Γ (mm/s) |
|---|---|---|---|---|---|---|
| P6R05 Rb-1 | Component 1 | 35.0 | 3.017 | 1.265 | – | 0.489 |
| | Component 2 | 16.5 | 0.75 | 0.55 | – | 0.489 |
| | Component 3 | 48.5 | 0.40 | 0.32 | – | 0.489 |
| | Component 4 | – | – | – | – | – |
| | Component 5 | – | – | – | – | – |
| P6R05 Rb-2 | Component 1 | 27.9 | 2.996 | 1.271 | – | 0.608 |
| | Component 2 | 12.5 | 0.80 | 0.60 | – | 0.608 |
| | Component 3 | 51.3 | 0.39 | 0.33 | – | 0.608 |
| | Component 4 | 8(1) | –0.6(1) | 0.29 | 50(1) | 0.608 |
| | Component 5 | – | – | – | – | – |
| P6R05 165D 535b | Component 1 | 41.5 | 2.954 | 1.272 | – | 0.465 |
| | Component 2 | 14.1 | 0.87 | 0.60 | – | 0.465 |
| | Component 3 | 44.4 | 0.35 | 0.34 | – | 0.465 |
| | Component 4 | – | – | – | – | – |
| | Component 5 | – | – | – | – | – |
| P6R05 165D 555b | Component 1 | 35.3 | 3.012 | 1.258 | – | 0.330 |
| | Component 2 | 19.6 | 0.51 | 0.49 | – | 0.330 |
| | Component 3 | 32.6 | 0.40 | 0.28 | – | 0.330 |
| | Component 4 | 6(1) | –0.2(1) | 0.80 | 52(1) | 0.330 |
| | Component 5 | 6.7 | 0.55 | 1.41 | – | 0.330 |
| P6R05 165D 575b | Component 1 | 36.3 | 3.030 | 1.253 | – | 0.370 |
| | Component 2 | 21.8 | 0.67 | 0.58 | – | 0.370 |
| | Component 3 | 37.9 | 0.53 | 0.29 | – | 0.370 |
| | Component 4 | – | – | – | – | – |
| | Component 5 | 4.0 | 0.42 | 1.54 | – | 0.370 |
| P6R05 165D 615b | Component 1 | 39.0 | 3.036 | 1.255 | – | 0.362 |
| | Component 2 | 29.0 | 0.53 | 0.46 | – | 0.362 |
| | Component 3 | 28.1 | 0.37 | 0.23 | – | 0.362 |
| | Component 4 | – | – | – | – | – |
| | Component 5 | 3.9 | 0.65 | 1.54 | – | 0.362 |
| P5R10 270C 525b | Component 1 | 44.7 | 3.033 | 1.259 | – | 0.328 |
| | Component 2 | 18.9 | 0.58 | 0.53 | – | 0.328 |
| | Component 3 | 33.6 | 0.40 | 0.28 | – | 0.328 |
| | Component 4 | – | – | – | – | – |
| | Component 5 | 2.8 | 0.46 | 1.51 | – | 0.328 |

Component 4, i.e. the magnetically split component, may be a combination of the spectra of e.g. maghemite, hematite, goethite and magnetite (Cornell and Schwertmann 2003). Due to low amount of these phases, they cannot be resolved from the background of the collected Mössbauer spectra.

Some other $Fe^{2+}$-containing mineral in the sample materials can cause component 5.

Assuming the recoil-free fraction to be the same for all components, the valence ratio ($Fe^{2+}/Fe^{3+}$) is the intensity of components 1 + 5 to that of components 2 + 3 (intensities are presented in Table 3-16). In the same way, the $Fe^{2+}$/Fe-total ratio is the intensity of components 1 + 5 to that of components 1 + 2 + 3 + 5. The ratio of paramagnetic $Fe^{2+}$ to $Fe^{3+}$ and the ratio of paramagnetic $Fe^{2+}$ to total paramagnetic Fe are presented in Table 3-17. It is assumed that pyrite ($Fe^{2+}$), which has similar quadrupole splitting and isomer shift values as Components 2 and 3 (Evans et al. 1982), has no significant effect on components 2 and 3. The latter components were assigned to $Fe^{3+}$.

The main difference in the spectra is the lower portion of Component 1 in the reference spectra (Figure 3-29). According to the chemical analyses the total amount of iron has not changed noticeably. Hence, the Mössbauer results indicate that part of the $Fe^{3+}$ originally present in the samples of the buffer blocks has been reduced to $Fe^{2+}$under the test conditions.

**Table 3-17. Ratio $Fe^{2+}/Fe^{3+}$ and $Fe^{2+}$/Fe-total**

| Sample | $Fe^{2+}/Fe^{3+}$ (paramagnetic only, components 1, 2, 3, 5) | $Fe^{2+}$/Fe-total (paramagnetic only, components 1, 2, 3, 5) |
|---|---|---|
| P6R05 Rb-1 | 0.538 | 0.350 |
| P6R05 Rb-2 | 0.437 | 0.304 |
| P6R05 165D 535b | 0.709 | 0.415 |
| P6R05 165D 555b | 0.805 | 0.446 |
| P6R05 165D 575b | 0.675 | 0.403 |
| P6R05 165D 615b | 0.751 | 0.429 |
| P5R10 270C 525b | 0.905 | 0.475 |

## 3.4 Results for profiles P5R06 250 and P6R08 355

### 3.4.1 Visual observations

Some visual observations were made during sampling. At the canister contact the bentonite buffer had a black or bluish glossy color (Figure 3-30b), which was assumed to be remnants of the lubricant used in the compression of buffer blocks. On the canister contact also white spots were noted (Figure 3-30c), which were assumed to be precipitated salts. A light brownish color appeared in the sawed surface of the bentonite within approximately 3-4 mm from the canister contact (Figure 3-30d).

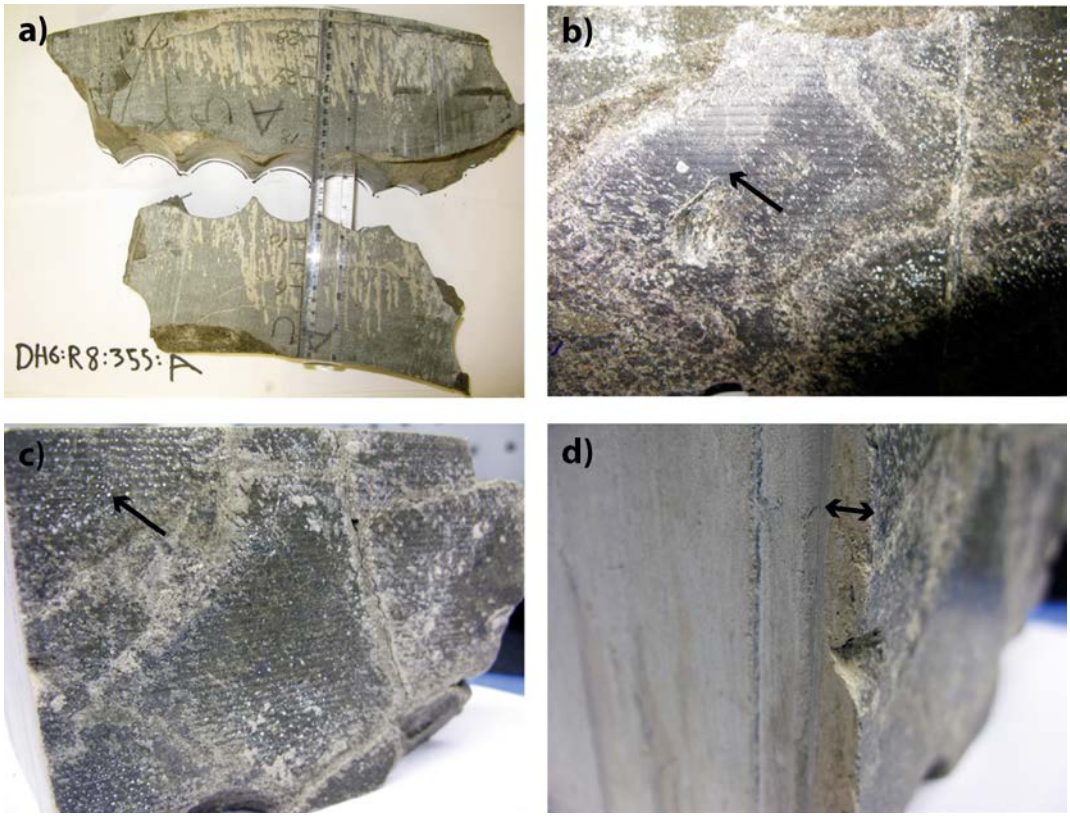


***Figure 3-30.*** *a) Buffer profile P6:R08 355A b) black lubricant at the canister contact c) white salt formations/spots at the canister contact. d) light brownish zone at the canister contact.*

### 3.4.2 Aqueous leachates

**Block P5:R06 250B**

The sector 250 of block P5:R06 was not fully water saturated at the retrieval and based on analyses of water soluble sulfate and chloride of the profile, there were no changes in the block samples compared to the reference samples (Table 3-18, Figure 3-31).

**Block P6:R08 355A**

Water-soluble sulfate had increased significantly from 3.5 mg/g (of dry clay) in reference samples to 17 mg/g (of dry clay) in sample 525b closest to the canister (Table 3-19, Figure 3-32). In other samples the level of water-soluble sulfate contents had remained the same as in reference samples.

The chloride content had clearly increased in the whole profile (0.31–0.52 mg/g) compared to the reference samples (0.05–0.09 mg/g) and the content of chloride was highest in the second innermost sample of the profile (sample 527b). The increase in Cl content was thought to indicate that P6:R08 355A buffer profile was saturated (at least to some level) with Äspö groundwater.

**Table 3-18. Water-soluble, major anions of bulk samples from profile P5:R06 250B.**

| Sample | $SO_4$ (mg/g) | Cl (mg/g) |
|---|---|---|
| 525b | 4.01 | 0.100 |
| 530b | 3.68 | 0.137 |
| 545b | 3.91 | 0.119 |
| 600b | 2.98 | 0.110 |
| 640b | 3.08 | 0.133 |
| 730b | 3.72 | 0.102 |
| 770b | 3.51 | 0.099 |
| 830b | 4.01 | 0.133 |
| R1b | 3.06 | 0.062 |
| R2b | 3.11 | 0.132 |

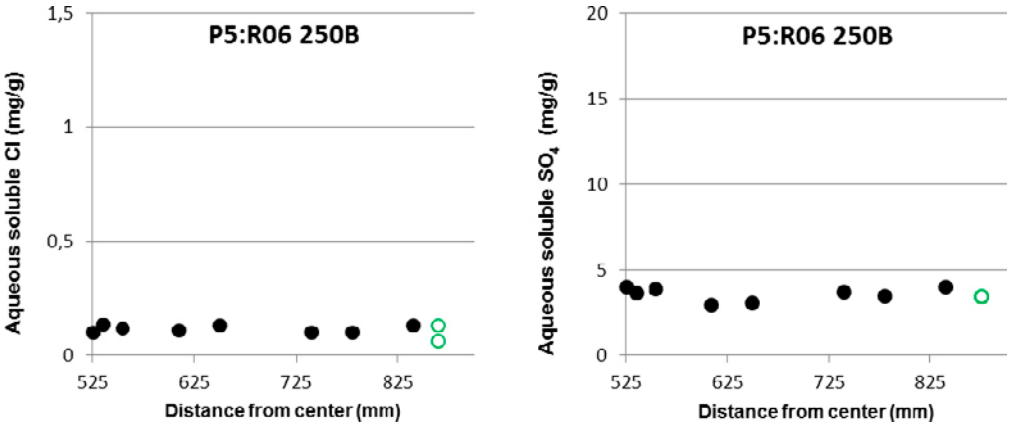


***Figure 3-31.*** *Water-soluble anions in bulk samples of P5:R06 250B plotted versus distance from the canister center. Reference samples are presented as green circles in the right end of the profile.*

**Table 3-19. Water-soluble, major anions of bulk samples from profile P6:R08 355A.**

| Sample | $SO_4$ (mg/g) | Cl (mg/g) |
|---|---|---|
| 525b | 17.2 | 0.335 |
| 527b | 2.65 | 0.515 |
| 574b | 3.47 | 0.360 |
| 620b | 3.61 | 0.384 |
| 735b | 3.79 | 0.352 |
| 786b | 2.35 | 0.311 |
| 837b | 2.83 | 0.342 |
| 846b | 3.88 | 0.369 |
| R1b | 3.49 | 0.054 |
| R2b | 3.46 | 0.088 |

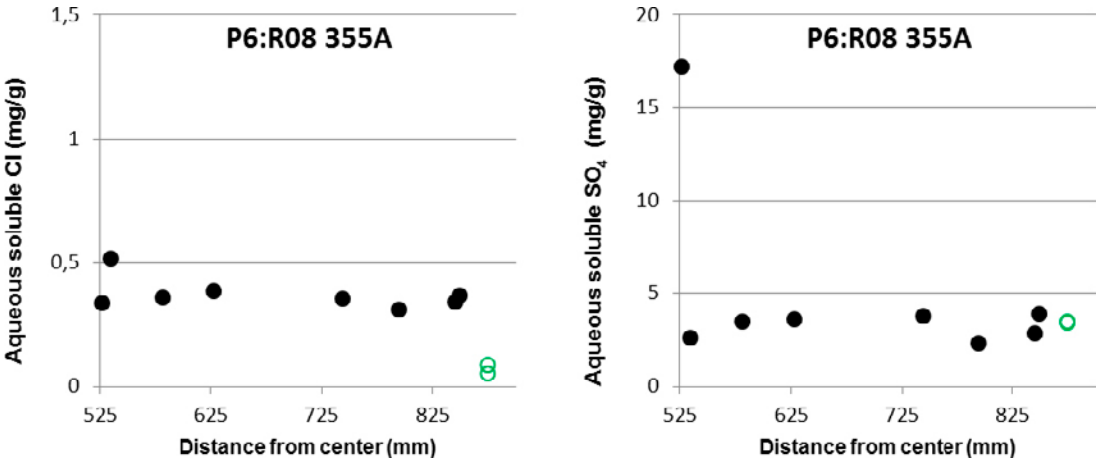


***Figure 3-32.*** *Water-soluble anions in bulk samples from P6:R08 355A plotted versus distance from the canister center. Reference samples are presented as green circles in the right end of the profile.*

### 3.4.3 Cation exchange capacity (CEC)

**Block P5:R06 250B**

The results of CEC determinations for samples of profile P5:R06 250B are shown in Table 3-20 and in Figure 3-33.

While CEC of the bulk samples 530–830 was more or less constant (mean 85.5, st.dev. 0.5), the values were on average 4 meq/100 g lower than CEC of the reference samples. This difference is larger than the normal scatter in the CEC determination on MX80 and suggests that an actual difference in CEC might exist between the block samples and the references. The CEC of the sample next to the heater (525) is considered to be uncertain due to the lubricant contamination in the sample.

In contrast, no significant change was observed in CEC of the < 0.5 µm fractions, which is more or less constant and basically the same as CEC of the references for the block. Hence, there are no indications that CEC of the smectite has changed. However, the fact that similar, contradictory CEC results were observed for block P6R05 (Section 3.3.2) calls for further investigation to establish the cause of this different trend in CEC of the bulk bentonite and of the purified smectite.

**Table 3-20. Cation exchange capacities for profile P5:R06 250B. nd = not determined.**

| Sample | Bulk Cu-trien [meq/100 g] | Clay Cu-trien [meq/100 g] |
|---|---|---|
| 525 | 89.8 | nd |
| 530 | 84.7 | 93.6 |
| 545 | 84.9 | 94.5 |
| 600 | 85.7 | 94.5 |
| 640 | 86.1 | 94.0 |
| 730 | 85.5 | 93.7 |
| 770 | 85.6 | 93.5 |
| 830 | 85.8 | 93.4 |
| R1 | 90.7 | 93.2 |
| R2 | 89.7 | 93.6 |

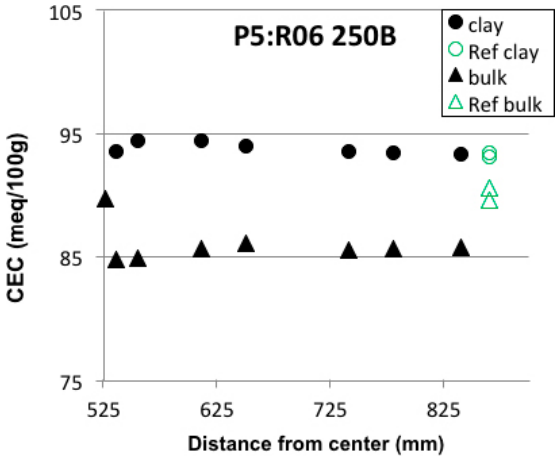


***Figure 3-33.*** *CEC values for P5R06 250B plotted versus distance from the canister center. Reference samples are presented as green circles in the right end of the profile.*

### Block P6:R08 355A

The results of the CEC determinations on the samples of P6:R08 355A are shown in Table 3-21 and in Figure 3-34. Again, CEC of the bulk samples 527–846 was more or less constant (mean value 85.1, st.dev. 0.5 meq/100 g), but somewhat lower than the CEC of the reference sample, although the difference was smaller than in block P5:R06, on average 2.5 meq/100 g. The innermost bulk sample 525b showed a decrease in CEC from 87 meq/100 g to 80 meq/100 g. However, the sum of exchangeable cations (see Table 3-23) was the same for all samples from the profile as well as for the reference samples. Such a clear difference in the CEC values and the exchangeable cation sums indicates that there is uncertainty in CEC value of sample 525b. A potential cause of the inconsistent result is the lubricant, which may have interfered with the CEC determination.

Also in this block, CEC-values of the < 0.5 µm fractions were rather constant and essentially the same as the reference CEC for the block.

**Table 3-21. Cation exchange capacities for profile P6R08 355A. nd = not determined.**

| Sample | Bulk Cu-trien [meq/100 g] | Clay Cu-trien [meq/100 g] |
|---|---|---|
| 525 | 79.9 | 91.9 |
| 527 | 85.5 | 93.9 |
| 574 | 85.7 | 94.2 |
| 620 | 85.4 | 94.0 |
| 735 | 84.7 | 94.6 |
| 786 | 84.3 | 93.6 |
| 837 | 85.5 | 92.8 |
| 846 | 84.8 | 92.7 |
| R1 | 87.6 | 92.6 |
| R2 | nd | nd |

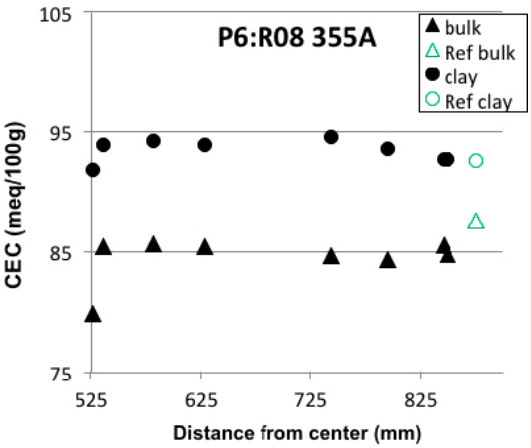


***Figure 3-34.*** *CEC values for P6:R08 355A plotted versus distance from the center. Reference samples are presented as green circles in the right end of the profile.*

### 3.4.4 Exchangeable cations

**Block P5:R06 250B**

Results of the exchangeable cation extractions for samples from profile P5:R06 250B are shown in Table 3-22 and in Figure 3-35.

In the sample taken from the canister contact (525b), the amount of exchangeable Ca had increased. However, as the sum of exchangeable cations was clearly higher than the measured CEC, it can be speculated that part of the exchangeable Ca originated from dissolution of Ca salts that have precipitated at the canister contact.

Exchangeable magnesium has decreased somewhat in most of the buffer profile but for the rest, no clear changes in exchangeable cation compositions between the P5:R06 250B samples and reference samples can be seen. The trends in the Mg and Ca distributions are similar to those observed in the parallel investigation of a“wet” profile from this block (cf. Section 3.3.2).

**Table 3-22. Exchangeable cations of samples from P5:R06 250B.**

| Sample | Ca [meq/100 g] | [%] | K [meq/100 g] | [%] | Mg [meq/100 g] | [%] | Na [meq/100 g] | [%] | Sum [meq/100 g] |
|---|---|---|---|---|---|---|---|---|---|
| 525b | 28.3 | 29 | 1.6 | 2 | 9.5 | 10 | 57.2 | 59 | 97 |
| 530b | 23.9 | 27 | 1.8 | 2 | 8.7 | 10 | 54.6 | 61 | 89 |
| 545b | 23.6 | 27 | 1.8 | 2 | 8.3 | 10 | 52.9 | 61 | 87 |
| 600b | 23.2 | 27 | 1.8 | 2 | 7.8 | 9 | 53.6 | 62 | 86 |
| 640b | 23.2 | 27 | 1.8 | 2 | 7.9 | 9 | 54.2 | 62 | 87 |
| 730b | 22.1 | 25 | 1.8 | 2 | 8.2 | 9 | 55.7 | 63 | 88 |
| 770b | 21.7 | 25 | 1.8 | 2 | 8.5 | 10 | 56.4 | 64 | 88 |
| 830b | 21.5 | 24 | 1.7 | 2 | 8.5 | 10 | 56.2 | 64 | 88 |
| R1b | 23.1 | 25 | 1.7 | 2 | 9.9 | 11 | 55.9 | 62 | 91 |
| R2b | 23.2 | 26 | 1.7 | 2 | 9.8 | 11 | 55.5 | 61 | 90 |

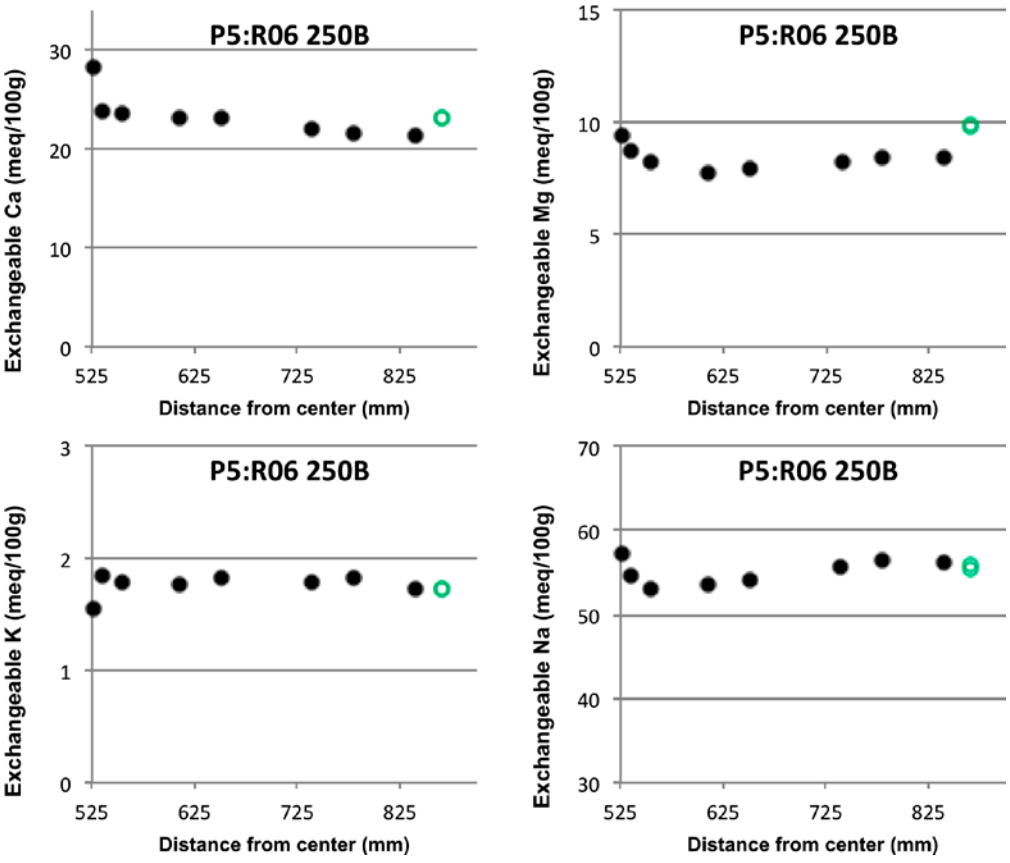


***Figure 3-35.*** *Exchangeable cations in samples from P5:R06 250B plotted versus distance from the center. Reference samples are presented as green circles in the right end of the profile.*

**Block P6:R08 355A**

The results of exchangeable cation extractions from profile P6:R08 355A are presented in Table 3-23 and in Figure 3-36.

Also in this profile, exchangeable magnesium seems to have decreased somewhat but the change is less pronounced than in profile P5:R06 250B.

For the rest, the saturation of exchange sites and the sum of exchangeable cations were alike in the block samples and the reference samples. The sum of exchangeable cations (Table 3-22) was overall slightly larger than cation exchange capacity (Table 3-21) of bulk materials, which indicates that small amount of easily soluble minerals, such as gypsum or carbonate, may have dissolved during the cation extraction.

**Table 3-23. Exchangeable cations of samples from P6:R08 355A.**

| Sample | Ca | | K | | Mg | | Na | | Sum |
|---|---|---|---|---|---|---|---|---|---|
| | [meq/100 g] | [%] | [meq/100 g] | [%] | [meq/100 g] | [%] | [meq/100 g] | [%] | [meq/100 g] |
| 525b | 23.1 | 25 | 1.5 | 2 | 8.7 | 10 | 57.7 | 63 | 91.0 |
| 527b | 22.1 | 24 | 1.4 | 2 | 8.9 | 10 | 58.9 | 65 | 91.3 |
| 574b | 22.0 | 25 | 1.5 | 2 | 8.2 | 9 | 57.9 | 65 | 89.6 |
| 620b | 22.1 | 25 | 1.5 | 2 | 8.2 | 9 | 56.8 | 64 | 88.6 |
| 735b | 21.5 | 24 | 1.6 | 2 | 8.1 | 9 | 57.9 | 65 | 89.2 |
| 786b | 21.5 | 24 | 1.6 | 2 | 8.1 | 9 | 56.9 | 65 | 88.0 |
| 837b | 21.5 | 24 | 1.5 | 2 | 8.4 | 10 | 56.6 | 64 | 88.0 |
| 846b | 22.1 | 25 | 1.5 | 2 | 8.2 | 9 | 57.4 | 64 | 89.2 |
| R1b | 22.4 | 26 | 1.5 | 2 | 9.3 | 11 | 54.4 | 62 | 87.7 |
| R2b | 22.9 | 26 | 1.5 | 2 | 9.5 | 11 | 55.6 | 62 | 89.4 |

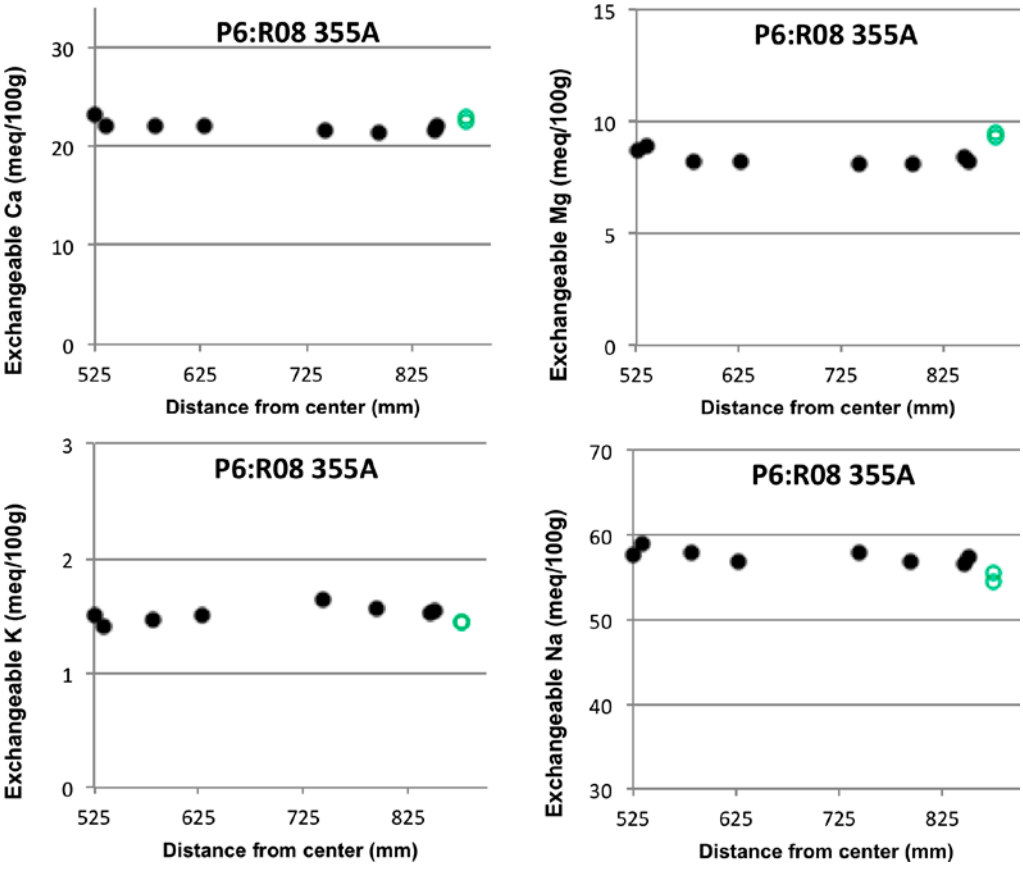


***Figure 3-36.*** *Exchangeable cations from P6:R08 355A plotted versus distance from the center. Reference samples are presented as green circles in the right end of the profile.*

### 3.4.5 Chemical composition of the bentonite

As the water content of the samples varied (see LOI in Tables 3-24 and 3-27), absolute concentrations of elements in the samples were difficult to compare without normalization. Additionally, as seen in Tables 3-26 and 3-29, the organic carbon content in samples closest to the canister was clearly increased (to 2.7 wt.% in P5:R06 250B, and to 3.0 wt.% in P6:R08 355A) compared to the reference samples (0.1 wt.% and 0.2 wt.%, respectively). Hence, in all graphs the chemical compositions are given on a water and organic carbon free basis (except C that is presented relative to dry mass) and the major oxides also as ratios.

**Block P5:R06 250B**

Total chemical compositions of bulk samples and clay fractions from profile P5:R06 250B are presented in Tables 3-24 to 3-26 and Figure 3-37 to Figure 3-39. Main oxides are presented in Table 3-24 and Figure 3-37.

An increase in the Mg content was noted towards the canister. Additionally, there might be a slight enrichment of Ca in the sample closest to the canister (525b). Si and Al displayed a maximum and sodium a minimum in the interval 30–130 mm from the canister, while K contents had remained at the reference level. However, due to the inherent correlations in constant-sum weight percentages data, the major oxide composition are compared also as the oxide ratios $SiO_2/Al_2O_3$ and $Al_2O_3/Fe_2O_3$. These ratios display only minor changes along the radius of the block and are numerically in the same range as the ratios for block P6:R08:355, as well as for the blocks studied in the parallel investigation presented in Section 3.3.3.

**Table 3-24. Total chemical composition of samples from P5:R06 250B. nd = not determined (< 0.5 µm fraction of sample 525 missing).**

| Sample | $SiO_2$ (wt.%) | $Al_2O_3$ (wt.%) | $Fe_2O_3$ (wt.%) | $TiO_2$ (wt.%) | MgO (wt.%) | CaO (wt.%) | $Na_2O$ (wt.%) | $K_2O$ (wt.%) | $P_2O_5$ (wt.%) | LOI (wt.%) | Sum (wt.%) | Total C (wt.%) | Total S (wt.%) |
|---|---|---|---|---|---|---|---|---|---|---|---|---|---|
| **Bulk** | | | | | | | | | | | | | |
| 525b | 51.83 | 16.74 | 3.15 | 0.12 | 2.20 | 1.16 | 1.77 | 0.40 | 0.07 | 22.3 | 99.83 | 2.69 | 0.35 |
| 530b | 59.76 | 19.28 | 3.67 | 0.14 | 2.45 | 1.24 | 2.07 | 0.51 | 0.05 | 10.7 | 99.92 | 0.57 | 0.27 |
| 545b | 60.79 | 19.60 | 3.56 | 0.14 | 2.45 | 1.23 | 1.27 | 0.55 | 0.04 | 10.2 | 99.94 | 0.21 | 0.23 |
| 600b | 60.45 | 19.45 | 3.55 | 0.14 | 2.40 | 1.15 | 1.28 | 0.47 | 0.05 | 10.8 | 99.91 | 0.24 | 0.23 |
| 640b | 60.02 | 19.46 | 3.55 | 0.14 | 2.41 | 1.14 | 1.26 | 0.49 | 0.06 | 11.3 | 99.91 | 0.20 | 0.25 |
| 730b | 59.53 | 19.31 | 3.44 | 0.14 | 2.38 | 1.10 | 2.02 | 0.48 | 0.04 | 11.4 | 99.95 | 0.20 | 0.26 |
| 770b | 59.56 | 19.35 | 3.56 | 0.14 | 2.37 | 1.15 | 2.07 | 0.52 | 0.04 | 11.1 | 99.93 | 0.19 | 0.26 |
| 830b | 58.71 | 19.05 | 3.61 | 0.14 | 2.38 | 1.11 | 2.08 | 0.48 | 0.05 | 12.2 | 99.93 | 0.21 | 0.24 |
| R1b | 55.01 | 18.03 | 3.33 | 0.13 | 2.19 | 1.13 | 1.85 | 0.48 | 0.05 | 17.6 | 99.94 | 0.18 | 0.31 |
| R2b | 55.33 | 17.73 | 3.31 | 0.13 | 2.19 | 1.03 | 1.93 | 0.42 | 0.05 | 17.7 | 99.95 | 0.18 | 0.26 |
| **Clay** | | | | | | | | | | | | | |
| 525c | nd | nd | nd | nd | nd | nd | nd | nd | nd | nd | nd | nd | nd |
| 530c | 58.49 | 20.69 | 3.75 | 0.12 | 2.40 | 0.01 | 2.61 | 0.01 | 0.02 | 11.8 | 99.94 | 0.36 | < 0.02 |
| 545c | 58.97 | 20.50 | 3.72 | 0.12 | 2.41 | 0.01 | 2.65 | 0.02 | 0.02 | 11.5 | 99.96 | 0.09 | < 0.02 |
| 600c | 58.78 | 20.79 | 3.81 | 0.12 | 2.47 | 0.01 | 2.73 | 0.01 | 0.01 | 11.2 | 99.94 | 0.08 | < 0.02 |
| 640c | 59.29 | 20.67 | 3.78 | 0.12 | 2.44 | 0.01 | 2.72 | 0.01 | 0.01 | 10.9 | 99.95 | 0.08 | < 0.02 |
| 730c | 58.88 | 20.78 | 3.67 | 0.12 | 2.38 | < 0.01 | 2.63 | 0.01 | 0.02 | 11.4 | 99.93 | 0.11 | < 0.02 |
| 770c | 58.59 | 20.84 | 3.70 | 0.12 | 2.38 | < 0.01 | 2.60 | 0.01 | 0.01 | 11.7 | 99.95 | 0.09 | < 0.02 |
| 830c | 58.56 | 20.68 | 3.71 | 0.12 | 2.38 | 0.01 | 2.63 | 0.01 | 0.02 | 11.8 | 99.95 | 0.10 | < 0.02 |
| R1c | 58.93 | 20.81 | 3.64 | 0.12 | 2.35 | 0.02 | 2.65 | 0.02 | 0.01 | 11.4 | 99.94 | 0.09 | < 0.02 |
| R2c | 58.90 | 20.78 | 3.59 | 0.12 | 2.33 | 0.01 | 2.71 | 0.01 | 0.02 | 11.4 | 99.95 | 0.08 | < 0.02 |

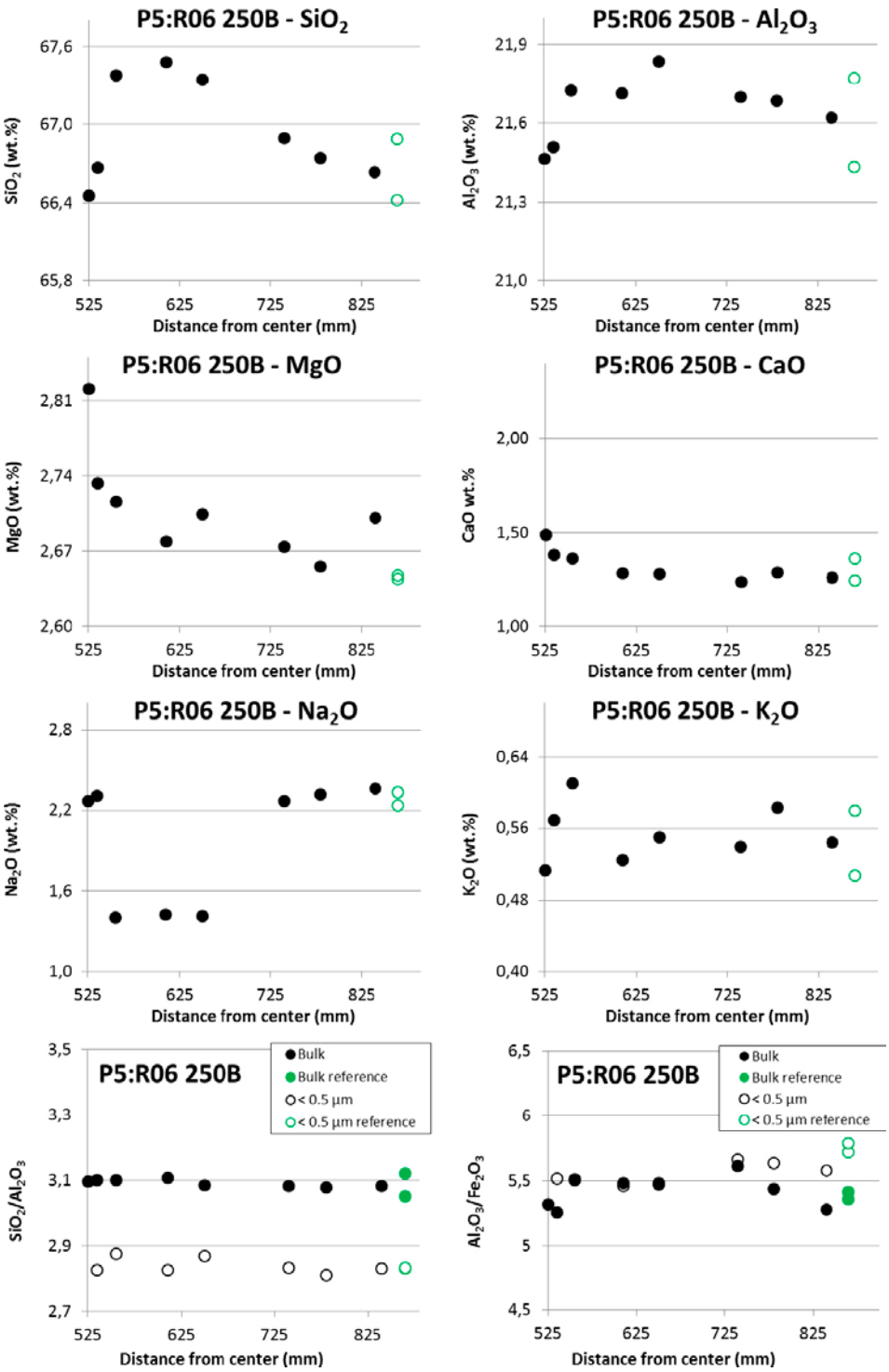


***Figure 3-37.*** *Major oxides in bulk samples and $SiO_2/Al_2O_3$- and $Al_2O_3/Fe_2O_3$-ratios in bulk samples and clay fractions from P5:R06 250B plotted versus distance from the center (< 0.5 µm fraction 525 is missing). All concentrations are presented on a water- and organic carbon-free basis. Reference samples are presented as green circles in the right end of the profile.*

Trace element concentrations in P5:R06 250B are shown in Table 3-25 and in Figure 3-38. Mo and Zn contents in the bulk material had increased near the canister (samples 525b and 530b), indicating the presence of lubricant (cf. lubricant composition in Table 3-1). The level of Zn was slightly elevated also in the clay fraction in the sample close to the canister (sample 530c) indicating that a small fraction of lubricant remained after the fractionation procedure. Mo and Zn contents were slightly elevated also in the outer part of the profile (sample 830b) but only in bulk material. Cu content was elevated only in the sample closest the canister (sample 525b) in the bulk material (the clay fraction of this sample was missing).

**Table 3-25. Trace element concentrations of samples from P5:R06 250B. Ba, Sr and Zr results are from total digestions, others from aqua regia extraction. nd = not determined.**

| Sample | Ba (ppm) | Mn (ppm) | Cd (ppm) | Co (ppm) | Cr (ppm) | Cu (ppm) | Pb (ppm) | Ni (ppm) | Th (ppm) | Mo (ppm) | Sr (ppm) | Zn (ppm) | Zr (ppm) |
|---|---|---|---|---|---|---|---|---|---|---|---|---|---|
| **Bulk** | | | | | | | | | | | | | |
| 525b | 318 | 46 | < 0.5 | < 1 | 3 | 35 | 31 | 3 | 33 | 186 | 218 | 729 | 177 |
| 530b | 278 | 55 | < 0.5 | < 1 | 2 | 3 | 41 | 3 | 40 | 10 | 300 | 102 | 200 |
| 545b | 261 | 50 | < 0.5 | < 1 | 3 | 2 | 33 | 3 | 39 | 3 | 284 | 68 | 219 |
| 600b | 361 | 56 | < 0.5 | 1 | 1 | 2 | 38 | 3 | 40 | 3 | 277 | 61 | 225 |
| 640b | 276 | 54 | < 0.5 | < 1 | < 1 | 2 | 36 | 3 | 38 | 3 | 265 | 76 | 230 |
| 730b | 326 | 51 | < 0.5 | < 1 | < 1 | 3 | 39 | 3 | 40 | 3 | 257 | 80 | 210 |
| 770b | 253 | 52 | < 0.5 | < 1 | < 1 | 2 | 38 | 3 | 38 | 2 | 253 | 71 | 192 |
| 830b | 293 | 52 | < 0.5 | < 1 | 1 | 3 | 35 | 3 | 38 | 5 | 267 | 121 | 202 |
| R1b | 359 | 46 | < 0.5 | < 1 | < 1 | 2 | 31 | 3 | 37 | 3 | 254 | 68 | 190 |
| R2b | 303 | 49 | < 0.5 | < 1 | 1 | 2 | 32 | 3 | 37 | 3 | 239 | 78 | 183 |
| **Clay** | | | | | | | | | | | | | |
| 525c | nd | nd | nd | nd | nd | nd | nd | nd | nd | nd | nd | nd | nd |
| 530c | 5 | 15 | < 0.5 | < 1 | 1 | 12 | 12 | 5 | 33 | < 1 | 5 | 53 | 146 |
| 545c | 8 | 17 | < 0.5 | < 1 | 1 | 15 | 14 | 4 | 33 | < 1 | 5 | 26 | 147 |
| 600c | < 5 | 14 | < 0.5 | < 1 | < 1 | 15 | 15 | 4 | 32 | < 1 | 5 | 25 | 150 |
| 640c | 7 | 8 | < 0.5 | < 1 | 2 | 15 | 11 | 4 | 29 | < 1 | 5 | 25 | 148 |
| 730c | 8 | 8 | < 0.5 | < 1 | 2 | 17 | 6 | 4 | 33 | < 1 | 5 | 22 | 150 |
| 770c | 6 | 11 | < 0.5 | < 1 | 5 | 16 | 9 | 5 | 31 | < 1 | 5 | 23 | 146 |
| 830c | 8 | 12 | < 0.5 | < 1 | 4 | 15 | 10 | 5 | 32 | < 1 | 5 | 25 | 150 |
| R1c | 10 | 7 | < 0.5 | < 1 | < 1 | 13 | 6 | 3 | 33 | < 1 | 6 | 26 | 148 |
| R2c | 8 | 7 | < 0.5 | < 1 | 1 | 12 | 8 | 3 | 34 | < 1 | 6 | 26 | 148 |

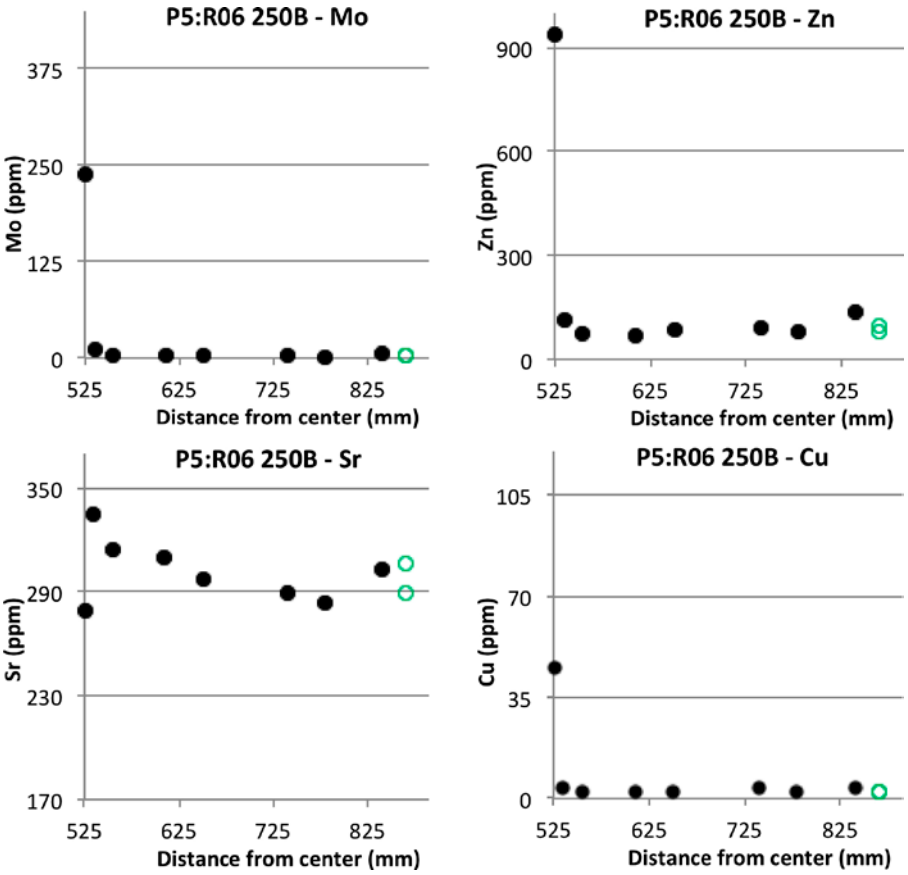


***Figure 3-38.*** *Contents of some minor indicator elements in bulk samples of P5:R06 250B plotted versus distance from the center. All concentrations are presented on water and organic carbon-free basis. Reference samples are presented as green circles in the right end of the profile.*

Organic carbon content had increased significantly in the two samples closest to the canister (from 0.1 wt.% in reference sample to 2.7 wt.% in sample 525b; Table 3-26, Figure 3-39). Iron might have been slightly reduced as indicated by the increase in $Fe^{2+}$ content from 0.6 wt.% in reference sample to 0.8 wt.% in sample 525b closest to the canister (Table 3-26, Figure 3-39).

**Table 3-26. Speciations of Fe, C, and S of bulk samples from P5:R06 250B.**

| Sample | Fe-Total (wt.%) | Fe-Fe3+ (wt.%) | Fe-Fe2+ (wt.%) | C-Total (wt.%) | C-Inorganic (wt.%) | C-Organic (wt.%) | S-Total (wt.%) | S-SO4 (wt.%) | S-Sulphidic (wt.%) |
|---|---|---|---|---|---|---|---|---|---|
| 525b | 2.20 | 1.43 | 0.77 | 2.69 | 0.04 | 2.65 | 0.35 | 0.25 | 0.10 |
| 530b | 2.57 | 2.19 | 0.37 | 0.57 | 0.06 | 0.51 | 0.27 | 0.23 | 0.04 |
| 545b | 2.49 | 2.18 | 0.31 | 0.21 | 0.08 | 0.13 | 0.23 | 0.19 | 0.04 |
| 600b | 2.48 | 2.09 | 0.40 | 0.24 | 0.06 | 0.18 | 0.23 | 0.16 | 0.07 |
| 640b | 2.48 | 2.09 | 0.39 | 0.20 | 0.07 | 0.13 | 0.25 | 0.17 | 0.08 |
| 730b | 2.41 | 1.97 | 0.44 | 0.20 | 0.06 | 0.14 | 0.26 | 0.17 | 0.09 |
| 770b | 2.49 | 2.09 | 0.40 | 0.19 | 0.06 | 0.13 | 0.26 | 0.22 | 0.04 |
| 830b | 2.52 | 2.15 | 0.37 | 0.21 | 0.06 | 0.15 | 0.24 | 0.23 | 0.01 |
| R1b | 2.33 | 1.72 | 0.61 | 0.18 | 0.06 | 0.12 | 0.31 | 0.18 | 0.13 |
| R2b | 2.32 | 1.69 | 0.63 | 0.18 | 0.06 | 0.12 | 0.26 | 0.14 | 0.12 |

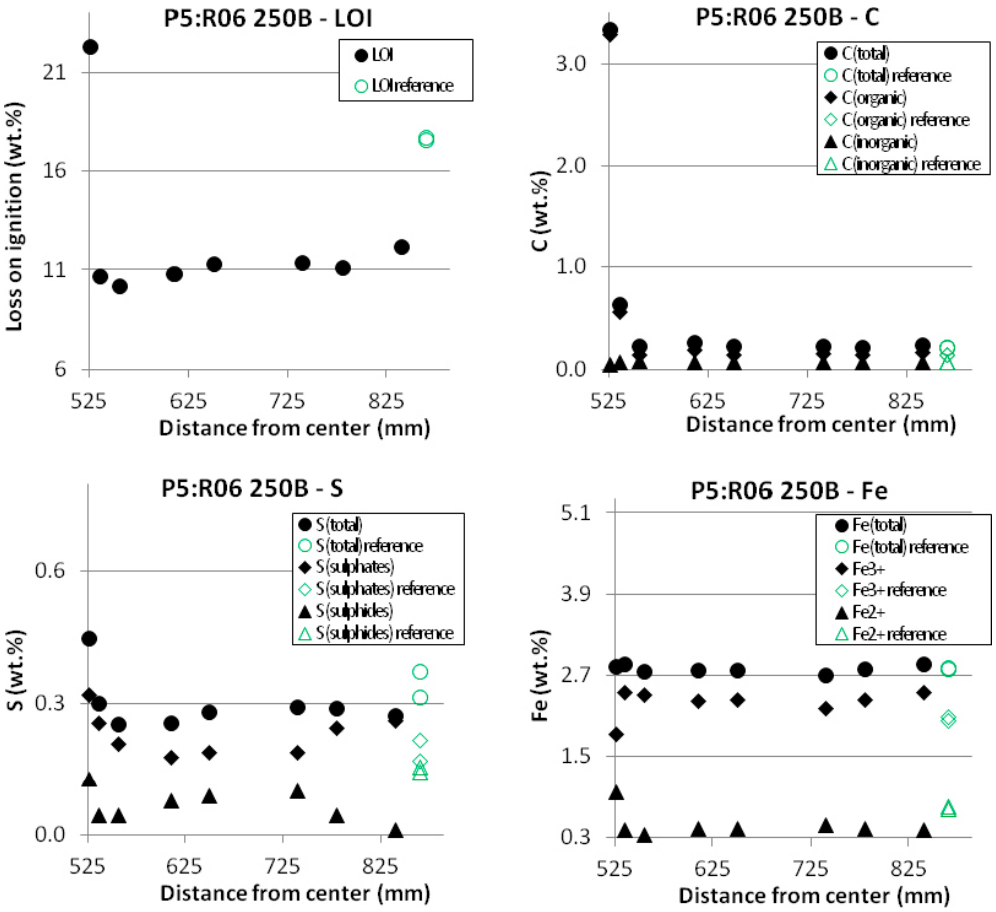


***Figure 3-39.*** *LOI, and contents of C, S and Fe, and their speciations in bulk samples from P5:R06 250B plotted against distance from the center. Carbon content is presented relative to dry mass, and S and Fe contents on a $H_2O$ and organic C-free basis. Reference samples are presented as green circles, triangles or diamonds in the right end of the profile.*

**Block P6:R08 355A**

Total chemical compositions of bulk samples and clay fractions from profile P6:R08 355A are presented in Tables 3-27 to 3-29 and Figure 3-40 to Figure 3-42. Main elements are presented in Table 3-27 and Figure 3-40.

An increase in the Mg content in the inner part of the block was noted also in this block, but the change was less than in the "warmer" block P5:R06. $SiO_2$ as well as $Al_2O_3$ concentrations had decreased in the innermost bulk samples. This decrease is believed to be mostly a "dilution" effect because both MgO and CaO had increased in the innermost samples. The increase in CaO was probably due to calcium sulphate precipitation, since also the sulphate content had increased drastically in sample 525b (Figure 3-42, Table 3-29). The ratios $SiO_2/Al_2O_3$ and $Al_2O_3/Fe_2O_3$ for both bulk samples and fine clay fractions display only minor changes along the radius of the block and are numerically almost equal to those of the samples from profile P5:R06 250 and also to the values obtained in the parallel investigation presented in Section 3.3.3 (cf. Figures 3-13 and 3-14).

Trace element analyses showed that the Cu content had increased in the innermost sample 525b, from 2-3 ppm in the reference sample to 99 ppm (Table 3-28, Figure 3-41). This increase is most likely due to bentonite interaction with the Cu canister. Also the Mo and Zn contents increased in the two innermost (525b and 527b) and the outermost (846b) samples (Table 3-28). This increase was accompanied by increase in organic carbon content (Table 3-29). Mo content increased from 2 ppm in reference samples up to 365 ppm in sample 525b and Zn content increased from approximately 90 ppm in reference samples up to 814 ppm in sample 525b. This increase indicated clearly the influence of the lubricant, which contains both these heavy metals: Mo as disulfide ($MoS_2$) and Zn as organic complex (zinc dialkyldithiophosphate). Cu and Zn, but not Mo, remained clearly elevated also in the purified and sodium-exchanged clay fraction indicating that they are probably bound to impurities, possibly organics, as the clay fraction of the two innermost and the outermost samples still contained considerable amounts of carbon.

**Table 3-27. Total chemical compositions of bulk samples and clay fractions for samples of Prototype profile P6:R08 355A.**

| Sample | $SiO_2$ (wt.%) | $Al_2O_3$ (wt.%) | $Fe_2O_3$ (wt.%) | $TiO_2$ (wt.%) | MgO (wt.%) | CaO (wt.%) | $Na_2O$ (wt.%) | $K_2O$ (wt.%) | $P_2O_5$ (wt.%) | LOI (wt.%) | Sum (wt.%) | Total C (wt.%) | Total S (wt.%) |
|---|---|---|---|---|---|---|---|---|---|---|---|---|---|
| **Bulk** | | | | | | | | | | | | | |
| 525b | 56.80 | 18.23 | 3.33 | 0.13 | 2.34 | 2.02 | 1.98 | 0.49 | 0.05 | 14.3 | 99.81 | 3.08 | 0.59 |
| 527b | 58.77 | 19.01 | 3.46 | 0.13 | 2.35 | 1.08 | 2.06 | 0.51 | 0.05 | 12.4 | 99.95 | 1.20 | 0.22 |
| 574b | 59.98 | 19.43 | 3.50 | 0.14 | 2.36 | 1.19 | 2.05 | 0.55 | 0.05 | 10.6 | 99.96 | 0.23 | 0.24 |
| 620b | 58.86 | 18.84 | 3.51 | 0.14 | 2.33 | 1.19 | 2.05 | 0.54 | 0.05 | 12.3 | 99.96 | 0.21 | 0.22 |
| 735b | 60.44 | 19.41 | 3.55 | 0.14 | 2.37 | 1.23 | 2.09 | 0.55 | 0.04 | 10.0 | 99.96 | 0.23 | 0.23 |
| 786b | 61.46 | 19.58 | 3.61 | 0.14 | 2.42 | 1.21 | 2.11 | 0.55 | 0.05 | 8.7 | 99.97 | 0.23 | 0.27 |
| 837b | 61.28 | 19.66 | 3.67 | 0.14 | 2.47 | 1.25 | 2.08 | 0.54 | 0.05 | 8.7 | 99.94 | 0.24 | 0.25 |
| 846b | 61.34 | 19.80 | 3.59 | 0.14 | 2.39 | 1.23 | 2.10 | 0.51 | 0.04 | 8.7 | 99.94 | 0.40 | 0.25 |
| R1b | 56.90 | 18.29 | 3.38 | 0.14 | 2.25 | 1.24 | 1.96 | 0.54 | 0.04 | 15.1 | 99.96 | 0.21 | 0.27 |
| R2b | 57.97 | 18.69 | 3.44 | 0.14 | 2.26 | 1.20 | 2.00 | 0.56 | 0.04 | 13.5 | 99.96 | 0.20 | 0.20 |
| **Clay** | | | | | | | | | | | | | |
| 525c | 58.50 | 20.44 | 3.68 | 0.12 | 2.34 | 0.02 | 2.56 | 0.03 | 0.01 | 12.2 | 99.93 | 2.37 | 0.03 |
| 527c | 59.24 | 20.87 | 3.65 | 0.12 | 2.37 | 0.02 | 2.58 | 0.02 | 0.02 | 11.0 | 99.96 | 1.07 | < 0.02 |
| 574c | 60.99 | 21.60 | 3.85 | 0.13 | 2.49 | 0.01 | 2.75 | 0.02 | 0.02 | 8.1 | 99.96 | 0.08 | < 0.02 |
| 620c | 61.01 | 21.61 | 3.88 | 0.13 | 2.49 | 0.02 | 2.75 | 0.02 | 0.02 | 8.0 | 99.98 | 0.09 | < 0.02 |
| 735c | 61.28 | 21.58 | 3.92 | 0.13 | 2.50 | 0.01 | 2.73 | 0.02 | 0.02 | 7.7 | 99.97 | 0.08 | < 0.02 |
| 786c | 61.35 | 21.75 | 3.87 | 0.13 | 2.46 | 0.02 | 2.65 | 0.01 | 0.02 | 7.7 | 99.97 | 0.09 | < 0.02 |
| 837c | 61.04 | 21.67 | 3.83 | 0.13 | 2.46 | 0.01 | 2.59 | 0.01 | 0.03 | 8.2 | 99.97 | 0.09 | < 0.02 |
| 846c | 60.43 | 21.40 | 3.85 | 0.13 | 2.44 | < 0.01 | 2.59 | 0.02 | 0.03 | 9.1 | 99.98 | 0.22 | < 0.02 |
| R1c | 60.78 | 21.51 | 3.76 | 0.13 | 2.42 | 0.02 | 2.65 | 0.01 | 0.02 | 8.6 | 99.98 | 0.10 | < 0.02 |
| R2c | 60.42 | 21.43 | 3.76 | 0.13 | 2.40 | 0.02 | 2.60 | < 0.01 | 0.02 | 9.2 | 99.98 | 0.10 | < 0.02 |

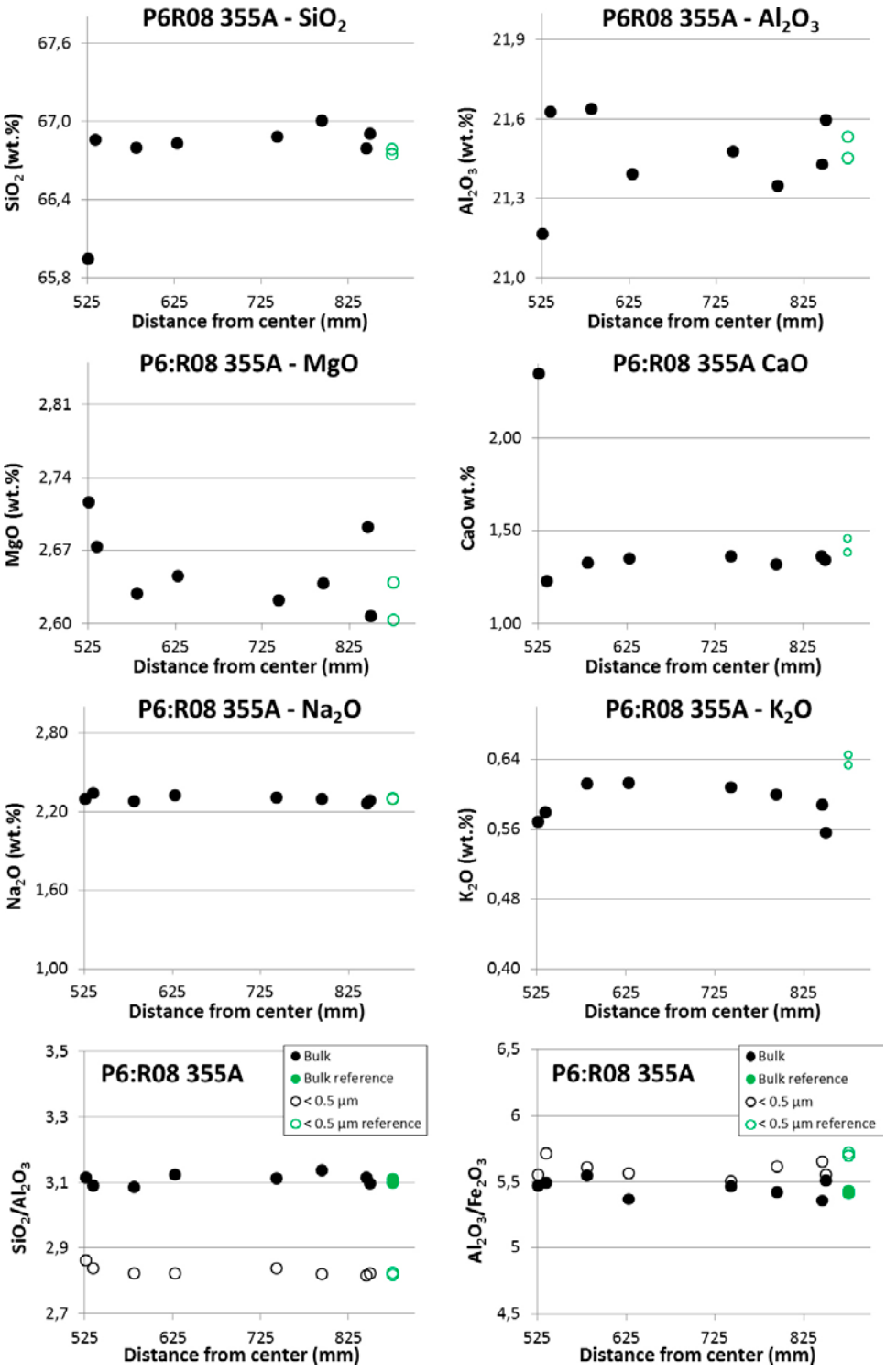


***Figure 3-40.*** *Major oxides in bulk samples and $SiO_2/Al_2O_3$- and $Al_2O_3/Fe_2O_3$-ratios in bulk samples and clay fractions from P6:R08 355A plotted against distance from the center. All concentrations are presented on a water- and organic carbon-free basis (except $SiO_2/Al_2O_3$- and $Al_2O_3/Fe_2O_3$-ratios). Reference samples are presented as green circles in the right end of the profile.*

**Table 3-28. Trace element concentrations of samples from Prototype profile P6:R08 355A. Ba, Sr and Zr results are results from total digestions, others from aqua regia extractions.**

| Sample | Ba (ppm) | Mn (ppm) | Cd (ppm) | Co (ppm) | Cr (ppm) | Cu (ppm) | Pb (ppm) | Ni (ppm) | Th (ppm) | Mo (ppm) | Sr (ppm) | Zn (ppm) | Zr (ppm) |
|---|---|---|---|---|---|---|---|---|---|---|---|---|---|
| **Bulk** | | | | | | | | | | | | | |
| 525b | 266 | 62 | < 0.5 | < 1 | < 1 | 99 | 31 | 7 | 38 | 365 | 165 | 814 | 194 |
| 527b | 284 | 55 | < 0.5 | < 1 | < 1 | 5 | 37 | 3 | 39 | 28 | 246 | 189 | 204 |
| 574b | 281 | 60 | < 0.5 | < 1 | < 1 | 2 | 40 | 3 | 41 | 3 | 253 | 85 | 213 |
| 620b | 318 | 57 | < 0.5 | < 1 | < 1 | 2 | 38 | 3 | 40 | 3 | 258 | 90 | 201 |
| 735b | 332 | 65 | < 0.5 | < 1 | < 1 | 2 | 38 | 3 | 42 | 2 | 271 | 120 | 209 |
| 786b | 314 | 57 | < 0.5 | < 1 | < 1 | 2 | 41 | 3 | 41 | 2 | 262 | 88 | 213 |
| 837b | 326 | 60 | < 0.5 | < 1 | < 1 | 2 | 44 | 3 | 42 | 2 | 277 | 75 | 233 |
| 846b | 318 | 59 | < 0.5 | < 1 | < 1 | 2 | 40 | 3 | 41 | 10 | 271 | 119 | 203 |
| R1b | 314 | 58 | < 0.5 | < 1 | < 1 | 3 | 36 | 3 | 40 | 2 | 251 | 85 | 212 |
| R2b | 362 | 55 | < 0.5 | < 1 | < 1 | 2 | 38 | 2 | 39 | 2 | 257 | 102 | 202 |
| **Clay** | | | | | | | | | | | | | |
| 525c | 7 | 3 | < 0.5 | < 1 | < 1 | 66 | 7 | 3 | 30 | 3 | 5 | 196 | 155 |
| 527c | < 5 | 10 | < 0.5 | < 1 | < 1 | 7 | 15 | 3 | 33 | < 1 | 5 | 109 | 151 |
| 574c | 8 | 13 | < 0.5 | < 1 | < 1 | 7 | 14 | 2 | 34 | < 1 | 5 | 30 | 157 |
| 620c | 7 | 8 | < 0.5 | < 1 | < 1 | 10 | 12 | 2 | 33 | < 1 | 5 | 28 | 155 |
| 735c | 6 | 17 | < 0.5 | < 1 | < 1 | 7 | 17 | 2 | 34 | < 1 | 5 | 29 | 156 |
| 786c | 8 | 8 | < 0.5 | < 1 | < 1 | 12 | 10 | 1 | 32 | < 1 | 5 | 20 | 156 |
| 837c | 6 | 11 | < 0.5 | < 1 | < 1 | 9 | 12 | 2 | 33 | < 1 | 5 | 26 | 152 |
| 846c | 6 | 12 | < 0.5 | < 1 | < 1 | 8 | 14 | 2 | 34 | < 1 | 5 | 44 | 152 |
| R1c | 6 | 5 | < 0.5 | < 1 | < 1 | 8 | 10 | 1 | 33 | < 1 | 5 | 26 | 155 |
| R2c | 7 | 4 | < 0.5 | < 1 | < 1 | 7 | 9 | 1 | 32 | < 1 | 5 | 25 | 153 |

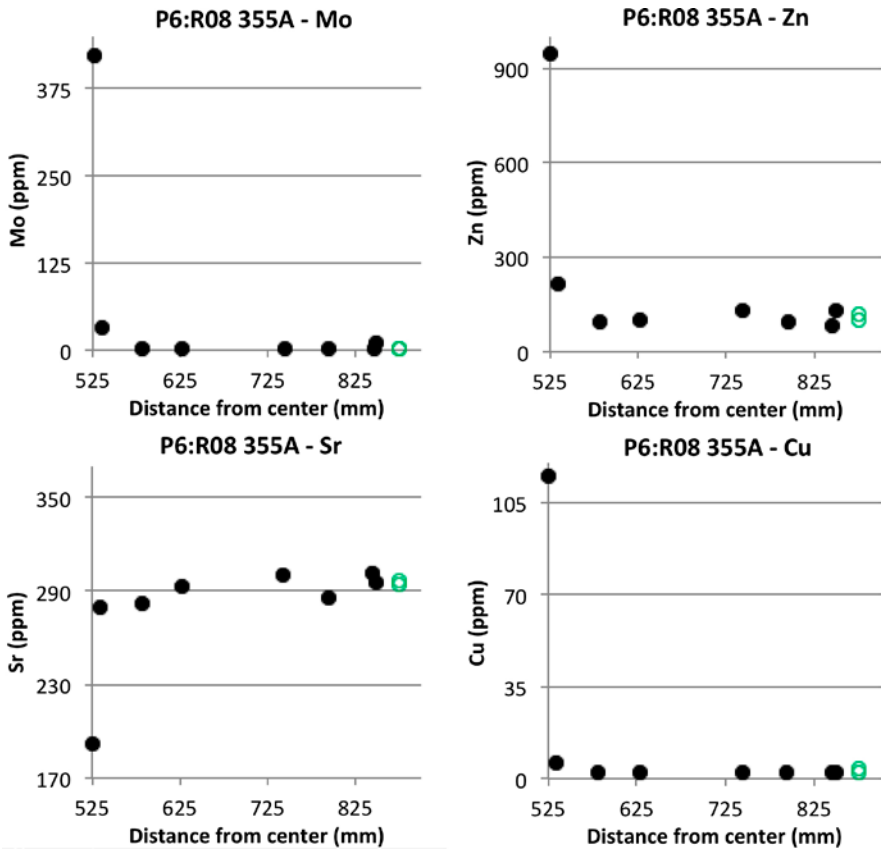


***Figure 3-41.*** *Contents of some minor indicator elements in bulk samples of P6:R08 355A plotted against distance from the center. All concentrations are presented on water- and organic carbon-free basis. Reference samples are presented as green circles in the right end of the profile.*

**Table 3-29. Speciations of Fe, C, and S of bulk samples from P6:R08 355A.**

| Sample | Fe-Total (wt.%) | Fe-$Fe^{3+}$ (wt.%) | Fe-$Fe^{2+}$ (wt.%) | C-Total (wt.%) | C-Inorganic (wt.%) | C-Organic (wt.%) | S-Total (wt.%) | S-$SO_4$ (wt.%) | S-Sulfidic (wt.%) |
|---|---|---|---|---|---|---|---|---|---|
| 525b | 2.33 | 1.44 | 0.89 | 3.08 | 0.08 | 3.00 | 0.59 | 0.58 | < 0.02 |
| 527b | 2.42 | 1.62 | 0.80 | 1.20 | 0.05 | 1.15 | 0.22 | 0.18 | 0.04 |
| 574b | 2.45 | 1.90 | 0.54 | 0.23 | 0.07 | 0.16 | 0.24 | 0.18 | 0.06 |
| 620b | 2.45 | 1.90 | 0.55 | 0.21 | 0.07 | 0.14 | 0.22 | 0.19 | 0.03 |
| 735b | 2.48 | 1.97 | 0.51 | 0.23 | 0.07 | 0.16 | 0.23 | 0.22 | < 0.02 |
| 786b | 2.52 | 2.07 | 0.46 | 0.23 | 0.07 | 0.16 | 0.27 | 0.20 | 0.07 |
| 837b | 2.57 | 2.10 | 0.47 | 0.24 | 0.08 | 0.16 | 0.25 | 0.19 | 0.06 |
| 846b | 2.51 | 2.07 | 0.44 | 0.40 | 0.07 | 0.33 | 0.25 | 0.24 | < 0.02 |
| R1b | 2.36 | 1.66 | 0.70 | 0.21 | 0.05 | 0.16 | 0.27 | 0.17 | 0.10 |
| R2b | 2.41 | 1.68 | 0.73 | 0.20 | 0.05 | 0.15 | 0.20 | 0.18 | 0.02 |

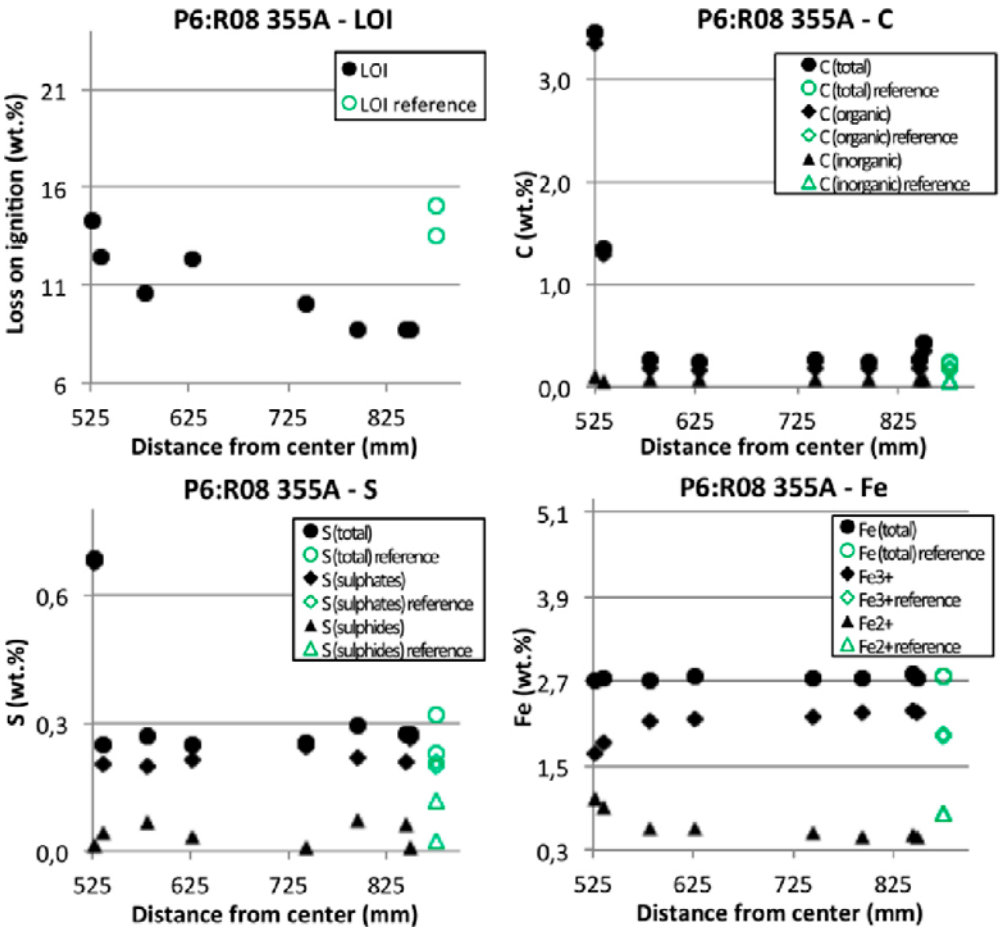


***Figure 3-42.*** *LOI and contents of C, S and Fe, and their speciations in bulk samples from P6:R08 355A plotted against distance from the center. Carbon content is presented on dry mass basis, and S and Fe contents on a $H_2O$- and organic C-free basis. Reference samples are presented as green circles, triangles, or diamonds in the right end of the profile.*

The total content of iron was constant in the P6:R08 355A profile (Table 3-29, Figure 3-42), but the speciation of Fe showed that in general the content of $Fe^{3+}$ had increased and that of $Fe^{2+}$ decreased in the profile compared to the reference samples, except in the two samples closest to the canister where the trend in iron speciation was the opposite. Mössbauer spectrometry data (Section 3.3.8) support the findings that $Fe^{2+}$ had increased in samples near the canister and the Mössbauer results are considered more reliable since these samples were handled under more strict anoxic conditions, unlike the samples used for the wet-chemical $Fe^{2+}$-analysis. Reduction of iron at the canister could be due to interaction with Cu or with the lubricant. However, it may be noted that iron was not reduced in the outermost sample (sample 846b) where the influence of lubricant was also observable.

The total content of carbon has increased in the two innermost samples, from 0.2 wt.% in reference samples up to 3.1 wt.% in sample 525b (Table 3-29, Figure 3-42). This increase was most probably caused by organic carbon in the lubricant used in block compression. A small increase (0.2 wt.%) in organic carbon content was noted also in the outermost sample, which again shows the influence of the lubricant.

The total content of sulfur had increased only in the innermost sample of the P6:R08 355A profile, from 0.3 wt.% in reference samples to 0.6 wt.% (Table 3-29, Figure 3-42). Although the lubricant contained several sources of sulfur, such as molybdenite ($MoS_2$) and Zn-dialkyldithiophosphate, the speciation study showed that this increase was due to increase in sulfates rather than sulfides (Table 3-29, Figure 3-42).

### 3.4.6 Structural formula of the smectite

The structural formula of smectite was calculated from chemical compositions of purified Na-homoionic clay fractions. Calculations were done according to Newman and Brown (1987) assuming that structural units contained 24 anions ($O_{20}(OH)_4$), but that unit cell and density were unknown.

In order to get the chemical composition of the pure smectite phase, illite was subtracted from the measured chemical composition of the clay fraction. The amount of illite was calculated from the K-content in the clay fraction using the ideal formula $K_{1.5}(Si_7Al)(Al_{3.5}Mg_{0.5})O_{20}(OH)_4$ for illite (K-content of 7.6%). The Al, Mg and Si contents were adjusted accordingly. The illite correction and other necessary appoximations were the same as those described in Section 3.3.4.

**Block P5:R06 250B**

The structural formulae of the smectite of samples from block P5:R06 250B are shown in Table 3-30.

The results indicate a slight increase in octahedral Mg in the innermost block samples (the sample from the bentonite/canister contact missing). Otherwise, there is no trend indicating changes in the smectite structural composition, layer charge, or charge distribution in the samples.

The resulting average formulae of the montmorillonite of references and block samples, respectively, are:

References: $Ca_{0.002}\ Na_{0.69}(Al_{3.12}\ Fe_{0.36}\ Mg_{0.47}\ Ti_{0.01})(Si_{7.86}\ Al_{0.14})\ O_{20}\ (OH)_4$

Block P5:R06: $Ca_{0.001}\ Na_{0.69}(Al_{3.11}\ Fe_{0.38}\ Mg_{0.48}\ Ti_{0.01})(Si_{7.85}\ Al_{0.15})\ O_{20}\ (OH)_4$

**Table 3-30. Calculated structural composition of smectite in profile P5:R06 250B. Sample 525 at the canister is missing.**

| | 530c | 545c | 600c | 640c | 730c | 770c | 830c | R1c | R2c |
|---|---|---|---|---|---|---|---|---|---|
| Si | 7.84 | 7.88 | 7.83 | 7.87 | 7.85 | 7.84 | 7.85 | 7.86 | 7.86 |
| Al | 0.16 | 0.12 | 0.17 | 0.13 | 0.15 | 0.16 | 0.15 | 0.14 | 0.14 |
| **Σ tet** | 8.00 | 8.00 | 8.00 | 8.00 | 8.00 | 8.00 | 8.00 | 8.00 | 8.00 |
| Al okt | 3.11 | 3.10 | 3.09 | 3.10 | 3.12 | 3.12 | 3.11 | 3.12 | 3.13 |
| Ti | 0.01 | 0.01 | 0.01 | 0.01 | 0.01 | 0.01 | 0.01 | 0.01 | 0.01 |
| Fe(III) | 0.38 | 0.37 | 0.38 | 0.38 | 0.37 | 0.37 | 0.37 | 0.37 | 0.36 |
| Mg | 0.48 | 0.48 | 0.49 | 0.48 | 0.47 | 0.47 | 0.48 | 0.47 | 0.46 |
| **Σ oct** | 3.98 | 3.97 | 3.98 | 3.97 | 3.97 | 3.98 | 3.98 | 3.97 | 3.96 |
| Ca | 0.001 | 0.001 | 0.001 | 0.001 | 0.001 | 0.001 | 0.001 | 0.003 | 0.001 |
| Na | 0.679 | 0.688 | 0.706 | 0.700 | 0.681 | 0.675 | 0.684 | 0.686 | 0.702 |
| **interlayer charge** | **0.68** | **0.69** | **0.71** | **0.70** | **0.68** | **0.68** | **0.69** | **0.69** | **0.70** |
| % tet. charge | 23 | 18 | 24 | 19 | 21 | 24 | 22 | 21 | 20 |
| molar weight | 745 | 745 | 746 | 746 | 745 | 745 | 745 | 745 | 745 |
| CEC calculated | 91 | 93 | 95 | 94 | 92 | 91 | 92 | 93 | 95 |
| CEC measured | 94 | 95 | 95 | 94 | 94 | 94 | 93 | 93 | 94 |

### Block P6:R08 355A

The structural formula of the smectite, calculated from chemical compositions of purified and homoionized Na-clay fractions, for samples from block P6:R08 355A are shown in Table 3-31. The results indicated that there might be a very small in decrease in the tetrahedral charge in samples 525c and 527c at the canister contact, whereas no significant change was observed in octahedral magnesium in this block.

The resulting average formulae of the montmorillonite of references and block samples, respectively, are similar in most details, also to the smectite formulae obtained for all other blocks investigated (cf. above and Section 3.3.4):

References: $Ca_{0.003}\ Na_{0.66}(Al_{3.13}\ Fe_{0.37}\ Mg_{0.47}\ Ti_{0.01})(Si_{7.85}\ Al_{0.15})\ O_{20}\ (OH)_4$

Block P6:R08: $Ca_{0.002}\ Na_{0.67}(Al_{3.12}\ Fe_{0.37}\ Mg_{0.47}\ Ti_{0.01})(Si_{7.85}\ Al_{0.15})\ O_{20}\ (OH)_4$

**Table 3-31. Calculated structural composition of smectite in profile P6:R08 355A. nd = not determined.**

| | 525c | 527c | 574c | 620c | 735c | 786c | 837c | 846c | R1c | R2c |
|---|---|---|---|---|---|---|---|---|---|---|
| Si | 7.88 | 7.87 | 7.84 | 7.84 | 7.85 | 7.85 | 7.85 | 7.85 | 7.86 | 7.85 |
| Al | 0.12 | 0.13 | 0.16 | 0.16 | 0.15 | 0.15 | 0.15 | 0.15 | 0.14 | 0.15 |
| **Σ tet** | 8.00 | 8.00 | 8.00 | 8.00 | 8.00 | 8.00 | 8.00 | 8.00 | 8.00 | 8.00 |
| Al | 3.11 | 3.13 | 3.11 | 3.11 | 3.11 | 3.13 | 3.13 | 3.12 | 3.13 | 3.13 |
| Ti | 0.01 | 0.01 | 0.01 | 0.01 | 0.01 | 0.01 | 0.01 | 0.01 | 0.01 | 0.01 |
| Fe(III) | 0.37 | 0.37 | 0.37 | 0.38 | 0.38 | 0.37 | 0.37 | 0.38 | 0.37 | 0.37 |
| Mg | 0.47 | 0.47 | 0.48 | 0.48 | 0.48 | 0.47 | 0.47 | 0.47 | 0.47 | 0.46 |
| **Σ oct** | **3.97** | **3.97** | **3.98** | **3.98** | **3.98** | **3.98** | **3.99** | **3.98** | **3.98** | **3.98** |
| Ca | 0.003 | 0.003 | 0.001 | 0.003 | 0.001 | 0.003 | 0.001 | 0.001 | 0.003 | 0.003 |
| Na | 0.670 | 0.665 | 0.687 | 0.687 | 0.680 | 0.658 | 0.646 | 0.654 | 0.665 | 0.656 |
| **interlayer charge** | **0.68** | **0.67** | **0.69** | **0.69** | **0.68** | **0.66** | **0.65** | **0.66** | **0.67** | **0.66** |
| % tet. charge | 18 | 20 | 23 | 23 | 22 | 23 | 23 | 23 | 21 | 22 |
| molar weight | 745 | 745 | 745 | 746 | 745 | 745 | 745 | 745 | 745 | 745 |
| CEC calculated | 91 | 90 | 93 | 93 | 92 | 89 | 87 | 88 | 90 | 89 |
| CEC measured | 92 | 94 | 94 | 94 | 95 | 94 | 93 | 93 | 93 | nd |

### 3.4.7 Mineralogical composition

The mineralogical composition of all samples was determined after:

– Identification of accessory minerals in the coarse fraction using optical microscopy.
– Identification of main minerals by X-ray diffraction analysis of randomly oriented bulk mounts.
– Identification of clay minerals by X-ray diffraction analysis of oriented clay fractions.
– Performing XRD full-pattern fitting with the Siroquant software.

#### *3.4.7.1 Optical microscopy of coarse fraction*

**Block P5:R06 250B**

Examples of identified accessory minerals from block P5:R06 250B using an optical microscopy are presented in Figure 3-43, and all accessory minerals identified with optical microscopy listed (together with minerals identified using X-ray diffraction) in Table 3-32. In addition to minerals listed in the table, all samples contained opaque minerals, that is, metal sulfides and/or oxides. A relatively large orthopyroxene crystal was identified with optical microscopy in sample 640b (Figure 3-43b). No differences between the samples from P5:R06 250B and reference samples were observed.

**Block P6:R08 355A**

Examples of identified accessory minerals from block P6:R08 355A using an optical microscopy are presented in Figure 3-44, and all accessory minerals identified with optical microscopy listed (together with minerals identified using X-ray diffraction) in Table 3-34. In addition to minerals listed in the table, all samples contained opaque minerals, that is, metal sulfides and/or oxides. No differences between the reference samples and P6:R08 355A samples were observed.

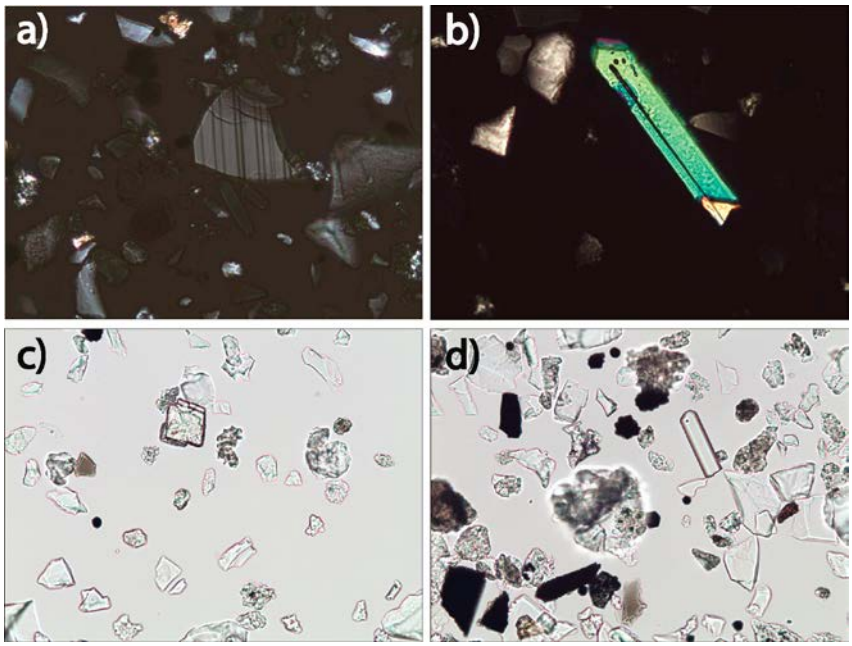


***Figure 3-43.*** *Examples of minerals identified with optical microscopy of samples of profile P5:R06 250B. a) Plagioclase grain showing typical lamellar twinning in cross-polarized light. b) Idiomorphic pyroxene crystal in cross-polarized light. c) High-relief carbonate crystals in plane-polarized light. d) Elongated apatite crystal and several opaque grains (of which some consist of several smaller crystals, presumably framboidal pyrite) in plane-polarized light. All pictures have been taken using 20× magnification objective.*

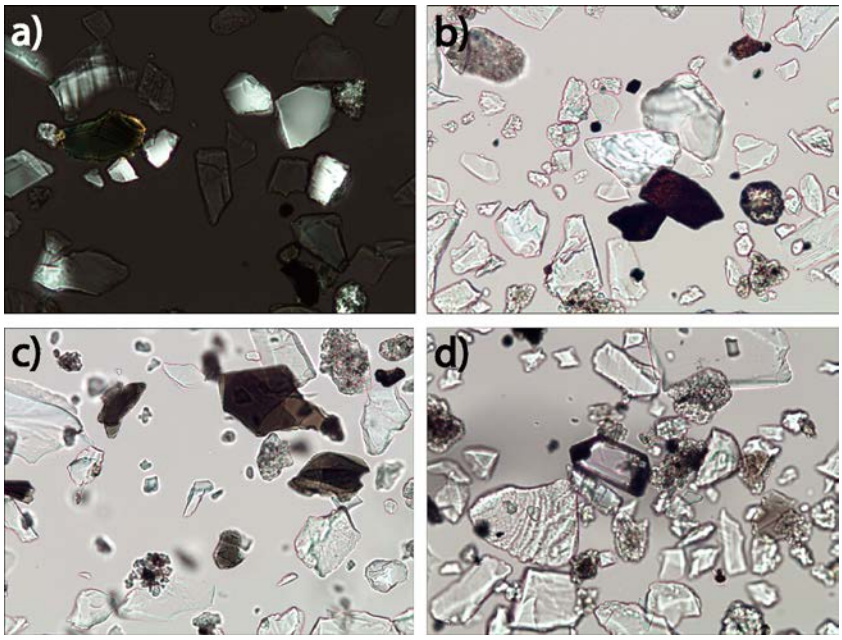


***Figure 3-44.*** *Examples of minerals identified with optical microscopy from P6:R08 355A samples. a) Microcline grain in the right upper corner showing typical grid structure in cross-polarized light. b) Opaque hematite crystals showing bright red tint in plane-polarized light. c) Brown mica flakes in plane-polarized light. d) High relief idiomorphic zircon crystal in plane-polarized light. All pictures have been taken using 20× magnification objective.*

#### *3.4.7.2 XRD*

**Block P5:R06 250B**

*Bulk material*

X-ray diffraction patterns of bulk samples from P5:R06 250B are presented in Figure 3-45, and minerals identified based on these patterns are presented in Table 3-32. The positions of the d(060) lines at approximately 59–63° 2θ (CuKα) are presented in Table 3-33, and a close-up of this region is presented in Figure 3-46.

Overall, there were no major changes in XRD patterns of the samples from P5:R06 250B compared to reference samples (Figure 3-45). The position of smectite d(001) line in bulk samples appeared to have increased slightly in sample 525b, which may indicate a change from Na-exchanged clay to Ca or Mg-exchanged clay. However, the observed increase in exchangeable Ca content in this sample could not be exclusively assigned to an actual increase in exchangeable Ca (see Table 3-22 and subsequent discussion). Thus, another potential explanation could be an interference with the lubricant.

**Table 3-32. Minerals identified with XRD (x) or optical microscopy (o) from P5:R06 250B. Uncertain identifications are in brackets.**

| Sample | Smectite | Quartz | Plagio-clase | K-feld-spar | Cristo-balite | Hematite | Gypsum | Pyroxene | Illite/ mica | Carbonate | Zircon | Apatite |
|---|---|---|---|---|---|---|---|---|---|---|---|---|
| 525b | x | x | x | x | x | | | | | | | |
| 530b | x | xo | xo | x | x | xo | | | o | o | o | |
| 545b | x | xo | xo | x | x | | | | xo | o | o | o |
| 600b | x | xo | xo | x | x | xo | | | xo | o | o | o |
| 640b | x | xo | xo | x | x | x | | o | o | o | o | o |
| 730b | x | xo | xo | x | x | x | | | o | o | o | o |
| 770b | x | xo | xo | x | x | | x | | o | o | o | o |
| 830b | x | xo | xo | x | x | | x | | o | o | | o |
| R1b | x | xo | xo | x | x | o | | | xo | o | o | o |
| R2b | x | x | x | x | x | | x | | | | | |

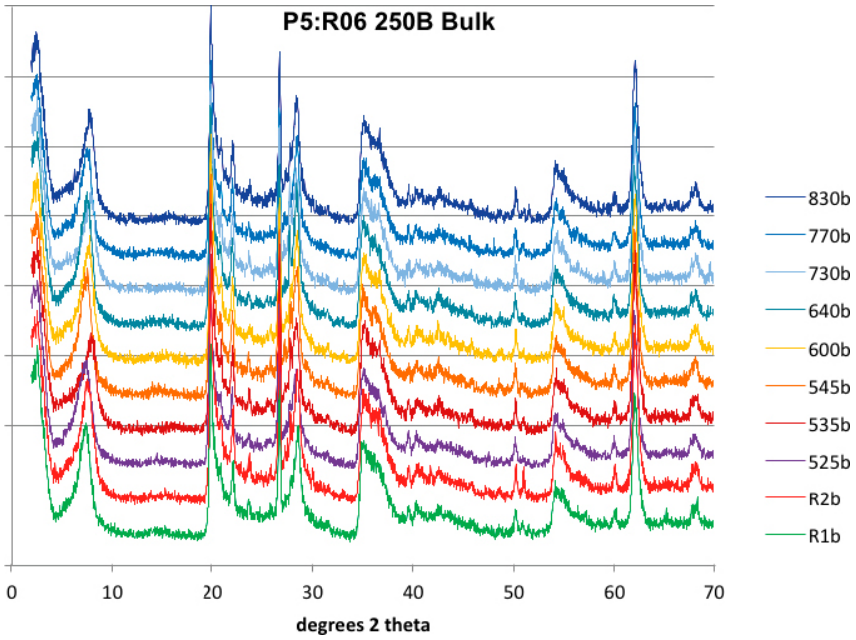


***Figure 3-45.*** *XRD patterns of random powders of bulk samples from profile P5:R06 250B.*

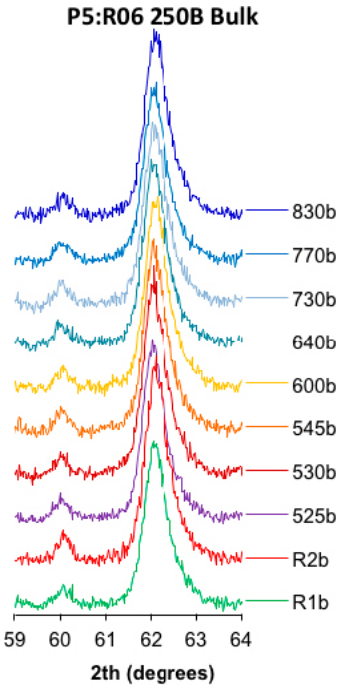


***Figure 3-46.*** *Close-up of the d(060) region in the XRD patterns of bulk samples from profile P5:R06 250B.*

*Clay fraction*

Despite careful purification of the clay fraction, homoionization to Mg-clay, and separation of the < 0.5 µm size fraction, a cristobalite peak at 4.04 Å was still present, but no other accessory minerals were noted (Table 3-33, Figure 3-47). Some variation in the smectite d(001) peak positions (air-dried mounts) can be seen, and may be caused by differences in relative humidity during the XRD-runs, or by variations in the thickness of the oriented mounts. It should also be noted that due to instrumental problems, the air-dried samples 530c, 545c, 600c, R1c, and R2c, were analyzed on different occasions, using a different X-ray diffraction device than used for the rest of the samples. The instrument used for the former samples was suspected of having a misalignment problem (cf. the following section). Based on XRD analysis of oriented mounts of the clay fractions and analyses of the d(060) regions of bulk samples, no change in clay mineralogy was noted.

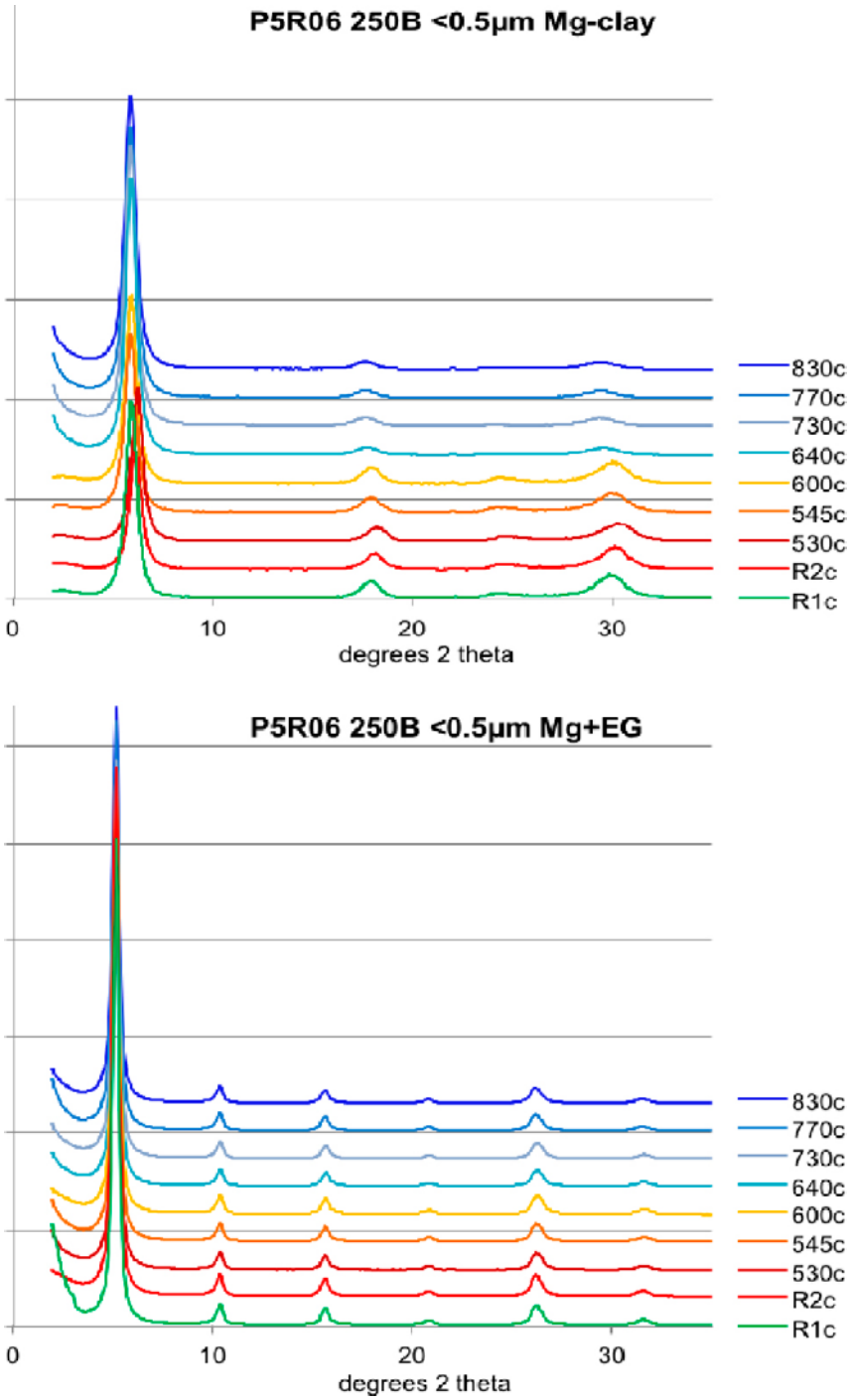


***Figure 3-47.*** *XRD patterns of air-dried (upper graph) and EG-solvated (lower graph) oriented clay fractions from profile P5:R06 250B. The air-dried samples R1c, R2c, 530c, 545c and 600c were analyzed using a different instrument than for the rest of the samples.*

**Table 3-33. Position of lines (in Å) used in identification of clay minerals. nd = not determined.**

| | Bulk samples | Mg-clay fraction | | | |
|---|---|---|---|---|---|
| Treatment | Randomly oriented | Oriented | Oriented+EG | | |
| Line/ interpretation | d(060) | d(001) | d(001) | d(002) | d(003) |
| 525 | 1.497 | nd | nd | nd | nd |
| 530 | 1.496 | 14.19 | 17.05 | 8.53 | 5.66 |
| 545 | 1.496; 1.508 | 15.01 | 17.06 | 8.53 | 5.66 |
| 600 | 1.496 | 14.93 | 17.06 | 8.52 | 5.65 |
| 640 | 1.497 | 15.03 | 17.03 | 8.52 | 5.65 |
| 730 | 1.497 | 15.13 | 17.04 | 8.52 | 5.65 |
| 770 | 1.496 | 15.12 | 17.07 | 8.54 | 5.66 |
| 830 | 1.496 | 15.12 | 17.06 | 8.54 | 5.67 |
| R1 | 1.496 | 14.89 | 17.03 | 8.53 | 5.66 |
| R2 | 1.496 | 14.40 | 17.09 | 8.54 | 5.67 |

## Block P6:R08 355A

*Bulk material*

X-ray diffraction patterns of bulk samples from P6:R08 355A are presented in Figure 3-48, and minerals identified based on these patterns are presented in Table 3-34. The positions of d(060) lines of clay minerals at approximately 59–63° 2θ (CuKα) are presented in Table 3-35, and a close-up of this region is shown in Figure 3-49.

Based on bulk XRD data, there were only a couple of differences in the XRD patterns of P6:R08 355A profile samples and reference samples. Firstly, gypsum ($CaSO_4$*$2H_2O$) showed more pronounced peaks at the canister contact than in reference samples, and was clearly present. Secondly, the samples that were taken just before (sample 620b) and after (sample 735b) the dismantling drill holes (see Figure 3-30), contained some unidentified peaks in the XRD patterns that were thought to be possible analytical artefacts, or impurities, maybe of organic origin, since no match was found in the mineral database. However, no evidence of such impurities was found in the chemical data. The position of the smectite d(001) line of the bulk sample 525b appeared to have increased a bit (Figure 3-48). No evidence of changes in exchangeable cation composition was, however, noted. No changes in peak positions or intensities was seen in the d(060) region (Figure 3-49).

**Table 3-34. Minerals identified with XRD (x) or optical microscopy (o). Uncertain identifications are in brackets.**

| Sample | Smectite | Quartz | Plagio-clase | K-feld-spar | Cristo-balite | Hematite | Gypsum | Unidentified | Illite/ mica | Carbonate | Zircon | Apatite |
|---|---|---|---|---|---|---|---|---|---|---|---|---|
| 525b | x | xo | xo | xo | x | | x | | o | o | | |
| 527b | x | xo | xo | x | x | (x)o | | | o | o | | |
| 574b | x | xo | xo | xo | x | xo | | | o | o | o | o |
| 620b | x | xo | xo | (o) | x | o | | x | o | o | o | |
| 735b | x | xo | xo | xo | x | o | | x | o | | o | o |
| 786b | x | xo | xo | (x) | x | xo | | | o | o | o | |
| 837b | x | xo | xo | o | x | x | | | o | o | o | |
| 846b | x | xo | xo | x | x | xo | | | o | o | o | o |
| R1b | x | xo | xo | xo | x | x | | | | o | | |
| R2b | x | xo | x | xo | x | xo | | | o | o | o | |

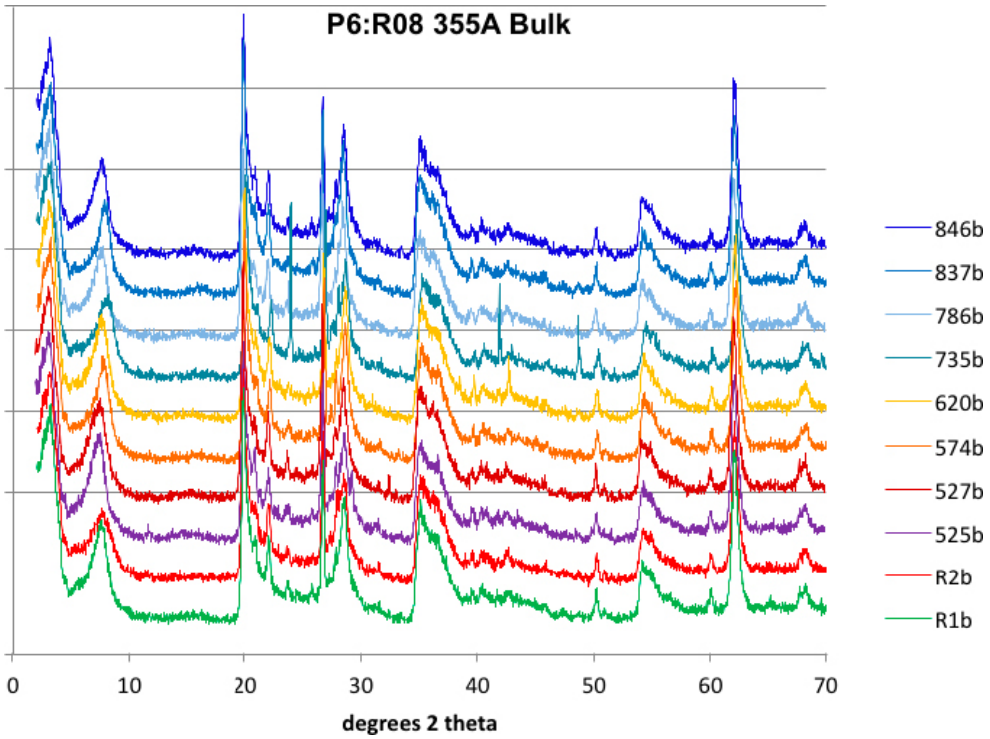


***Figure 3-48.*** *XRD patterns of random powders of bulk samples from P6:R08 355A.*

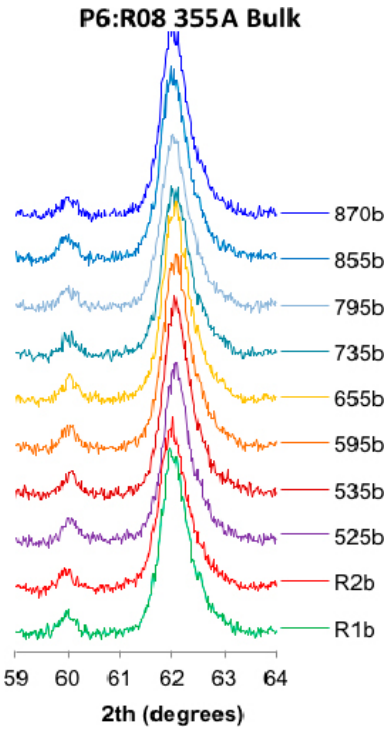


***Figure 3-49.*** *Close-up of the d(060) region in the XRD patterns of the Prototype profile P6:R08 355 A.*

*Clay fraction*

Based on other analyses of the clay fractions and of the position of the smectite d(060) peak in random samples, no significant changes in clay mineralogy were indicated, and yet, large variations in the position of the smectite basal reflections were seen among the samples. Furthermore, after EG-solvation several of the samples displayed irrational diffraction patterns, i.e. the d-spacings of the basal reflections did not obey the Bragg law, and the relative peak intensities were anomalous.

For this reason, a second set of oriented mounts was prepared of the Mg-saturated fine clay fractions, which were scanned both in an air-dried and EG-solvated state using another XRD-instrument (Seifert 3000 TT at Lund University; scan parameters according to Section 3.2.6) to test the reproducibility of the diffraction patterns. The XRD-patterns of the re-scanned samples did not reproduce the previously observed anomalies. The first series of X-ray scans was therefore rejected because the instrument used was suspected of having an incorrect alignment. For the sake of completeness, the XRD-data from the first scans are presented in Appendix 2.

In the second scan, the smectite in the air-dried, Mg-saturated state had basal spacings ranging from 14.9 to 15.1 Å (relative humidity 50 ± 10%). No significant difference was seen in the expansion behaviour of the smectite, which expanded to ~ 17 Å upon EG-solvation in all samples. The EG-solvated clay of both block and reference samples produced almost identical series of basal reflections, whose d-spacings closely obeyed the Bragg law (d(*00l*) = d(001)/*l*, where *l* is the integral order). The first to fifth order peaks are indicated in Figure 3-50 and their d-values are listed in Table 3-35. The expansion behaviour is indicative of well-ordered stacking sequences of smectite with insignificant interstratification.

Despite careful separation of the < 0.5 µm fraction, a cristobalite/opal peak at 4.03 Å was still present in all oriented XRD patterns but no other accessory minerals were identified (Figure 3-50).

**Table 3-35. Position of important lines (in Å) used in identification of clay minerals in profile P6R08 355A.**

| | Random bulk sample | Oriented air-dried Mg-clay | Oriented EG-solvated Mg-clay | | | | |
|---|---|---|---|---|---|---|---|
| | d(060) | d(001) | d(001) | d(002) | d(003) | d(004) | d(005) |
| 525c | 1.496 | 15.0 | 16.9 | 8.47 | 5.63 | 4.23 | 3.38 |
| 527c | 1.497 | 15.0 | 17.0 | 8.49 | 5.65 | 4.24 | 3.40 |
| 574c | 1.498 | 14.9 | 16.9 | 8.46 | 5.63 | 4.23 | 3.38 |
| 620c | 1.497 | 15.0 | 16.9 | 8.47 | 5.63 | 4.23 | 3.38 |
| 735c | 1.497 | 15.1 | 16.9 | 8.45 | 5.63 | 4.23 | 3.38 |
| 786c | 1.497 | 15.0 | 16.9 | 8.44 | 5.63 | 4.22 | 3.38 |
| 837c | 1.496 | 15.0 | 16.9 | 8.47 | 5.63 | 4.23 | 3.38 |
| 846c | 1.498 | 15.1 | 17.1 | 8.53 | 5.66 | 4.26 | 3.41 |
| R-1c | 1.496 | 15.1 | 16.9 | 8.46 | 5.63 | 4.23 | 3.38 |
| R-2c | 1.495 | 15.0 | 16.9 | 8.46 | 5.63 | 4.23 | 3.39 |

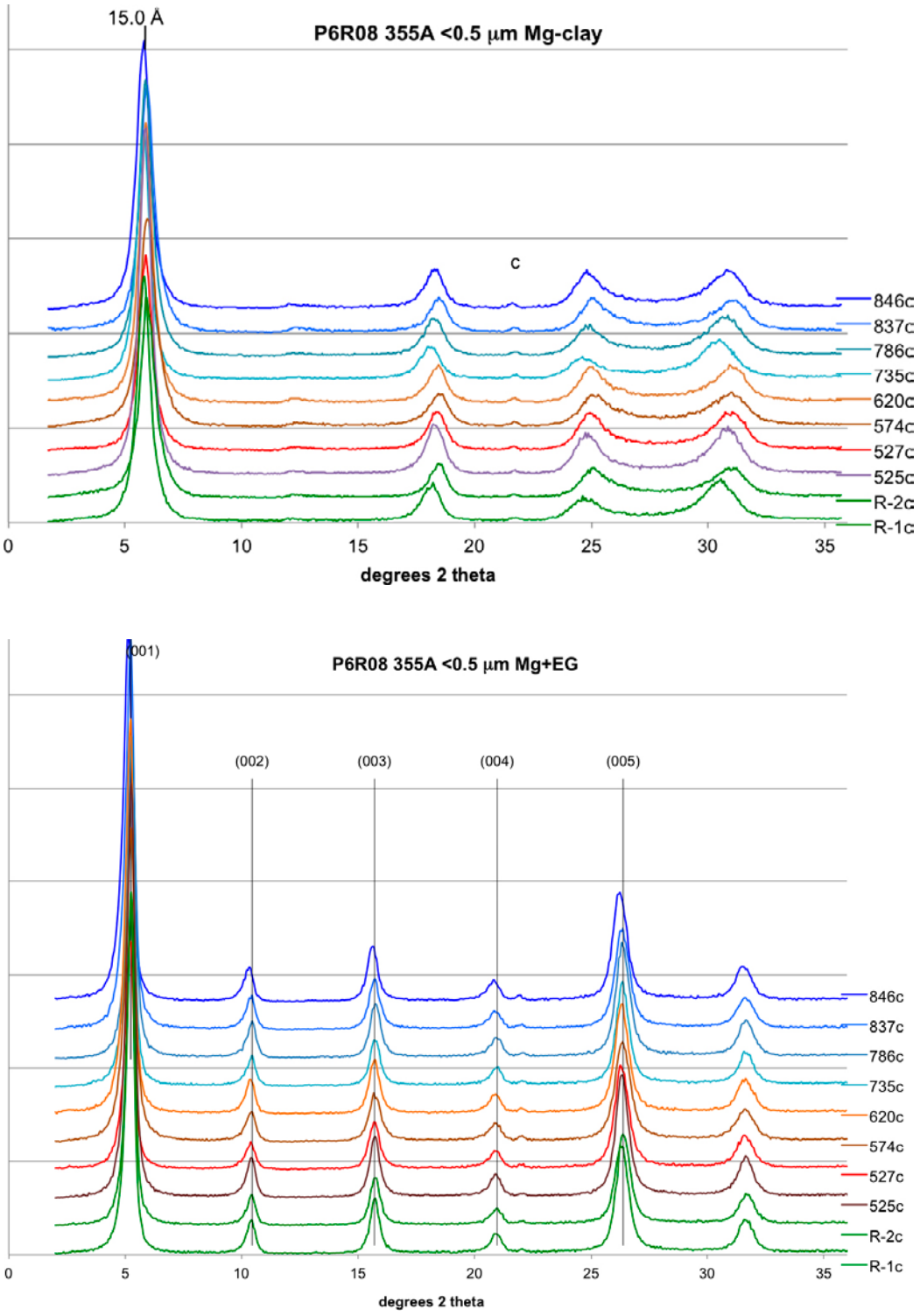


***Figure 3-50.*** *XRD patterns of air-dried (upper) and EG-solvated (lower) oriented Mg-saturated clay fractions from block P6:R08 direction 355A. c = cristobalite. The first (001) to fifth (005) order basal reflections are indicated in the EG-solvated profiles and d-values listed in Table 3-35.*

### *3.4.7.3 Rietveld refinement*

**Block P5:R06 250B**

Mineralogical compositions determined using Rietveld refinement are shown in Table 3-36. To assess the validity of the results, normative compositions were calculated for some minor or trace minerals assuming that all sulfate-sulfur was bound to gypsum ($CaSO_4*2H_2O$), all molybdenium to molybdenite ($MoS_2$), or that all inorganic carbon was bound to calcite ($CaCO_3$). As seen in Table 3-36, minor and trace mineral contents may be extensively overestimated as exemplified by the normative molybdenite content of sample 525b, or underestimated as shown by normative carbonate contents of all samples. Thus, all differences in mineralogical compositions are within the analytical uncertainty limits, and there are no changes in the mineralogical composition in block P5:R06 250B.

**Block P6:R08 355A**

Mineralogical compositions quantified with Siroquant software are presented in Table 3-37. To assess the validity of the results, normative compositions were calculated for some minor or trace minerals from the chemical compositions of bulk samples assuming that all sulfate sulfur was bound to gypsum ($CaSO_4*2H_2O$), or that all inorganic carbon was bound to calcite ($CaCO_3$). Analysis of mineralogical compositions with Rietveld refinement showed an increase in gypsum at the canister contact. Calculations based on the chemical analysis suggested an increase from 1.1 wt.% in the reference samples to 3.6 wt.% at the canister contact.

**Table 3-36. Mineralogical compositions for block P5:R06 250B quantified with the Siroquant software. Smectite and illite contents are adjusted by the potassium content of the clay fraction. For comparison, gypsum, calcite, and molybdenite calculated from chemical compositions are shown in parenthesis.**

| Sample | Smectite | Quartz | Plagio-clase | K-feld-spar | Cristo-balite | Hem-atite | Gypsum | Pyroxene | Molyb-denite | Illite/ mica | Calcite | Zircon | Apatite |
|---|---|---|---|---|---|---|---|---|---|---|---|---|---|
| 525b | 91.3 | 3.2 | 3.8 | 0.3 | 1.1 | | (1.7) | | 0.4 (0.04) | | (0.4) | | |
| 530b | 87.0 | 3.9 | 5.5 | 2.2 | 0.7 | 0.3 | (1.4) | | | 0.1 | 0.3 (0.5) | 0.0 | |
| 545b | 88.1 | 3.5 | 5.5 | 1.7 | 0.8 | | (1.1) | | | 0.2 | 0.2 (0.6) | 0.0 | 0.0 |
| 600b | 88.8 | 3.5 | 4.7 | 1.5 | 0.8 | 0.4 | (1.0) | | | 0.1 | 0.1 (0.5) | 0.0 | 0.0 |
| 640b | 87.2 | 3.0 | 4.9 | 1.4 | 1.0 | 0.1 | (1.0) | 2.2 | | 0.1 | 0.2 (0.6) | 0.0 | 0.0 |
| 730b | 86.9 | 3.8 | 5.8 | 2.2 | 0.5 | 0.5 | (1.0) | | | 0.1 | 0.2 (0.5) | 0.0 | 0.0 |
| 770b | 87.8 | 3.2 | 4.5 | 1.7 | 1.0 | | 1.6 (1.3) | | | 0.1 | 0.2 (0.5) | 0.0 | 0.0 |
| 830b | 87.6 | 3.5 | 4.9 | 1.3 | 0.7 | | 1.7 (1.4) | | | 0.1 | 0.1 (0.5) | | 0.0 |
| R1b | 90.1 | 3.1 | 3.5 | 1.0 | 1.3 | 0.6 | (1.2) | | | 0.2 | 0.2 (0.5) | 0.0 | 0.0 |
| R2b | 86.3 | 3.5 | 4.8 | 2.2 | 1.0 | 0.4 | 1.6 (0.9) | | | 0.1 | 0.1 (0.5) | 0.0 | 0.0 |

**Table 3-37. Mineral compositions for block P6:R08 355A as quantified with Siroquant software. Smectite and illite contents are adjusted by the potassium content of the clay fraction. For comparison, minor/trace mineral compositions (gypsum and calcite) calculated from chemical compositions of bulk samples are shown in parenthesis.**

| Sample | Smectite | Quartz | Plagio-clase | K-feld-spar | Cristo-balite | Hem-atite | Gypsum | Illite | Calcite | Zircon | Apatite |
|---|---|---|---|---|---|---|---|---|---|---|---|
| 525b | 87.8 | 4.0 | 3.3 | 0.8 | 1.0 | | 2.5 (3.6) | 0.3 | 0.2 (0.7) | | |
| 527b | 89.7 | 4.3 | 2.8 | 0.9 | 1.3 | 0.4 | (1.1) | 0.2 | 0.1 (0.4) | | |
| 574b | 88.6 | 3.6 | 3.8 | 2.2 | 0.7 | 0.6 | (1.1) | 0.2 | 0.3 (0.5) | 0.0 | 0.0 |
| 620b | 89.2 | 3.5 | 3.3 | 1.7 | 1.3 | 0.6 | (1.2) | 0.2 | 0.1 (0.6) | 0.0 | |
| 735b | 86.8 | 3.4 | 5.7 | 2.6 | 0.7 | 0.3 | (1.3) | 0.2 | 0.3 (0.6) | 0.0 | 0.0 |
| 786b | 87.7 | 3.6 | 5.4 | 1.6 | 1.1 | 0.4 | (1.2) | 0.1 | 0.1 (0.6) | 0.0 | |
| 837b | 89.1 | 3.6 | 4.3 | 1.3 | 1.1 | 0.4 | (1.1) | 0.1 | 0.1 (0.6) | 0.0 | |
| 846b | 88.4 | 3.3 | 4.3 | 1.7 | 1.3 | 0.7 | (1.4) | 0.2 | 0.1 (0.6) | 0.0 | 0.0 |
| R1b | 89.2 | 3.4 | 4.0 | 1.1 | 1.6 | 0.5 | (1.1) | 0.1 | 0.1 (0.4) | | |
| R2b | 89.2 | 3.3 | 4.7 | 0.9 | 1.2 | 0.5 | (1.1) | 0.1 | 0.0 (0.5) | 0.0 | |

#### *3.4.7.4 FTIR*

**Block P5:R06 250B**

FTIR patterns of bulk samples from block P5:R06 250B are shown in Figure 3-51 and for clay fractions in Figure 3-52. Band positions and corresponding band assignments are shown in Tables 3-38 to 3-39.

Based on FTIR analysis, bulk samples from P5:R06 250B consisted mainly of montmorillonite, which had bands at wavenumbers 3,637, 1,048, 919, 882, 851, 621, and 527 $cm^{-1}$. Compared to the reference samples an increase in intensity of organic impurities was observed in samples closest to the canister (525b and 530b). These organic impurities appeared at wavenumbers of 2,930 $cm^{-1}$ and 2,855 $cm^{-1}$.

It also appeared as there was a decrease in the intensity of the carbonate band at 1,420 $cm^{-1}$ especially in sample 530b. However, this observation (decrease in carbonate content) is not in line with the chemical and mineralogical compositions.

Clay fractions of P5:R06 250B consisted mainly of montmorillonite, which appeared at wavenumbers at 3,640, 1,047, 919, 882, 848, 622, and 526 $cm^{-1}$. In addition to montmorillonite, also amorphous silica or cristobalite was present appearing at wavenumber 799 $cm^{-1}$. No differences among the samples were noted in the smectite FTIR band intensities or positions (Figure 3-52, Table 3-39). Thus, no change in clay mineralogy or smectite composition was noted. The different shape of FTIR patterns of the clay fractions compared to the FTIR patterns of bulk samples is due to the background calibration with a moist KBr disc.

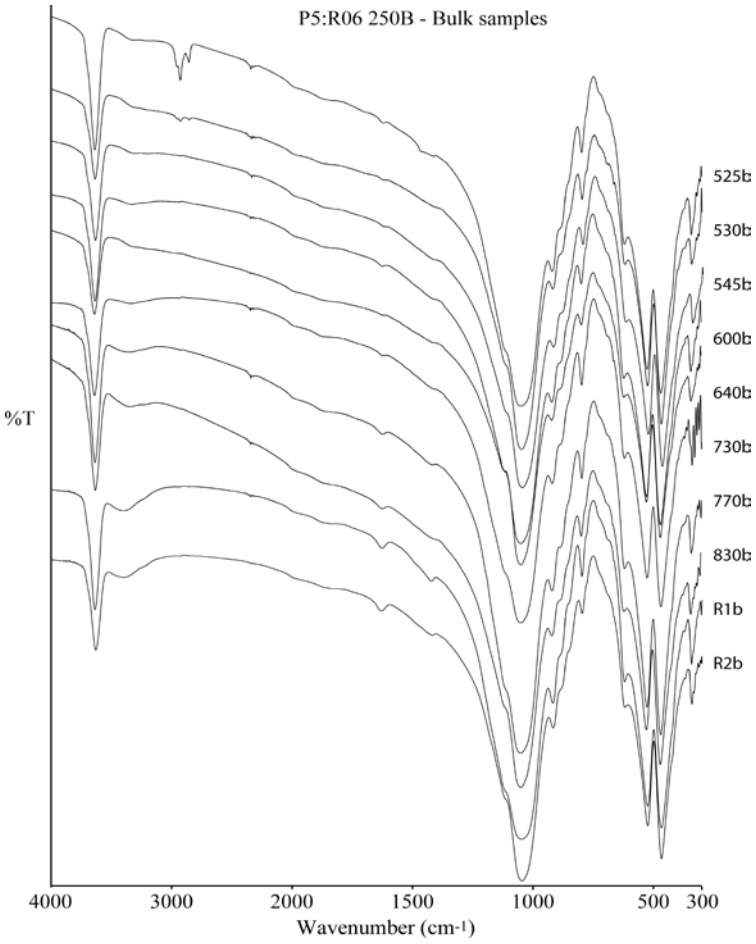


***Figure 3-51.*** *The FTIR patterns of bulk samples from block P5:R06 250B.*

**Table 3-38. The position of FTIR absorption bands of bulk samples from block P5:R06 250B, and band assignments (S = smectite, Q = quartz).**

| | OH-stretching bands (S) | $H_2O$-stretching | (Organic impurities) | (Organic impurities) | $H_2O$-bending | $CO_3^{2-}$ (Carbonates) | Si-O stretching, Si-O-Si | Si-O stretching, Tetrahedral Si (S, Q) | OH-bending, AlAlOH (S) | OH-bending, AlFeOH (S), $CO_3^{2-}$ (Calcite) | OH-bending, AlMgOH (S) | Si-O stretching (Q, free Si-O) | Si-O (Q) | Si-O (Feldspars) | Si-O (S) | Coupled Al-O + Si-O bending | Si-O bending (S) | Si-O bending (S) |
|---|---|---|---|---|---|---|---|---|---|---|---|---|---|---|---|---|---|---|
| 525b | 3,638 | 3,337 | 2,927 | 2,856 | 1,624 | 1,413 | 1,117 | 1,048 | 919 | 886 | 853 | 798 | 778 | 728 | 694 | 621 | 526 | 470 |
| 530b | 3,639 | 3,319 | 2,928 | 2,855 | 1,622 | – | 1,118 | 1,048 | 919 | 883 | 851 | 798 | 778 | 728 | 694 | 620 | 526 | 468 |
| 545b | 3,639 | 3,327 | – | – | 1,622 | 1,417 | 1,118 | 1,048 | 919 | 881 | 848 | 798 | 777 | 727 | 695 | 620 | 527 | 469 |
| 600b | 3,638 | 3,339 | – | – | 1,622 | 1,414 | 1,120 | 1,048 | 919 | 881 | 850 | 798 | 778 | 729 | 695 | 621 | 527 | 468 |
| 640b | 3,639 | 3,317 | – | – | 1,622 | 1,413 | 1,117 | 1,048 | 919 | 882 | 850 | 797 | 777 | 729 | 695 | 621 | 527 | 468 |
| 730b | 3,638 | 3,339 | – | – | 1,624 | 1,413 | 1,116 | 1,051 | 919 | 884 | 848 | 798 | 779 | 728 | 694 | 621 | 526 | 469 |
| 770b | 3,637 | 3,358 | – | – | 1,623 | 1,415 | 1,115 | 1,051 | 920 | 885 | 850 | 798 | 778 | 728 | 695 | 622 | 527 | 470 |
| 830b | 3,636 | 3,350 | – | – | 1,624 | 1,413 | 1,119 | 1,048 | 918 | 883 | 851 | 798 | 778 | 728 | 695 | 621 | 526 | 468 |
| R1b | 3,635 | 3,396 | – | – | 1,627 | 1,421 | 1,119 | 1,048 | 918 | 883 | 852 | 798 | 778 | 729 | 694 | 622 | 525 | 468 |
| R2b | 3,635 | 3,404 | – | – | 1,631 | 1,420 | 1,119 | 1,047 | 917 | 882 | 850 | 798 | 777 | 729 | 695 | 621 | 525 | 468 |

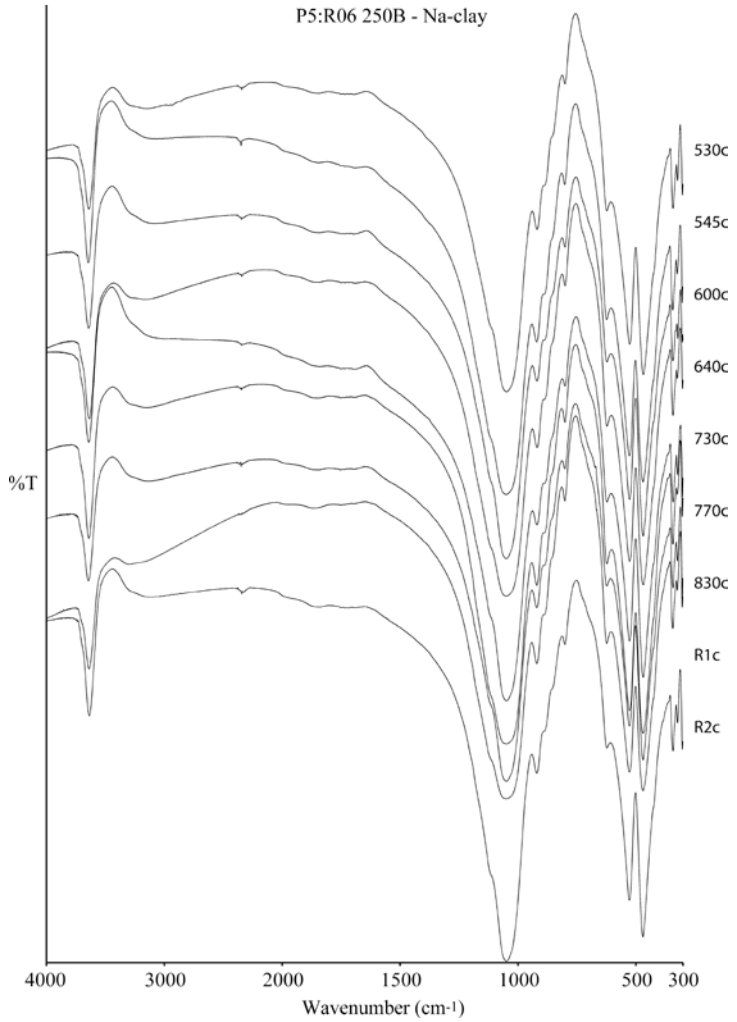


***Figure 3-52.*** *The FTIR patterns of clay fractions from block P5:R06 250B.*

**Table 3-39. The position of FTIR absorption bands of clay fractions from block P5:R06 250B, and band assignments (S = smectite, Q = quartz, nd = not determined).**

| | OH-stretching bands (S) | $H_2O$-stretching | (Organic impurities) | (Organic impurities) | $H_2O$-bending | $CO_3^{2-}$ (Carbonates) | Quartz, Cristobalite, Plagioclase | Si-O stretching, Si-O-Si | Si-O stretching, Tetrahedral Si (S, Q) | OH-bending, AlAlOH (S) | OH-bending, AlFeOH (S) | OH-bending, AlMgOH (S) | Si-O stretching (Q, free Si-O) | Si-O (Q) | Si-O (Feldspars) | Si-O (S) | Coupled Al-O+ Si-O bending | Si-O bending (S) | Si-O bending (S) |
|---|---|---|---|---|---|---|---|---|---|---|---|---|---|---|---|---|---|---|---|
| 525c | nd | nd | nd | nd | nd | nd | nd | nd | nd | nd | nd | nd | nd | nd | nd | nd | nd | nd | nd |
| 530c | 3,640 | 3,279 | – | – | – | – | – | 1,122 | 1,047 | 918 | 885 | 851 | 796 | – | – | – | 623 | 525 | 467 |
| 545c | 3,639 | 3,283 | – | – | – | – | – | 1,122 | 1,047 | 919 | 883 | 848 | 799 | – | – | – | 623 | 526 | 468 |
| 600c | 3,640 | 3,292 | – | – | – | – | – | 1,117 | 1,048 | 919 | 880 | 848 | 796 | – | – | – | 621 | 526 | 468 |
| 640c | 3,640 | 3,320 | – | – | – | – | – | 1,115 | 1,048 | 919 | 880 | 848 | 800 | – | – | – | 623 | 526 | 468 |
| 730c | 3,640 | 3,297 | – | – | – | – | – | 1,117 | 1,047 | 919 | 880 | 846 | 796 | – | – | – | 621 | 526 | 468 |
| 770c | 3,639 | 3,284 | – | – | – | – | – | 1,117 | 1,047 | 919 | 880 | 848 | 800 | – | – | – | 622 | 526 | 468 |
| 830c | 3,640 | 3,320 | – | – | – | – | – | 1,122 | 1,044 | 919 | 878 | 848 | 801 | – | – | – | 621 | 526 | 468 |
| R1c | 3,639 | 3,320 | – | – | – | – | – | 1,124 | 1,044 | 919 | 880 | 848 | 800 | – | – | – | 623 | 526 | 468 |
| R2c | 3,638 | 3,277 | – | – | – | – | – | 1,117 | 1,047 | 920 | 885 | 848 | 796 | – | – | – | 623 | 526 | 469 |

### Block P6:R08 355A

FTIR patterns of bulk samples from block P6:R08 355A are shown in Figure 3-53 and for clay fractions in Figure 3-55. Band positions and corresponding band assignments are shown in Tables 3-40 and 3-42.

**Table 3-40. The position of FTIR absorption bands of bulk samples from block P6:R08 355A, and band assignments (S = smectite, Q = quartz).**

| | OH-stretching bands (S) | $H_2O$-stretching | (Organic impurities) | (Organic impurities) | $H_2O$-bending | $CO_3^{2-}$ (Carbonates) | Si-O stretching, Si-O-Si | Si-O stretching, Tetrahedral Si (S, Q) | OH-bending, AlAlOH (S) | OH-bending, AlFeOH (S), $CO_3^{2-}$ (Calcite) | OH-bending, AlMgOH (S) | Si-O stretching (Q, free Si-O) | Si-O (Q) | Si-O (Feldspars) | Si-O (S) | Coupled Al-O+Si-O bending | Si-O bending (S) | Si-O bending (S) |
|---|---|---|---|---|---|---|---|---|---|---|---|---|---|---|---|---|---|---|
| 525b | 3,637 | 3,409 | 2,927 | 2,851 | 1,622 | 1,431 | 1,105 | 1,047 | 915 | 890 | 854 | 798 | 779 | 729 | 696 | 620 | 525 | 467 |
| 527b | 3,632 | 3,423 | 2,931 | 2,861 | 1,629 | – | 1,117 | 1,060 | 918 | 890 | 859 | 798 | 780 | 720 | 694 | 618 | 524 | 467 |
| 574b | 3,436 | 3,428 | 2,930 | 2,855 | 1,627 | 1,431 | 1,112 | 1,047 | 916 | 880 | 852 | 798 | 779 | 727 | 691 | 618 | 525 | 467 |
| 620b | 3,637 | 3,429 | 2,927 | 2,851 | 1,631 | 1,421 | 1,109 | 1,045 | 913 | 883 | 854 | 798 | 779 | 727 | 689 | 611 | 525 | 467 |
| 735b | 3,636 | 3,422 | 2,922 | 2,852 | 1,628 | 1,412 | 1,109 | 1,047 | 918 | 887 | 848 | 798 | 774 | 724 | 698 | 615 | 525 | 467 |
| 786b | 3,637 | 3,428 | 2,927 | 2,851 | 1,629 | 1,418 | 1,117 | 1,047 | 915 | 887 | 852 | 798 | 776 | 722 | 694 | 618 | 525 | 467 |
| 837b | 3,637 | 3,422 | 2,917 | 2,851 | 1,629 | 1,419 | 1,109 | 1,047 | 913 | 883 | 847 | 798 | 774 | 724 | 696 | 618 | 525 | 467 |
| 846b | 3,637 | 3,427 | 2,931 | 2,870 | 1,636 | 1,419 | 1,112 | 1,047 | 916 | 883 | 847 | 798 | 776 | 727 | 696 | 618 | 526 | 467 |
| R1b | 3,633 | 3,434 | 2,922 | 2,851 | 1,633 | 1,424 | 1,114 | 1,043 | 913 | 883 | 850 | 798 | 776 | 727 | 689 | 618 | 523 | 466 |
| R2b | 3,635 | 3,436 | 2,913 | 2,851 | 1,637 | 1,424 | 1,107 | 1,043 | 913 | 887 | 847 | 798 | 777 | 729 | 692 | 618 | 523 | 466 |

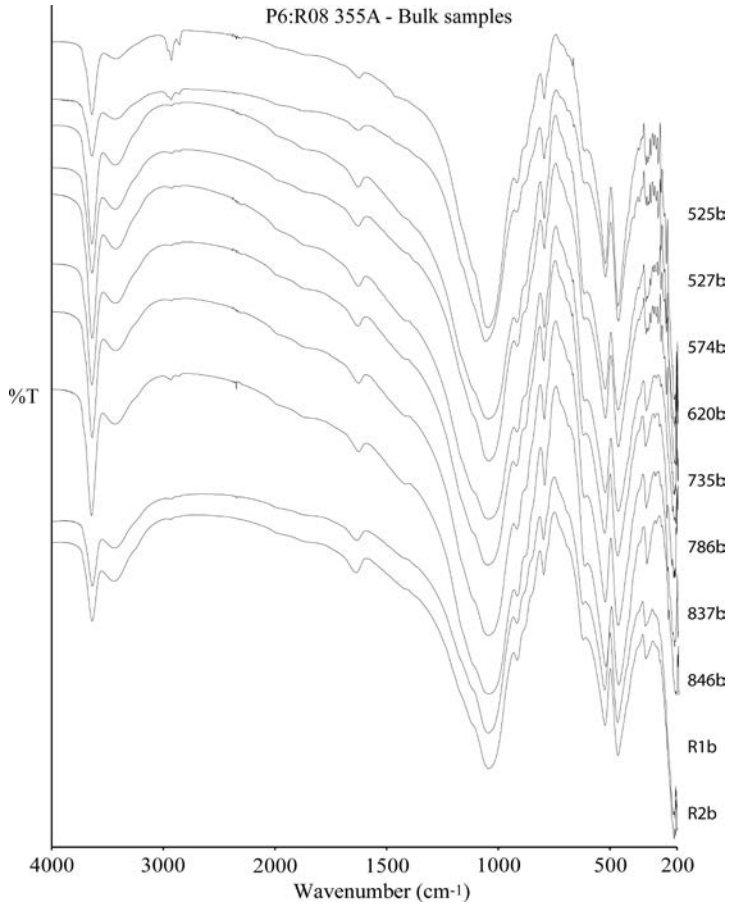


***Figure 3-53.*** *The FTIR patterns of bulk samples from block P6:R08 355A.*

Based on FTIR analysis bulk samples from P6:R08 355A consisted mainly of montmorillonite, which had bands at wavenumbers 3,636, 1,047, 915, 884, 851, 618, and 525 $cm^{-1}$. Bulk samples 525b, 535b, and 870b, which correspond to the two innermost and the outermost samples of block P6:R08 355A, showed an increase in the intensity of bands that can be assigned to organic impurities. These organic impurities appear at wavenumbers of 2,930 $cm^{-1}$, and 2,850 $cm^{-1}$. Also, it appeared that there was a decrease in the intensity of the carbonate band at 1,420 $cm^{-1}$ in the inner part of the profile (samples 525b and 527b). However, this observation (decrease in carbonate contents) is not in line with results of the chemical and mineralogical analyses.

FTIR pattern of the black substance floating on top of the suspension of sample 525b is presented in Figure 3-54 and band positions and their assignments in Table 3-41. In contrast to all other FTIR patterns reported in this report, Figure 3-54 presents FTIR pattern of a sample that was not dried at 150°C to remove the moisture, since organic material may start to decompose at temperatures used for removal of adsorbed water from clay samples.

The FTIR analysis of the black floating substance confirmed that the substance is lubricant, as it consisted mostly of organic substances that produced bands at 3,230, 2,955, 2,921, 3,873, 2,850, 1,576, 1,539, 1,469, 1,435, 1,419 and 1,348 $cm^{-1}$. Also the FTIR bands of minerals typical of the original bentonite (especially those of montmorillonite) were recognizable in this sample, even though not included in the bands listed.

Clay fractions of P6:R08 355A consisted mainly of montmorillonite, which appeared at wavenumbers at 3,637, 1,048, 919, 879, 847, 619, and 526 $cm^{-1}$. There was no change in intensities or positions of bands in the clay fractions of profile P6:R08 355A compared to reference samples, except bands at wavenumbers 2,930 $cm^{-1}$ and at 2,850 $cm^{-1}$ in two samples (525c and 527c) closest to the canister contact, which were arising from organic impurities (Figure 3-55, Table 3-42), similarly as in bulk samples. Hence, no change in clay mineralogy or smectite composition was noted. In addition to montmorillonite, free Si or cristobalite band was present and appeared at wavenumber 799 $cm^{-1}$.

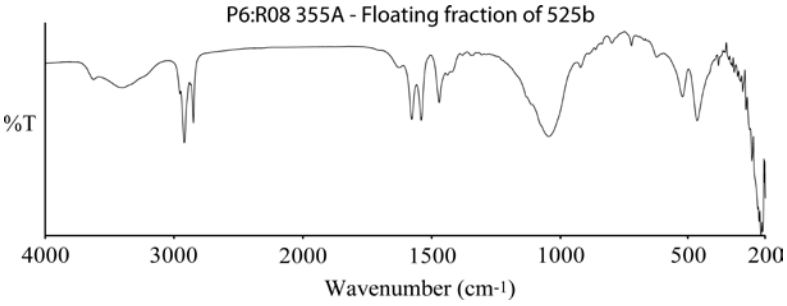


***Figure 3-54.*** *The FTIR pattern of black floating material extracted from sample 525b, block P6:R08 355A.*

**Table 3-41. The positions of FTIR absorption bands and band assignments (except those of smectite) for the black material that floated on top of sample 525b.**

| |  | C-H | $CH_3$ | $CH_2$(stearate) | $CH_3$ | $CH_2$ (stearate) | $COO^-$ (stearate) | N-H | $CH_3$, $CH_2$ | C-O stretching | $CO-CH_2$ | $CH_2$, $COO^-$ (stearate) |
|---|---|---|---|---|---|---|---|---|---|---|---|---|
| 525b black | | 3,229 | 2,955 | 2,921 | 2,873 | 2,850 | 1,576 | 1,539 | 1,469 | 1,435 | 1,419 | 1,348 |

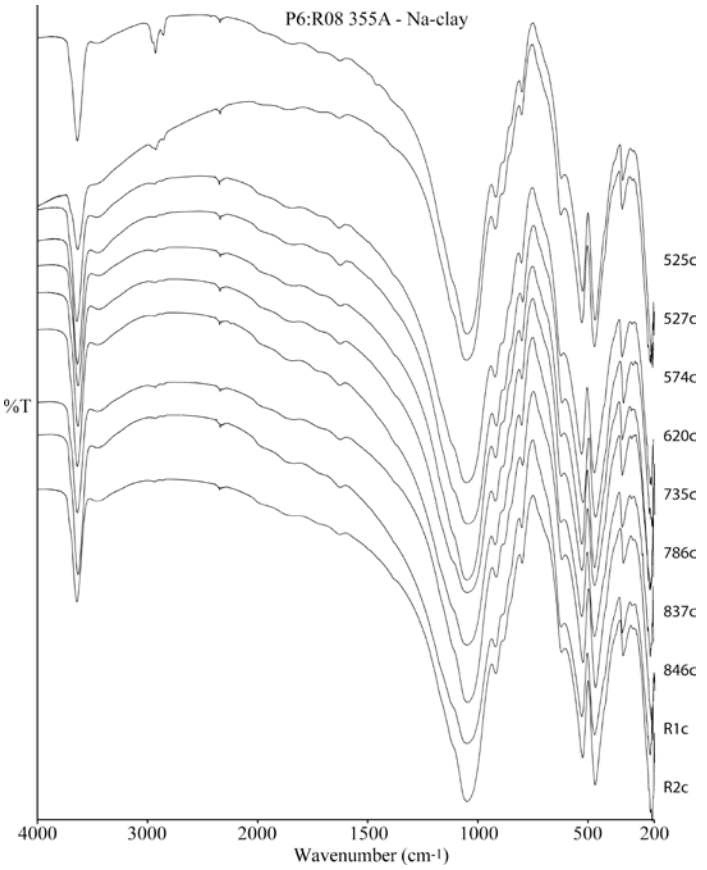


***Figure 3-55.*** *The FTIR patterns of clay fractions from block P6:R08 355A.*

**Table 3-42. The position of FTIR absorption bands of P6:R08 355A clay fractions, and band assignments.**

| | OH-stretching bands (S) | $H_2O$-stretching | (Organic impurities) | (Organic impurities) | $H_2O$-bending | $CO_3^{2-}$ (Carbonates) | Quartz, Cristobalite, Plagioclase | Si-O stretching, Si-O-Si | Si-O stretching, Tetrahedral Si (S, Q) | OH-bending, AlAlOH (S) | OH-bending, AlFeOH (S) | OH-bending, AlMgOH (S) | Si-O stretching (Q, free Si-O) | Si-O (Q) | Si-O (Feldspars) | Si-O (S) | Coupled Al-O+Si-O bending | Si-O bending (S) | Si-O bending (S) |
|---|---|---|---|---|---|---|---|---|---|---|---|---|---|---|---|---|---|---|---|
| 525c | 3,637 | 3,442 | 2,927 | 2,851 | 1,627 | 1,461 | – | 1,114 | 1,048 | 919 | 878 | 843 | 800 | – | – | – | 620 | 525 | 468 |
| 527c | 3,629 | 3,448 | 2,927 | 2,851 | 1,624 | 1,459 | – | 1,114 | 1,051 | 919 | 878 | 850 | 800 | – | – | – | 620 | 526 | 468 |
| 574c | 3,637 | 3,437 | – | – | 1,624 | – | – | 1,114 | 1,047 | 919 | 880 | 847 | 799 | – | – | – | 620 | 526 | 468 |
| 620c | 3,636 | 3,442 | – | – | 1,624 | – | – | 1,119 | 1,047 | 919 | 880 | 850 | 795 | – | – | – | 623 | 527 | 468 |
| 735c | 3,637 | 3,437 | – | – | 1,627 | – | – | 1,114 | 1,048 | 919 | 878 | 845 | 799 | – | – | – | 620 | 526 | 468 |
| 786c | 3,637 | 3,423 | – | – | 1,624 | – | – | 1,117 | 1,047 | 919 | 883 | 843 | 798 | – | – | – | 620 | 526 | 468 |
| 837c | 3,637 | 3,433 | – | – | 1,627 | – | – | 1,114 | 1,047 | 919 | 880 | 847 | 799 | – | – | – | 618 | 523 | 468 |
| 846c | 3,637 | 3,452 | – | – | 1,627 | – | – | 1,117 | 1,048 | 919 | 878 | 843 | 795 | – | – | – | 621 | 526 | 468 |
| R1c | 3,637 | 3,437 | – | – | 1,627 | – | – | 1,117 | 1,048 | 916 | 878 | 847 | 799 | – | – | – | 618 | 526 | 468 |
| R2c | 3,637 | 3,428 | – | – | 1,629 | – | – | 1,119 | 1,048 | 919 | 878 | 845 | 798 | – | – | – | 618 | 526 | 468 |

## 3.5 Results for profile P6R10 210

### 3.5.1 Visual observations

Parts of the bentonite buffer had a darker tone in the innermost 1 cm towards the copper canister. This discoloration disappeared upon drying (Figure 3-56), indicating that it may be due to a redox active element such as iron in the bentonite clay. Approximately 1 mm of the surface of the clay at the clay-canister interface was also discoloured, but this discoloration did not disappear upon drying and was attributed to the Molykote lubricant used during the block manufacturing (Figure 3-56; compare also with Figure 3-30). In some parts approximately 0–5 mm from the canister, a white, crystalline phase could be seen. This was attributed to a precipitated salt and was specifically sampled for XRD analysis.


***Figure 3-56.*** *In some parts of the buffer the innermost 1 cm was darker; this darkness irreversibly disappeared upon drying.*

### 3.5.2 Fe K and Cu K X-ray absorption spectroscopy (XANES)

X-ray absorption spectroscopy was used to study the redox chemistry of the iron and copper phases in the bentonite clay. This technique has successfully been used to analyze Fe(II)/Fe-total ratios in bentonite (Kumpulainen et al. 2011). XANES spectra of the innermost sample (0.5 mm from canister) and of the original MX-80 clay show that the exposed sample has an absorption edge at a lower energy compared to the original clay (Figure 3-57), which means that the former sample has higher Fe(II)/Fe-total ratio. Both the experiment sample at 0.5 mm and the original clay are situated in between the Fe(II) and the Fe(III) references (Figure 3-57), indicating that both samples are mixtures of Fe(II) and Fe(III). By linear combination analysis using the reference spectra it was possible to determine the numerical value of the Fe(II)/Fe-total ratio semi-quantitatively, and all six samples analysed (0.5–47 mm from canister) had elevated Fe(II) content in relation to the original clay (Figure 3-58). This is the first time this is found in a field experiment with bentonite and copper canisters and is also supported by the Mössbauer analyses performed in parallel on comparable samples (Table 3-17).

Cu K XANES spectra were collected for the two innermost samples (0.5 mm and 3.5 mm from the canister), however only in the innermost sample an absorption edge could be measured, hence in the 3.5 mm sample the Cu content was too low to measure for the used setup. The Cu-spectrum of the bentonite sample was compared to malachite (basic Cu(II)-carbonate) and Cu(II)-montmorillonite (ion exchanged from Na-montmorillonite by Clay Technlogy). The exposed bentonite sample had an absorption edge at lower energy compared to the Cu(II) references (Figure 3-59). The very low signal introduces a high uncertainty, but the result indicated that the copper phase in the bentonite was not comparable to a well defined Cu(II)-phase, such as e.g. an oxide/silicate/carbonate. Instead the phase could be metallic copper, a Cu(I)-phase, or some type of sulfide of (Cu(I) or Cu(II)) that sometimes behaves differently compared to, for instance, oxides.

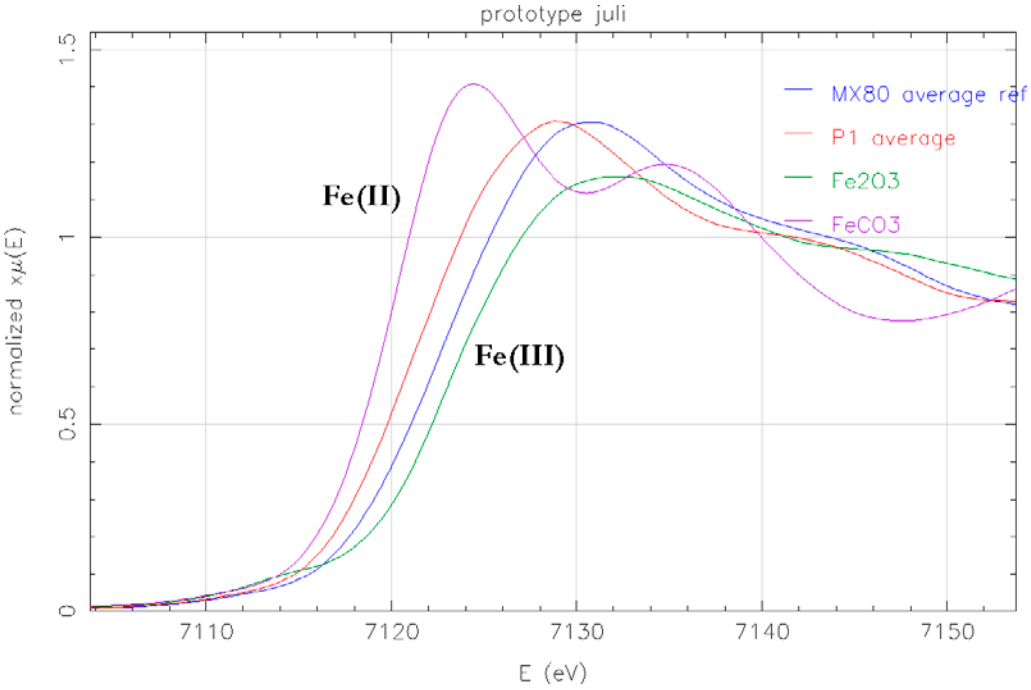


***Figure 3-57.*** *Fe K XANES spectra of (from the left): Fe(II)-carbonate (siderite; Ivigtut), P1 (bentonite sample 0.5 mm from the canister, P6R10 210 525b), MX-80 reference sample and Fe(III)-oxide (hematite; $Fe_2O_3$). The change in the absorption curve reflects the difference in the Fe(II)/Fe(III) ratio.*

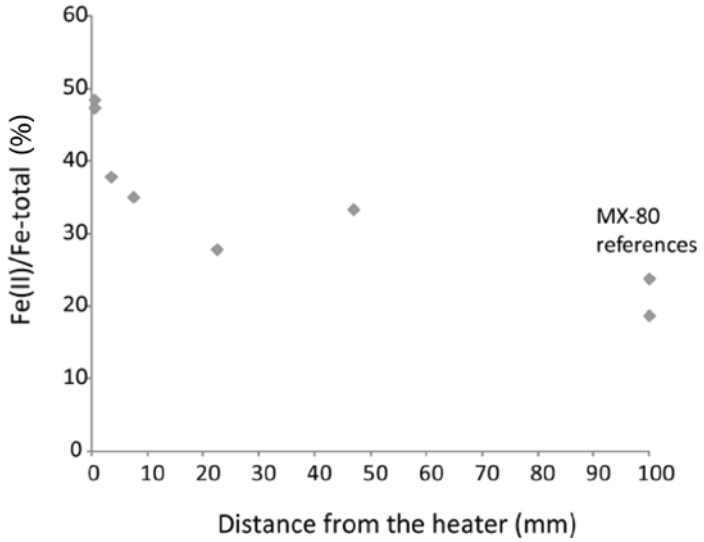


***Figure 3-58.*** *The Fe(II)/Fe-total content as a function of the distance from the canister in profile P6R10 210 (0–47 mm from the canister surface). The Fe(II)/Fe-total ratio was determined using linear combination fit of reference XANES spectra.*

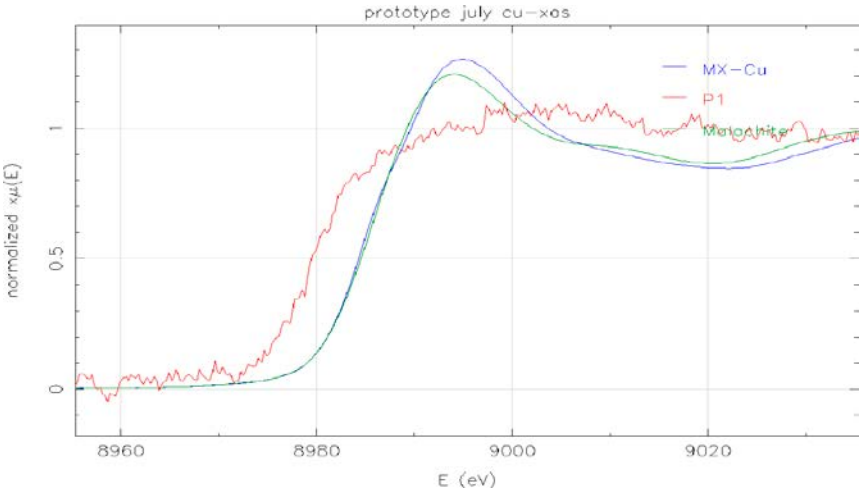


***Figure 3-59.*** *Cu K XANES spectrum of (from the left): the P1 sample (sample P6R10 210 525b from the canister/bentonite interface), Wyoming Cu(II)-montmorillonite (ion exchanged montmorillonite; Clay Technology) and malachite (basic Cu(II)-carbonate).*

### 3.5.3 Synchroton powder X-ray diffraction

One profile was sampled (P6 R10 210) as well as a white precipitate that was visually observable in some other samples from the same section. A change in the montmorillonite basal spacing (001 reflection) towards higher spacing was observed (Figure 3-60a). This is normally seen when the ratio of divalent to monovalent interlayer cations increases, as smectites with divalent cations (e.g. $Ca^{2+}$, $Mg^{2+}$) hold more water at ambient relative humidity compared to smectites with monovalent cations (e.g. $Na^{+}$). Secondly, a rather strong reflection was visible between the 001 reflection and the 4.5 Å hk reflection. This reflection was also found in the sampled white precipitate and was attributed to gypsum (Figure 3-60b), which is naturally present in the MX-80 bentonite, and in this case enriched in the innermost part towards the canister (see also Figure 3-15). The d-value of the 060 reflection differs between dioctahedral and trioctahedral smectites, hence a change in the octahedral sheet of the montmorillonite crystal structure would likely have an impact on the position of the 060 reflection. By fitting a Gaussian function to the 060 d-value by a least square method, a statistical analysis of the variation could be performed, but no changes could be observed (Figure 3-60c).

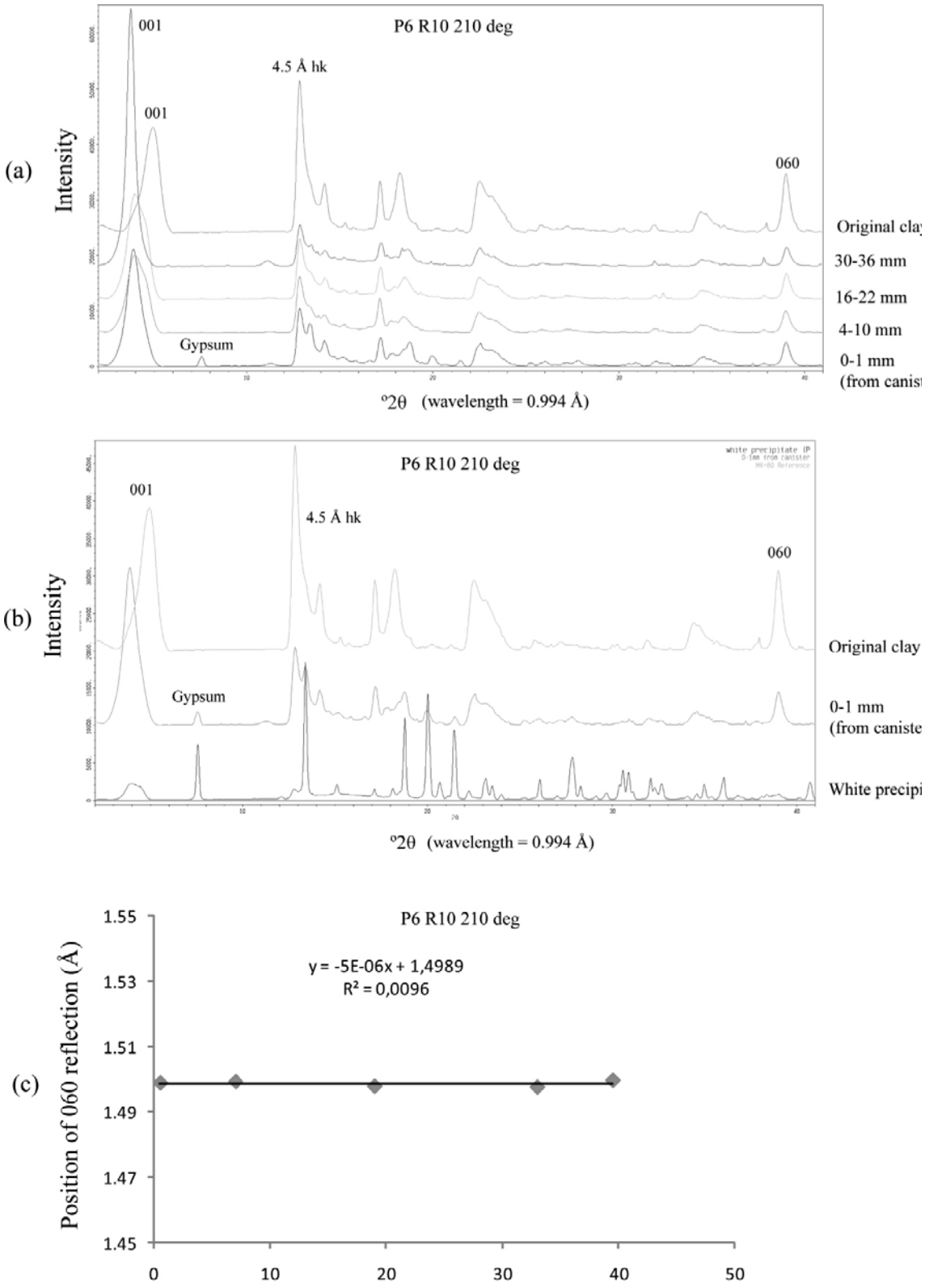


***Figure 3-60.*** *a and b. Synchrotron powder XRD data for bulk samples and a precipitate from profile P6R10 210, 0–36 mm from the canister. c. the fitted d-value of the 060 reflection. Wavelength = 0.994 Å.*

## 3.6 Summary of the chemical-mineralogical investigations

At the retrieval in 2011 the bentonite buffers in deposition hole 5 and 6 had been subjected to elevated temperature and wetting by saline water from the host rock for almost eight years. The recorded temperature evolution at mid height in the buffers showed that the maximum temperature never exceeded ~ 85ºC during the test period, which is below the maximum temperature stipulated in the design criteria for the KBS-3 concept. The outer parts of both buffers were never heated above ~ 60ºC. Higher temperature had, however, been maintained for longer time in deposition hole 5 than in deposition hole 6.

The state of the buffers in terms of water content and water saturation at the excavation showed that none of the two buffers was homogeneous after almost 8 years of wetting, and large variations existed, both between the deposition holes, between blocks from the same hole, and also within one and the same block. While subjected to similar temperature regimes, the water supply, and thus the saturation, differed in the two analysed profiles in block R06 from deposition hole 5 – one profile was "wet" ($w>0.27$) and one was "dry" ($w<0.21$). The two blocks (R05 and R08) from deposition hole 6 had been subjected to rather similar temperature evolution and the water content at the excavation was similar and intermediate of the two extremes in block R06 from deposition hole 5.

The top blocks (R10) from the two buffers represented a somewhat "cooler" regime but the number/ type of analyses performed was limited and specialized and included only the innermost centimeters of the blocks.

The results of the chemical and mineralogical analyses performed in parallel at different laboratories are summarized below:

- Due to the wetting with groundwater (~ 8,000 mg Cl/L) the chloride concentration in the three saturated profiles had increased 3 to 6-fold. Soluble accessory minerals in the bentonite, mainly gypsum but also calcite in one profile, had been redistributed and re-precipitated close to the canister. In contrast, the chloride and sulfate concentrations in the "dry" profile had remained at the level of the reference bentonite.
- The major change in the exchangeable cation pool was a small but general loss in magnesium relative to the reference concentration, in a large part of all four profiles investigated.
- Non-exchangeable magnesium in bulk samples (MgO evaluated on ignited basis) had increased relative the reference level in the inner parts of all four profiles investigated, suggesting a transfer of magnesium along the thermal gradient, and accumulation in the warmest part of the buffer. The maximum increases in Mg were observed in the profiles from the warmest block (P5R06). The sink for magnesium could not be identified with any of the methods used (XRD, FTIR, SEM) but the Mg-bearing phase(s) was apparently very fine-grained and of low solubility, since the magnesium concentration was higher than the reference level also in most of the $< 0.5$ µm fraction of these samples.
- The FTIR-and XRD-characteristics, the calculated structural smectite formulae, and the CEC properties of the purified, Na-converted $< 0.5$ µm fractions provided no significant evidence of any structural changes in the montmorillonite. All formula calculations were, however, based on the assumption that all magnesium in the chemical analyses was in the octahedral sheet of the smectite, and it remains to be established whether this allocation of magnesium has a true structural foundation, or whether a neoformed phase is the sink for magnesium.
- The bentonite blocks for the buffers had been compacted by a tentative method in which a lubricant had been applied to the walls of the mold used in the block manufacturing. The samples of the inner (and outer) surfaces of the blocks investigated were clearly contaminated by "organic carbon" (2–3% C) and had elevated concentrations of S, Mo, Zn, and P, which are some of the main constituents of the lubricant. Apart from causing inflated concentration values for these "indicator" elements, the lubricant also causes dilution effects in several of the analyses of the contaminated samples, which must be considered in interpretations of the data.

- In general, CEC of the contaminated block surfaces deviated significantly from CEC of the reference samples, but the former values must be considered uncertain because of the dilution effect in the analysis, and also because the lubricant may interfere in the CEC determination. For the rest, the variation in CEC within the blocks was small, but some blocks tended to have systematically lower CEC -by up to 4 meq/100 g- than the corresponding reference bentonite. This difference was larger than the normal scatter in CEC determinations on MX80 by the Cu-trien method, and suggested that an actual difference in CEC might exist between the exposed and unexposed bentonite in some blocks. In contrast, CEC of the < 0.5 μm fractions from block samples and references was comparable, suggesting that CEC of the smectite was unchanged. The fact that these somewhat contradictory results were observed for at least two blocks that were examined by different laboratories calls for further investigations to establish the cause of the different trends in CEC of the bentonite and of the smectite.
- Samples of the canister/bentonite interface (~ 1 mm thick samples) had elevated copper concentrations in all blocks, but the maximum concentration of the profiles was variable, ranging from 35 to 670 ppm Cu. Area analyses (50 μm × 50 μm) performed from the canister/bentonite interface to a depth of ~ 1 mm by use of SEM-EDX showed that copper was irregularly distributed – the copper content ranged from background values up to a few weight % in nearby areas, with a mean value of 1.9 weight % for the first 200 μm. Copper existed mainly in a non-exchangeable form and, according to Cu K XANES spectra, copper was probably present either as a Cu(I)-phase, some type of sulfide, or as metallic copper.
- Mössbauer spectroscopy and Fe K XANES performed on samples from the inner part of the buffer in deposition hole 6 showed an increase in the ratio Fe(II)/Fe(III) of the field-exposed bentonite. As no increase in total iron was observed, this indicates reduction of Fe(III) to Fe(II) under field-conditions. The electron source for the reduction is currently unknown.

# 4 Conclusions

The stability of smectite in different geological environments was one of the reasons for selecting smectite-rich clay, such as bentonite, as buffer material in the Swedish KBS-3 concept for a repository for high-level radioactive waste. Nevertheless, the results of geochemical modeling and laboratory experiments predict that chemical/mineralogical perturbations will occur in a buffer of bentonite under the hydrothermal regime that is expected under repository-like conditions.

The investigation of MX-80 bentonite subjected to heating at temperatures up to ~ 85° C and wetting by groundwater in the eight-year long Prototype Repository field-test showed that dissolution/precipitation- and cation exchange reactions along with the water saturation under non-isothermal conditions resulted in redistribution of soluble accessory minerals in the bentonite, such as gypsum and calcite. These phases accumulated in the warmest parts of the buffers, where also a – so far unidentified – magnesium phase of low solubility precipitated. No structural alteration of the montmorillonite was detected. At the contact with the canister, small amounts of copper had been incorporated in the bentonite due to corrosion of the canister. At the retrieval, the ratio Fe(II)/Fe(III) of bentonite from the inner part of the buffer was higher than in references indicating reduction of iron under field-conditions.

A minor increase of the brittleness of the bentonite in the warmer parts of the buffer was observed, but no evident coupling was found between the change of the hydro-mechanical behavior of the bentonite and the geochemical changes. The field-exposed bentonite also had somewhat lower hydraulic conductivity than the reference specimens, but this change was not correlated to the position of the samples in the buffer, and thus, not to the maximum temperature to which the samples had been exposed.

The hydro-mechanical changes and the main geochemical reactions highlighted in the investigation of the Prototype Repository buffer are qualitatively analogous to observations made in investigations of the previous field tests LOT and CRT, which had the same components, i.e. buffers of MX-80 bentonite and heaters/canisters of copper, but were of shorter duration and run at slightly (CRT) or significantly higher temperatures (LOT).

# 5 Chemical and mineralogical characterization of the tunnel backfill material

## 5.1 Introduction

The Prototype Repository field experiment consisted of six full-scale deposition holes with copper canisters and bentonite buffers. The gallery was divided into two sections (cf. Figure 1-2) and the corresponding two compartments of the deposition tunnel had been sealed with a plug of concrete (Portland cement) after completed backfilling of the tunnel. The backfill material was a mixture of crushed rock and bentonite that had been compacted to the target density *in situ* in the tunnel.

Numerous laboratory and field observations, studies of natural analogues, and numerical modeling have demonstrated that the reactions in concrete generate a diffusive hyper-alkaline plume, which will modify the porewater chemistry in the bentonite near a concrete/bentonite interface. The pore fluid chemistry of concretes is complex and depends on the concrete composition and its alteration stage and evolves over time from K-Na-Ca-OH- to Ca-OH-dominated. Apart from fast cation exchange reactions, slow reactions between the fluid and smectite and/or other minerals in the bentonite will occur, and secondary phases may precipitate. These reactions may consume or generate hydroxide ions and the sequence of neoformed phases will also evolve over time and in space (review in Gaucher and Blanc 2006, Devol-Brown et al. 2007, Savage et al. 2007, De Windt et al. 2008, Alexander et al. 2013).

This part of the Prototype report presents chemical and mineralogical characteristics of the tunnel backfill material in the vicinity of one of the concrete plugs after the eight year-long field test, during which the backfill was subjected to hydration by a natural Na-Ca-Cl type groundwater (~ 8,000 mg $Cl^-$/L) and to contact with leachates from the concrete. The state of the backfill material at the time of excavation in terms of water content and dry density is shown in Figure 1-9 and Figure 1-10.

## 5.2 Materials and methods

### 5.2.1 Materials

The backfill material consisted of Na-converted bentonite (30% by dry weight) from the island of Milos, Greece (delivered through LKAB), and ballast (70%) consisting of the excavated TBM-muck of granodioritic bedrock, crushed to grain sizes ranging from 0 to 20 mm (Gunnarsson 2002). Since the aim of the analyses was to provide mineralogical and chemical data for characterisation of the bentonite, it was considered essential that a fairly pure and representative fraction of the bentonite could be extracted from the backfill without changing, for instance, the soluble salt content and the exchangeable cation pool. The bulk backfill material was therefore dried at 50°C, aggregates cemented by clay were crushed gently by use of a pestle and mortar, and the fraction < 1 mm was separated by dry-sieving.

After homogenisation by grinding, the < 1 mm fraction was analyzed together with the Na-converted < 0.5 µm fraction according to the flow chart in Figure 5-1. The procedure used for purification and homo-ionisation of the latter fraction was the same as described in Section 3.2.2.

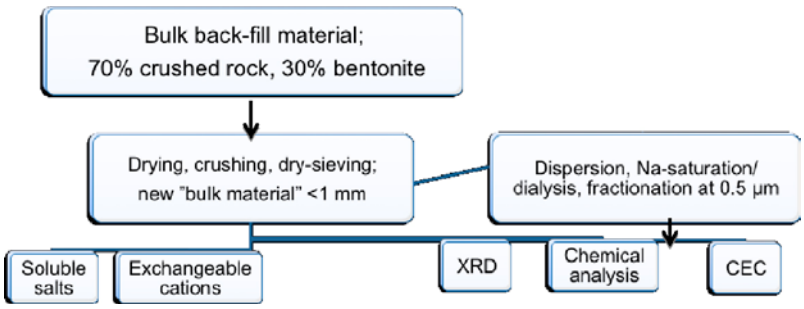


***Figure 5-1.*** *Flow chart showing the sample pretreatments and analyses.*

### 5.2.2 Sampling

Large pieces with an average width of about 10 cm were cut out from the backfill material *in situ* along a profile perpendicular to the inner concrete plug in the outer section II, at mid height in the deposition tunnel (cf. Figure 1-13). Awaiting analysis, the block pieces were stored in evacuated and welded bags of aluminum laminate. A total of eight laboratory samples with a width of 20 mm were taken of selected large pieces in the interval 0–1 m. The innermost 120 mm at the plug was sampled contiguously. The sample taken 1 meter from the concrete was used as reference, since no backfill material was available that had not been exposed to tunnel conditions. Samples were labeled according to the general nomenclature rules given in Section 1.3.2, for instance, a sample labeled PBF 50b means that it consists of material from the Prototype BackFill, 50 millimeters from the inner concrete plug (in section II). A suffix **b** or **c** indicates whether the sample consists of bulk material (in this case material < 1 mm) or the clay fraction (in this case material < 0.5 µm).

The samples and analytical methods are listed in Table 5-1.

**Table 5-1. Samples and chemical/mineralogical analyses of the tunnel backfill material from the Prototype field test. Figures indicate the number of analyses.**

| Sample Id | "Bulk" < 1 mm | | | | | | Na-saturated < 0.5 µm fraction | | | |
|---|---|---|---|---|---|---|---|---|---|---|
| | Water-soluble salt | Chemical composition | Exchange. cations | CEC | XRD random | SEM-EDX | Chemical composition | CEC | XRD oriented | Greene-Kelly/CEC |
| PBF 10 | 1 | 1 | 1 | 2 | 1 | 1 | 1 | 2 | 1 | 3 |
| PBF 30 | 1 | 1 | 1 | 2 | 1 | | 1 | 2 | 1 | 2 |
| PBF 50 | 1 | 1 | 1 | 2 | 1 | | 1 | 2 | 1 | 2 |
| PBF 70 | 1 | 1 | 1 | 2 | 1 | | 1 | 2 | 1 | 2 |
| PBF 90 | 1 | 1 | 1 | 2 | 1 | | 1 | 2 | 1 | 2 |
| PBF 110 | 1 | 1 | 1 | 2 | 1 | | 1 | 2 | 1 | 4 |
| PBF 150 | 1 | 1 | 1 | 2 | 1 | | 1 | 2 | 1 | 2 |
| PBF 1000 | 1 | 1 | 1 | 2 | 1 | | 1 | 2 | 1 | 4 |

### 5.2.3 Methods

The samples have been analyzed for the same parameters and by the same methods as the buffer bentonite (described in Section 3.2) with addition of some parameters (Greene-Kelly test, grain-size distribution, pH) as follows:

- Cation exchange capacity (CEC) of the < 1 mm and < 0.5 µm fractions by exchange against Cu(II)-triethylenetetramine.
- CEC of the < 0.5 µm fractions was also determined after Li-saturation and heating according to the so called Greene-Kelly test (Greene-Kelly 1955). The samples were washed three times with aqueous 3M LiCl, four times with 0.01M LiCl in 90% ethanol and thereafter once with 95% ethanol with subsequent heating at 250°C overnight. CEC was thereafter determined by exchange with Cu(II)-triethylenetetramine. The experimental procedure followed Lim and Jackson (1986).
- Exchangeable cations by exchange against $NH_4^+$ in ethanol solution followed by ICP-AES analysis of the extract.
- Non-reactive solutes and soluble salts by aqueous leaching (solid:liquid ratio 1:100), followed by analysis of anions by ion chromatography (IC).
- Chemical composition of the < 1 mm and < 0.5 µm fractions using standard digestion techniques for silicates, followed by ICP atomic emission and mass spectroscopic analyses for determination of major and minor elements.
- Carbon and sulfur by evolved gas analysis using a Leco-furnace equipped with IR-detectors.

- Mineralogy of the < 1 mm and < 0.5 µm fractions by X-ray diffraction analysis of random powders and oriented mounts, respectively.
- Morphology of the < 1 mm fraction of the innermost sample was studied and areal element analyses (mapping) were performed by use of SEM-EDX.
- Grain-size distribution of the < 1 mm fraction by wet sieving and sedimentation after dispersion in 0.5% $Na_4P_2O_7$.
- pH with a universal pH indicator after dispersion of the material in a solid:liquid ratio of 1:3.

## 5.3 Results

### 5.3.1 Composition of the < 1 mm fraction of the backfill material

#### *5.3.1.1 Aqueous leachates*

The concentration of anions extracted by dispersion of the < 1 mm fraction in deionized water are listed in Table 5-2 and the distribution of the major anions chloride and sulfate (as $SO_4$-S) in the profile is plotted in Figure 5-2.

**Table 5-2. Major anions in mg/g dry mass, extracted by dispersion of the < 1 mm fraction in deionized water in a solid:liquid ratio of 1:100.**

| Sample id | F | Cl | $NO_3$-N | $SO_4$-S |
|---|---|---|---|---|
| | mg/g | mg/g | mg/g | mg/g |
| PBF 10 | 0.014 | 2.91 | 0.010 | 0.751 |
| PBF 30 | 0.021 | 2.66 | 0.014 | 0.676 |
| PBF 50 | 0.016 | 2.23 | 0.013 | 0.575 |
| PBF 70 | 0.017 | 2.57 | 0.011 | 0.680 |
| PBF 90 | 0.021 | 2.90 | 0.011 | 0.662 |
| PBF 110 | 0.014 | 2.86 | 0.009 | 0.686 |
| PBF 150 | 0.015 | 1.91 | 0.016 | 0.375 |
| PBF 1000 | 0.021 | 1.12 | 0.010 | 0.979 |

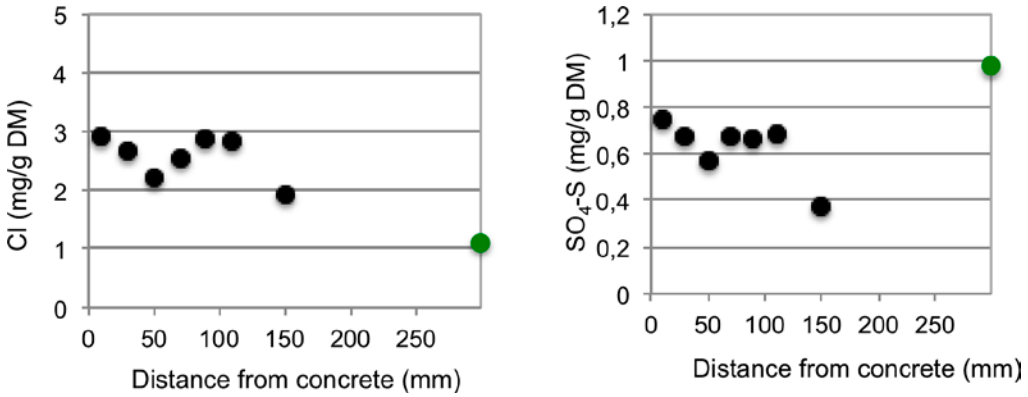


***Figure 5-2.*** *The distribution of $Cl^-$ and $SO_4$-S (mg/g dry mass) in the < 1 mm fraction of the backfill 0–160 mm from the concrete plug. The concentrations in the reference sample 1 m from the concrete are plotted in green on the right axis.*

The groundwater used for saturating the backfill material contains ~ 8,100 mg Cl/L (mean value for the period 2006–2011; Table 1-1) and is the primary source of chloride in the backfill material. The concentration of chloride is two to three times higher in the interval 0–12 cm from the concrete plug than 1 meter away from the plug, which probably reflects the higher water content/lower density of the backfill material at the plug (cf. Figure 1-9 and Figure 1-10).

The bentonite used for the backfill material has a total sulfur content of 0.32% (Johannesson 2005) and its inventory of gypsum is probably the primary source of sulfate, since the crushed rock is almost devoid of sulfur (Table 5-7), and sulfate is a minor anion in the groundwater (cf. Table 1-1). The maximum sulfate concentration corresponds to ~ 0.5% gypsum and is found in the reference sample taken 1 meter from the concrete plug. A minimum in sulfate appears 15 cm from the plug, from which values increase towards the plug, but the sulfate concentration is still somewhat lower than in the reference sample 1 meter from the plug (Figure 5-2).

#### *5.3.1.2 pH*

The initial pH of the < 1 mm fraction of the backfill material was measured one hour after dispersion. However, due to the bentonite's buffering capacity, the pH may change over time. Therefore, the pH was also measured after 4 days, when it was considered to be stabilized. At this point, it would appear that the pH is slightly higher in the samples closest to the concrete plug, with pH 9 in the backfill material samples up to 40 mm from the plug and pH 8.5 in all samples further away from the plug (Table 5-3). While it is not possible to obtain more precise pH measurements when a universal pH indicator is used, it is clear that there is not a pronounced pH gradient present.

#### *5.3.1.3 Grain-size distribution*

The backfill material was a mixture of crushed rock with a grain size 0–20 mm and bentonite from Milos. The latter had been ground to a powder in which particles < 74 μm made up 90–95%. The bentonite content in the backfill was between 28 and 32% by dry weight (Gunnarsson 2002).

The < 1 mm fraction separated by dry-sieving made up approximately one third of the dry mass of the bulk backfill material. The grain-size distribution of the < 1 mm fraction (Table 5-4) suggests that particles 1–0.06 mm, which consists almost exclusively of crushed rock, make up between 29 and 34% of the material. The grain-size distribution further indicates that the proportion of particles < 2 μm, and hence, the smectite content, is quite variable (39 to 46%). Therefore uncertainties related to material heterogeneity have to be considered besides "normal" analytical uncertainties for most chemical/mineralogical parameters determined.

#### *5.3.1.4 Exchangeable cations and cation exchange capacity*

The data on the exchangeable cations are compiled in Table 5-5 and plotted in Figure 5-3.

**Table 5-3. pH-values of the < 1 mm fraction, measured with a universal pH indicator after dispersion in deionized water in a solid:liquid ratio of 1:3.**

| Sample id | pH 1 h | pH 4 days |
|---|---|---|
| PBF 10 | 9 | 9 |
| PBF 30 | 9 | 9 |
| PBF 50 | 9 | 8.5 |
| PBF 70 | 8.5 | 8.5 |
| PBF 90 | 8.5 | 8.5 |
| PBF 110 | 9 | 8.5 |
| PBF 150 | 9 | 8.5 |
| PBF 1000 | 9 | 8.5 |

**Table 5-4. Grain-size of the fraction < 1 mm of the Prototype backfill material.**

| Sample id | 1–0.06 weight % | 0.06–0.002 weight % | < 0.002 mm weight % |
|---|---|---|---|
| PBF 10 | 33.9 | 24.6 | 41.5 |
| PBF 30 | 30.7 | 24.0 | 45.3 |
| PBF 50 | 31.2 | 25.7 | 43.1 |
| PBF 70 | 32.7 | 23.3 | 44.0 |
| PBF 90 | 31.9 | 22.2 | 45.9 |
| PBF 110 | 33.8 | 27.2 | 38.9 |
| PBF 150 | 32.4 | 25.5 | 42.1 |
| PBF 1000 | 29.4 | 27.4 | 43.2 |

**Table 5-5. Exchangeable cations in the < 1 mm fraction of the Prototype backfill. Cations extracted by exchange against $NH_4^+$ in ethanol solution.**

| Sample id | Ca | | K | | Mg | | Na | | Sum |
|---|---|---|---|---|---|---|---|---|---|
| | meq/100 g | % | meq/100 g | % | meq/100 g | % | meq/100 g | % | meq/100 g |
| PBF 10 | 5.8 | 10 | 3.3 | 5.8 | 1.5 | 2.7 | 46 | 81 | 57 |
| PBF 30 | 8.1 | 14 | 3.8 | 6.5 | 1.7 | 3.0 | 44 | 77 | 58 |
| PBF 50 | 8.3 | 15 | 3.6 | 6.3 | 1.9 | 3.3 | 43 | 76 | 57 |
| PBF 70 | 8.3 | 15 | 3.4 | 6.2 | 2.2 | 4.0 | 41 | 75 | 55 |
| PBF 90 | 10.4 | 18 | 2.8 | 5.0 | 3.0 | 5.3 | 40 | 71 | 56 |
| PBF 110 | 9.7 | 18 | 2.8 | 5.0 | 3.0 | 5.4 | 40 | 72 | 55 |
| PBF 150 | 10.5 | 19 | 2.7 | 5.0 | 5.7 | 10.5 | 35 | 65 | 54 |
| PBF 1000 | 8.1 | 14 | 1.6 | 2.9 | 6.2 | 10.9 | 41 | 72 | 57 |
| Milos bentonite | 11.2 | 11 | 2.0 | 1.9 | 6.9 | 7.0 | 85 | 81 | 105 |

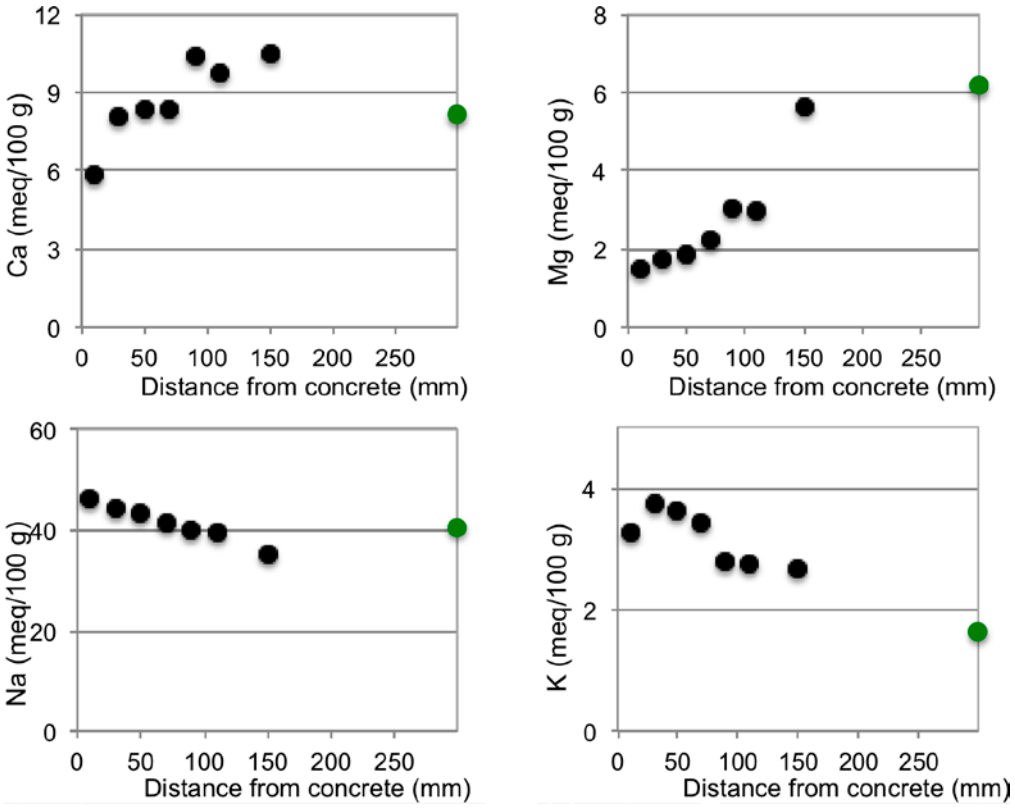


***Figure 5-3.*** *Exchangeable Ca, Mg, K, and Na plotted versus the distance from the concrete plug. Values for the reference backfill sample from 1 m are plotted in green on the right axis.*

The exchangeable magnesium concentration has decreased in the innermost 12 cm of the backfill compared to the concentration in the distal reference sample at 1 meter. The desorption of magnesium from exchange sites in the bentonite at the concrete is most likely an effect of the precipitation of a low-solubility magnesium phase(s) indicated in the chemical data on the < 0.5 mm fraction (cf. Section 5.3.2.3), which controlled the porewater concentration. Analogous observations have been reported in previous studies on bentonite/cement interactions (e.g. Gaucher and Blanc 2006, Karnland et al. 2009, Dohrmann et al. 2013).

Calcium is one of the essential cations in leachates from cement, but the exchangeable calcium concentration decreases in the backfill sample PBF 10 proximal to the concrete plug. Other chemical data, as well as XRD-data, show a clear increase in calcium carbonate/calcite in this sample, again suggesting that precipitation reactions at the concrete exerted major control on the pore fluid composition, and hence, on the pool of exchangeable cations.

Both divalent exchangeable cations have been replaced primarily by sodium, but an increase is seen also in potassium at the concrete plug. Accordingly, the relative proportion of sodium has increased from 70 to 80% and that of potassium from 3 to 6% at the concrete plug (Table 5-5 and Figure 5-4).

The sum of cations exceeds, however, the CEC-values in all samples by 10 meq/100 g or more, and this fact reflects the problems inherent with extraction methods for exchangeable cations. The alcohol solution used for extraction certainly minimizes dissolution of gypsum and calcite, but non-reactive solutes and easily soluble salts, such as chlorides and carbonates of alkali metals, if present, will dissolve in this extractant and, thus, contribute to the measured exchangeable cation pool. Small amounts of halite (NaCl) are indicated in the X-ray diffractogram of sample PBF10, and halite dissolution during extraction will necessarily result in excessive cation sums and inflated values for "exchangeable" sodium. The chloride content in the samples from the interval 0–12 cm at the concrete plug (Table 5-2) corresponds to between 6 and 9 meq cations/100 g.

The cation exchange capacity of the < 1 mm fractions are listed in Table 5-6 together with values for the pure bentonite and crushed rock, and are plotted in Figure 5-5 (left).

The CEC-values of the < 1 mm fractions vary unsystematically between 41 and 47 meq/100 g. CEC of ground rock particles (initial grain size 1,000–63 µm) is near zero. The range of variation is larger than the normal scatter in the Cu-trien method, as demonstrated in inter-laboratory tests of the method (Dohrmann et al. 2012). According to the grain size data for the < 1 mm fractions, the proportion of particles < 2 µm varies from 39 to 46% (Table 5-4), which means that also the smectite content of the samples is likely to vary. The heterogeneity of the sample population appears to have a rather strong influence on CEC, as suggested by a relatively high correlation ($R^2$=0.67) between CEC and the proportion of clay-sized particles (Figure 5-5 right), and the variations related to material heterogeneity would probably mask potential small-scale CEC changes coupled to mineralogical changes in the proximity of the concrete.

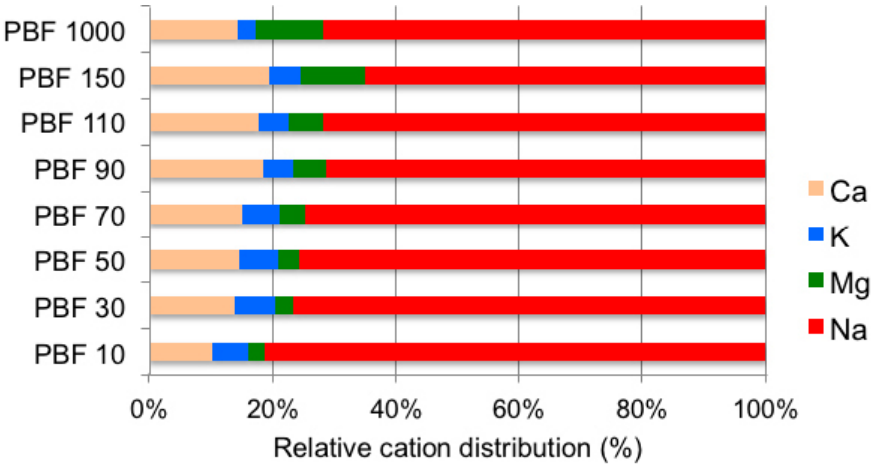


***Figure 5-4.*** *Relative proportions of the exchangeable cations extracted by exchange against $NH4^+$ in ethanol solution.*

**Table 5-6. The cation exchange capacity of the < 1 mm fraction from the backfill material.**

| Sample id | < 1 mm fraction | | |
|---|---|---|---|
| | CEC-1 meq/100 g | CEC-2 | CEC-mean |
| PBF 10 | 40 | 43 | 42 |
| PBF 30 | 45 | 48 | 46 |
| PBF 50 | 45 | 43 | 44 |
| PBF 70 | 43 | 41 | 42 |
| PBF 90 | 48 | 45 | 47 |
| PBF 110 | 41 | 41 | 41 |
| PBF 150 | 45 | 43 | 44 |
| PBF 1000 | 45 | 45 | 45 |
| Milos bentonite | 88 | 88 | 88 |
| Crushed rock | ~ 0 | | |

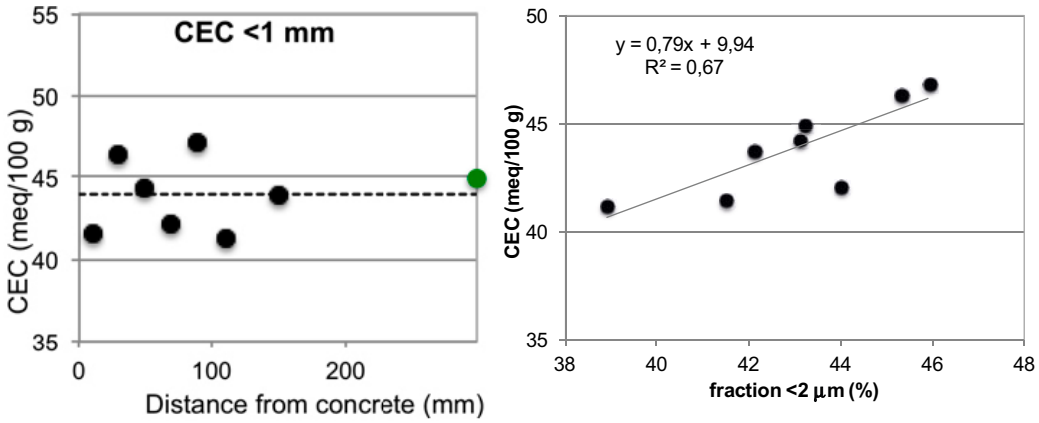


*Figure 5-5. Left: Cation exchange capacity of the < 1 mm fractions plotted versus the distance from the concrete plug. Values for the reference backfill sample from 1 m are plotted in green on the right axis. Right: Plot of the cation exchange capacity of the < 1 mm fractions versus the proportion of particles < 2 µm (%).*

#### *5.3.1.5 Mineralogy*

Comparison of the mineralogy of the reference sample PBF 1000, the crushed rock and the bentonite (Figure 5-6) confirms that the < 1 mm fraction contains a significant proportion of crushed rock particles. In addition to the major "bentonite minerals" smectite, calcite ($CaCO_3$), dolomite ($CaMg(CO_3)_2$), quartz (plus trace amounts of gypsum and pyrite), the < 1 mm fraction of the backfill material contains large amounts of quartz, plagioclase, potassium feldspar and minor amounts of Mg/Fe-rich minerals, such as chlorite, biotite and amphibole, originating from the crushed granodiorite.

XRD-profiles of the < 1 mm fraction of all backfill samples are shown in Figure 5-7, where the strongest peaks of the major minerals are indicated together with the (001) basal reflection of the smectite. The previously dried samples were equilibrated at ambient relative humidity (RH 50 ± 10%) prior to X-ray scanning.

The shape and width of the (001) smectite reflection vary somewhat among the samples but all samples have the peak centered around 12.5 Å, which is typical of the monolayer hydrate of Na-smectite and consistent with the composition of the exchangeable cation pool, showing sodium to be the predominant cation in all samples (Table 5-5).

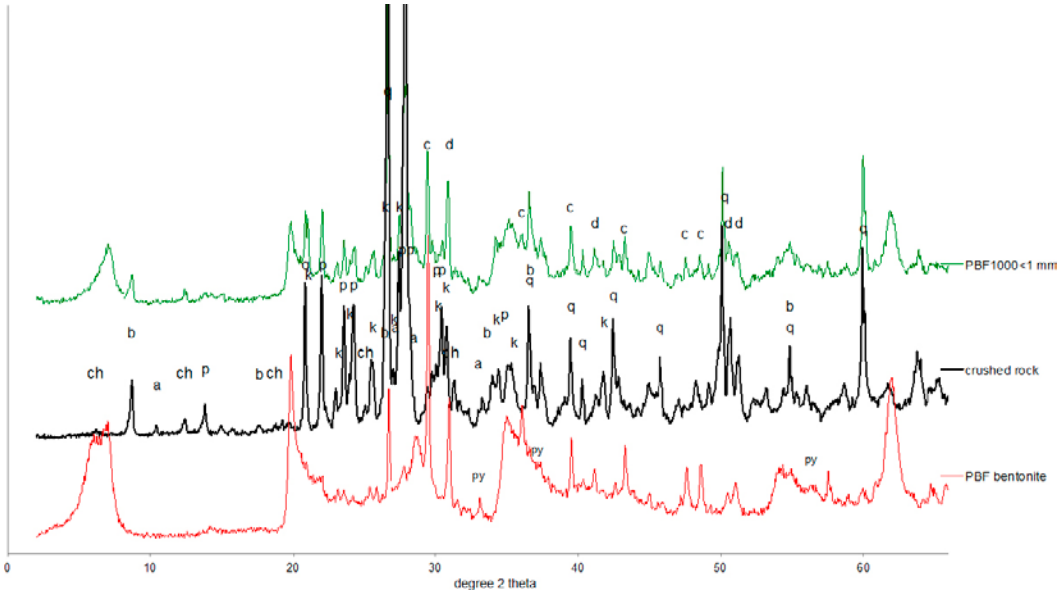


***Figure 5-6.*** *Comparison of the mineralogy of the < 1 mm fraction of the backfill reference and of the pure crushed rock and bentonite. a = amphibole; b = biotite; c = calcite; ch = chlorite; d = dolomite; k = potassium feldspar; p = plagioclase; py = pyrite; q = quartz. Random powder. CuKα radiation.*

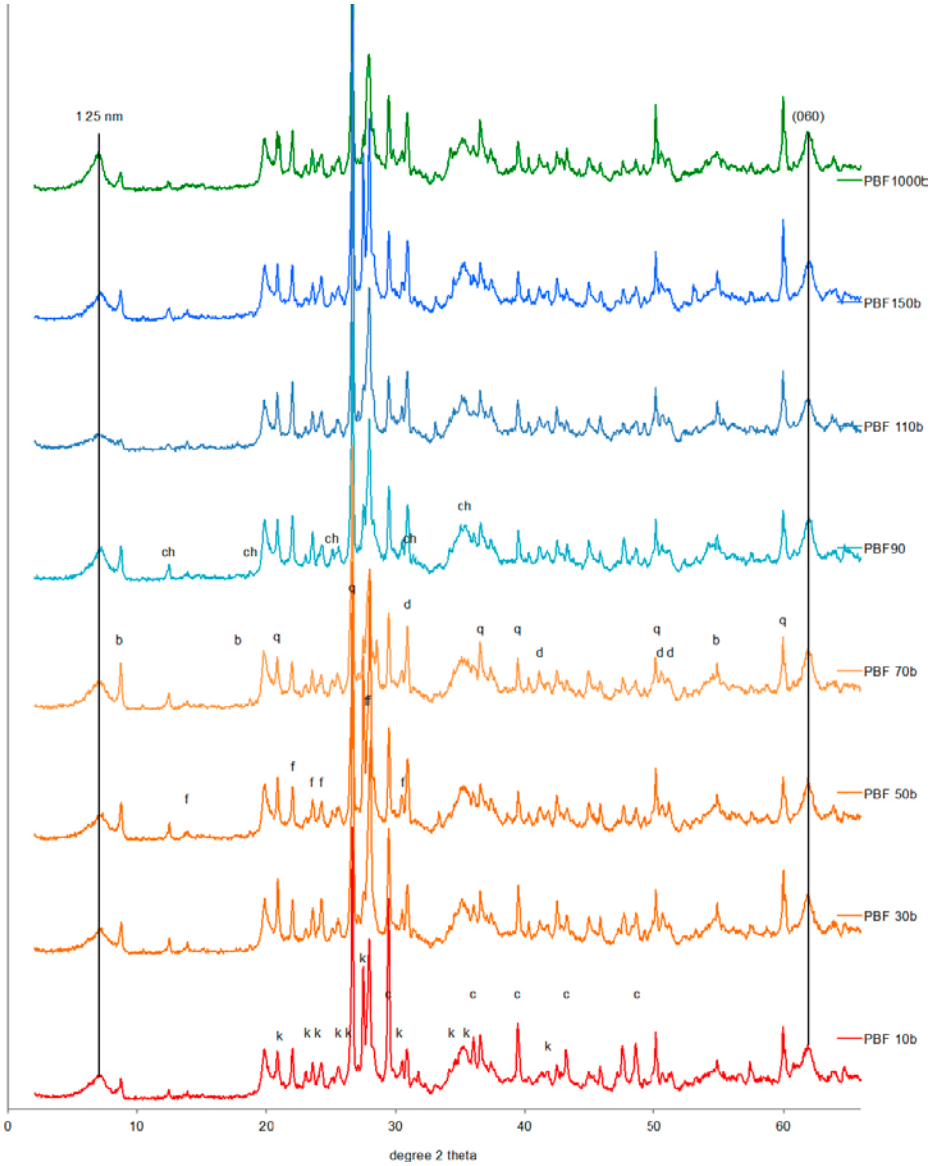


***Figure 5-7.*** *XRD-profiles of random powders of the < 1 mm fractions. b = biotite; c = calcite; d = dolomite; f = plagioclase; k = K-feldspar; q = quartz; ch = chlorite. CuKα radiation.*

Also the (060) hk-peak of smectite is indicated in Figure 5-7. This reflection is useful for distinguishing di- and trioctahedral sub-groups of clay minerals because it includes the *b* cell dimension, which is more sensitive to the size of the cations and to site occupancy in the octahedral sheet than are the *a* or *c* cell dimensions. The d-value is 1.49–1.50 Å in all samples, which is typical of the dioctahedral sub-group of smectites, to which montmorillonite and beidelllite belong. A small peak at 60.5° 2θ (d=1.53 Å) may be the (060)-reflections of biotite and chlorite, which are trioctahedral phyllosilicates, but identification is uncertain due to an overlapping peak of calcite in this region.

The most conspicuous mineralogical change is seen in the two samples PBF 10 and 30 0 to 4 cm from the concrete plug. In these samples the intensity of the calcite peaks has increased, along with a decrease of the intensity of the dolomite peaks, suggesting neoformation of the former carbonate phase and partial dissolution of the latter. A close–up of the 2θ-interval 25–66°, where most of the carbonate peaks appear, is shown for the innermost samples and the reference sample in Figure 5-8.

Dedolomitization, i.e. the transformation of dolomite into new Mg-rich minerals, such as brucite ($Mg(OH)_2$) or hydrotalcite ($Mg_6Al_2CO_3(OH)_{16}*4H_2O$), and calcite, has been observed in several previous studies on interactions between carbonate-bearing bentonites/argillites and hyper-alkaline solutions (e.g. Adler et al. 2000, Devol-Brown et al. 2007, De Windt et al. 2008). None of these secondary Mg-minerals has, however, been identified in the XRD-profiles of the backfill samples, but the chemical data for the < 0.5 µm fraction (Section 5.3.2.3) clearly indicate that a Mg-phase of low solubility has precipitated in the samples at the concrete. This neoformed Mg-phase is apparently amorphous to X-rays.

It should also be emphasized that several of the potential calcium-bearing reaction products of the interaction of cement pore fluids with bentonite (e.g. calcium silicate hydrates, CSH) tend to be X-ray amorphous due to poor crystallinity.

A variation in the intensity of the feldspar peaks can be seen among the samples, but both the excellent {010} and {001} cleavage of feldspars, which promotes preferred orientation, and their coarse grain size may give a random variation in peak intensities. Moreover, quantitative variations in feldspar content may actually exist because of the heterogeneity of the material.

In the X-ray diffractogram of sample PBF10 a weak reflection can be seen of halite (NaCl), which crystallized when the sample was dried.

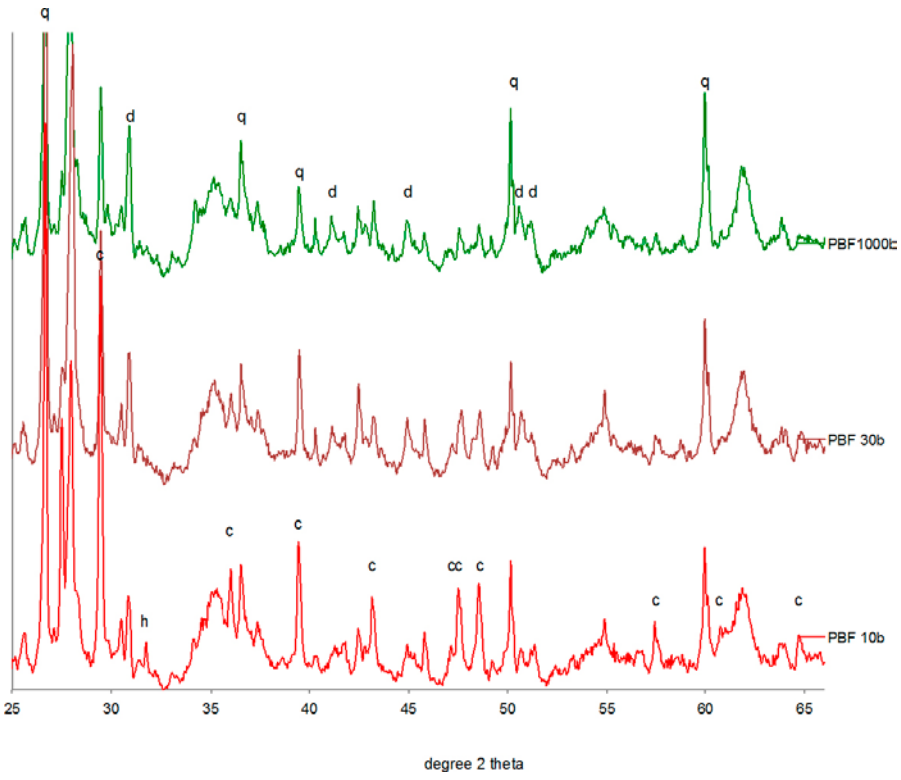


***Figure 5-8.*** *Close-up of the interval 25–66° 2θ of the XRD- profiles of samples proximal to the concrete plug and the reference sample 1 meter from the concrete. c = calcite; d = dolomite; h = halite (NaCl); q = quartz. Random powders. CuKα radiation.*

#### 5.3.1.6 Chemical composition

The chemical composition of the < 1 mm fractions is given in Table 5-7.

The total sulfur content of the reference backfill material is 0.26% (detection limit 0.02%). The majority of sulfur originates from the bentonite (total sulfur content 0.32%; Johannesson 2005), while the sulfur inventory of the crushed rock is very low, 0.04% S (Table 5-7), and sulfate is a minor anion in the Äspö groundwater. According to the data on water-soluble salts (Table 5-2), 40% of the total sulfur exists as soluble sulfate minerals in the reference sample. The source of the remaining insoluble sulfur fraction is primarily sulfides although trace amounts of sulfates of low solubility (e.g. $BaSO_4$) and/or organic sulfur compounds might also exist.

Both the soluble and the insoluble sulfur contents are somewhat lower in the interval 0–160 mm of the backfill than in the reference sample at 1 meter (Figure 5-9). The distribution of the sulfur species further suggests that the insoluble fraction is predominant in all samples except sample PBF 10, in which the proportion of the sulfur fractions is shifted, possibly due to sulfide oxidation during and/or after the field test. At the sampling, the backfill material had a black or dark grey color, which slowly changed to yellowish upon exposure to air, indicating oxidation.

Acid-soluble carbon in the backfill material < 1 mm originates primarily from carbonates, while the main source of the remnant, acid-insoluble carbon fraction is organic matter. The acid soluble carbon content is fairly constant within the profile (0.82–0.92% C) except for the innermost sample PBF 10, in which the content has increased to 1.2% C (Figure 5-10). The increase in carbonate carbon is paralleled by an almost stoichiometrically equivalent increase in CaO (24 and 28 millimoles, respectively), and corresponds to an increase in $CaCO_3$ by 2.4%. Hence, the chemical data clearly indicate an uptake of Ca due to carbonate precipitation in the interval 0–4 cm of the backfill, which is consistent with the mineralogical data showing that the calcite content of the backfill has increased in this interval. In order to eliminate effects of variations in the exchangeable calcium content, the non-exchangeable CaO content has been calculated and is plotted together with the total CaO content in Figure 5-10.

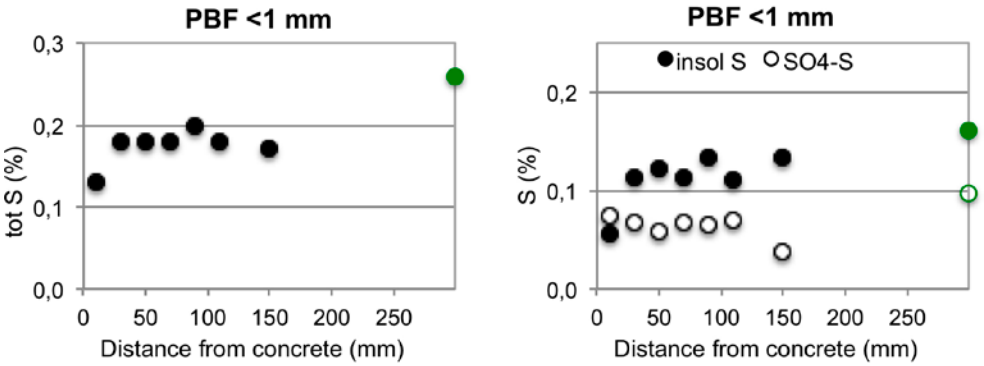


*Figure 5-9. Distribution of total S (left) and sulfate-S and insoluble S (right) in the < 1 mm fraction of the backfill 0–160 mm from the concrete plug. The concentrations of the reference sample taken 1 m from the concrete are plotted in green on the right axis.*

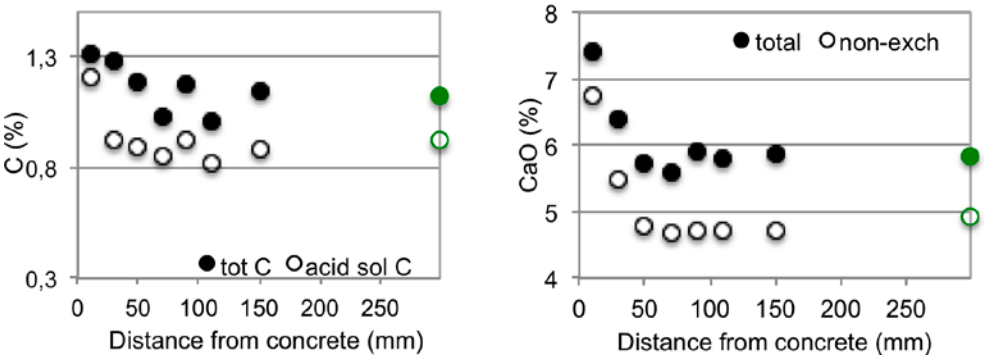


*Figure 5-10. The distribution of total and acid-soluble carbon (left) and total and non-exchangeable CaO (right) in the < 1 mm fraction of the backfill 0–160 mm from the concrete plug. The concentrations of the reference sample taken 1 m from the concrete are plotted in green on the right axis.*

**Table 5-7. Chemical composition of the < 1 mm fractions of the tunnel backfill samples. DL = detection limit.**

| Sample id | $SiO_2$ % | $Al_2O_3$ % | $Fe_2O_3$ % | MgO % | CaO % | $Na_2O$ % | $K_2O$ % | $TiO_2$ % | $P_2O_5$ % | MnO % | $Cr_2O_3$ % | LOI % | Sum % | tot C % | tot S % | Acid sol C % |
|---|---|---|---|---|---|---|---|---|---|---|---|---|---|---|---|---|
| DL | 0.01 | 0.01 | 0.04 | 0.01 | 0.01 | 0.01 | 0.01 | 0.01 | 0.01 | 0.01 | 0.002 | –5.1 | 0.01 | 0.02 | 0.02 | 0.02 |
| PBF 10 | 53.95 | 15.79 | 5.01 | 3.59 | 7.40 | 3.64 | 2.15 | 0.74 | 0.23 | 0.09 | 0.005 | 7.0 | 99.62 | 1.31 | 0.13 | 1.20 |
| PBF 30 | 54.42 | 16.02 | 5.26 | 3.63 | 6.39 | 3.59 | 2.24 | 0.77 | 0.26 | 0.10 | 0.005 | 6.9 | 99.64 | 1.28 | 0.18 | 0.93 |
| PBF 50 | 54.9 | 16.23 | 5.45 | 3.46 | 5.72 | 3.45 | 2.38 | 0.77 | 0.24 | 0.10 | 0.005 | 6.9 | 99.61 | 1.19 | 0.18 | 0.89 |
| PBF 70 | 55.25 | 16.14 | 5.58 | 3.47 | 5.60 | 3.4 | 2.22 | 0.78 | 0.26 | 0.10 | 0.004 | 6.8 | 99.63 | 1.03 | 0.18 | 0.85 |
| PBF 90 | 54.67 | 16.57 | 5.35 | 3.50 | 5.89 | 3.51 | 2.12 | 0.76 | 0.25 | 0.10 | 0.005 | 6.9 | 99.63 | 1.18 | 0.2 | 0.92 |
| PBF 110 | 55.24 | 16.31 | 5.39 | 3.42 | 5.80 | 3.49 | 2.13 | 0.79 | 0.25 | 0.10 | 0.004 | 6.7 | 99.62 | 1.01 | 0.18 | 0.82 |
| PBF 150 | 54.90 | 16.47 | 5.48 | 3.63 | 5.88 | 3.21 | 2.08 | 0.84 | 0.25 | 0.11 | 0.005 | 6.8 | 99.64 | 1.14 | 0.17 | 0.88 |
| PBF 1000 | 55.03 | 16.35 | 5.38 | 3.6 | 5.84 | 3.32 | 2.06 | 0.8 | 0.25 | 0.10 | 0.004 | 6.9 | 99.63 | 1.12 | 0.26 | 0.92 |
| rock 1–0.06 mm | 60.54 | 16.68 | 4.44 | 2.15 | 5.12 | 4.32 | 3.16 | 0.69 | 0.22 | 0.09 | 0.005 | 2.1 | 99.55 | 0.41 | 0.04 | 0.31 |

| Sample id | Sc ppm 1 | Ba ppm 1 | Be ppm 1 | Co ppm 0.2 | Cs ppm 0.1 | Ga ppm 0.5 | Hf ppm 0.1 | Nb ppm 0.1 | Rb ppm 0.1 | Sn ppm 1 | Sr ppm 0.5 | Ta ppm 0.1 | Th ppm 0.2 | U ppm 0.1 | V ppm 8 | W ppm 0.5 |
|---|---|---|---|---|---|---|---|---|---|---|---|---|---|---|---|---|
| PBF 10 | 12 | 1,194 | < 1 | 13.2 | 6.5 | 17.7 | 5.8 | 11.3 | 86.1 | 2 | 794.0 | 0.9 | 9.7 | 4.9 | 117 | 0.8 |
| PBF 30 | 12 | 1,225 | 1 | 13.2 | 7.4 | 18.0 | 4.9 | 9.8 | 86.3 | 2 | 701.2 | 0.8 | 9.1 | 4.9 | 128 | 1.1 |
| PBF 50 | 12 | 1,414 | 1 | 13.6 | 7.4 | 17.9 | 5.0 | 10.8 | 89.7 | 2 | 766.1 | 0.9 | 9.4 | 5.0 | 130 | 1.2 |
| PBF 70 | 12 | 1,246 | 3 | 15.2 | 7.4 | 17.5 | 5.6 | 9.9 | 88.0 | 2 | 702.3 | 0.8 | 10.1 | 5.2 | 134 | 0.9 |
| PBF 90 | 13 | 1,169 | < 1 | 13.0 | 6.6 | 17.4 | 5.2 | 10.5 | 77.3 | 2 | 697.3 | 1.1 | 8.8 | 4.3 | 122 | 1.0 |
| PBF 110 | 12 | 1,210 | 3 | 14.2 | 6.6 | 18.1 | 5.5 | 10.7 | 80.9 | 2 | 753.5 | 0.9 | 9.3 | 4.5 | 127 | 0.8 |
| PBF 150 | 13 | 1,178 | 2 | 14.8 | 6.7 | 17.4 | 4.8 | 11.1 | 80.2 | 2 | 719.4 | 0.9 | 10.9 | 4.9 | 133 | 1.0 |
| PBF 1000 | 13 | 1,196 | 4 | 19.0 | 7.5 | 18.5 | 5.1 | 11.4 | 80.6 | 2 | 695.2 | 1.0 | 9.8 | 4.9 | 119 | 1.5 |
| rock 1–0.06 mm | 11 | 1,623 | 1 | 13.1 | 1.9 | 19.5 | 3.8 | 12.4 | 99.3 | 2 | 1,326.3 | 0.9 | 15.8 | 3.6 | 73 | 0.8 |

| Sample id | Zr ppm 0.1 | Y ppm 0.1 | La ppm 0.1 | Ce ppm 0.1 | Pr ppm 0.02 | Nd ppm 0.3 | Sm ppm 0.05 | Eu ppm 0.02 | Gd ppm 0.05 | Tb ppm 0.01 | Dy ppm 0.05 | Ho ppm 0.02 | Er ppm 0.03 | Tm ppm 0.01 | Yb ppm 0.05 | Lu ppm 0.01 |
|---|---|---|---|---|---|---|---|---|---|---|---|---|---|---|---|---|
| PBF 10 | 237.7 | 23.6 | 43.5 | 94.9 | 10.98 | 39.9 | 7.08 | 1.58 | 5.32 | 0.85 | 4.03 | 0.85 | 2.59 | 0.38 | 2.53 | 0.37 |
| PBF 30 | 202.4 | 22.7 | 40.6 | 85 | 10.26 | 36.4 | 6.68 | 1.59 | 5.19 | 0.79 | 4.2 | 0.82 | 2.41 | 0.35 | 2.34 | 0.35 |
| PBF 50 | 203.8 | 23.7 | 43 | 91.1 | 10.78 | 36.8 | 7.09 | 1.63 | 5.5 | 0.82 | 4.35 | 0.85 | 2.5 | 0.38 | 2.35 | 0.34 |
| PBF 70 | 215.5 | 23.3 | 41.3 | 88.7 | 10.5 | 42.3 | 6.86 | 1.62 | 5.44 | 0.77 | 4.08 | 0.79 | 2.39 | 0.36 | 2.34 | 0.37 |
| PBF 90 | 212.5 | 20.3 | 38.9 | 83.1 | 9.68 | 37.5 | 6.06 | 1.45 | 4.91 | 0.73 | 3.89 | 0.82 | 2.22 | 0.34 | 2.18 | 0.34 |
| PBF 110 | 214.2 | 23.3 | 47.4 | 97.9 | 11.47 | 42.1 | 7.42 | 1.72 | 5.86 | 0.87 | 4.53 | 0.89 | 2.47 | 0.37 | 2.39 | 0.37 |
| PBF 150 | 197.3 | 24.5 | 45.2 | 99.7 | 11.66 | 40.9 | 7.66 | 1.74 | 5.89 | 0.86 | 4.24 | 0.85 | 2.52 | 0.38 | 2.57 | 0.38 |
| PBF 1000 | 206.9 | 25 | 44.3 | 98.8 | 11.6 | 41.9 | 7.49 | 1.7 | 5.8 | 0.89 | 4.57 | 0.96 | 2.58 | 0.4 | 2.68 | 0.38 |
| rock 1–0.06 mm | 157.9 | 24.9 | 55.2 | 120.3 | 13.75 | 51.8 | 8.26 | 1.82 | 6.31 | 0.89 | 4.21 | 0.87 | 2.48 | 0.36 | 2.31 | 0.32 |

| Sample id | Mo ppm 0.1 | Cu ppm 0.1 | Pb ppm 0.1 | Zn ppm 1 | Ag ppm 0.1 | Ni ppm 0.1 | As ppm 0.5 | Au ppm 0.5 | Cd ppm 0.1 | Sb ppm 0.1 | Bi ppm 0.1 | Hg ppm 0.01 | Tl ppm 0.1 | Se ppm 0.5 |
|---|---|---|---|---|---|---|---|---|---|---|---|---|---|---|
| PBF 10 | 0.7 | 21.3 | 7 | 63 | < 0.1 | 15.5 | 2.9 | 1.5 | 0.1 | 0.1 | < 0.1 | 0.13 | 0.4 | < 0.5 |
| PBF 30 | 1.7 | 21 | 7.7 | 69 | < 0.1 | 13.9 | 3 | < 0.5 | 0.1 | 0.2 | < 0.1 | 0.17 | 0.6 | 0.5 |
| PBF 50 | 0.8 | 21.4 | 7.2 | 67 | < 0.1 | 14.5 | 2.3 | 2 | 0.1 | 0.2 | < 0.1 | 0.17 | 0.6 | < 0.5 |
| PBF 70 | 1.3 | 25.6 | 7.6 | 69 | < 0.1 | 16.4 | 3.1 | 1.4 | 0.2 | 0.2 | < 0.1 | 0.17 | 0.6 | < 0.5 |
| PBF 90 | 1.2 | 23.6 | 7.8 | 67 | < 0.1 | 15.4 | 4.4 | 1.3 | 0.2 | 0.2 | < 0.1 | 0.17 | 0.4 | < 0.5 |
| PBF 110 | 1 | 24.1 | 7.3 | 70 | < 0.1 | 16.8 | 3.8 | 1.5 | 0.2 | 0.2 | < 0.1 | 0.16 | 0.4 | < 0.5 |
| PBF 150 | 0.9 | 23 | 7.2 | 68 | < 0.1 | 15.9 | 3.5 | < 0.5 | 0.2 | 0.2 | < 0.1 | 0.15 | 0.5 | < 0.5 |
| PBF 1000 | 1.3 | 30.1 | 7.4 | 64 | < 0.1 | 16.3 | 3.7 | 2.1 | 0.1 | 0.2 | < 0.1 | 0.16 | 0.5 | < 0.5 |
| rock 1–0.06 mm | 0.8 | 22.6 | 2.7 | 64 | < 0.1 | 19.6 | 0.6 | < 0.5 | < 0.1 | < 0.1 | < 0.1 | 0.01 | 0.3 | < 0.5 |

The total magnesium content of the < 1 mm fractions is more or less constant and in the same range as in the reference sample (Figure 5-11). The distribution of the non-exchangeable fraction of Mg displays, however, a small increase towards the concrete, which is consistent with a transfer of magnesium from the pore fluid/exchange sites to the solid fraction by precipitation, indicated in other chemical data (cf. exchangeable cations in 5.3.1.4; chemistry of the 0.5 µm fraction in 5.3.2.3).

35–40% of the total sodium content is exchangeable sodium. The gradual increase in total sodium towards the concrete plug (Figure 5-11 right) is largely related to the exchangeable fraction, while no significant variation is seen in non-exchangeable sodium.

Also the non-exchangeable potassium content is fairly constant within the profile, apart from a small maximum 4–6 cm from the concrete, the cause of which remains to be identified.

The distribution pattern of the major oxides $SiO_2$ and $Al_2O_3$ displays a more or less distinct decrease towards the concrete, which fully or partially is caused by the inherent correlations in constant-sum weight percentages data, i.e. an increase in one component (CaO + acid soluble C in this case) results in an apparent decrease in other, major components. For this reason, the oxides of Si and Al have tentatively been corrected for the "excessive" $CaCO_3$ in the innermost backfill samples, and plotted together with the raw data in Figure 5-12. No distinct tendencies can be seen in the distribution patterns after this correction, considering that the heterogeneity of the < 1 mm fractions is likely to produce some scatter in the chemical data. The ratio $SiO_2/Al_2O_3$ is constant within the analytical uncertainties.

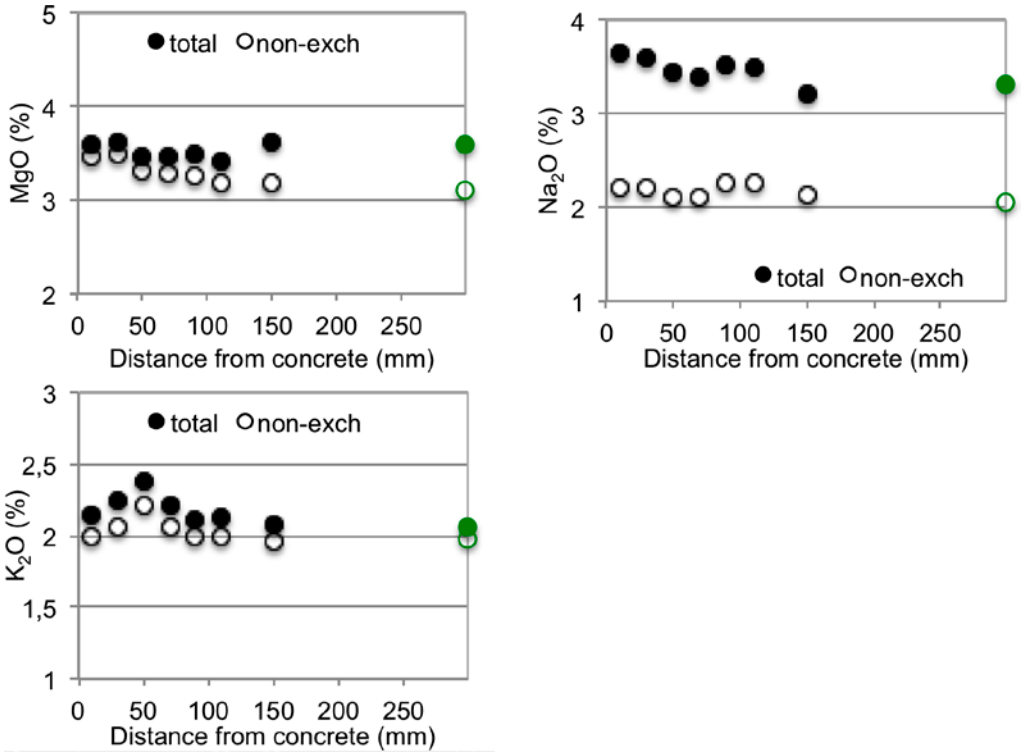


***Figure 5-11.*** *The distribution of total and non-exchangeable MgO, $Na_2O$ and $K_2O$ in the < 1 mm fraction of the backfill 0–160 mm from the concrete plug. The concentrations of the reference backfill sample 1 m from the concrete are plotted in green on the right axis.*

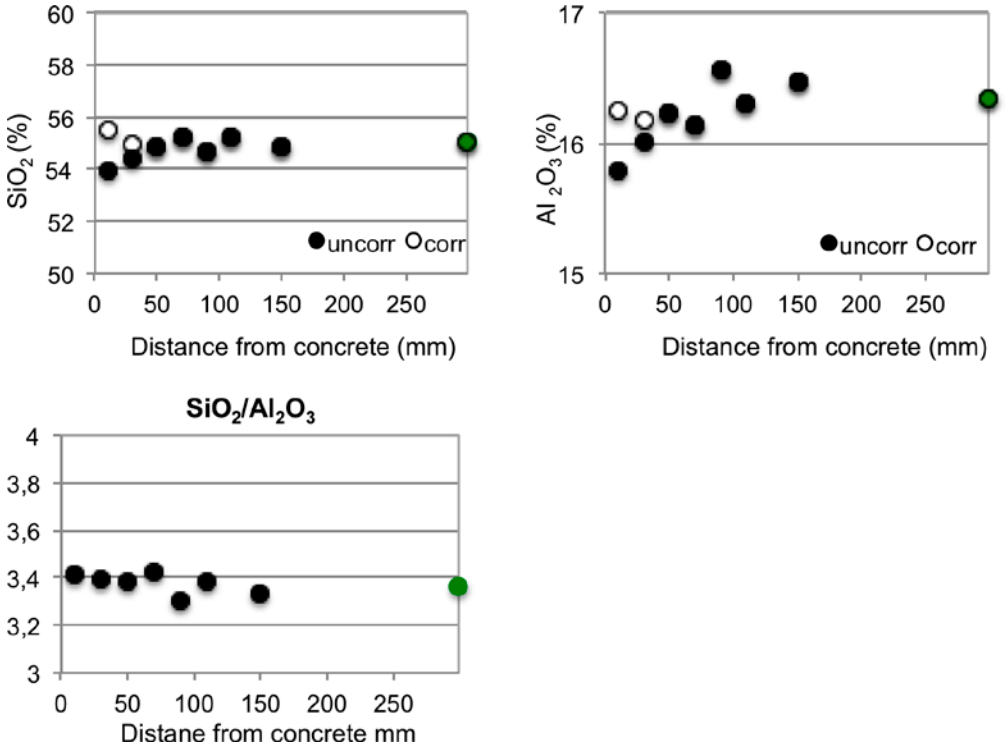


***Figure 5-12.*** *The distribution of $SiO_2$, $Al_2O_3$ and their ratio in the < 1 mm fraction of the backfill 0–160 mm from the concrete plug. uncorr = raw data; corr = data for the innermost samples corrected for "excessive" $CaCO_3$ (cf. text). The concentrations of the reference sample 1 m from the concrete are plotted in green on the right axis.*

#### 5.3.1.7 Scanning electron microscopy and EDX-analysis

The analyzed specimen taken close to the concrete plug consisted of a fine-grained material with sporadic, well-crystallized minerals (Figure 5-13). A close-up of a cluster of idiomorphic crystals with clearly developed habit planes is shown in Figure 5-14.

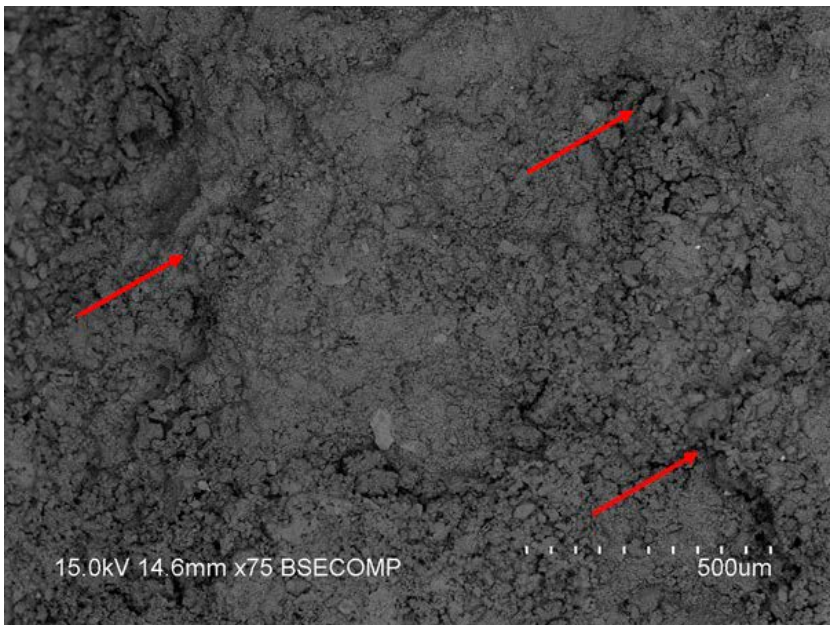


***Figure 5-13.*** *Backscatter overview of tunnel backfill material close to the concrete plug. Arrows mark the positions of the area analyses presented in Table 5-8.*

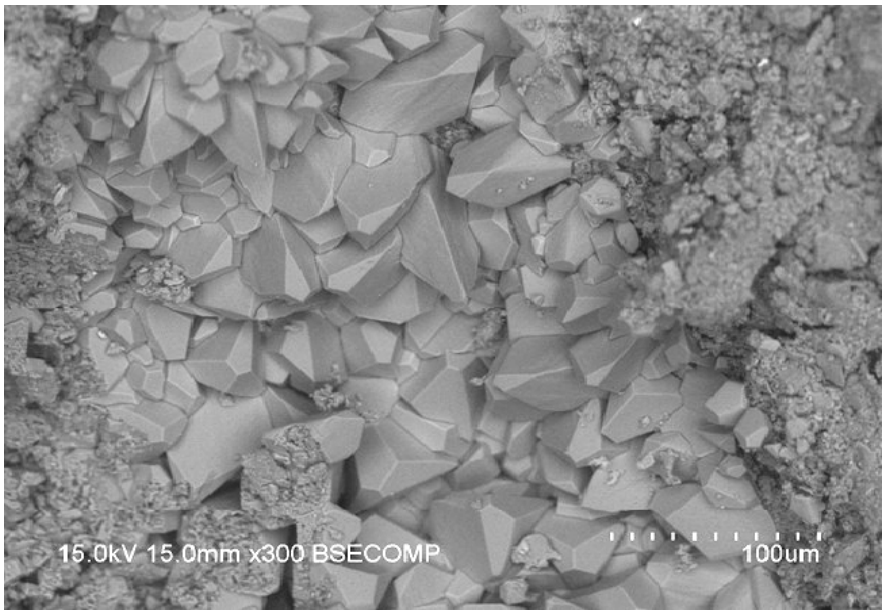


***Figure 5-14.*** *Close-up of a cluster of idiomorphic crystals at one of the arrows in Figure 5-13.*

The mass ratio of the elements Ca:C:O in the cluster of crystals was 35:10:55 (Table 5-8), which may be compared with 40:12:48 in ideal calcite. Calcite crystals are extremely varied in habit and often highly complex, but crystals of scalenohedral habit with rhombohedral truncations, as shown in Figure 5-14, are common.

Area analyses showed that the element distribution in the poorly crystalline matrix was similar to that of the cluster of crystals and, hence, close to that of calcite (Table 5-8).

**Table 5-8. Element distribution in the matrix of two areas 50 µm × 50 µm, and in the cluster of idiomorphic crystals (Figures 5-13 and 5-14). Contents in weight percent. σ = standard deviation in individual analyses.**

| Element | matrix 1 | σ matrix 1 | matrix 2 | σ matrix 2 | Ca-mineral | σ Ca mineral |
|---|---|---|---|---|---|---|
| C | 9.5 | 0.7 | 9.6 | 0.6 | 8.1 | 0.3 |
| Na | 0.9 | 0.1 | 0.6 | 0.1 | 0.7 | 0.0 |
| Mg | 2.2 | 0.1 | 1.7 | 0.1 | 2.1 | 0.0 |
| Al | 3.2 | 0.1 | 2.2 | 0.1 | 2.4 | 0.0 |
| Si | 9.5 | 0.1 | 6.6 | 0.1 | 7.8 | 0.1 |
| K | 0.9 | 0.1 | 0.5 | 0.1 | 0.7 | 0.0 |
| Ca | 21.9 | 0.2 | 29.0 | 0.2 | 29.5 | 0.1 |
| Fe | 1.6 | 0.1 | 1.1 | 0.1 | 1.8 | 0.1 |
| O | 50.2 | 1.1 | 48.5 | 1.0 | 46.7 | 0.6 |

## 5.3.2 Composition of the < 0.5 µm fraction of the backfill material

### *5.3.2.1 Cation exchange capacity*

The CEC values of the purified, Na-converted fractions < 0.5 µm (Table 5-9 and Figure 5-15 left) display a clear gradient towards the concrete plug, and the CEC of the contact sample is 10 meq/100 g higher than that of the reference sample 1 meter from the plug.

Calcium silicate hydrates (CSH) and zeolites have high/very high cation exchange capacities and are among the predicted reaction products in numerical modeling of interactions between cement pore fluids and bentonite and have been reported in many laboratory studies (review in Gaucher and Blanc 2006, Devol-Brown et al. 2007, Savage et al. 2007). Neither CSH-minerals, which tend to be poorly crystalline, nor zeolites have been detected by XRD-analysis, but the resolution of this

**Table 5-9. The cation exchange capacity of the < 0.5 µm fraction from the backfill material before and after Li-saturation and heating at 250°C. n.d. = not determined.**

| Sample id. | < 0.5 µm fraction | | | < 0.5 µm fraction after Li-saturation+heating | | | | |
|---|---|---|---|---|---|---|---|---|
| | CEC-1 | CEC-2 | CEC-mean | CEC-1 | CEC-2 | CEC-3 | CEC-4 | CEC-mean |
| | meq/100 g | | | meq/100 g | | | | |
| PBF 10 | 98 | 98 | 98 | 19 | 21 | 19 | n.d. | 20 |
| PBF 30 | 95 | 99 | 97 | 17 | 16 | n.d. | n.d. | 17 |
| PBF 50 | 97 | 97 | 97 | 14 | 13 | n.d. | n.d. | 13 |
| PBF 70 | 96 | 96 | 96 | 13 | 14 | n.d. | n.d. | 14 |
| PBF 90 | 93 | 90 | 91 | 14 | 15 | n.d. | n.d. | 15 |
| PBF 110 | 92 | 92 | 92 | 19 | 19 | 20 | 20 | 20 |
| PBF 150 | 92 | 93 | 93 | 12 | 11 | n.d. | n.d. | 12 |
| PBF 1000 | 88 | 89 | 88 | 13 | 16 | 15 | 16 | 15 |

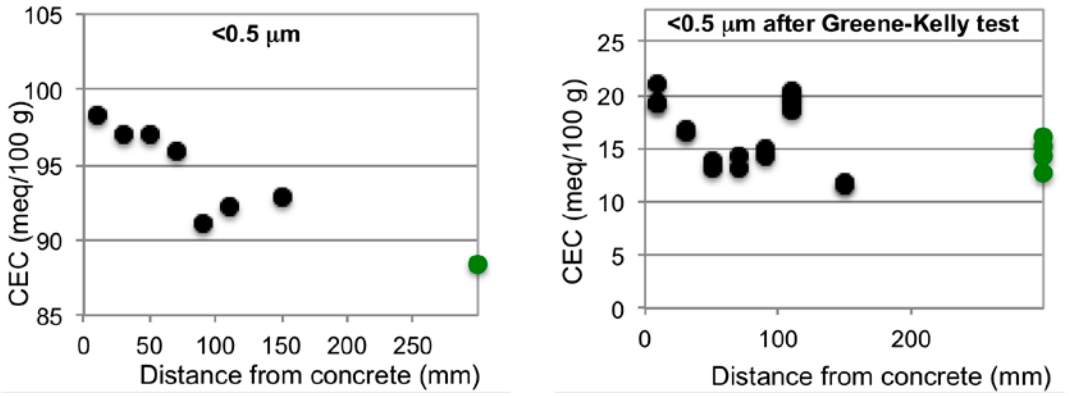


***Figure 5-15.*** *Cation exchange capacity of the < 0.5 µm fractions before (left) and after (right) Li-saturation and heating at 250°C. Mean values of duplicate determinations in the left diagram; values for all determinations in the right diagram. Values for the reference samples from 1 m are plotted in green on the right axis.*

method may be inadequate for detecting trace constituents (< 1%). The Cu(II)-trien method tends, on the other hand, to give significantly underestimated CEC-values for most zeolites because the Cu(II)-trien organic complex is usually much larger than the size of the zeolitic channels and, thus, sterically hindered from access of most of the exchange sites (Meier and Kahr 1999).

Alternatively, an increase in CEC may result if the smectite is structurally changed, which is an observed early effect of smectite-hyperalkaline fluid interactions in several laboratory studies (e.g. Bouchet et al. 2005, Ramírez et al. 2005, Karnland et al. 2007). The increase of the charge has generally been attributed to dissolution of silica in the tetrahedral sheet of montmorillonite, which resulted in beidellite formation (Bouchet et al. 2005, Karnland et al. 2007).

To test the latter possibility, the CEC of the fractions < 0.5 µm was determined after the clay had been saturated with lithium and heated overnight at 250°C (Greene-Kelly test). Upon heating, small cations like Li are believed to migrate from the interlayer positions into the vacant octahedral sites, thereby neutralising the octahedral charge (the Hofmann-Klemen effect; Hofman and Klemen 1950). Accordingly, the remnant CEC of a smectite after Li-saturation and heating should represent the tetrahedral charge. The test is used diagnostically for distinguishing montmorillonite (octahedral charge >> tetrahedral charge) from beidellite (octahedral charge < tetrahedral charge) on the significant loss in cation exchange capacity and expandability exhibited by heated Li-montmorillonite but not by heated Li-beidellite.

The CEC of the Li-converted fractions < 0.5 µm after heating is compiled in Table 5-9 and presented in Figure 5-15 (right), in which all replicate measurements have been plotted to demonstrate the repeatability in the method. The remnant CEC, which is attributable mainly to the tetrahedral charge, make up 13 to 21% of the total charge and motivates that the smectite is classified as montmorillonite.

The maximum CEC value is certainly found in the contact sample at the concrete, but the sample taken 11 cm away from the concrete has equally high CEC, which makes interpretations ambiguous.

#### 5.3.2.2 Mineralogy

XRD-profiles of oriented mounts of the Mg-exchanged < 0.5 µm fractions of the backfill samples are shown in Figure 5-16 (air-dried clay) and Figure 5-17 (EG-solvated clay).

The (001) basal spacing of the Mg-saturated, air-dried smectite ranges between 14.4 and 14.6 Å (relative humidity 50% ± 10) in all samples. The smectite expands to 16.9 Å upon EG-solvation and the d-value is still more or less identical in all samples, as shown in the close-up in Figure 5-17 (right). The expansion behavior is typical of EG-solvated, Mg-saturated montmorillonite.

As can also be seen in the diffraction pattern of the EG-solvated clay, the smectite of all samples proximal to the concrete matches the basic features of the smectite in the reference sample. Hence, the series of basal reflections deviates little from a complete periodic diffraction pattern, which is indicative of well-ordered stacking-sequences with insignificant interstratification.

Calcium silicate hydrates and zeolites are common reaction products and have been reported in many laboratory studies (review in Gaucher and Blanc 2006, Devol-Brown et al. 2007, Savage et al. 2007, De Windt et al. 2008). Neither of these potential secondary phases, nor the secondary Mg-phase that is indicated in the chemistry of the < 0.5 µm fraction, can be detected in the XRD-traces, but it should be remembered that several of the potential reaction products of cement pore fluids-bentonite interactions tend to be poorly crystalline and their detection by XRD-analysis is therefore generally problematic.

However, the XRD-profiles clearly show that < 0.5 µm fractions are not pure montmorillonite, but contain traces of quartz, feldspar and chlorite, some reflections of which are overlapped by the basal reflections of smectite. The close-up of the region 10–33° 2θ in Figure 5-18, where both the air-dried and EG-solvated profiles are shown, further reveals that the peak intensities produced by these minerals decrease in the innermost sample(s), in which peaks become broad and diffuse. Those of quartz and feldspar are barely detectable in the contact sample PBF 10, suggesting a more or less complete dissolution of these minerals at the concrete.

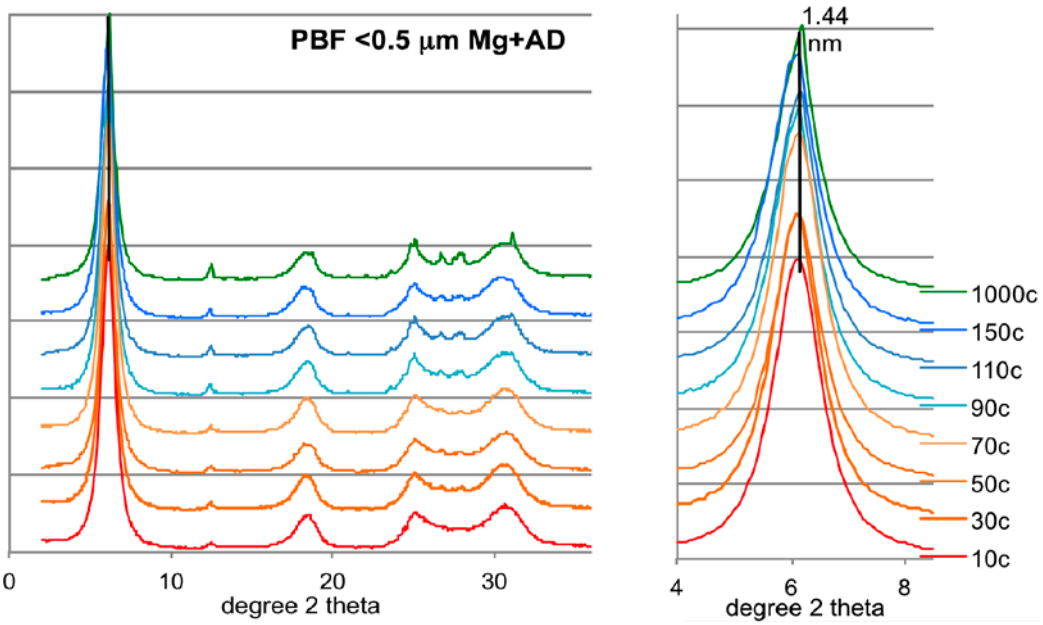


***Figure 5-16.*** *XRD-profiles of oriented mounts of the Mg-exchanged, air-dried < 0.5 µm fractions of the backfill samples. The d-value of the first order basal reflection of smectite is indicated in the close-up to the right. CuKα radiation.*

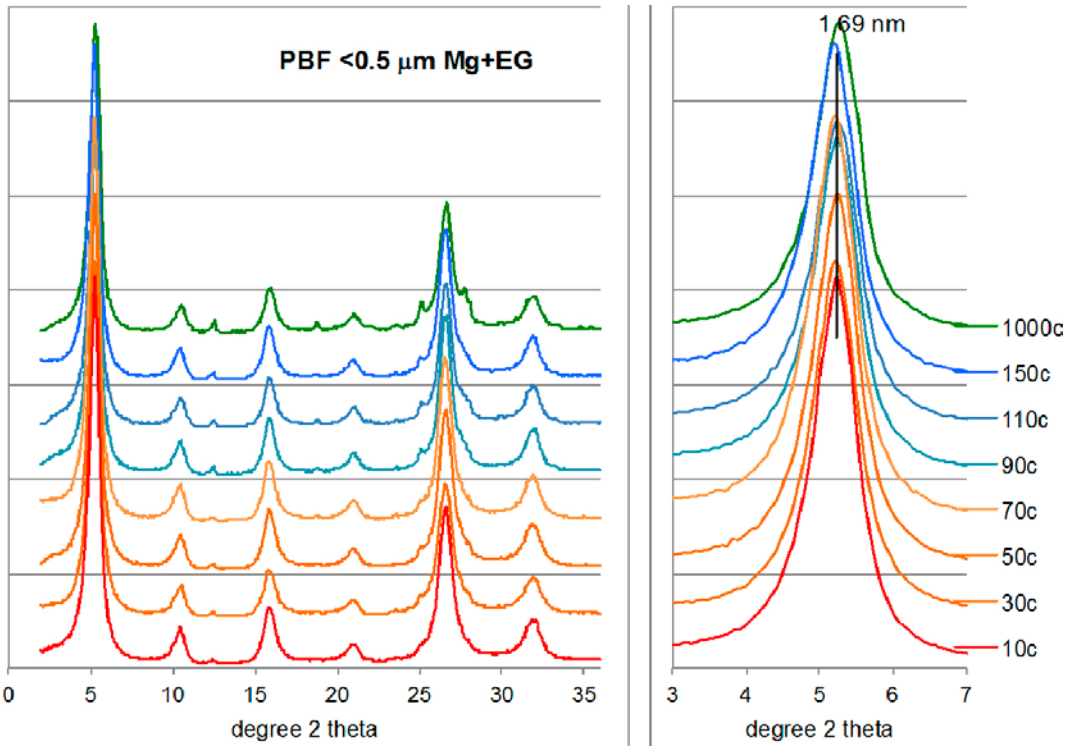


***Figure 5-17.*** *XRD-profiles of oriented mounts of the Mg-exchanged, EG-solvated < 0.5 µm fractions of the backfill samples. The position of the first order basal reflection of smectite is indicated in the close-up to the right. CuKα radiation.*

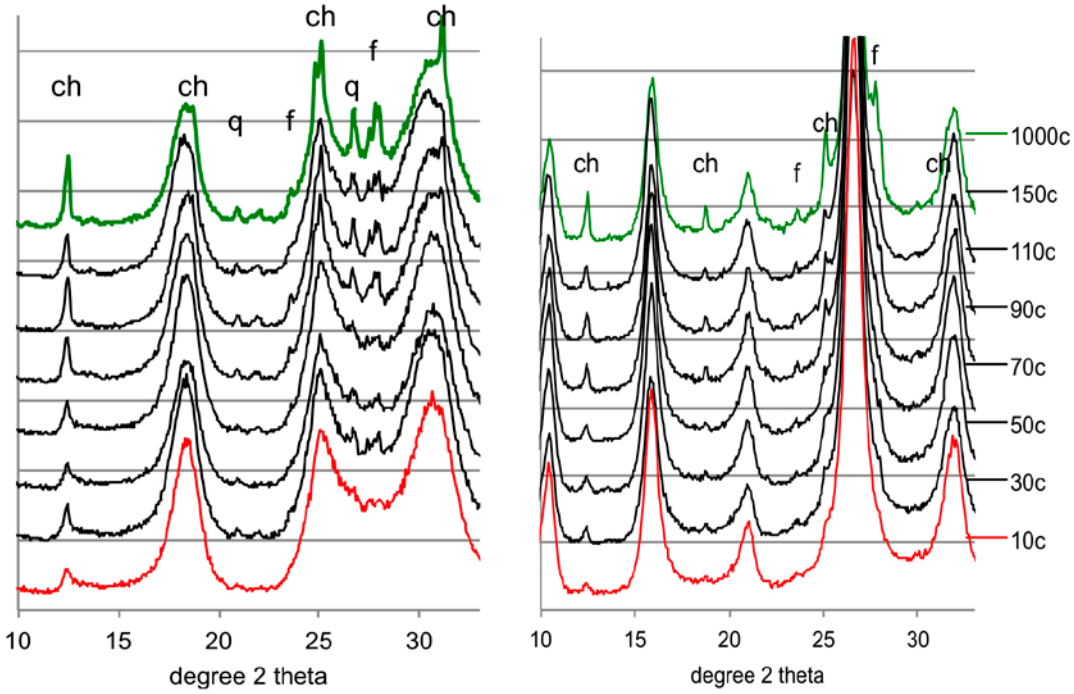


***Figure 5-18.*** *Close-up of the interval 10–33° 2θ of the XRD-profiles of oriented mounts of the Mg-exchanged, air-dried (left) and EG-solvated (right) < 0.5 µm fractions of the backfill samples. ch = the second to fifth order basal peak of chlorite (the first order peak is overlapped by the first order smectite peak); f = feldspar; q = quartz. CuKα radiation.*

#### 5.3.2.3 Chemical composition

The chemical composition of the Na-converted < 0.5 µm fraction of the backfill samples is given in Table 5-10. Calculation of the structural formula of the smectite based on the chemistry of the < 0.5 µm fraction was considered too uncertain because the XRD-data clearly showed that this fraction was not pure smectite. Nevertheless, some clear trends are seen in the composition of the < 0.5 µm fraction as a whole, as demonstrated in Figure 5-19 by some selected parameters.

The magnesium distribution displays a distinct gradient towards the concrete and has increased from 3.64% in the reference sample at 1 meter to a maximum of 5.55% in the innermost 2 cm of the backfill. Prior to the chemical analysis, soluble minerals had been removed more or less completely in the separation, homo-ionisation and dialysis of the fine clay fraction. Accordingly, the contribution from exchangeable magnesium or soluble phases like Mg-carbonates to the magnesium content of the Na-converted < 0.5 µm fraction must be subordinate and the substantial increase (~ 2% MgO) in the innermost centimeters of the backfill is most likely caused by precipitation of a low-solubility Mg-phase. Magnesium for this secondary phase was apparently derived from the original exchange population in the backfill (Section 5.3.1.4) but also supplied by dissolution of Mg-rich minerals, such as dolomite, chlorite (cf. XRD-data) and possible also smectite.

Potassium and calcium exhibit a diametrically different distribution compared to magnesium (Figure 5-19) and decrease towards the concrete. Both elements are constituents of the feldspars, the most fine-grained particles of which appear to have been partially dissolved in the contact sample PBF 10 but supplementary high-resolution analyses are required to verify the suggested coupling between the chemistry and mineralogy.

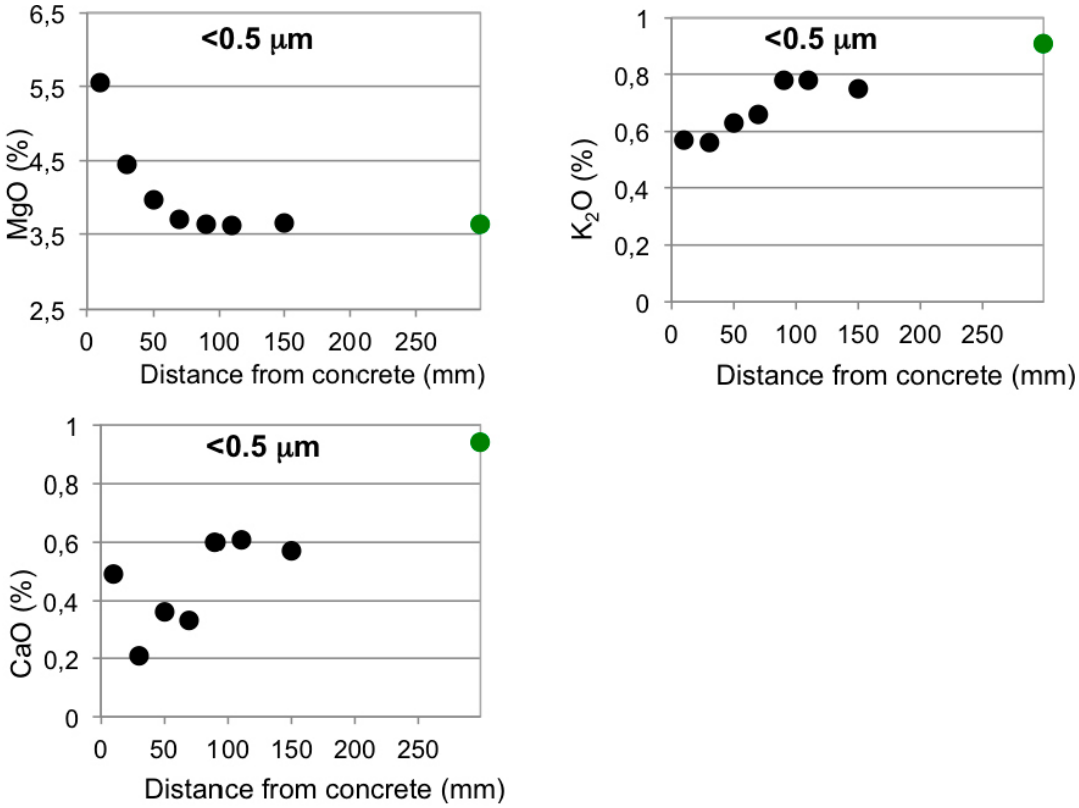


***Figure 5-19.*** *The distribution of MgO, $K_2O$ and CaO in the Na-converted < 0.5 m fraction of the backfill 0–160 mm from the concrete plug. The concentrations of the reference backfill sample 1 m from the concrete are plotted in green on the right axis.*

**Table 5-10. Chemical composition of the Na-saturated < 0.5 µm fractions of the backfill samples. DL = detection limit.**

| Sample id | $SiO_2$ | $Al_2O_3$ | $Fe_2O_3$ | MgO | CaO | $Na_2O$ | $K_2O$ | $TiO_2$ | $P_2O_5$ | MnO | $Cr_2O_3$ | LOI | Sum | tot C | tot S | Sc |
|---|---|---|---|---|---|---|---|---|---|---|---|---|---|---|---|---|
| | % | % | % | % | % | % | % | % | % | % | % | % | % | % | % | ppm |
| DL | 0.01 | 0.01 | 0.04 | 0.01 | 0.01 | 0.01 | 0.01 | 0.01 | 0.01 | 0.01 | 0.002 | -5.1 | 0.01 | 0.02 | 0.02 | 1 |
| PBF 10 | 58.44 | 19.31 | 5.65 | 5.55 | 0.49 | 2.57 | 0.57 | 0.65 | 0.08 | 0.07 | 0.005 | 6.4 | 99.82 | 0.13 | < 0.02 | 16 |
| PBF 30 | 58.98 | 20.16 | 5.6 | 4.45 | 0.21 | 2.91 | 0.56 | 0.64 | 0.05 | 0.05 | 0.002 | 6.2 | 99.85 | 0.16 | < 0.02 | 15 |
| PBF 50 | 59.13 | 20.42 | 5.79 | 3.96 | 0.36 | 2.74 | 0.63 | 0.69 | 0.06 | 0.04 | 0.003 | 6.0 | 99.84 | 0.08 | < 0.02 | 16 |
| PBF 70 | 59.30 | 20.31 | 5.82 | 3.70 | 0.33 | 2.86 | 0.66 | 0.70 | 0.06 | 0.03 | 0.003 | 6.1 | 99.86 | 0.07 | < 0.02 | 16 |
| PBF 90 | 59.22 | 20.07 | 5.70 | 3.64 | 0.60 | 2.75 | 0.78 | 0.78 | 0.09 | 0.04 | 0.004 | 6.2 | 99.84 | 0.10 | 0.04 | 16 |
| PBF 110 | 59.45 | 20.13 | 5.61 | 3.62 | 0.61 | 2.78 | 0.78 | 0.78 | 0.11 | 0.04 | 0.004 | 5.9 | 99.83 | 0.09 | 0.04 | 16 |
| PBF 150 | 59.25 | 20.34 | 5.63 | 3.66 | 0.57 | 2.78 | 0.75 | 0.78 | 0.09 | 0.04 | 0.004 | 6.0 | 99.85 | 0.08 | 0.04 | 16 |
| PBF 1000 | 58.83 | 20.09 | 5.65 | 3.64 | 0.94 | 2.58 | 0.91 | 0.83 | 0.16 | 0.04 | 0.004 | 6.2 | 99.83 | 0.10 | 0.06 | 15 |

| Sample id | Ba | Be | Co | Cs | Ga | Hf | Nb | Rb | Sn | Sr | Ta | Th | U | V | W | Zr |
|---|---|---|---|---|---|---|---|---|---|---|---|---|---|---|---|---|
| | ppm | ppm | ppm | ppm | ppm | ppm | ppm | ppm | ppm | ppm | ppm | ppm | ppm | ppm | ppm | ppm |
| DL | 1 | 1 | 0.2 | 0.1 | 0.5 | 0.1 | 0.1 | 0.1 | 1 | 0.5 | 0.1 | 0.2 | 0.1 | 8 | 0.5 | 0.1 |
| PBF 10 | 90 | < 1 | 12.9 | 11.7 | 18.4 | 3.7 | 7.6 | 50.1 | 3 | 51.2 | 0.3 | 8.7 | 4.2 | 171 | 1.1 | 139.6 |
| PBF 30 | 71 | 3 | 13.9 | 13.1 | 19.5 | 4.1 | 7.5 | 48.3 | 2 | 42.8 | 0.4 | 9.6 | 4.2 | 171 | 1.0 | 139.5 |
| PBF 50 | 101 | 2 | 13.3 | 12.4 | 18.8 | 3.6 | 7.1 | 50.3 | 2 | 50.8 | 0.4 | 9.0 | 4.4 | 182 | 0.8 | 147.1 |
| PBF 70 | 101 | < 1 | 13.5 | 10.9 | 18.9 | 4.0 | 7.8 | 49.7 | < 1 | 55.3 | 0.6 | 10.0 | 4.5 | 173 | 1.5 | 147.0 |
| PBF 90 | 170 | 5 | 13.4 | 11.1 | 19.0 | 3.9 | 10.5 | 49.6 | 1 | 94.3 | 0.6 | 10.6 | 4.8 | 181 | 0.7 | 153.4 |
| PBF 110 | 153 | 3 | 12.1 | 9.9 | 18.3 | 4.3 | 8.5 | 48.4 | 1 | 95.7 | 0.6 | 10.3 | 5.3 | 165 | 1.3 | 147.0 |
| PBF 150 | 157 | 5 | 16.5 | 9.6 | 18.6 | 4.2 | 7.0 | 48.2 | 2 | 86.8 | 0.6 | 11.1 | 4.6 | 166 | 1.0 | 152.2 |
| PBF 1000 | 209 | 3 | 15.3 | 10.1 | 18.9 | 3.1 | 7.1 | 51.4 | 1 | 131.1 | 0.6 | 11.4 | 5.7 | 160 | 1.2 | 151.6 |

| Sample id | Y | La | Ce | Pr | Nd | Sm | Eu | Gd | Tb | Dy | Ho | Er | Tm | Yb | Lu | Mo |
|---|---|---|---|---|---|---|---|---|---|---|---|---|---|---|---|---|
| | ppm | ppm | ppm | ppm | ppm | ppm | ppm | ppm | ppm | ppm | ppm | ppm | ppm | ppm | ppm | ppm |
| DL | 0.1 | 0.1 | 0.1 | 0.02 | 0.3 | 0.05 | 0.02 | 0.05 | 0.01 | 0.05 | 0.02 | 0.03 | 0.01 | 0.05 | 0.01 | 0.1 |
| PBF 10 | 11.9 | 24.0 | 46.1 | 4.93 | 18 | 3.86 | 0.89 | 3.79 | 0.46 | 2.63 | 0.4 | 1.17 | 0.22 | 1.48 | 0.15 | 0.1 |
| PBF 30 | 11.2 | 21.1 | 43.4 | 4.66 | 19.5 | 3.18 | 0.77 | 2.88 | 0.38 | 2.06 | 0.38 | 1.01 | 0.2 | 1.3 | 0.14 | < 0.1 |
| PBF 50 | 12.9 | 23.9 | 43.4 | 5.04 | 19.6 | 4.11 | 1.01 | 3.5 | 0.41 | 2.19 | 0.49 | 1.33 | 0.18 | 1.14 | 0.14 | 0.2 |
| PBF 70 | 10.2 | 22.7 | 42.2 | 5.05 | 16.1 | 3.66 | 0.93 | 3.1 | 0.4 | 1.84 | 0.48 | 1.13 | 0.14 | 1.22 | 0.18 | 0.1 |
| PBF 90 | 14.5 | 28.4 | 54.6 | 6.13 | 20.9 | 4.73 | 1.11 | 3.97 | 0.56 | 3.55 | 0.49 | 1.52 | 0.22 | 1.75 | 0.23 | 0.2 |
| PBF 110 | 14.0 | 28.2 | 51.0 | 6.24 | 24.0 | 4.54 | 1.03 | 3.76 | 0.52 | 2.8 | 0.49 | 1.43 | 0.24 | 1.61 | 0.22 | 0.2 |
| PBF 150 | 15.1 | 28.3 | 51.0 | 6.11 | 24.7 | 4.58 | 1.01 | 3.51 | 0.5 | 2.94 | 0.55 | 1.61 | 0.20 | 1.55 | 0.20 | 0.2 |
| PBF 1000 | 17.3 | 31.0 | 58.8 | 6.81 | 25.4 | 4.76 | 1.3 | 4.32 | 0.62 | 3.79 | 0.64 | 2.05 | 0.24 | 1.82 | 0.25 | 0.3 |

| Sample id | Cu | Pb | Zn | Ag | Ni | As | Au | Cd | Sb | Bi | Hg | Tl | Se |
|---|---|---|---|---|---|---|---|---|---|---|---|---|---|
| | ppm | ppm | ppm | ppm | ppm | ppm | ppm | ppm | ppm | ppm | ppm | ppm | ppm |
| DL | 0.1 | 0.1 | 1 | 0.1 | 0.1 | 0.5 | 0.5 | 0.1 | 0.1 | 0.1 | 0.01 | 0.1 | 0.5 |
| PBF 10 | 27.5 | 10.4 | 73 | < 0.1 | 10.7 | 1.4 | 3.9 | 0.1 | 0.1 | 0.1 | 0.21 | 0.2 | < 0.5 |
| PBF 30 | 28.6 | 9.9 | 72 | < 0.1 | 10.4 | 1.2 | 2.3 | 0.1 | < 0.1 | < 0.1 | 0.25 | 0.3 | < 0.5 |
| PBF 50 | 27.1 | 10.9 | 63 | < 0.1 | 9.4 | 1.2 | 2.4 | 0.2 | < 0.1 | < 0.1 | 0.32 | 0.3 | < 0.5 |
| PBF 70 | 29.2 | 10.5 | 72 | < 0.1 | 9.5 | 1.4 | 1.4 | 0.2 | < 0.1 | < 0.1 | 0.26 | 0.2 | < 0.5 |
| PBF 90 | 26.7 | 10.5 | 69 | < 0.1 | 10.8 | 2.3 | 2.6 | 0.2 | 0.1 | < 0.1 | 0.25 | 0.2 | < 0.5 |
| PBF 110 | 26.8 | 9.9 | 69 | < 0.1 | 10.7 | 2.0 | 2.7 | < 0.1 | < 0.1 | < 0.1 | 0.20 | 0.2 | < 0.5 |
| PBF 150 | 32.8 | 10.3 | 79 | < 0.1 | 13.2 | 2.2 | 0.6 | 0.1 | < 0.1 | < 0.1 | 0.26 | 0.2 | < 0.5 |
| PBF 1000 | 37.4 | 11.7 | 84 | < 0.1 | 14.5 | 2.4 | 1.5 | 0.2 | < 0.1 | < 0.1 | 0.30 | 0.2 | 0.6 |

## 5.4 Summary and conclusions

A mixture of bentonite from Milos, containing mainly calcite and dolomite in addition to smectite, and 70% ballast of crushed granodioritic rock with grain-sizes 0–20 mm was used as tunnel backfill material in the Prototype Repository field test. The deposition tunnel had been sealed with plugs of concrete produced of Portland cement. The backfill had been subjected to hydration by groundwater from the host rock at Äspö HRL and – in the vicinity of the plugs – to contact with leachates from the concrete for almost eight years at the time of retrieval. The chemical and mineralogical investigations of the < 1 mm and the < 0.5 μm fractions of the tunnel backfill material, sampled at a 2 centimeter-scale within the interval 0–16 cm from the inner concrete plug, suggest that modifications of the backfill mineralogy had occurred as follow:

- Cation exchange reactions in the interval 0–8 cm from the concrete involved replacement of exchangeable magnesium and calcium primarily by sodium, but a significant increase was seen also in exchangeable potassium.
- Neoformed calcite and an apparently amorphous, secondary Mg-phase of low solubility had precipitated in the innermost centimeters of the backfill. These precipitation reactions must have exerted major control on the pore fluid composition, and hence, on the pool of exchangeable cations in the backfill material.
- XRD-data for the < 1 mm fractions indicated that the increase in calcite in the innermost centimeters of the backfill was paralleled by a decrease in dolomite. Transformation of dolomite into an Mg-rich phase of low solubility and calcite and/or other Ca-rich minerals is suggested one major mechanism by which magnesium and calcium were reused in secondary phases.
- XRD-data for the < 0.5 μm fractions suggest that fine-grained chlorite, quartz and feldspars were partially dissolved in the samples proximal to the concrete.
- No secondary phases were detected in the XRD-analysis of the < 0.5 μm fractions, from which calcite was removed by the purification procedure, but several of the potential reaction products of cement pore fluids-bentonite interactions tend to be poorly crystalline and their detection by XRD-analysis is therefore generally problematic. The secondary Mg-phase in the samples proximal to the concrete was thus identified only through a substantial increase in the MgO-content of the Na-converted, carbonate-free < 0.5 μm fractions. To enable phase identification, higher spatial sampling resolution and/or supplementary high-resolution scanning analyses are probably necessary.
- CEC of the < 0.5 μm fraction had increased by 10 meq/100 g in the sample proximal to the concrete compared with the reference sample. A potential beidellitization of the montmorillonite would increase the CEC, but tests of the expansion behavior and of the charge distribution provided no clear evidence of any structural changes in the smectite.
- The cation exchange properties of the secondary Mg-phase is not known and other, undetected, secondary phases with exchange capacity may exist.

The tunnel backfill material for the Prototype Repository was prepared of crushed rock and bentonite, and was compacted *in situ* in the tunnel. The technique for backfilling the deposition tunnels was, however, changed after the installation of the Prototype test to improve the function of the tunnel backfill, which, among other things, is to prevent upward heaving of the buffer and sustain the multi-barrier system by restricting groundwater flow through the tunnels. According to the current reference technique, pre-compacted bentonite blocks will be used, together with a filling of bentonite pellets close to the tunnel walls, i.e. the hydro-mechanical and chemical-mineralogical properties of the currently recommended backfill material will be different from those of the backfill used in the Prototype test.

# References

SKB's (Svensk Kärnbränslehantering AB) publications can be found at www.skb.se/publications.


**Adler M, Mäder U, Waber H N, 2000.** The role of multicomponent cation exchange and dedolomitisation in argillaceous rock at conditions of high-pH. Goldschmidt 2000, an International Conference for Geochemistry, Oxford, UK, 3–8 September 2000. Journal of Conference Abstracts 5, 120.

**Alexander W R, Milodowski A E, Pitty A F, Hardie S M, Kemp J C, Rushton J C, Siathas A, Siathas Av, Mackenzie A B, Korkeakoski P, Norris S, Sellin P, Rigas M, 2013.** Bentonite reactivity in alkaline solutions: interim results of the Cyprus Natural Analogue Project (CNAP). Clay Minerals 48, 235–249.

**Ammann L, Bergaya F, Lagaly G, 2005.** Determination of the cation exchange capacity of clays with copper complexes revisited. Clay Minerals 40, 441–453.

**Arlinger J, Bengtsson A, Edlund J, Eriksson L, Johansson J, Lydmark S, Rabe L, Pedersen K, 2013.** Prototype repository – Microbes in the retrieved outer section. SKB P-13-16, Svensk Kärnbränslehantering AB.

**Belyayeva N I, 1967.** Rapid method for the simultaneous determination of the exchange capacity and content of exchangeable cations in solonetzic soils. Soviet Soil Science, 1,409–1,413.

**Bouchet A, Cassagnabère A, Parneix J C, 2005.** Batch experiments: results on the bentonite MX80. In Ecoclay II: Effect of cement on clay barrier performance – Phase II. Final report. EUR 21921, European Commission, 79–87.

**Brindley G W, Brown G (eds), 1980.** Crystal structures of clay minerals and their x-ray identification. London: Mineralogical Society (Mineralogical Society Monograph) 5.

**Börgesson L, Johannesson L-E, Sandén T, Hernelind J, 1995.** Modelling of the physical behaviour of water saturated clay barriers. Laboratory tests, material models and finite element application. SKB TR 95-20, Svensk Kärnbränslehantering AB.

**Carlson S, Clausén M, Gridneva L, Sommarin B, Svensson C, 2006.** XAFS experiments at beamline I811, MAX-lab synchrotron source, Sweden. Journal of Synchrotron Radiation 13, 359–364.

**Cerenius Y, Ståhl K, Svensson L A, Ursby T, Oskarsson Å, Albertsson J, Liljas A, 2000.** The crystallography beamline I711 at MAX II. Journal of Synchrotron Radiation 7, 203–208.

**Cornell R M, Schwertmann U, 2003.** The iron oxides: structure, properties, reactions, occurences and uses. 2nd ed. Weinheim: Wiley-VHC.

**Craig R F, 1992.** Soil Mechanics. Fifth edition, Chapman & Hall. London, England.

**Devol-Brown I, Tinseau E, Bartier D, Mifsud A, Stammose D, 2007.** Interaction of Tournemire argillite (Aveyron, France) with hyperalkaline fluids: batch experiments performed with powdered and/or compacted materials. Physics and Chemistry of the Earth, Parts A/B/C 32, 320–333.

**De Windt L, Marsal F, Tinseau E, Pellegrini D, 2008.** Reactive transport modelling of geochemical interactions at a concrete/argillite interface, Tournemire site (France). Physics and Chemistry of the Earth, Parts A/B/C 33 S295-S305.

**Dohrmann R, Genske D, Karnland O, Kaufhold S, Kiviranta L, Olsson S, Plötze M, Sandén T, Sellin P, Svensson D, Valter M, 2012.** Interlaboratory CEC and exchangeable cation study of bentonite buffer materials: I. Cu(II)-triethylenetetramine method. Clays and Clay Minerals 60, 162–175.

**Dohrmann R, Olsson S, Kaufhold S, Sellin P, 2013.** Mineralogical investigations of the first package of the alternative buffer test – II. Exchangeable cation population rearrangement. Clay Minerals 48, 215–233.

**Dohrmann, R., Kaufhold, S, 2013.** Mineralogical investigations of buffers samples of the deposition holes 5 and 6 from the prototype repository experiment in Äspö, Sweden.BGR internal report, Hannover, 24 pages. Archive number 0131513.

**Drever J I, 1973.** The preparation of oriented clay mineral specimen for x-ray diffraction analysis by a filter-membrane peel technique. American Mineralogist, 58, 553–554.

**Dueck A, Börgesson L, Johannesson L-E, 2010.** Stress-strain relation of bentonite at undrained shear. Laboratory tests to investigate the influence of material composition and test technique. SKB TR-10-32, Svensk Kärnbränslehantering AB.

**Dueck A, Johannesson L-E, Kristensson O, Olsson, S, 2011a.** Report on hydro-mechanical and chemical-mineralogical analyses of the bentonite buffer in Canister Retrieval Test. SKB TR-11-07, Svensk Kärnbränslehantering AB.

**Dueck A, Johannesson L-E, Kristensson O, Olsson S, Sjöland A, 2011b.** Hydro-mechanical and chemical-mineralogical analyses of the bentonite buffer from a full-scale field experiment simulating a high-level waste repository. Clays and Clay Minerals 59, 595–607.

**Evans B J, Johnson R G, Senftle F E, Blaine Cecil C, Dulong F, 1982.** The $^{57}$Fe Mössbauer parameters of pyrite and marcasite with different provenances. Geochimica et Cosmochimica Acta 46, 761–775.

**Farmer V C (ed), 1974.** The infrared spectra of minerals. London: Mineralogical Society.

**Farmer V C, Russell J D, 1967.** Infrared absorption spectrometry in clay studies. Clays and Clay Minerals 15, 121–142.

**Gaucher E C, Blanc P, 2006.** Cement/clay interactions – a review: experiments, natural analogues, and modeling. Waste Management 26, 776–788.

**Greene-Kelly R, 1955.** Dehydration of montmorillonite minerals. Mineralogical Magazine 30, 604–615.

**Gunnarsson, D, 2002.** Äspö Hard Rock Laboratory. Backfill production for Prototype Repository. SKB IPR-02-20, Svensk Kärnbränslehantering AB.

**Goudarzi R, 2012.** Prototype Repository – Sensor data report (period 100917–110101). Report no 24. SKB P-12-12, Svensk Kärnbränslehantering AB.

**Hofmann U, Klemen R, 1950.** Verlust der Austauschfähigkeit von Lithiumionen an Bentonit durch Erhitzung. Zeitschrift für anorganische Chemie 262, 95–99.

**Hogarth D D, Brown F F, Pritchard A M, 1970.** Biabsorption, Mössbauer spectra, and chemical investigation of five phlogopite samples from Quebec. The Canadian Mineralogist 10, 710–722.

**Jackson M L, 1975.** Soil chemical analysis: advanced course. 2nd ed. Madison, Wisconsin.

**Jodin-Caumon M-C, Mosser-Ruck R, Rousset D, Randi A, Cathelineau M, Michau N, 2010.** Effect of thermal gradient on iron-clay interactions. Clays and Clay Minerals 58, 667–681.

**Johannesson L-E, 2005.** Äspö Hard Rock Laboratory. Prototype Repository. Laboratory tests on the backfill material in the Prototype Repository. SKB IPR-05-11, Svensk Kärnbränslehantering AB.

**Johannesson L-E, 2013.** Prototype Repository. Measurements of water content and density of the retrieved buffer material from deposition hole 5 and 6 and the backfill in the outer section of the Prototype Repository. SKB P-13-14, Svensk Kärnbränslehantering AB.

**Johannesson L-E, Hagman P, 2013.** Prototype Repository. Method for opening and retrieval of the outer section. SKB P-13-15. Svensk Kärnbränslehantering AB.

**Karnland O, Olsson S, Nilsson U, 2006.** Mineralogy and sealing properties of various bentonites and smectite-rich clay materials. SKB TR-06-30, Svensk Kärnbränslehantering AB.

**Karnland O, Olsson S, Nilsson U, Sellin P, 2007.** Experimentally determined swelling pressures and geochemical interactions of compacted Wyoming bentonite with highly alkaline solutions. Physics and Chemistry of the Earth, Parts A/B/C 32, 275–286.

**Karnland O, Olsson S, Dueck A, Birgersson M, Nilsson U, Hernan-Håkansson T, Pedersen K, Nilsson S, Eriksen T, Rosborg B, 2009.** Long term test of buffer material at the Äspö Hard Rock Laboratory, LOT project. Final report on the A2 test parcel. SKB TR-09-29, Svensk Kärnbränslehantering AB.

**Karnland O, Olsson S, Sandén T, Fälth B, Jansson M, Eriksen T, Svärdström K, Rosborg B, Muurinen A, 2011.** Long term test of buffer material at the Äspö Hard Rock Laboratory, LOT project. Final report on the A0 test parcel. SKB TR-09-31, Svensk Kärnbränslehantering AB.

**Kiviranta L, Kumpulainen S, 2011.** Quality control and characterization of bentonite materials. Posiva Working Report 2011-84, Posiva Oy, Finland.

**Kumpulainen S, Kiviranta L, Carlsson T, Muurinen A, Svensson D, Sasamoto H, Yui M, Wersin P, Rosch D, 2011.** Long-term alteration of bentonite in the presence of metallic iron. SKB R-10-52, Svensk Kärnbrandslehantering AB.

**Lim C H, Jackson M L, 1986.** Expandable phyllosilicate reactions with lithium on heating. Clays and Clay Minerals 34, 346–352.

**Madejová J, Komadel P, 2001.** Baseline studies of the Clay Minerals Society source clays: infrared methods. Clays and Clay Minerals 49, 410–432.

**Meier L P, Kahr G, 1999.** Determination of the cation exchange capacity (CEC) of clay minerals using the complexes of copper(II) ion with triethylenetetraamine and tetraethylenepentamine. Clays and Clay Minerals 47, 386–388.

**Moore D M, Reynolds R C, 1989.** X-ray diffraction and the identification and analysis of clay minerals. Oxford: Oxford University Press.

**Newman A C D, Brown G, 1987.** The chemical constitution of clays. In Newman A C D (ed). Chemistry of clays and clay minerals. Harlow: Longman. (Mineralogical Society Monograph 6), 1–128.

**Olsson S, Karnland O, 2011.** Mineralogical and chemical characteristics of the bentonite in the A2 test parcel of the LOT field experiments at Äspö HRL, Sweden. Physics and Chemistry of the Earth, Parts A/B/C 36, 1,545–1,553.

**Persson G, Broman O, 2000.** Äspö Hard Rock Laboratory. Prototype Repository. Project plan FIKW-CT-2000-00055. SKB IPR-00-31, Svensk Kärnbränslehantering AB.

**Ramírez S P, Vieillard A, Bouchet A, Cassagnabère A, Meunier E, Jacquot E, 2005.** Alteration of the Callovo-Oxfordian Clay from Meuse-Haute Marne underground laboratory (France) by alkaline solution. I. A XRD and CEC study. Applied Geochemistry 20, 89–99.

**Russell J D, 1987.** Infrared methods. In Wilson M J (ed). A handbook of determinative methods in clay mineralogy. Glasgow: Blackie, 133–173.

**Savage D, Walker C, Arthur R, Rochelle C, Oda C, Takase H, 2007.** Alteration of bentonite by hyperalkaline fluids: a review of the role of secondary minerals. Physics and Chemistry of the Earth, Parts A/B/C 32, 287–297.

**SKB, 2006.** Long-term safety for KBS-3 repositories at Forsmark and Laxemar – a first evaluation. Main Report of the SR-Can project. SKB Technical Report TR-06-09, Svensk Kärnbränslehantering AB.

**SKB, 2010.** Design, production and initial state of the buffer. SKB TR-10-15, Svensk Kärnbränslehantering AB.

**Svemar C, Pusch R, 2000.** Äspö Hard Rock Laboratory. Prototype Repository. Project description FIKW-CT-2000-00055. SKB IPR-00-30, Svensk Kärnbränslehantering AB.

**Wagner F E, Wagner U, 2004.** Mössbauer spectra of clays and ceramics. Hyperfine Interactions 154, 35–82.

**Åkesson M, Olsson S, Dueck A, Nilsson U, Karnland O, Kiviranta L, Kumpulainen S, Lindén J, 2012.** Temperature buffer test. Hydromechanical and chemical/mineralogical characterizations. SKB P-12-06, Svensk Kärnbränslehantering AB.

# Appendix 1

# Report on the P6_R05 series and R10-270-525 B+Tech bentonite samples

J. Lindén
*Department of Physics, Åbo Akademi, FIN-20500 Turku, Finland*
(Dated: April 5, 2012)

## I. EXPERIMENTAL

Six samples were investigated, each consisting of ∼ 55 mg dry powder mixed with epoxy glue evenly spread on an area of ∼3,0 $cm^2$ on a thin Fe-free aluminum foil. Upon receival the samples were immediately stored under a protective $N_2$ atmosphere in a glove box (concentration of $O_2/H_2O$ less than 4 ppm) prior to the Mössbauer measurements. The grinding of the coarse powders with a agate mortar, the handling and manucaturing of the absorbers (including the time reserved for the epoxy to harden) was done in the gloveboxe. The epoxy protected absorbers were exposed to ambient air for ∼ 30 minutes when transfered to the vacuum chamber of the crysotat used for cooling the samples to 77 K. The measured samples were labelled: P6_R05_R, P6_R05_165_D535, P6_R05_165_D555, P6_R05_165_D575, P6_R05_165_D615, and R10-270-525. Two separate absorbers were produced from the reference sample P6_R05_R, one in the beginning of the measurement (january 2012) and the other towards the end (March 2012). Thus all in all seven spectra were recorded. All spectra were collected at 77 K in transmission mode using a sinusoidal velocity scale with a maximum Doppler velocity of ∼ 10.1 mm/s. The velocity was chosen to allow detection of the magnetic lines of Fe oxides and hydroxides. For paramagnetic samples the scale is a a bit too large, but as shown by the spectra measured in 2009 weak magnetic lines are likely to be present. The geometry, i.e. source-to-detector distance, absorber area and collimation was the same for all samples, as well as the the settings for the gamma-ray window. Data were collected for seven days for each sample,.

Sample cooling was achieved using an Oxford ITC-4 continuous-flow cryostat operated with liquid nitrogen. The 14.4-keV Mössbauer quanta were produced by a Cyclotron Co. $^{57}Co$:*Rh* (25 mCi Apr. 2009) source and detected using a LND 4546 porportional counter with a beryllium window. A Fast ComTec MA-250 velocity transducer was used for moving the source. It was equipped with a Halder MR-351 Drive unite. The data was gathered using a Fast ComTec MCA-3 multichannel-analyzer PCI card in an ordinary desktop PC. The measurement was done in the multiscaling mode.

The spectra were fitted using a home-made nonlinear least-squares fit program, utilizing spectral components corresponding to four paramagnetic doublets and one magnetic sextet. For the paramagnetic components parameters used in the fit were: The quadrupole splitting $\Delta$, in mm/s, the isomer shift $\delta$ with respect to $\alpha$-Fe, in mm/s and the spectral intensities $I$ in %. For the magnetic component, additionally, the internal field $B$, in T and its gaussian distribution $\Delta B$, in T were included as fit parameters. All components were constrained to have a common line width $\Gamma$, in mm/s.

## II. RESULTS AND DISCUSSION

The fitted spectra are displayed in the figures 1-7. The five components used for the analysis, all corresponding to various Fe species, are shown. The magnetic sextet (Component 4, drawn in brown) and the paramagnetic Component 5 (drawn in green) were not visible in all spectra and hence included only when possible to fit to the data.

By visual inspection of the spectra the main difference between the spectra is the lower portion of Component 1 in the reference spectra. These reference spectra also dsiplay a rather high line-width, perhaps due to poorer crystallinity as compared to the other samples. The deterioration of crystallinity could be the cause of the difference between the two reference spectra. The one recorded later has a larger line width and also contains hints of magnetic (trivalent) iron. The original capsule (provided by the customer) containing the sample material was by no-means hermetic. Still, it seems unlikely that an oxidation would occur in an $N_2$ atmosphere with such a low $O_2$ content.

In most cases the dominating component is paramagnetic with a huge quadrupole splitting $\Delta \approx 3.0$ mm/s (Component 1 in TABLE 1). It has also a large isomer shift typical of divalent Fe. The same component was reported in the study by Carlsson & coworkers.[1] It is typical for Fe containing bentonite samples. On the inner slope of the first line of Component 1 additional paramagnetic features are seen. These were fitted using two quadrupole components (Components 2 and 3), as a single component was not enough to explain these features. Both components are due to trivalent Fe, based on the isomer-shift values. Only one such component was reported in Ref. 1. However, they might correspond to almost the same chemical environment, reflecting a less than perfect local crystallinity of the trivalent Fe species. This may be true if it is the result of a low-temperature oxidation of the divalent component. The second divalent component (Component 5) has a very high isomer shift, compatible only with high-spin $Fe^{2+}$, like

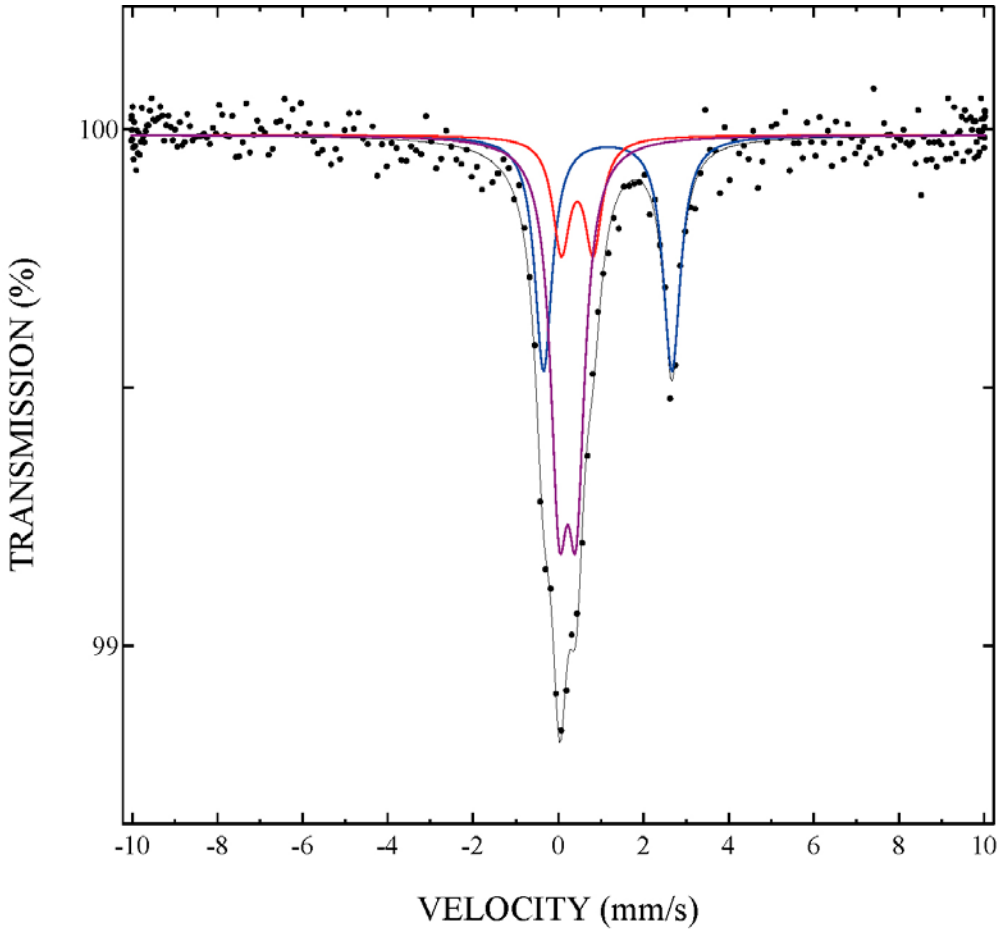


FIG. 1: Mössbauer spectrum recorded from sample P6_R05_R at 77 K (1st sample). Components of the fit are displayed above the spectrum. They are: Component 1 in blue, Component 2 in red, and Component 3 in violet.

Component 1. However, the quadrupole splitting for Component 5 is much smaller than for Component 1. Therefore, it must originate from a different surrounding than Component 1. In many cases the isomer shift value of Component 5 is very close to the upper limit given in literature value.[2] Furthermore, for the present sample series the isomer shift value for Component 2 is rather high (up to 0.6 mm/s relative to $\alpha$ iron). Although still compatible with high-spin $Fe^{3+}$ it could in principle be due to low-spin $Fe^{2+}$, where as the two other divalent components (1 and 5) are clearly in the high-spin state, judging by the isomer shift values. Whether, the Hund's-rule violating low-spin states really exists or not in these particular samples remains speculative, as long as information on the local symmetry surrounding the Fe atoms is lacking.

The are weak magnetic features in two spectra spectra, but due to the very low concentration of magnetic iron the fitted parameters of the magnetic Mössbauer component are very uncertain. When a paramagnetic doublet becomes magnetically split all the intensity is distributed over six resonance lines and the detection limit increases

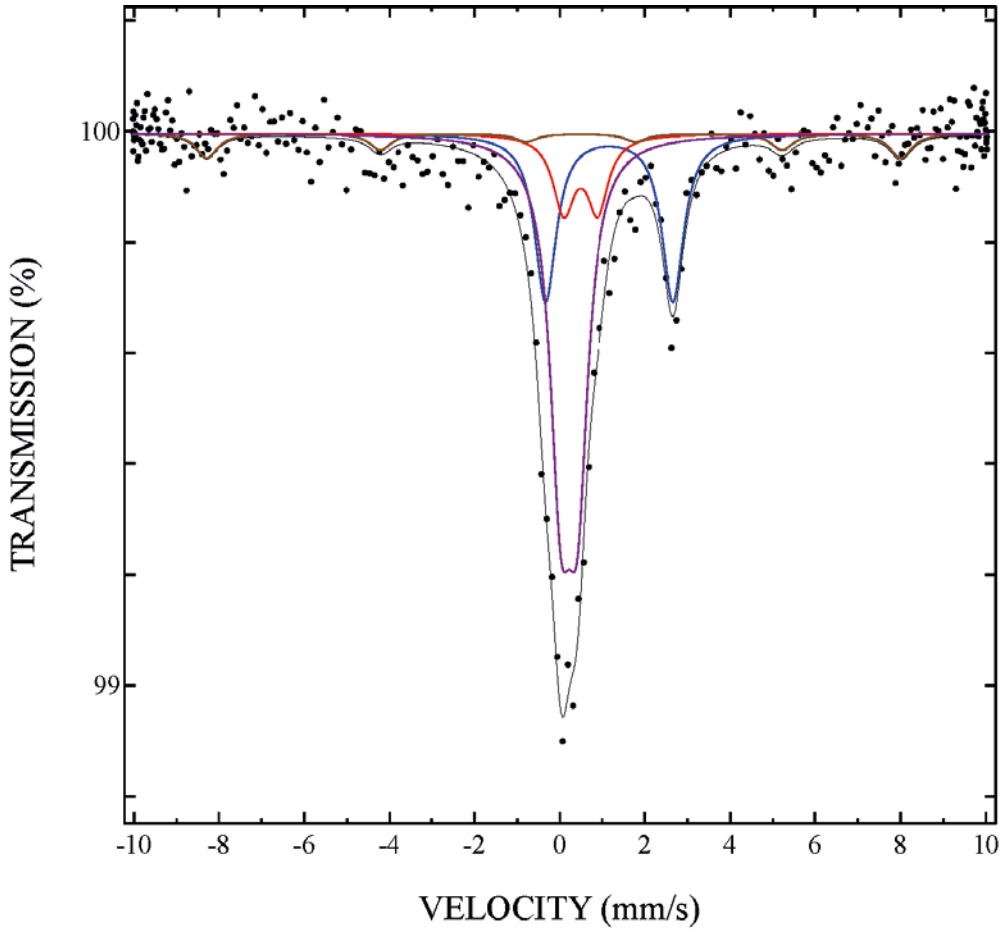


FIG. 2: Mössbauer spectrum recorded from sample P6_R05_R at 77 K (2nd sample). Components of the fit are displayed above the spectrum. They are: Component 1 in blue, Component 2 in red, Component 3 in violet, and Component 4 in brown.

approximately with 4, i.e. the concentration of a hypothetical magnetic Fe species could be four times higher than a paramagnetic one and still remain undetected in the Mössbauer spectrum. The fitted internal field for the magnetic component (Component 4) was 50-55 T, with uncertainties of at least 1 T. These values should in principle be due to $Fe^{3+}$, as divalent Fe seldom exhibits internal field exceeding $\sim$ 48 T. However, the isomer shift values of 0.8 mm/s (Fig. 4, TABLE 1) is no longer compatible with high-spin $Fe^{3+}$. On the other hand, a systematic error caused by the uncertainty in the quadrupole splitting is the most likely explanation for this discrepancy. There is also a possibility that there are more than one magnetic component (like e.g. in magnetite), which can not be ruled out due to the very weak statistics for the magnetic lines. Assignment to a specific Fe oxide or hydroxide should therefore not be attempted. Instead one only give a rough estimate of the concentration of magnetic trivalent iron in the samples, see Table I.

From Table I one immediately obtains the main result, i.e. the ratio of paramagnetic $Fe^{2+}$ to $Fe^{3+}$, by assuming the

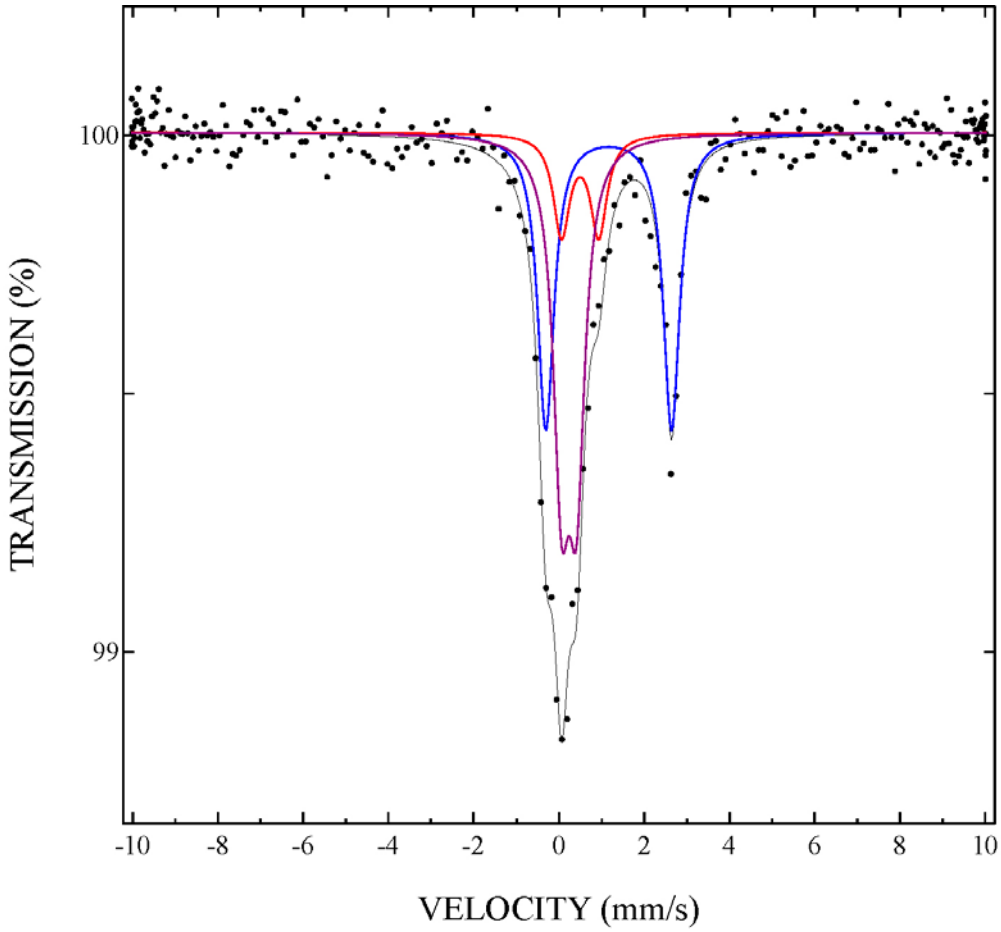


FIG. 3: Mössbauer spectrum recorded from sample P6_R05_165_D535 at 77 K. Components of the fit are displayed above the spectrum. They are: Component 1 in blue, Component 2 in red, Component 3 in violet.

recoil-free fraction to be the same for all components and omitting the possibility of low-spin $Fe^{2+}$: 0.538 (P6_R05_R ref1), 0.437 (P6_R05_R ref 2), 0.709 (D535), 0.805 (D555), 0.675 (D575), 0.751 (D615) and 0.905 (R10-270-525). In this estimate the magnetic Fe was ignored. In case the magnetic Fe, when present, is lumped together with the other trivalent components (Component 2 and 3) the following results are obtained for the ratio of divalent to trivalent Fe: 0.437 (P6_R05_R ref 2) and 0.724 (D555).

## III. CONCLUSIONS

Seven bentonite absorbers from six samples were measured by $^{57}Fe$ Mössbauer spectroscopy at 77 K. The ratio of paramagnetic $Fe^{2+}$ to $Fe^{3+}$ was obtained. Traces (6-8 % of the total intensity) of magnetic (trivalent) Fe was

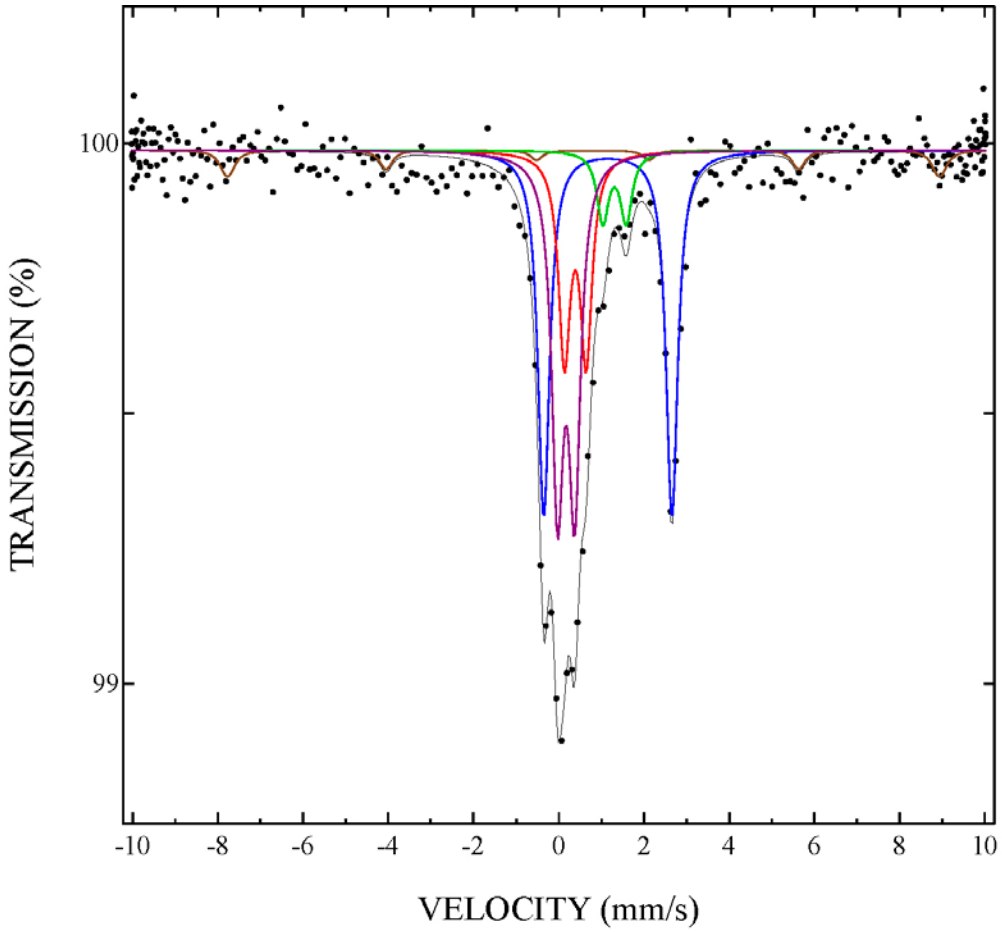


FIG. 4: Mössbauer spectrum recorded from sample P6_R05_165_D555 at 77 K. Components of the fit are displayed above the spectrum. They are: Component 1 in blue, Component 2 in red, Component 3 in violet, Component 4 in brown, and Component 5 in green.

observed in two spectra. Divalent Fe occurred in two distinct surroundings, one with a huge qudrupole splitting of $\sim 3.0$ mm/s, typical of bentonite samples[1] and the other in much smaller concentrations and a smaller quadrupole splitting. Paramagnetic $Fe^{3+}$ occurred in the shape of two components with similar hyperfine paramaters, suggesting that they might originate from similar chemical surroundings, although the difference in isomer shift values might point in the opposite direction.

The nature of the magnetic component could perhaps be studied by SQUID-magnetometry. A ferri- or ferromagnetic component would be observed immediately. An antiferromagnetic component would also be seen by the existence of a Néel temperature, although it may located be far above room-temperature.

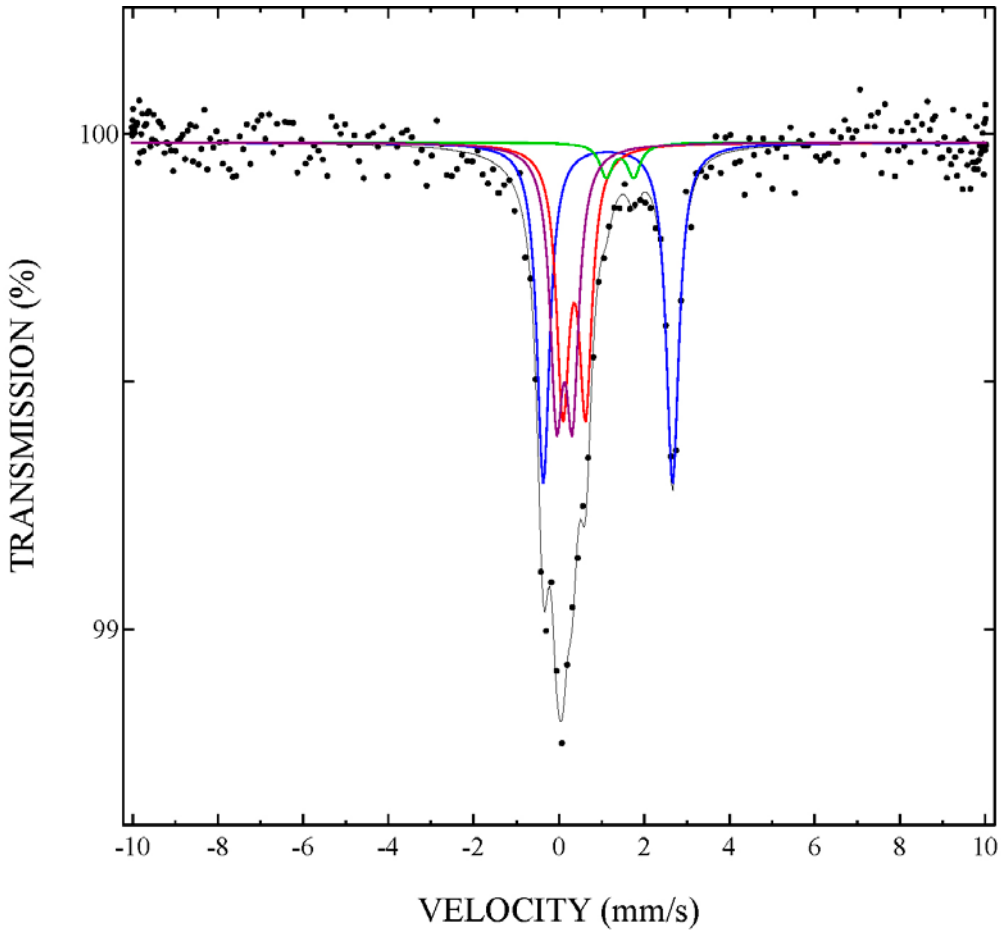


FIG. 6: Mössbauer spectrum recorded from sample P6_R05_165_D615 at 77 K. Components of the fit are displayed above the spectrum. They are: Component 1 in blue, Component 2 in red, Component 3 in violet, and Component 5 in green.

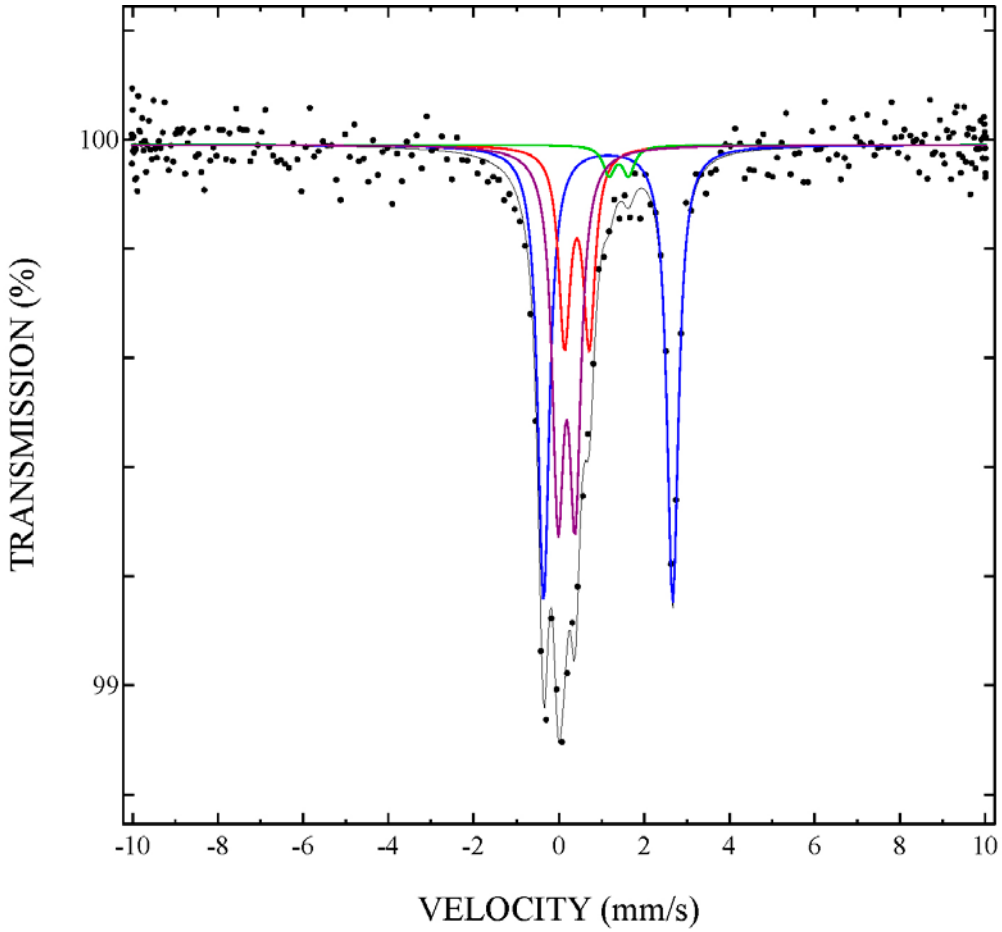


FIG. 7: Mössbauer spectrum recorded from sample R10-270-525 at 77 K. Components of the fit are displayed above the spectrum. They are: Component 1 in blue, Component 2 in red, Component 3 in violet, and Component 5 in green.

TABLE I: Hyperfine parameters of the bentonite samples. The $\chi^2$ value is given in the parentheses after the sample lable. A short-hand notation for the sample labels is used.

| | I (%) | Δ (mm/s) | δ(mm/s) | B(T) | Γ(mm/s) |
|---|---|---|---|---|---|
| R05R, ref1 (0.89981) | | | | | |
| Component 1 | 35.0 | 3.017 | 1.265 | | 0.489 |
| Component 2 | 16.5 | 0.75 | 0.55 | | 0.489 |
| Component 3 | 48.5 | 0.40 | 0.32 | | 0.489 |
| R05R, ref2 (1.02229) | | | | | |
| Component 1 | 27.9 | 2.996 | 1.271 | | 0.608 |
| Component 2 | 12.5 | 0.80 | 0.60 | | 0.608 |
| Component 3 | 51.3 | 0.39 | 0.33 | | 0.608 |
| Component 4 | 8(1) | -0.6(1) | 0.29 | 50(1) | 0.608 |
| D535 (1.15870) | | | | | |
| Component 1 | 41.5 | 2.954 | 1.272 | | 0.465 |
| Component 2 | 14.1 | 0.87 | 0.60 | | 0.465 |
| Component 3 | 44.4 | 0.35 | 0.34 | | 0.465 |
| D555 (0.95985) | | | | | |
| Component 1 | 35.3 | 3.012 | 1.258 | | 0.330 |
| Component 2 | 19.6 | 0.51 | 0.49 | | 0.330 |
| Component 3 | 32.6 | 0.40 | 0.28 | | 0.330 |
| Component 4 | 6(1) | -0.2(1) | 0.80 | 52(1) | 0.330 |
| Component 5 | 6.7 | 0.55 | 1.41 | | 0.330 |
| D575 (1.06049) | | | | | |
| Component 1 | 36.3 | 3.030 | 1.253 | | 0.370 |
| Component 2 | 21.8 | 0.67 | 0.58 | | 0.370 |
| Component 3 | 37.9 | 0.53 | 0.29 | | 0.370 |
| Component 5 | 4.0 | 0.42 | 1.54 | | 0.370 |
| D615 (0.99782) | | | | | |
| Component 1 | 39.0 | 3.036 | 1.255 | | 0.362 |
| Component 2 | 29.0 | 0.53 | 0.46 | | 0.362 |
| Component 3 | 28.1 | 0.37 | 0.23 | | 0.362 |
| Component 5 | 3.9 | 0.65 | 1.54 | | 0.362 |
| 270-525 (0.93777) | | | | | |
| Component 1 | 44.7 | 3.033 | 1.259 | | 0.328 |
| Component 2 | 18.9 | 0.58 | 0.53 | | 0.328 |
| Component 3 | 33.6 | 0.40 | 0.28 | | 0.328 |
| Component 5 | 2.8 | 0.46 | 1.51 | | 0.328 |

# Appendix 2

## Rejected XRD-scans of oriented mounts of the clay fractions from profile P6R08 355A.

The first X-ray scans of oriented mounts of the fine clay fractions from profile P6R08 355A produced diffractograms with large variations in the position of the smectite basal reflections. Furthermore, after EG-solvation several of the samples displayed irrational diffraction patterns, i.e. the d-spacings of the basal reflections did not obey the Bragg law, and the relative peak intensities were anomalous.

For this reason, a second set of oriented mounts was prepared of the Mg-saturated fine clay fractions, which were scanned both in an air-dried and EG-solvated state using another XRD-instrument (Seifert 3000 TT at Lund University; scan parameters according to Section 3.2.6) to test the reproducibility of the diffraction patterns. The XRD-patterns of the re-examined samples did not reproduce the anomalies observed in the first scan. The first series of X-ray scans was therefore rejected because the instrument used was suspected of having an incorrect alignment. For completeness, the XRD-profiles from the first scans are presented below in Figure A2-1 and d-values are listed in Table A2-1.

**Table A2-1. Position of important lines (in Å) used in identification of clay minerals.**

| | Bulk samples | Mg-clay fraction | | | | |
|---|---|---|---|---|---|---|
| **Treatment** | **Randomly oriented** | **Oriented air-dried** | **Oriented+EG** | | | **Interpreted minerals** |
| **Line/interpretation** | **d(060)** | **d(001)** | **d(001)** | **d(002)** | **d(003)** | |
| 525 | 1.496 | 14.27 | 16.41 | 8.35 | 5.57 | Smectite, Cristobalite |
| 527 | 1.497 | 14.03 | 16.25 | 8.39 | 5.59 | Smectite, Cristobalite |
| 574 | 1.498 | 14.29 | 16.45 | 8.45 | 5.60 | Smectite, Cristobalite |
| 620 | 1.497 | 13.06 | 16.19 | 8.31 | 5.55 | Smectite, Cristobalite |
| 735 | 1.497 | 14.03 | 16.46 | 8.40 | 5.59 | Smectite, Cristobalite |
| 786 | 1.497 | 14.52 | 17.83 | 8.57 | 5.66 | Smectite, Cristobalite |
| 837 | 1.496 | 13.78 | 16.11 | 8.35 | 5.57 | Smectite, Cristobalite |
| 846 | 1.498 | 14.11 | 16.40 | 8.42 | 5.60 | Smectite, Cristobalite |
| R1 | 1.496 | 14.20 | 16.89 | 8.49 | 5.63 | Smectite, Cristobalite |
| R2 | 1.495 | – | – | – | – | Smectite |

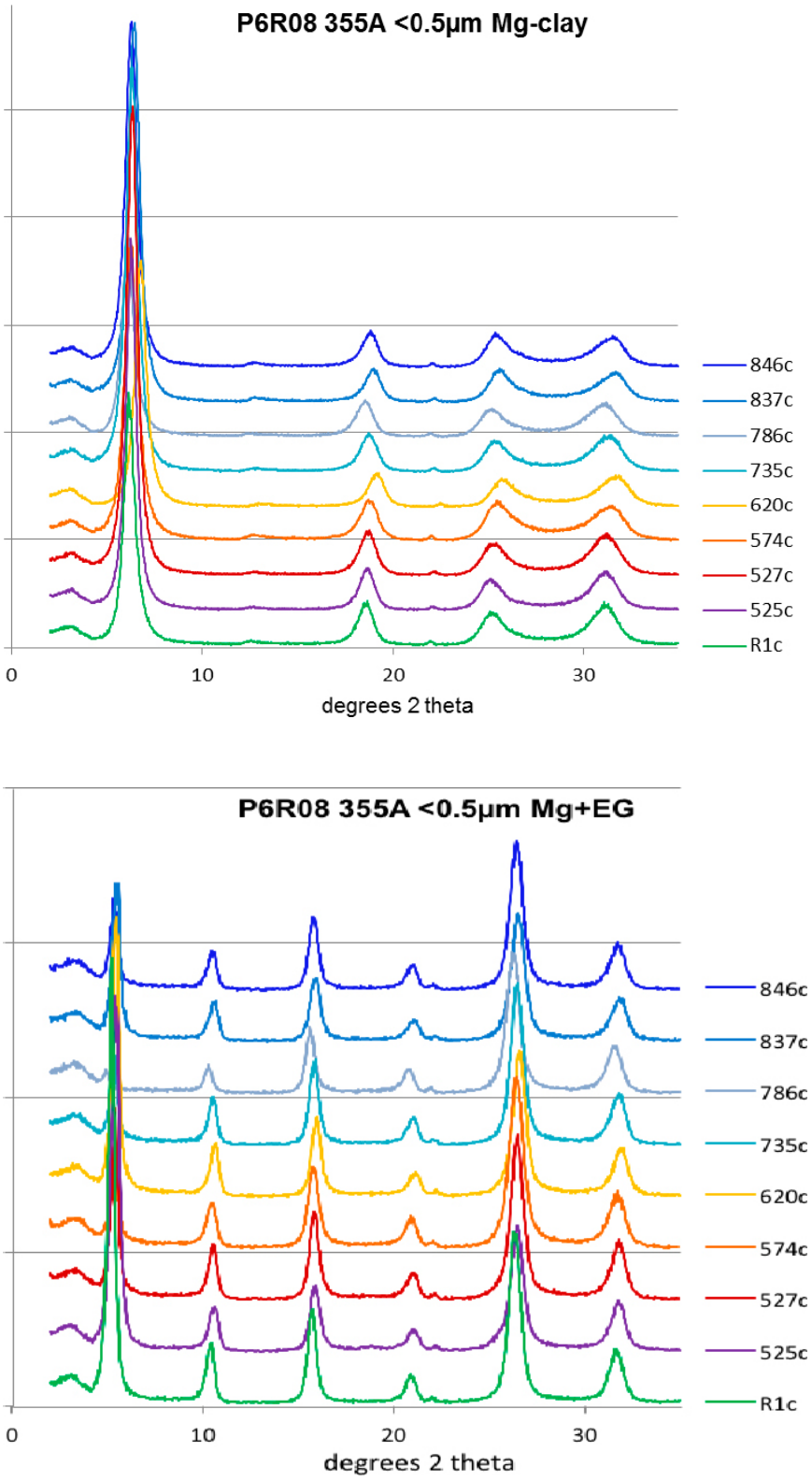


***Figure A2-1.*** *XRD-patterns of air-dried (upper) and EG-solvated (lower) oriented clay fractions from block P6:R08 direction 355A.*